

WASM: Mineral, Energy and Chemical Engineering

**Linking between Multi-scale Behaviours of Brittle Rocks at
Deep Underground Excavation**

Ran Tao

0000-0002-0896-0888

**This thesis is presented for the Degree of
Doctor of Philosophy
of
Curtin University**

October 2022

Declaration

To the best of my knowledge and belief this thesis contains no material previously published by any other person except where due acknowledgement has been made.

This thesis contains no material which has been accepted for the award of any other degree or diploma in any university.

Signature: 

Date: October 2022

Abstract

Rock fracturing is a hot issue in rock engineering. Under high stress, the rocks show different mechanisms on the different scale. The macroscopic fractures development is associated with the microscopic damage evolution. Therefore, this research investigated the failure mechanism based on multi-scale analysis methods. Specifically, the multi-scale is classified into three scales, including micro-scale (grain scale), meso-scale (laboratory scale), and macro-scale (field scale). Under micro-scale, this research analysed quantitative images based on the methods of scanning electron microscopy (SEM) and digital image processing to investigate the micro-structures characteristics. The ratio of tensile damage to shear damage was collected to determine the characteristics of the damage evolution process including initiating stage, propagation stage and failure stage under uniaxial compression tests and triaxial compression tests. Under meso-scale, an updated grain-based model (GBM) was constructed and calibrated, which had a large range of grain size distribution. Moreover, a modified heterogeneity index was proposed to present the heterogeneity induced by grain size. Based on a series of compression tests by GBM, this research investigated the influence of microscopic factors on rock behaviours, including heterogeneity, grain size, mineral distribution, grain shape, and micro-circular defects. Under macro-scale, the GBM was firstly constructed for field scale rock mass containing drives and stope. By comparing with the in-situ observation, this research could effectively mimic the failure modes and damage depth.

Acknowledgements

Firstly, I am sincerely grateful for my supervisors Dr. Mostafa Sharifzadeh, Dr. Hyong Doo Jang for their wonderful guidance and generous support at all stages of my thesis. I also would like to extend my appreciation to my co-supervisor Prof. Erkan Topal and chairman Dr. Boris Albjanic to guide me throughout this research.

I would like to thank Prof. Xia-Ting Feng and Dr. Yan Zhang from Northeast University (China) for providing the laboratory data. I also thank Dr. Saddat from Adelaide University (Australia) and Dr. Bo Hu from Chongqing Jiaotong University (China) for providing related support of grain-based model. I would appreciate Dr. Peter Mikula from Mikula Geotechnics Pty Ltd (Australia) for his great guidance and support based on industry engineering knowledge and experience as well.

Finally, I would like to thank my family and friends. They provide a great support on my life and mentality.

Copyright Statement

I have obtained permission from the copyright owners to use any third-party copyright material reproduced in the thesis (e.g. questionnaires, artwork, unpublished letters), or to use any of my own published work (e.g. journal articles) in which the copyright is held by another party (e.g. publisher, co-author).

Table of Contents

Declaration.....	i
Abstract.....	ii
Acknowledgements.....	iii
Copyright Statement	iv
Table of Contents.....	v
List of Figures	ix
List of Tables.....	xiv
Chapter 1 . Introduction	1
1.1 Introduction	2
1.2 Problem Statement.....	2
1.3 Thesis Objectives	3
1.4 Thesis Outline	3
Chapter 2 . Multiscale Rock Behaviours Mechanisms and Analysis Methods	6
2.1 Introduction	7
2.2 Multi-scale Behaviour Mechanisms	7
2.2.1 Grain Scale Behaviours	7
2.2.2 Laboratory Scale Behaviours	8
2.2.3 Field Scale Behaviours	10
2.3 Physical Methods	12
2.4 Numerical Methods	15
2.4.1 Finite Element Method (FEM)	16
2.4.2 Discrete Element Method (DEM).....	16
2.4.3 Grain-Based Model (GBM).....	17
2.5 Conclusion	19
Chapter 3 . Analysis of Mafic Rocks Microstructure Damage and Failure Process under Compression Test Using Quantitative Scanning Electron Microscopy and Digital Images Processing	30
3.1 Introduction	31
3.2 Background.....	33
3.2.1 Classification of Micro-structures before Test.....	33
3.2.2 Classification of Crack Types after Tests	35
3.3 Experiment Procedure and Micro-cracks Measurement	37
3.3.1 Experiment Procedures	37
3.3.2 Micro-cracks Measurement Procedure.....	38
3.4 Statistical Analysis of Results.....	42

3.4.1 Pre-existing Micro-structures Analysis	42
3.4.2 Post-test Crack Types Analysis.....	47
3.5 Discussion.....	50
3.5.1 Damage Properties under Micro-scale	50
3.5.2 Comparison of Microscopic Damage and Mesoscopic Failure	52
3.6 Conclusion	53
Chapter 4 . The Role of Mineralogical Characteristics of Mafic Rock on its Behaviours Based on Grain-Based Model and Modified Heterogeneity Index und Uniaxial Compression Tests	56
4.1 Introduction	57
4.2 Grain-Based Model Background.....	60
4.3 GBM Specimen Preparation Process	61
4.3.1 Grain Size Distribution and Specimen Dimension	61
4.3.2 Scenarios of Model Setup	64
4.4 GBM Calibration.....	66
4.4.1 Calibration Procedure	66
4.4.2 GBM Micro-parameters.....	67
4.4.3 Calibrated Model Compared with Experimental Result	68
4.5 Results and Discussion	70
4.5.1 Influence of Heterogeneity Index.....	70
4.5.2 Influence of Mineral Distribution	73
4.5.3 Influence of Grain Size.....	76
4.6 Conclusion	81
Chapter 5 . Grain Shape Effect on Rock Behaviours under Uniaxial Compression Test Using Grain Based Model by Inputting Controlled Voronoi Tessellation Data	86
5.1 Introduction	87
5.2 Grain Base Model by Controlled Voronoi Tessellation	90
5.3 Experiment Preparation.....	91
5.3.1 Experiment Procedure	91
5.3.2 Micro-parameters Calibration	93
5.3.3 Construction of Different Grain Shapes.....	95
5.4 Analysis of Grain Shape Effect.....	96
5.4.1 Influence on Rock Macroscopic Mechanical Properties	97
5.4.2 Influence on Fracture Characteristics.....	99
5.5 Conclusion	104

Chapter 6 . Influence of Micro-circular Defects on Fracture Development of Mafic Specimen under Uniaxial Compression Test Using Grain-Based Model	109
6.1 Introduction	110
6.2 Specimen Preparation	113
6.2.1 Experiment Procedure	113
6.2.2 Calibration and Microscopic Mechanical Parameters	115
6.2.3 Model Setup.....	117
6.3 Model Response with Single Hole	118
6.3.1 Effect of Circular Defect Location.....	119
6.3.1 Effect of Inclination Angle of Grain Boundary	121
6.4 Model Response with Double Holes	124
6.4.1 Effect of Bridge Length between Two Holes	127
6.4.2 Effect of Bridge Angle between Two Holes	129
6.5 Conclusion	132
Chapter 7 . Application of Grain-Based Model on Rock Behaviours of Field-scale Tunnel Based on Multiscale Analysis	138
7.1 Introduction	139
7.2 Engineering Background and Specimen Construction.....	141
7.2.1 Background of Mine Site.....	142
7.2.2 Experimental Results	143
7.2.3 Microscopic Parameters Calibration.....	143
7.2.4 Field-scale Numerical Model Construction	146
7.3 Numerical Results	147
7.3.1 One Drive	147
7.3.2 Two Drives.....	149
7.3.3 Two Drives with Stope	150
7.4 Discussion.....	153
7.4.1 Damage Depth.....	153
7.4.2 In-situ Failure	156
7.5 Conclusion	159
Chapter 8 . Conclusions, Challenges and Recommendations	165
8.1 Introduction	166
8.2 Overall Conclusions	166
8.3 Current Challenges	171
8.4 Recommendations for Future Work.....	172
Appendix A: Code of grains construction (Lab-scale)	174

Appendix B: Code of grains construction (Field-scale)	176
Appendix C: Code of specimen construction (Lab-scale)	187
Appendix D: Code of rock mass construction (field-scale).....	188
Appendix E: Code of contact installation.....	191
Appendix F: Code of pre-existing fracture or stope excavation.....	196

List of Figures

Figure 2-1: SEM images showing micro-structural defects in granite: intra-grain cracks (left image), and inter-grain cracks (right image) (modified from Sharifzadeh et al., 2017).....	7
Figure 2-2: Stress-strain diagram determining the stages and thresholds of brittle failure process (after Martin, 1993; Martin & Christiansson, 2009, Eberhardt et al., 2017).....	9
Figure 2-3: The types of rockburst induced by different source mechanisms: (a) strainburst mechanism in hard brittle rock (b) buckling burst mechanism in laminated rock mass (c) fault-slip burst mechanism induced by remote seismic event and shear displacement of discontinuities (modified after Ortlepp & Stacey, 1994)	11
Figure 2-4: Relationship between the failure depth and the maximum tangential stress, as proposed by: (a) Martin et al. (1999), (b) Diederichs et al. (2010), and (c) Perras & Diederics (2016).	12
Figure 2-5: Physical experiments containing different types of flaws: (a) single crack (Zhou et al., 2018), (b) two parallel cracks (Cao et al., 2015), (c) two unparallel cracks (Lee & Jeon, 2011), (d) ellipse hole (Li et al., 2017), (e) different shapes (Zeng et al., 2018), (f) single crack with double holes (Wu et al., 2020), (g) single hole with double cracks (Wu et al., 2020), (h) single hole with multiple cracks (Yang et al., 2019), (i) double holes with multiple cracks (Lin et al., 2020), and (j) multiple holes distribution (Huang et al., 2017)	13
Figure 2-6: Scaled physical experiments: (a) spalling cavern (Zhu et al., 2011), (b) heaving tunnel (Seki et al., 2008), (c) horizontal strata (He et al., 2010), and (d) weak interlayer (Huang et al., 2013)	15
Figure 2-7: Typical grain-based model: (a) square grain model, (b) triangular grain model, (c) polygon grain model, and (d) particle grain model (modified after Li et al., 2019).....	18
Figure 3-1: Investigation structure	33
Figure 3-2: Loading path graph (Left: UCS test; Right: Triaxial test).....	37
Figure 3-3: Fractured specimens (Left: UCS test; Right: Triaxial test)	38
Figure 3-4: Six fragments after tests (1~3 fragments from UCS test; 4~6 fragments from triaxial compressive test).....	38
Figure 3-5: Procedure of digital image processing.	39
Figure 3-6: Zeiss Ultra Plus Scanning Electron Microscope.....	40

Figure 3-7: The main steps of digital image processing (a: SEM image input; b: Binarization or thresholding; c: Image enhancement including despeckle and fillhole; d: skeletonization or thinning cracks)	41
Figure 3-8: Two kinds of speckles	42
Figure 3-9: Pre-existing microstructural defects classification on mafic specimens	43
Figure 3-10: Two patterns of heterogeneity in mafic specimens	44
Figure 3-11: Two growth patterns of particle lattice boundaries in mafic specimen	45
Figure 3-12: Statistics of pre-existing micro-cracks properties of mafic specimens ((A) Percentage of three types of micro-cracks, (B) Geometry properties)	47
Figure 3-13: Statistics of micro-cracks properties measured after test ((A) Percentage of three types of post-test micro-cracks, (B) Geometry properties of post-test micro-cracks) ..	48
Figure 3-14: Statistics of post-test micro-cracks under two types of tests.....	49
Figure 4-1: Different DEM numerical methods to mimic rock specimens (Modified after Potyondy & Cundall, 2004; Cho et al., 2007; Ivars et al., 2008; Hofmann et al., 2015)	60
Figure 4-2: Steps of generation of a grain-based model (modified after Hofmann et al., 2015)	61
Figure 4-3: Particle movement after contact breakage for (a) parallel bond contact and (b) smooth-joint contact (modified after Bahrani et al., 2014)	61
Figure 4-4: Histograms of grain size distribution of each constituent mineral (a: cross-section of mafic sample; b: Pyroxene; c: Plagioclase Feldspar; d: Biotite)	62
Figure 4-5: Grain-Based Model by different scenarios with different MHI	66
Figure 4-6: The stress-strain plots of numerical result and experimental result under uniaxial compression test	69
Figure 4-7: Experimental and numerical test comparison	70
Figure 4-8: Stress-Strain plots of models with different heterogeneity index after UCS tests	71
Figure 4-9: The grain-based models with different heterogeneity index: (a) specimen grain structure (b) macroscopic fracture after UCS tests (c) experimental specimen after UCS tests	72

Figure 4-10: Stress-strain plots of models with different mineral distribution types for Scenario 1	74
Figure 4-11: The grain-based models with different mineral distribution for Scenario 1: (a) specimen grain structure (b) macroscopic fracture after UCS tests	75
Figure 4-12: The grain-based models with different mineral distribution for Scenario 4: (a) specimen grain structure (b) macroscopic fractures after UCS test	76
Figure 4-13: Macroscopic mechanical properties of lowly heterogeneous models with different grain size and different seed number.....	77
Figure 4-14: Lowly heterogeneous models with different grain size: (a) specimen grain structure (b) macroscopic fracture after UCS test.....	78
Figure 4-15: Macroscopic mechanical properties of highly heterogeneous models with different grain size and different seed number.....	79
Figure 4-16: Highly heterogeneous models with different grain size: (a) specimen grain structure (b) macroscopic fracture after UCS test.....	81
Figure 5-1: Grain shapes shown by SEM images (left) and GBM (right).	89
Figure 5-2: Voronoi tessellation generation procedure: (a) nodes distribution (b) Delaunay triangulation network (c) voronoi tessellation generation.....	90
Figure 5-3: Research procedure.	93
Figure 5-4: The construction of three types of grain shapes by voronoi tessellation.	95
Figure 5-5: UCS and modulus of three types of grain models with different slenderness ratio	97
Figure 5-6: Comparison of grain models with same ratio of maximum axial length to minimum axial length (a) hexagon grain models (b) rectangular grain models.	99
Figure 5-7: Fractures of hexagon grain models with different slenderness ratio	101
Figure 5-8: Fractures of rectangular grain models with different slenderness ratio.....	103
Figure 5-9: Fractures of shield-shaped grain models with different slenderness ratio	104
Figure 6-1: Classification of pre-existing defects types (modified after Li et al., 2012; Fan et al., 2015; Lin et al., 2015; Zeng et al., 2018; Yang et al., 2019; Lin et al., 2020; Wu et al., 2020).	113

Figure 6-2: Research procedure to investigate hard rock failure mechanisms with single-hole and double-holes by GBM.....	114
Figure 6-3: Three selected numerical specimens after UCS tests with enlarged view.	118
Figure 6-4: Schematic views and SEM images of micro-circular defect types: (a) & (d) intra-grain hole (b) & (e) inter-grain hole (c) & (f) trans-grain hole.....	119
Figure 6-5: Failures of models with different circular defect types under UCS tests.....	120
Figure 6-6: Average damaged area of each circular defect type.....	120
Figure 6-7: Crack propagation and failure types with different pre-existing hole location and grain boundary inclined angle (modified after Yang et al., 2019).	124
Figure 6-8: The schematic view of the model with double holes.	125
Figure 6-9: Failures of Model #1 specimen with double holes and different bridge length and angle.....	126
Figure 6-10: Failures of Model #2 specimen with double holes and different bridge length and angle.....	126
Figure 6-11: Failures of Model #3 specimen with double holes and different bridge length and angle.....	127
Figure 6-12: Average damage area of models with different bridge length between two holes.	128
Figure 6-13: Failure mechanisms of interaction of two holes with varying distances for Model #3.	128
Figure 6-14: (a) Average damage area and (b) maximum axial displacement of numerical specimens with different bridge angles (α) between two holes.	130
Figure 6-15: Crack propagation and failure types of numerical models and experimental specimens with different bridge angle (modified after Huang et al., 2017; Liu et al., 2019).132	
Figure 7-1: Research procedure.	142
Figure 7-2: In-situ stress vs depth.....	143
Figure 7-3: Comparison of numerical result and experimental result: (a) stress-strain plot (b) fractures	145
Figure 7-4: Particles (left) and grains (right) distribution for almost $\frac{1}{4}$ of model.	147

Figure 7-5: Ultimate failure models containing single drive under in-situ stress at different buried depth	149
Figure 7-6: Ultimate failure models containing two drives with different dip angles under in-situ stress at 400m depth	150
Figure 7-7: Actual stope between two drives: (a) stope scanned by CMS (b) view from upper drive.....	151
Figure 7-8: Ultimate failure models containing two drives connected by stope with different width at the dip angle of 55° and 70°	152
Figure 7-9: Damage depth schematic	153
Figure 7-10: One drive at different depth	154
Figure 7-11: The ratio of damage depth to radius of drive at different depth	154
Figure 7-12: Damaged region of ore drives with different dip angles: (a) Lower drive (b) Upper drive.....	155
Figure 7-13: Damage ratio at different location and dipping angle	156
Figure 7-14: The schematics of three main failures around the surface: (a) buckling (b) rock ejection, and (c) tensile fractures formed by the procedure (i) initial geometry (ii) crack initiation (iii) crack propagation (iv) failure (modified after Orlepp & Stacey, 1994; Germanovich & Dyskin 2000; Li et al., 2019).....	157
Figure 7-15: Ore drive failure close to stope: (a) cross-section scanning (b) in-situ failure.	158
Figure 7-16: Hanging wall failure: (a) cross-section view of scanning, (b) in-situ failure, (c) void after rehab.	158
Figure 7-17: In-situ failure	159

List of Tables

Table 2-1: Overview of the numerical studies on rock behaviours at various scales.	21
Table 3-1: Classification and characteristics of micro-structures and micro-cracks in mafic rocks.	34
Table 3-2: Post-test crack types of mafic specimens.	36
Table 3-3: Damage parameter for each specimen under different stage.	52
Table 4-1: Mineral content and size of mafic specimen.	63
Table 4-2: Data of constituent mineral grain size and heterogeneity index for four scenarios.	66
Table 4-3: Microscopic mechanical parameters for parallel bond and particles.	68
Table 4-4: Microscopic mechanical parameters for smooth-joint contact.	68
Table 4-5: Comparison of experimental and numerical macroscopic mechanical parameter.	69
Table 4-6: The grain sizes of five types of models with high heterogeneity index.	76
Table 4-7: The grain sizes of five types of models with high heterogeneity index.	79
Table 5-1: The node position and their distance of each grain shape.	91
Table 5-2: Microscopic mechanical parameters for parallel bond and particles.	94
Table 5-3: Microscopic mechanical parameters for smooth-joint contact.	94
Table 6-1: Microscopic mechanical parameters for parallel bond and particles.	116
Table 6-2: Microscopic mechanical parameters for smooth-joint contact of mafic specimen.	116
Table 7-1: Microscopic mechanical parameters for parallel bond and particles.	144
Table 7-2: Microscopic mechanical parameters for smooth-joint contact.	144
Table 7-3: Comparison of experimental and numerical macroscopic mechanical parameter.	145
Table 7-4: Grain size and particle size distribution in the model.	147

Chapter 1 . Introduction

1.1 Introduction

In underground excavation, the rock mass behaviours around the tunnel are attributed to the complex geological structures, high in-situ stress, and seismic events. The actual formation of failure at deep underground excavation is always due to fracture development from fine cracks coalescence accompanied by stress concentration. Therefore, the characterization of multiscale rock behaviours is a key issue for the understanding of stress-induced damage in rock mechanics, which includes micro-scale or grain scale, meso-scale or laboratory, and macro-scale or field scale.

1.2 Problem Statement

The studies of brittle rock behaviours have been addressed at a wide range of scales from the micro-scale, e.g. micro-cracks and grain boundaries; through the meso-scale, e.g. fractures in specimens under compression and tensile tests; to the macro-scale, e.g. geological structures in the field rock mass. The rock show different behaviour mechanisms at different scales. At the grain scale, most of the studies focus on the characteristics of heterogeneity, micro-cracks, and mineral composition. At the laboratory scale, most of the studies focus on the rock cracking process, which mainly includes crack initiation, crack propagation, and crack coalescence. At the field scale, most of the studies focus on the mechanisms of failures around the underground excavation, such as failure governed by geological discontinuities and failure governed by high in-situ stress. Macroscopic rock failure is associated with the complicated cracking mechanisms that are involved in the cracking process, and the microscopic factors have a significant influence on rock mechanical properties. Therefore, all scales behaviours are subjected to fracturing damage which influences the engineering performance.

The major difficulty of study on multiscale rock behaviours is investigating the relationship between all scale behaviours, which requires the damage intensity and mechanisms at each scale. A major component of this research is to develop a novel approach or numerical modelling to investigate the process

and mechanisms of underground engineering failure induced by microscopic damage evolution.

1.3 Thesis Objectives

The main objective of this thesis is to gain a better understanding of the multiscale rock behaviours mechanisms. The insight findings will be used to improve the numerical modelling techniques for the evaluation of field-scale tunnel stability. The detail objectives are identified as:

- i. Investigate the microstructures classification and microscopic damage evolution process.
- ii. Investigate the influence of microscopic factors on macroscopic properties under laboratory scale tests, such as heterogeneity, grain size, grain shape, and micro-defects.
- iii. Improve the current numerical model to simulate the field scale failure based on the microscopic damage effect.

1.4 Thesis Outline

- i. **Chapter 2:** Multiscale rock behaviours mechanisms and numerical methods.

Chapter 2 provides a deep insight into the current researches on rock behaviours and their mechanisms at different scales. This chapter also provides current physical methods and numerical methods in terms of finite element methods, discrete element methods, and grain-based models. All numerical methods provide some examples to list their features, applications, and software.

- ii. **Chapter 3:** Analysis of mafic rocks microstructure damage and failure process under compression test using quantitative scanning electron microscopy and image processing.

Chapter 3 provides an overview of the rock characteristics at micro-scale. It provides the classification of microstructures, pre-existing cracks, and deformed cracks based on the scanning electron microscope technique. With

the aid of digital image processing, the quantitative images provide a statistical analysis of micro-cracks, including percentage, length, and area of pre-existing cracks and deformed cracks. Based on the crack area measured by the technique of digital image processing, the ratio of tensile damage to shear damage illustrate the characteristics of the damage evolution process under uniaxial and triaxial compression tests.

- iii. **Chapter 4:** The role of mineralogical characteristics of mafic rock on its behaviours based on the grain-based model and modified heterogeneity index under compression tests.

Chapter 4 provides an updated grain-based model to mimic highly heterogeneous specimens with a large range of grain size distribution. According to the model setup, a modified heterogeneity index is proposed to describe the heterogeneity induced by the grain size of constituent minerals. This chapter also investigates the influence of heterogeneity, grain size, and mineral distribution on rock mechanical properties and fracturing characteristics.

- iv. **Chapter 5:** Grain shape effect on rock behaviours under uniaxial compression test using the grain-based model by inputting controlled Voronoi tessellation data.

Chapter 5 provides the approach of the grain-based model to investigate the influence of grain shape on rock mechanical properties and fracturing characteristics. Current studies on grain shape effects are based on loose granular particles or unbreakable grains, and the grain-based models are always established by random shapes. This chapter uses controlled nodes of Voronoi tessellation to build three main shapes of models with different slenderness ratios, including hexagon grains, rectangular grains, and shield-shaped grains. The mechanical properties and failure modes of all models are figured out in this chapter.

- v. **Chapter 6:** Influence of micro-circular defects on fracture development of mafic specimen under uniaxial compression test using grain-based model.

Chapter 6 provides the influence of circular defects on fracture development under uniaxial compression tests. This chapter uses a grain-based model containing circular defects to investigate the interaction between grain boundaries and holes, including intra-grain holes, inter-grain holes, and trans-grain holes. The models containing double circular defects show the influence of bridge length and bridge angle between two holes on the interaction between two holes.

- vi. **Chapter 7:** Application of grain-based model on stability analysis of field-scale tunnel based on multiscale properties.

Chapter 7 applies the grain-based model on field scale rock mass simulation. The micro-scale grains containing particles are the first time to construct the surrounding rock mass, which could investigate the influence of microscopic damage evolution on field-scale failure. The failure mechanisms and damage depth from the numerical results are compared with the actual in-situ failures, which verifies the application of the grain-based model on large-scale engineering problems on the concept of multiscale rock behaviours.

- vii. **Chapter 8:** Conclusions.

Chapter 8 provides overall conclusions and findings in this research. It also addresses the current challenges and recommendations for future work to improve the studies on multiscale rock behaviours.

Chapter 2 . Multiscale Rock Behaviours Mechanisms and Analysis Methods

2.1 Introduction

Under the condition of high stress, the rock show different internal mechanisms at different scales. Brittle fracturing studies have been carried out at multiscale, including cracks development and grain fracturing at the micro-scale, the failure of the specimen under laboratory tests at meso-scale, and in-situ failure around excavation at macro-scale. Understanding rock behaviours at multiscale plays a significant role in studies of rock mechanics. Therefore, it is essential to develop a suitable method to capture the damage evolution process and the fracture development process, which could present the influence of microscopic behaviours on macroscopic behaviours.

2.2 Multi-scale Behaviour Mechanisms

2.2.1 Grain Scale Behaviours

Natural rocks contain numerous microstructures in terms of grain boundaries, micro-cracks, cleavage, pores or voids, and heterogeneity (Sharifzadeh et al., 2017). According to the characteristics of the micro-cracks location, the micro-cracks are classified into three types, including (i) inter-granular crack along the grain boundaries, (ii) intra-granular crack within the grain, (iii) trans-granular crack cross several grains and boundaries (Simmon & Richter, 1976; Kranz, 1983; He et al., 2010). The micro-cracks observed by scanning electron microscope (SEM) are shown in Figure 2-1.

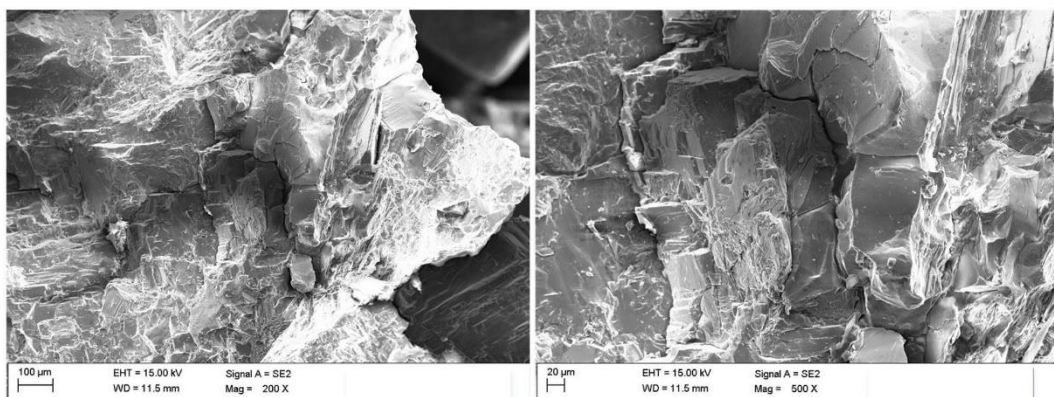


Figure 2-1: SEM images showing micro-structural defects in granite: intra-grain cracks (left image), and inter-grain cracks (right image) (modified from Sharifzadeh et al., 2017)

Additionally, heterogeneity in rocks is presented in different forms (Lan et al., 2010; Peng et al., 2017). The main factors inducing heterogeneity could be divided into three types: mineral composition, grain geometries (e.g. grain shape and size), and micro-

defects. Therefore, numerous researches contributed the studies of the influence of the mineral characteristics and the pre-existing micro-cracks on rock mechanical properties.

Numerous laboratory tests revealed that the same rock-type specimen could present different behaviours and mechanical properties due to material heterogeneity (Martin, 1993). Blair and Cook (1998) illustrated that the material heterogeneity could cause stress concentration, which would accelerate the rock failure in the loading process. Tang et al. (2005) indicated that the homogeneous specimen has a higher strength than the heterogeneous specimen. Nicksiar and Martin (2014) pointed out that the material heterogeneity induced by different grain size could impact the peak strength and crack initiation stress of the specimen.

Not only mineral heterogeneity, but also micro-cracks heterogeneity due to different dimension and orientation has a significant influence on rock behaviours. Griffith (1920) defined the relationship between pre-existing crack length and tensile stress for fracturing at the tips of cracks, which can cause crack growth. Numerous studies confirmed that the smaller length of cracks or grain size will lead to stronger materials (Brace, 1961; Wong et al., 1996; Nicksiar & Martin, 2014). In these cases, the grain boundary is regarded as the stress concentration crack due to the weaker bond. Griffith (1924) also indicated that the inclined cracks can cause a rise in stress concentration. Lajtai (1971) illustrated that the stress concentration is close to the crack tip, and it has the highest stress concentration at 30° between the crack orientation and the maximum principal stress.

2.2.2 Laboratory Scale Behaviours

A vast number of researches contributed to the fundamental theories and findings on the process and characteristics of brittle rock failure during laboratory tests. Griffith (1920) proposed the concept that the weakness of brittle materials is associated with the presence of very small discontinuities or flaws with different dimensions and orientations, which results in stress concentration. Based on the Griffith theory, numerous studies determined the rock failure process, which can be classified into several stages or thresholds based on the stress characteristics, including (i) crack closure (CC), (ii) linear elastic deformation, (iii) crack initiation (CI) and stable crack growth, (iv) crack damage (CD) and unstable crack propagation, (v) failure (peak

strength), and (vi) post-peak behaviour (softening and rupture) (Brace, 1964; Bieniawski, 1967; Eberhardt et al., 2017).

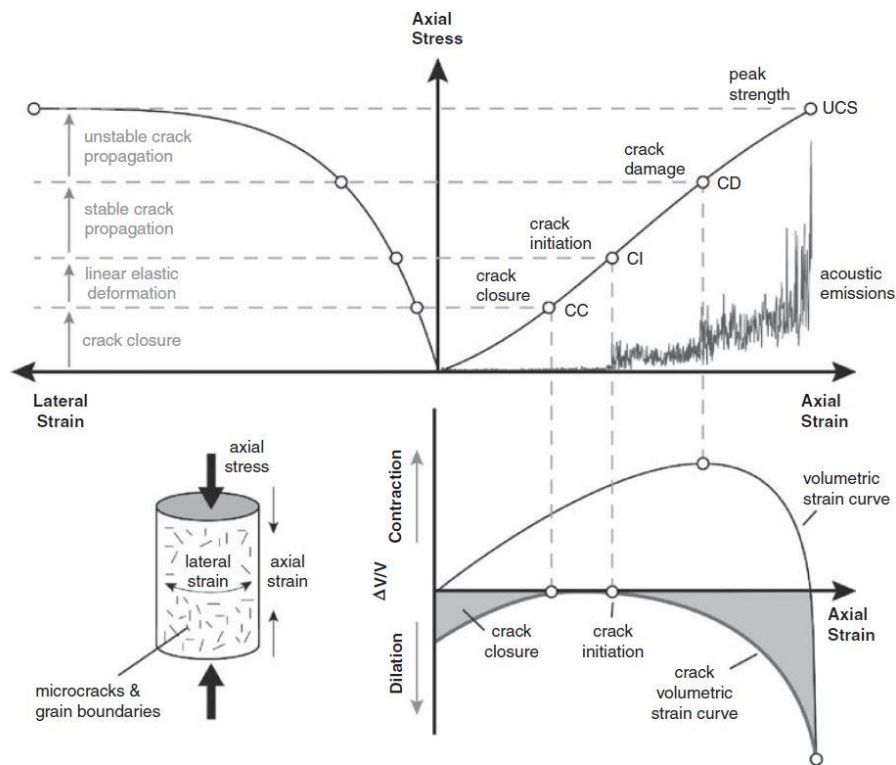


Figure 2-2: Stress-strain diagram determining the stages and thresholds of brittle failure process (after Martin, 1993; Martin & Christiansson, 2009, Eberhardt et al., 2017)

Figure 2-2 presents the typical stress-strain curve and volumetric strain curve with AE monitoring data to determine the stages and thresholds of the brittle failure process. Specifically, the first stage is the crack closure, and the stress-strain curve during this stage is non-linear. Following crack closure, the second stage is linear elastic deformation, which could be used to determine Young's modulus and Poisson's ratio. Crack initiation means that the stress level could lead to micro-fracturing, which is identified by the point at the end of the linear curve. Additionally, the crack initiation is the beginning of increase in crack emission, according to the acoustic emission (AE) monitoring (Cai et al., 2004). According to the in-situ and laboratory monitoring, Martin (1997) indicated that the stress of crack initiation is usually 0.3 – 0.5 times of the uniaxial compressive strength (UCS). After crack initiation, stable crack growth keeps going until the stress reaches the threshold of unstable crack growth, where is the threshold of crack damage. The AE events increases significantly during this stage (Martin, 1993; Diederichs et al., 2004). During the stage of unstable crack growth, the

smaller cracks tend to coalesce into larger cracks and the materials could not support the increase of loading, where the stress level reaches the peak strength.

2.2.3 Field Scale Behaviours

In deep underground mining and civil activities, underground opening suffers a series of engineering problems due to complicated conditions, such as high in-situ stress, complex geological structures, and seismic events. Rockburst is one of the most severe problems encountered during deep underground excavation, which is generally defined as a sudden failure of the rock mass with a violent release of elastic energy and is associated with a seismic event (Ortlepp and Stacey, 1994; Linkov, 1996; Kaiser & Cai, 2012; Li et al., 2019). In order to prevent this phenomenon, numerous researches contributed to the rockburst mechanism and the rockburst damage.

The rockburst is generally induced by a sudden release of strain energy due to seismic events, which has been stored within the rock mass (Cai, 2013). According to field monitoring, the seismic event with energy less than 100 kJ did not cause the rockburst, while the event with energy larger than 1.5 GJ absolutely caused the rockburst (Salamon, 1983). Ortlepp and Stacey (1994) indicated that the damage induced by the seismic event could be rock fragments ejection due to kinetic energy close to excavation and shear displacement due to kinetic energy located in a weak plane. Cai (2013) classified the source as remote seismic events and stress changes close to excavation. Additionally, the rockburst could be divided into five types based on the source mechanism: (i) strainburst causing superficial spalling with violent fragments ejection (Figure 2-3a), (ii) buckling burst causing outward expulsion of large slabs parallel to surface (Figure 2-3b), (iii) face crush – pillar burst causing violent expulsion of rock from stope face or pillar sides, (iv) shear rupture causing violent shear fracture through intact rock mass, and (v) fault-slip burst causing sudden movement on existing fault (Figure 2-3c) (Ortlepp & Stacey, 1994; Ortlepp, 2001; Mazaira & Konicek, 2015).

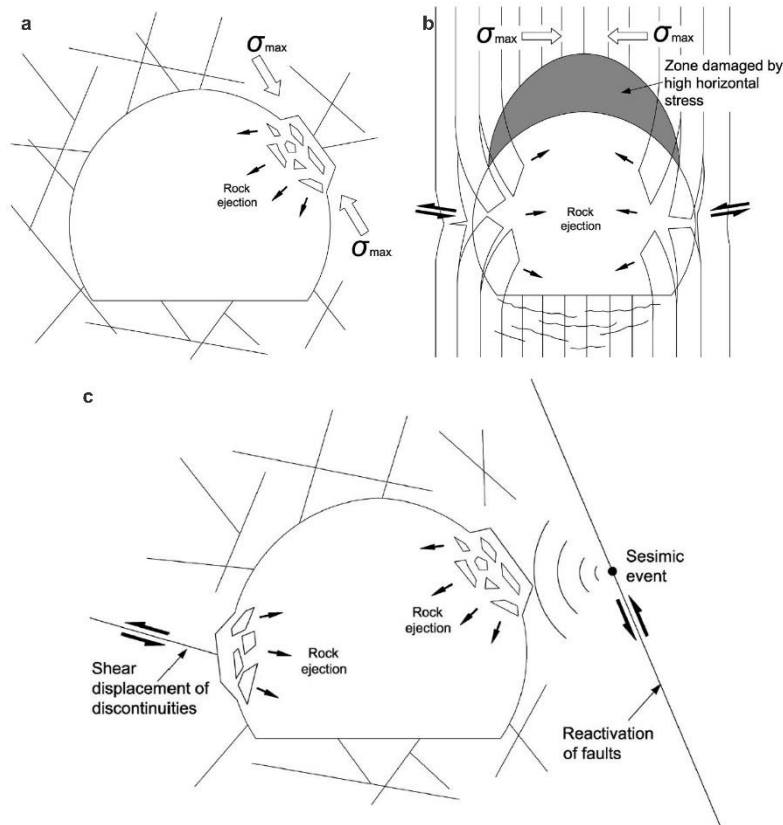


Figure 2-3: The types of rockburst induced by different source mechanisms: (a) strainburst mechanism in hard brittle rock (b) buckling burst mechanism in laminated rock mass (c) fault-slip burst mechanism induced by remote seismic event and shear displacement of discontinuities (modified after Ortlepp & Stacey, 1994)

As another key point in the study of rockburst, the damage mechanism also has been carried out. Based on the field observation, the most common damage induced by rockburst could be divided into five types, including (i) rock ejection, (ii) rock deformation of laminated rock induced by buckling mechanism, (iii) large convergence induced by buckling of roof and wall, and heave of floor, (iv) shear displacement due to large faults, and (v) arch collapse due to kinematic movement along geological structures (Ortlepp & Stacey, 1994; Kaiser et al., 1996; Cai, 2013).

The depth of stress-induced damage in brittle rock is also important for the design of deep underground excavations. Depending on the damage intensity and extent of brittle fracturing, three main damage zones around the underground opening in order of occurrence from opening surface to deep rock mass can be defined as: Highly Damaged Zone (HDZ), Excavation Damaged Zone (EDZ), and Excavation Influence Zone (EIZ) (Diederichs & Martin, 2010; Siren et al., 2015; Perras & Diederichs, 2016). Based on several cases involving brittle failure, Martin et al. (1999) proposed a linear

empirical relationship between the depth of failure and the maximum tangential compressive stress based on UCS (Figure 2-4a). Diederichs et al. (2010) updated the relationship based on the stress level of crack initiation (Figure 2-4b). Perras and Diederichs (2016) determined a group of constants to present a relationship for failure depth for each zone, including HDZ, inner EDZ with interconnected damage, and outer EDZ with partially connected or isolated damage (Figure 2-4c).

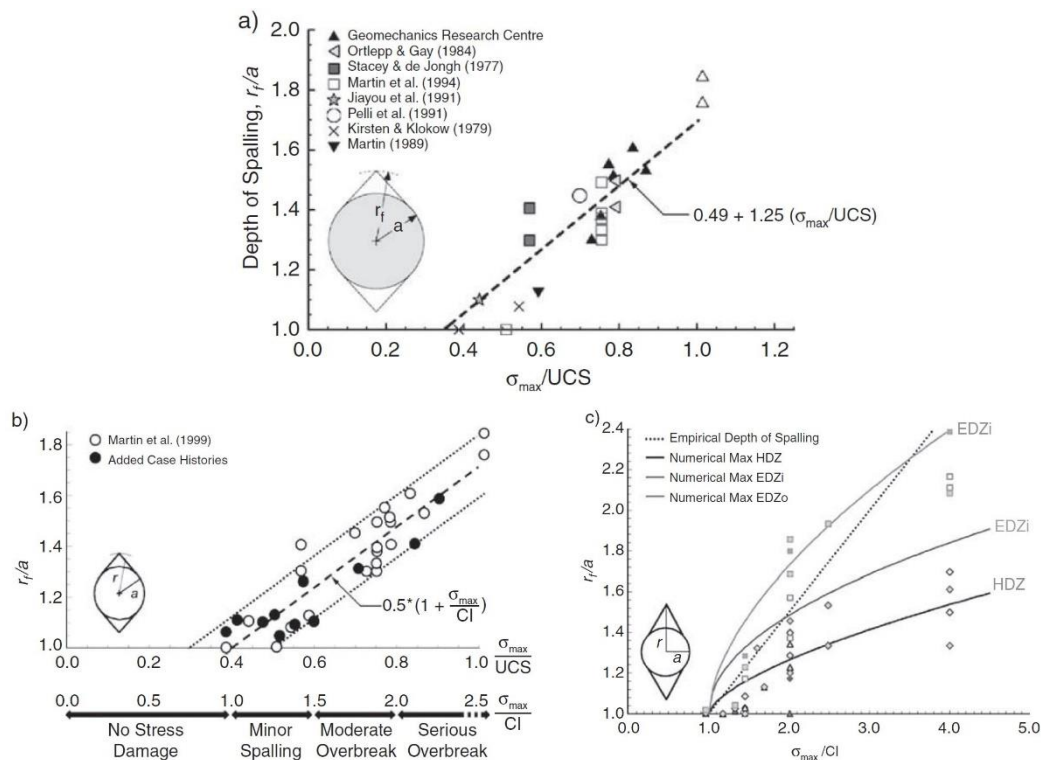


Figure 2-4: Relationship between the failure depth and the maximum tangential stress, as proposed by: (a) Martin et al. (1999), (b) Diederichs et al. (2010), and (c) Perras & Diederichs (2016).

2.3 Physical Methods

The behaviour of natural rock is very complex at different scales, which could use different methods to investigate and capture multiscale behaviours. One of the factors influencing rock mechanical properties is micro-structural defects and heterogeneity. With the development of techniques, several methods could provide insight into the fracture characteristics and failure mechanism at the mineral scale, such as scanning electron microscopes (SEM) applied to the investigation of mineral composition and crystalline structures (He et al., 2010; Zuo et al., 2014; Zhou et al., 2018), acoustic emission (AE) monitoring applied on crack development (Eberhardt, 1998; Diederichs

et al., 2004), and X-ray CT scanning applied on fracturing mechanism (Jia et al., 2013; Nasseri et al., 2014).

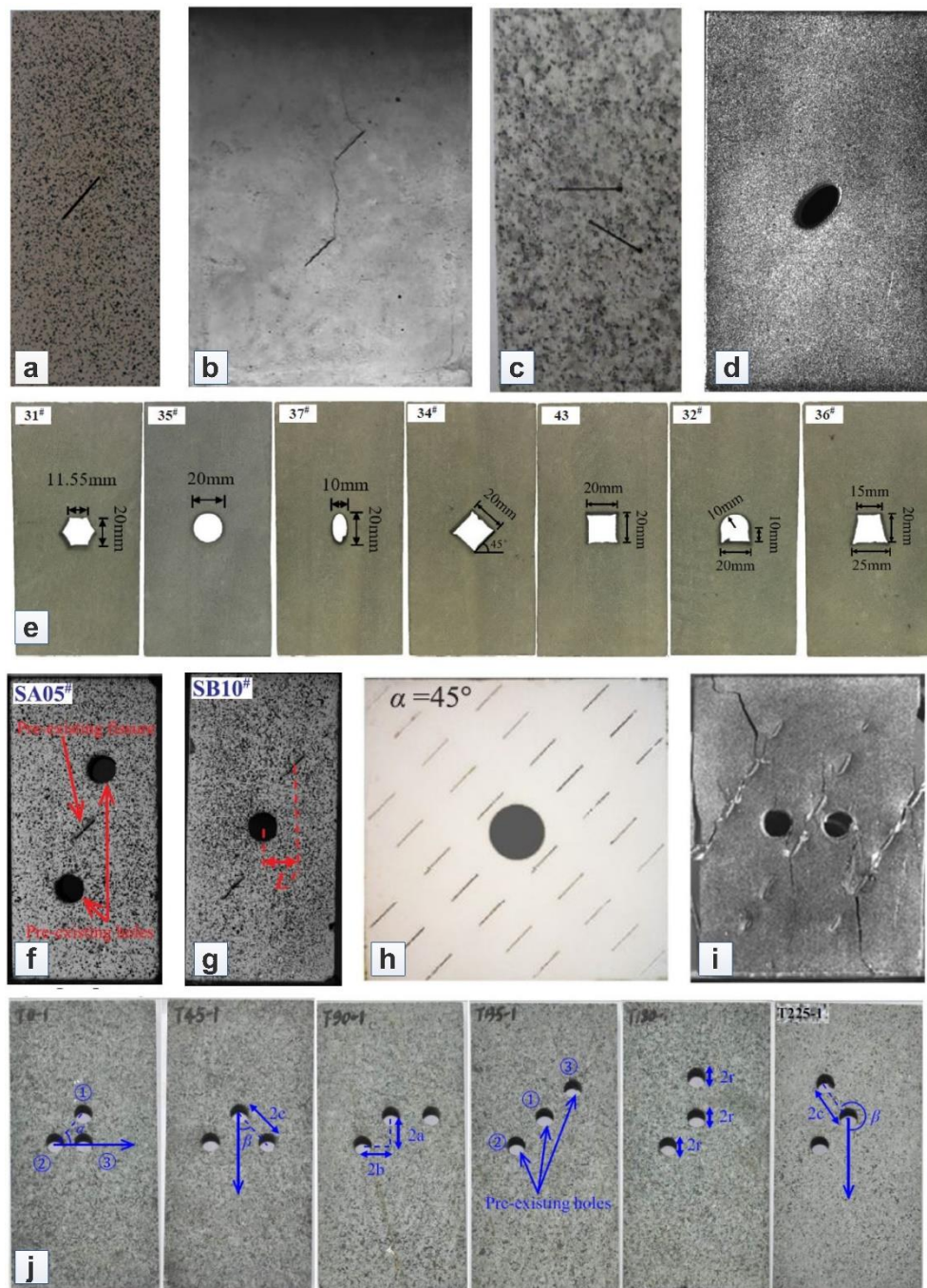


Figure 2-5: Physical experiments containing different types of flaws: (a) single crack (Zhou et al., 2018), (b) two parallel cracks (Cao et al., 2015), (c) two unparallel cracks (Lee & Jeon, 2011), (d) ellipse hole (Li et al., 2017), (e) different shapes (Zeng et al., 2018), (f) single crack with double holes (Wu et al., 2020), (g) single hole with double cracks (Wu et al., 2020), (h) single hole with multiple cracks (Yang et al., 2019), (i) double holes with multiple cracks (Lin et al., 2020), and (j) multiple holes distribution (Huang et al., 2017)

Under mesoscale (laboratory scale), numerous studies constructed the physical specimen containing pre-existing flaws to investigate the mechanical and cracking behaviours, in terms of crack-like flaws and hole-like flaws. Specifically, a series of physical experiments were carried out to investigate the influence of characteristics (e.g. orientation and layout) of crack-like flaws on rock behaviours, including single crack (Wong & Einstein, 2009a; Yang & Jing, 2011; Zhou et al., 2018), parallel double cracks (Wong & Chau, 1998; Wong & Einstein, 2009b; Cao et al., 2015), two unparallel cracks (Lee & Jeon, 2011), and multiple cracks (Yang et al., 2012; Zhou et al., 2014; Cao et al., 2016). Moreover, considering the tunnel shape under the macroscale and pores under the microscale, numerous physical experiments indicated that the rock behaviours are influenced by hole-like flaws due to several factors, including hole size (Wong et al., 2006), hole shape (Zeng et al., 2018; Wu et al., 2020; Zhang et al., 2021), the inclined angle of ellipse hole (Li et al., 2017), and holes distribution with different bridge length and bridge angle (Lin et al., 2015; Huang et al., 2017; Liu et al., 2019). Finally, several physical experiments were carried out to investigate the rock behaviours and interaction between flaws based on the mixed flawed specimens, in terms of single hole combined double cracks (Chen et al., 2017; Wu et al., 2020), double holes combined single crack (Wu et al., 2020), single hole combined multiple cracks (Wang et al., 2017; Yang et al., 2019), and double holes combined multiple cracks (Lin et al., 2020).

In order to investigate the failure mechanism and damage characteristics around the underground opening, Martin et al. (1993) utilised a field-scale circular test tunnel to examine the failure process and investigate the mechanism of notch formation and development. Considering the time and capital consumption, most of the researchers investigate the rock behaviours by in-situ observation of actual failure during engineering activities. Additionally, some researchers investigate the field scale failure based on the scaled physical tests. These tests could present different damage mechanisms, such as spalling (Zhu et al., 2011) and heaving (Seki et al., 2008). It also can indicate the influence of different geological conditions, such as horizontal strata (He et al., 2010) and the weak interlayer (Huang et al., 2013).

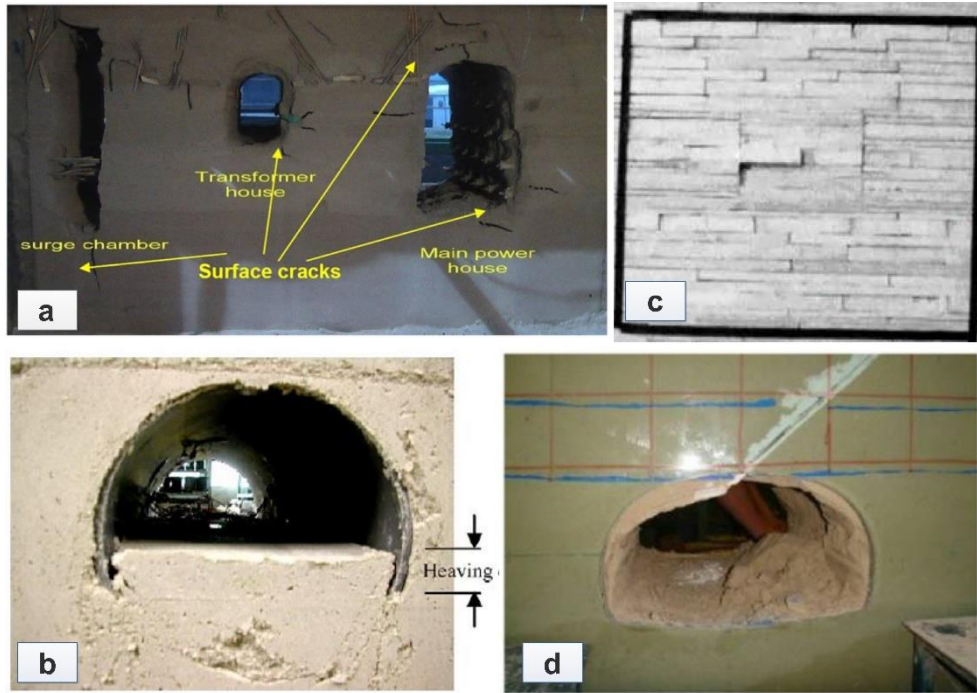


Figure 2-6: Scaled physical experiments: (a) spalling cavern (Zhu et al., 2011), (b) heaving tunnel (Seki et al., 2008), (c) horizontal strata (He et al., 2010), and (d) weak interlayer (Huang et al., 2013)

2.4 Numerical Methods

As an important approach, numerical simulation is widely applied in studies of rock behaviours. Natural rock is very complex, so it is necessary to include the following conditions into the model for properly simulating the rock mass (Jing, 2003): (i) the presence of natural discontinuities, (ii) properties variation at different locations (i.e. rock heterogeneity), (iii) properties variation in the different direction (i.e. rock anisotropy), (iv) properties variation at different scales, and (v) stress state.

According to the computation types, there are three main categories, including continuum method (e.g. finite element method), discontinuum method (e.g. discrete element method), and hybrid method (e.g. finite-discrete element method). The decision for choosing suitable numerical methods is based on (i) potential failure mechanisms, (ii) joint spacing and frequency, and (iii) size of joints with respect to the size of the project (Hamdi, 2015). Generally, it is suggested that the continuum method could be applied to intact or massive rock mass and heavily jointed rock mass where is valid for a continuum assumption. The discontinuum or hybrid model is used to simulate the discontinuities behaviour and intact rock fracturing.

2.4.1 Finite Element Method (FEM)

In the continuum method, a key fundamental assumption is that the deformation of a material induced by external loads must be continuous. All neighbouring material towards the problem domain remain the same neighbourhood throughout the deformation, which means that the rotation and detachment of mesh are unavailable.

The continuum method has been widely used in the study of field-scale rock behaviours due to efficient computation. As one of the most common methods, the finite element method (FEM) is effective to handle material heterogeneity and anisotropy, and complex boundary conditions. The FEM has been applied to the investigation mechanical mechanism of the failure zone of surrounding rock (Diederichs, 2007; Huang et al., 2013; Li et al., 2014; Zhu et al., 2020).

Additionally, the code of real fracture process analysis (RFPA) combines the principles of FEM and elastic fracture mechanics, which is composed of elements with different properties induced by Weibull distribution (Zhu et al., 2005). RFPA was employed to investigate the fracture mechanism of heterogeneous rock at both the laboratory scale and engineering problems at the field scale (Tang & Kaiser, 1998; Wang et al., 2009; Liang et al., 2019).

2.4.2 Discrete Element Method (DEM)

The natural rock mass contains numerous discontinuities, which limits the continuum approach to capture sliding and large displacement. The discrete element method (DEM) proposed by Cundall (1971) is the most widely used discontinuum approach to mimic rock mass by blocks or particles bonded together with discontinuities. The main advantage of the discontinuum method compared to the continuum method is the movement of blocks or particles.

The DEM is widely applied on different scale. The particle or particle cluster could represent grain, so it is commonly used to investigate the microscale and mesoscale rock behaviours. Numerous studies employed DEMs to investigate the influence of factors on rock mechanical properties and fracturing characteristics, including heterogeneity (Lan et al., 2010; Peng et al., 2017a; Liakas et al., 2017; Nagaso et al., 2019), grain size (Hofmann et al., 2015; Gui et al., 2016; Peng et al., 2017b; Manso et

al., 2019), and pre-existing flaws (Fakhimi et al., 2002; Fan et al., 2015; Liu et al., 2018; Saadat & Taheri, 2019). Although DEM has high computation consumption for field scale simulation, it is still popular since the model could explicitly and directly present the actual failure conditions (e.g. separation and sliding in rock mass). For example, Wang and Tannant (2004) utilized the particle bonded model (PBM) to investigate the fracture around highly stressed tunnel and the impact of the thin liner for ground control. Lan et al. (2013) constructed the polygon-based DEM by Voronoi tessellation to analyse the in-situ rock mass damage evolution. Boon et al. (2015) employed DEM to simulate the blocky rock mass for support design. Karampinos et al. (2015) constructed DEM to study the mechanism of deformation and buckling in the foliated rock mass. Wang and Cai (2020) proposed the discrete fracture network combined DEM (DFN-DEM) to simulate the mechanical response of jointed rock mass based on the field mapping data.

2.4.3 Grain-Based Model (GBM)

Recently, considering the influence of mineral structure on rock behaviours, the grain-based model (GBM) is widely developed both on the discontinuum approach and the continuum approach. Based on the grain shape, three main grain-based methods are categorized (Figure 2-7): square grain method, block or polygon grain method, and particle grain method (Li et al., 2019).

The square grain method is implemented in continuum methods of the Fast Lagrangian Analysis of Continua (FLAC) and the RFPA. The model consists of a series of homogeneous and isotropic square elements, which construct irregularly shaped grains (Zhang & Wong, 2018). With the assistance of digital image processing (DIP), it has high accuracy in presenting the heterogeneity induced by grain geometry. This method is applied to a series of experiment simulations, including UCS tests (Li et al., 2003; Liu et al., 2004), and Brazilian disc tests (Chen et al., 2004; Yu et al., 2015). However, this method has limitations: (i) could not present the characteristics of grain boundaries, and (ii) the fracture is depended on the element degradation rather on the realistic separation or sliding.

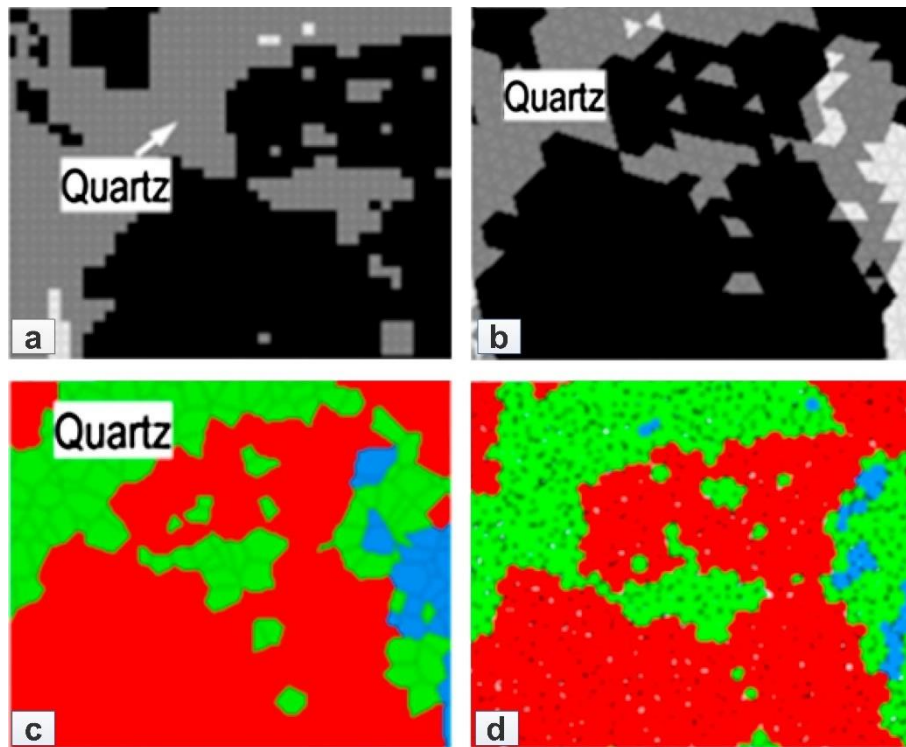


Figure 2-7: Typical grain-based model: (a) square grain model, (b) triangular grain model, (c) polygon grain model, and (d) particle grain model (modified after Li et al., 2019)

The block (polygon) grain methods are widely applied in DEMs by the universal distinct element code (UDEC) and 3D distinct element code (3DEC). The model consists of a series of blocks and the fracturing is presented by debonding of neighbouring blocks, so the block grain method could reproduce the discontinuities and directly simulate the behaviours of separation and sliding. This method is divided into the triangular grain model and the polygon grain model based on the block shape, where the polygon grains generated by Voronoi tessellation provide more actual morphology (Gao et al., 2016). Moreover, the triangular grain model contributes a smoother pathway and results in lower UCS due to the less possibility of interlocking grains compared with Voronoi tessellation (Ghazvinian et al., 2014; Mayer & Stead, 2017). This block grain method is widely used on numerous numerical tests to investigate the influence of heterogeneity on rock mechanical properties and fracturing characteristics (Lan et al., 2010; Chen & Konietzky, 2014; Nicksiar & Martin, 2014; Gui et al., 2016; Tan et al., 2016; Park et al., 2017). Although this method explicitly and directly presents heterogeneity and fracturing, it has limits on grain crushing and rotation (Lan et al., 2013).

The particle grain method provides some novel ideas in GBM. The initial particle grain method uses circular (2D) or spherical (3D) to simulate sand and soil (Powrie et al.,

2005). The bonded particle model (e.g. parallel bond model) was proposed, where each particle is regarded as a mineral grain. However, the circular and smooth particles lead to a low strength ratio of UCS to tensile strength compared to laboratory results (Cho et al., 2007; Yoon et al., 2012). The irregular grain aggregation could increase the grain interlocking and present a rough grain surface (Li et al., 2016). This aggregation is regarded as the cluster or clump, which effectively increase the strength ratio. However, the clumped particles are hard to break due to their rigid bodies, which does not agree with the actual conditions (Erarslan & Williams, 2012). Ivars et al. (2008) proposed the smooth-joint model (SJM) to simulate the sliding behaviour at the interface between particle pairs. The smooth-joint contact would lose its effect when the large deformation occurs (Mehranpour & Kulatilake, 2017), which is suitable to simulate the grain boundary. Potyondy (2010) proposed a grain-based model, which consists of grain (e.g. parallel bond model) and grain boundary (e.g. smooth-joint contact). Recently, this GBM is approved that it could effectively mimic actual heterogeneous rock behaviours due to the crushable grain and grain boundary generated by smooth-joint contact (Bewick et al., 2013; Bahrani et al., 2014).

2.5 Conclusion

According to the previous studies of brittle fracturing behaviours at different scales, both grain fracturing and rock mass failure are associated with the development of pre-existing flaws or discontinuities, which could be divided into three main stages, including initiation, propagation, and coalescence. With the development of numerical methods, it is possible to simulate the discrete fracturing process in more detail. The overview of different numerical methods is listed in Table 2-1 from the aspect of application area, code, crushing ability, and advantages/ disadvantages. After comparison of all numerical methods, GBM implemented in particle flow code (PFC) is a suitable method applied on micro- and meso-scale simulation due to the following factors: (i) grain crush is available; (ii) smooth-joint contact regarded as the grain boundary could lose effect as large deformation occurs; (iii) polygon grain shape generated by Voronoi tessellation could mimic actual rock heterogeneity induced by grain geometry, grain dimension, and mineral composition. In the following chapters, the brittle fracturing behaviours at different scales would be characterized based on

GBM and develop the GBM for field scale simulation containing micro-structures to reveal the relationship between multiscale rock behaviours.

Table 2-1: Overview of the numerical studies on rock behaviours at various scales.

Method	Code	Application	Results	Features	Authors
FEM	RFPA	Uniaxial compression test	Failure process of granite	Square grain model; element degradation for fracture	Li et al., 2003; Liu et al., 2004
FEM	RFPA	Biaxial compression test	Fracturing process around underground excavation	Heterogeneity in rock properties; cracking spontaneously occur	Zhu et al., 2005
FEM	Phase2	Field scale tunnel	Spalling depth prediction in massive brittle rocks	Damage zone; no directly fracturing	Diederichs, 2007
DEM	PFC-PBM	Triaxial compression test	The influence of heterogeneity induced by mineral composition on strength	Heterogenous specimens containing weaker material; the weak material is not randomly distributed	Liakas et al., 2017
DEM	PFC-PBM	Brazilian disc test	Mechanical properties impacted by various clump size	Clumped particle grains; rigid grain	Manso et al., 2019
DEM	PFC-PBM	Field scale tunnel	Fracture around a highly stressed and lining tunnel	Lower strength due to circular and smooth surface of particle	Wang & Tannat, 2004
DEM	UDEC-GBM	Uniaxial compression test	Stress governed by microheterogeneity of grain	Polygon grain model; more realistic grain morphology; unbreakable grain	Lan et al., 2010; Chen & Konietzky, 2014; Gui et al., 2016
DEM	UDEC-GBM	Field scale tunnel	In-situ rock mass damage evolution	Capture damage evolution process; unbreakable grain	Lan et al., 2013
DEM	PFC-GBM	Uniaxial compression test	The influence of micro-factors	Polygon grains; grain crushing is available; heterogeneous mineral composition; dual contacts for grain and grain boundary	Nicksiar & Martin, 2014; Hofmann et al., 2015; Peng et al., 2017a;
DEM	PFC-GBM	Uniaxial compression test	Influence of pre-existing flaw	Lack of field scale model due to huge computation consumption	Saadat & Taheri, 2019

Reference

- Bahrani, N., Kaiser, P. K., & Valley, B. (2014). Distinct element method simulation of an analogue for a highly interlocked, non-persistently jointed rockmass. *International Journal of Rock Mechanics & Mining Sciences*, 71: 117-130.
- Bewick, R. P., Kaiser, P. K., Bawden, W. F., & Bahrani, N. (2013). DEM simulation of direct shear: 1. rupture under constant normal stress boundary conditions. *Rock Mechanics and Rock Engineering*, 1647-1671.
- Bieniawski, Z. T. (1967). Mechanism of brittle rock fracture: Part I - Theory of the fracture process. *International Journal of Rock Mechanics and Mining Science*, 395-406.
- Blair, S. C., & Cook, N. G. (1998). Analysis of compressive fracture in rock using statistical techniques: Part II. Effect of microscale heterogeneity on macroscopic deformation. *International Journal of Rock Mechanics and Mining Sciences*, 849-861.
- Boon, C. W., Housby, G. T., & Utili, S. (2015). Designing Tunnel Support in Jointed Rock Masses Via the DEM. *Rock Mechanics and Rock Engineering*, 48: 603-632.
- Brace, W. F. (1964). Brittle fracture of rocks. In W. R. Judd, *State of Stress in the Earth's Crust: Proceedings of the International Conference* (pp. 110-178). Santa Monica: American Elsevier Publishing Co.
- Brace, W. F. (1961). Dependence of fracture strength of rocks on grain size. *Bulletin of the Mineral Industries Experiment Station, Mining Engineering Series, Rock Mechanics*, 76: 99-103.
- Cai, M. (2013). Principles of rock support in burst-prone ground. *Tunnelling and Underground Space Technology*, 36: 46-56.
- Cai, M., Kaiser, P. K., Tasaka, Y., Maejima, T., Morioka, H., & Minami, M. (2004). Generalized crack initiation and crack damage stress thresholds of brittle rock masses near underground excavations. *International Journal of Rock Mechanics and Mining Sciences*, 41: 833-847.
- Cao, P., Liu, T., Pu, C., & Lin, H. (2015). Crack propagation and coalescence of brittle rock-like specimens with pre-existing cracks in compression. *Engineering Geology*, 187: 113-121.
- Cao, R.-h., Cao, P., Fan, X., Xiong, X., & Lin, H. (2016). An experimental and numerical study on mechanical behavior of ubiquitous-joint brittle rock-like specimens under uniaxial compression. *Rock Mechanics and Rock Engineering*, 49: 4319-4338.
- Chen, M. L., Jing, H. W., Ma, X. J., Su, H. J., Du, M. R., & Zhu, T. T. (2017). Fracture evolution characteristics of sandstone containing double fissures and a single circular hole under uniaxial compression. *International Journal of Mining Science and Technology*, 27: 499-505.
- Chen, S., Yue, Z. Q., & Tham, L. G. (2004). Digital image-based numerical modeling method for prediction of inhomogeneous failure. *International Journal of Rock Mechanics and Mining Sciences*, 41: 939-957.
- Chen, W., & Konietzky, H. (2014). Simulation of heterogeneity, creep, damage and lifetime for loaded brittle rocks. *Tectonophysics*, 633: 164-175.
- Cho, N., Martin, C. D., & Sego, D. C. (2007). A clumped particle model for rock. *International Journal of Rock Mechanics and Mining Sciences*, 997-1010.
- Cundall, P. (1971). A computer model for simulating progressive large-scale movements in blocky rock systems. *Proceeding of the Symposium of the International Society of Rock Mechanics*, (pp. 11-18). Nancy, France.

- Diederichs, M. S. (2007). The 2003 Canadian Geotechnical Colloquium: Mechanistic interpretation and practical application of damage and spalling prediction criteria for deep tunnelling. *Canadian Geotechnical Journal*, 44: 1082-1116.
- Diederichs, M. S., & Martin, C. D. (2010). Measurement of Spalling Parameters from Laboratory Testing. *European Rock Mechanics Symposium (EUROCK2010)* (pp. 323-326). Lausanne: CRC Press.
- Diederichs, M. S., Carter, T., & Martin, C. D. (2010). Practical rock spall predictions in tunnels. *World Tunnel Congress 2010* (pp. 1-8). Vancouver: Tunnelling Association of Canada.
- Diederichs, M. S., Kaiser, P. K., & Eberhardt, E. (2004). Damage initiation and propagation in hard rock during tunnelling and the influence of near-face stress rotation. *International Journal of Rock Mechanics and Mining Sciences*, 41: 785-812.
- Eberhardt, E., Diederichs, M. S., & Rahjoo, M. (2017). Pre-peak brittle fracture damage. In Feng, *Rock Engineering* (pp. 623-657).
- Eberhardt, E. B. (1998). Brittle rock fracture and progressive damage in uniaxial compression. *Ph.D. thesis, Department of Geological Sciences, University of Saskatchewan, Saskatoon.*
- Erarslan, N., & Williams, D. J. (2012). Investigating the effect of cyclic loading on the indirect tensile strength of rocks. *Rock Mechanics and Rock Engineering*, 327-340.
- Fakhimi, A., Carvalho, F., Ishida, T., & Labuz, J. F. (2002). Simulation of failure around a circular opening in rock. *International Journal of Rock Mechanics and Mining Sciences*, 39: 507-515.
- Fan, X., Kulatilake, P., & Chen, X. (2015). Mechanical behavior of rock-like jointed blocks with multi-non-persistent joints under uniaxial loading: A particle mechanics approach. *Engineering Geology*, 190: 17-32.
- Gao, F., Stead, D., & Elmo, D. (2016). Numerical simulation of microstructure of brittle rock using a grain-breakable distinct element grain-based model. *Computers and Geotechnics*, 203-217.
- Ghazvinian, E., Diederichs, M. S., & Quey, R. (2014). 3D random Voronoi grain-based models for simulation of brittle rock damage and fabric-guided micro-fracturing. *Journal of Rock Mechanics and Geotechnical Engineering*, 6: 506-521.
- Griffith, A. A. (1920). The phenomena of rupture and flow in solids. *Philosophical Transactions of the Royal Society of London, Series A: Mathematical and Physical Sciences*, 163-198.
- Griffith, A. A. (1924). The theory of rupture. In C. B. Biezeno, & J. M. Burgers, *Proceedings of first international congress for applied mechanics* (pp. 55-63).
- Gui, Y., Zhao, Z., Ji, J., Wang, X., Zhou, K., & Ma, S. (2016). The grain effect of intact rock modelling using discrete element method with Voronoi grains. *Géotechnique Letters*, 6: 136-143.
- Hamdi, P. (2015). Characterization of Brittle Damage in Rock from the Micro to Macro Scale. *Ph.D. thesis, Department of Earth Sciences, Simon Fraser University.*
- He, M. C., Gong, W. L., Zhai, H. M., & Zhang, H. P. (2010). Physical modeling of deep ground excavation in geologically horizontal strata based on infrared thermography. *Tunnelling and Underground Space Technology*, 25: 366-376.
- He, M., Nie, W., Han, L., & Ling, L. (2010). Microcrack analysis of Sanya granite fragments from rockburst tests. *Mining Science and Technology*, 20: 238-243.

- Hofmann, H., Babadagli, T., Yoon, J. S., & Zang, A. (2015). A grain based modelling study of mineralogical factors affecting strength, elastic behaviour and micro fracture development during compression tests in granites. *Engineering Fracture Mechanics*, 147: 261-275.
- Huang, F., Zhu, H., Xu, Q., Cai, Y., & Zhuang, X. (2013). The effect of weak interlayer on the failure pattern of rock mass around tunnel - Scaled model tests and numerical analysis. *Tunnelling and Underground Space Technology*, 35: 207-218.
- Huang, Y.-H., Yang, S.-Q., Ranjith, P. G., & Zhao, J. (2017). Strength failure behavior and crack evolution mechanism of granite containing pre-existing non-coplanar holes: Experimental study and particle flow modeling. *Computers and Geotechnics*, 88: 182-198.
- Ivars, D. M., Potyondy, D. O., Pierce, M., & Cundall, P. A. (2008). The smooth-joint contact model. *8th. World Congress on Computational Mechanics/5th. European Congress on Computational Methods in Applied Sciences and Engineering*. Venics, Italy.
- Jia, L., Chen, M., Zhang, W., Xu, T., Zhou, Y., Hou, B., & Jin, Y. (2013). Experimental study and numerical modeling of brittle fracture of carbonate rock uniaxial compression. *Mechanics Research Communications*, 50: 58-62.
- Jing, L. R. (2003). A review of techniques, advances and outstanding issues in numerical modelling for rock mechanics and rock engineering. *International Journal of Rock Mechanics and Mining Sciences*, 40: 283-353.
- Kaiser, P. K., & Cai, M. (2012). Design of rock support system under rockburst condition. *Journal of Rock Mechanics and Geotechnical Engineering*, 4: 215-227.
- Kaiser, P. K., Tannant, D. D., & McCreath, D. R. (1996). *Canadian rockburst support handbook*. Sudbury, Ontario: Geomechanics Research Centre, Laurentian University.
- Karampinos, E., Hadjigeorgiou, J., Hazzard, J., & Turcotte, P. (2015). Discrete element modelling of the buckling phenomenon in deep hard rock mines. *International Journal of Rock Mechanics & Mining Sciences*, 80: 346-356.
- Lajtai, E. Z. (1971). A theoretical and experimental evaluation of Griffith theory of brittle fracture. *Tectonophysics*, 11: 129-156.
- Lan, H., Martin, C. D., & Andersson, J. C. (2013). Evolution of In Situ Rock Mass Damage Induced by Mechanical-Thermal Loading. *Rock Mechanics and Rock Engineering*, 46: 153-168.
- Lan, H., Martin, C. D., & Hu, B. (2010). Effect of heterogeneity of brittle rock on micromechanical extensile behavior during compression loading. *Journal of Geophysical Research Solid Earth*, 115, 414-431.
- Lee, H., & Jeon, S. (2011). An experimental and numerical study of fracture coalescence in pre-cracked specimens under uniaxial compression. *International Journal of Solids and Structures*, 48: 979-999.
- Li, C. C., Mikula, P., Simser, B., Hebblewhite, B., Joughin, W., Feng, X., & Xu, N. (2019). Discussions on rockburst and dynamic ground support in deep mines. *Journal of Rock Mechanics and Geotechnical Engineering*, 11: 1110-1118.
- Li, D., Zhu, Q., Zhou, Z., Li, X., & Ranjith, P. G. (2017). Fracture analysis of marble specimens with a hole under uniaxial compression by digital image correlation. *Engineering Fracture Mechanics*, 183: 109-124.

- Li, L., Lee, P. K., Tsui, T., Tham, L. G., & Tang, C. A. (2003). Failure process of granite. *International Journal of Geomechanics*, 3: 84-98.
- Li, X. F., Li, H. B., Liu, Y. Q., Zhou, Q. C., & Xia, X. (2016). Numerical simulation of rock fragmentation mechanisms subject to wedge penetration for TBMs. *Tunnelling and Underground Space Technology*, 53: 96-108.
- Li, X., Li, H., & Zhao, J. (2019). The role of transgranular capability in grain-based modelling of crystalline rocks. *Computers and Geotechnics*, 110: 161-183.
- Li, Y., Zhang, D., Fang, Q., Yu, Q., & Xia, L. (2014). A physical and numerical investigation of the failure mechanism of weak rocks surrounding tunnels. *Computers and Geotechnics*, 61: 292-307.
- Liakas, S., O'Sullivan, C., & Saroglou, C. (2017). Influence of heterogeneity on rock strength and stiffness using discrete element method and parallel bond model. *Journal of Rock Mechanics and Geotechnical Engineering*, 9: 575-584.
- Liang, Z., Gong, B., & Li, W. (2019). Instability analysis of a deep tunnel under triaxial loads using a three-dimensional numerical method with strength reduction method. *Tunnelling and Underground Space Technology*, 86: 51-62.
- Lin, P., Wong, R. H., & Tang, C. A. (2015). Experimental study of coalescence mechanisms and failure under uniaxial compression of granite containing multiple holes. *International Journal of Rock Mechanics & Mining Sciences*, 77: 313-327.
- Lin, Q., Cao, P., Meng, J., Cao, R., & Zhao, Z. (2020). Strength and failure characteristics of jointed rock mass with double circular holes under uniaxial compression: Insights from discrete element method modelling. *Theoretical and Applied Fracture Mechanics*, 109: 102692.
- Linkov, A. M. (1996). Rockburst and the instability of rock masses. *International Journal of Rock Mechanics and Mining Sciences & Geomechanics Abstracts*, 33: 727-732.
- Liu, H. Y., Roquete, M., Kou, S. Q., & Lindqvist, P. A. (2004). Characterization of rock heterogeneity and numerical verification. *Engineering Geology*, 72: 89-119.
- Liu, X.-R., Yang, S.-Q., Huang, Y.-H., & Cheng, J.-L. (2019). Experimental study on the strength and fracture mechanism of sandstone containing elliptical holes and fissures under uniaxial compression. *Engineering Fracture Mechanics*, 205: 205-217.
- Liu, Y., Dai, F., Lu, D., Xu, N., & Feng, P. (2018). Experimental investigation on the fatigue mechanical properties of intermittently jointed rock models under cyclic uniaxial compression with different loading parameters. *Rock Mechanics and Rock Engineering*, 51: 47-68.
- Manso, J., Marcelino, J., & Caldeira, L. (2019). Effect of the clump size for bonded particle model on the uniaxial and tensile strength ratio of rock. *International Journal of Rock Mechanics and Mining Sciences*, 131-140.
- Martin, C. D. (1993). Strength of Massive Lac du Bonnet Granite Around Underground Opening. *Ph.D. Thesis, University of Manitoba, Winnipeg, Canada*, 278p.
- Martin, C. D. (1997). Seventeenth Canadian Geotechnical Colloquium: The effect of cohesion loss and stress path on brittle rock strength. *Canadian Geotechnical Journal*, 34: 698-725.
- Martin, C. D., & Christiansson, R. (2009). Estimating the potential for spalling around a deep nuclear waste repository in crystalline rock. *International Journal of Rock Mechanics and Mining Sciences*, 46: 219-228.

- Martin, C. D., Kaiser, P. K., & McCreath, D. R. (1999). Hoek-Brown parameters for predicting the depth of brittle failure around tunnels. *Canadian Geotechnical Journal*, 36: 136-151.
- Mayer, J. M., & Stead, D. (2017). Exploration into the causes of uncertainty in UDEC grain boundary models. *Computers and Geotechnics*, 82: 110-123.
- Mazaira, A., & Konicek, P. (2015). Intense rockburst impacts in deep underground construction and their prevention. *Canadian Geotechnical Journal*, 52: 1426-1439.
- Mehranpour, M. H., & Kulatilake, P. H. (2017). Improvements for the smooth joint contact model of the particle flow code and its applications. *Computers and Geotechnics*, 87: 163-177.
- Nagaso, M., Mikada, H., & Takekaea, J. (2019). The role of rock strength heterogeneities in complex hydraulic fracture formation - Numerical simulation approach for the comparison to the effects of brittleness. *Journal of Petroleum Science and Engineering*, 172: 572-587.
- Nasseri, M. H., Goodfellow, S. D., Lombos, L. E., & Young, R. P. (2014). 3-D transport and acoustic properties of Fontainebleau sandstone during true-triaxial deformation experiments. *International Journal of Rock Mechanics and Mining Sciences*, 69: 1-18.
- Nicksiar, M., & Martin, C. D. (2014). Factors affecting crack initiation in low porosity crystalline rocks. *Rock Mechanics and Rock Engineering*, 1165-1181.
- Ortlepp, W. D. (2001). The behaviour of tunnels at great depth under large static and dynamic pressures. *Tunnelling and Underground Space Technology*, 16: 41-48.
- Ortlepp, W. D., & Stacey, T. R. (1994). Rockburst mechanisms in tunnels and shafts. *Tunnelling and Underground Space Technology*, 9: 59-65.
- Park, J. W., Park, C., Song, J. W., & Park, E. S. (2017). Polygonal grain-based distinct element modeling for mechanical behavior of brittle rock. *International Journal for Numerical and Analytical Methods in Geomechanics*, 41: 880-898.
- Peng, J., Wong, L. N., & Teh, C. I. (2017a). Influence of grain size heterogeneity on strength and micro-cracking behaviour of crystalline rocks. *Journal of Geophysical Research: Solid Earth*, 1054-1073.
- Peng, J., Wong, L. N., & Teh, C. I. (2017b). Effect of grain size-to-particle size ratio on micro-cracking behavior using a bonded-particle grain-based model. *International Journal of Rock Mechanics and Mining Sciences*, 100: 207-217.
- Perras, M. A., & Diederichs, M. S. (2016). Predicting excavation damage zone depths in brittle rocks. *Journal of Rock Mechanics and Geotechnical Engineering*, 8: 60-74.
- Potyondy, D. O. (2010). A Grain-Based Model for Rock: Approaching the True Microstructure. *Proceedings of Rock Mechanics in the Nordic Countries 2010*, (p. 10). Kongsberg, Norway.
- Powrie, W., Ni, Q., Harkness, R. M., & Zhang, X. (2005). Numerical modelling of plane strain tests on sands using a particulate approach. *Géotechnique*, 55: 297-306.
- Saadat, M., & Taheri, A. (2019). A numerical approach to investigate the effects of rock texture on the damage and crack propagation of a pre-cracked granite. *Computers and Geotechnics*, 89-111.
- Salamon, M. (1983). Rockburst hazard and the fight for its alleviation in South African gold mines. In: *Rockbursts - Prediction and Control* (pp. 11-36). London, UK: Institute of Mines and Metallurgy.

- Seki, S., Kaise, S., Morisaki, Y., Azetaka, S., & Jiang, Y. (2008). Model experiments for examining heaving phenomenon in tunnels. *Tunnelling and Underground Space Technology*, 23: 128-138.
- Sharifzadeh, M., Feng, X.-t., Zhang, X., Qiao, L., & Zhang, Y. (2017). Challenges in multi-scale hard rock behaviour evaluation at deep underground excavations. *12th Iranina and 3rd Regional Tunnelling Conference*. Tunnelling and Climate Change.
- Simmons, G., & Richter, D. (1976). Microcracks in rocks. In R. G. Strens, *The Physics and Chemistry of Minerals and Rocks* (pp. 105-137). Toronto: John Wiley & Sons.
- Siren, T., Kantia, P., & Rinne, M. (2015). Considerations and observations of stress-induced and construction-induced excavation damage zone in crystalline rock. *International Journal of Rock Mechanics and Mining Sciences*, 73: 165-174.
- Tan, X., Konietzky, H., & Chen, W. (2016). Numerical simulation of heterogeneous rock using discrete element model based on digital image processing. *Rock Mechanics and Rock Engineering*, 49: 57-64.
- Tang, C. A., & Kaiser, P. K. (1998). Numerical Simulation of Cumulative Damage and Seismic Energy Release During Brittle Rock Failure—Part I Fundamentals. *International Journal of Rock Mechanics and Mining Science*, 113-121.
- Tang, C. A., Wong, R. H., Chau, K. T., & Lin, P. (2005). Modeling of compression-induced splitting failure in heterogeneous brittle porous solids. *Engineering Fracture Mechanics*, Vol.72: 597-615.
- Wang, C., & Tannant, D. D. (2004). Rock fracture around a highly stressed tunnel and the impact of a thin liner for ground control. *International Journal of Rock Mechanics and Mining Sciences*.
- Wang, S. H., Lee, C. I., Ranjith, P. G., & Tang, C. A. (2009). Modeling the effect of heterogeneity and anisotropy on the excavation damage/disturbed zone (EDZ). *Rock Mechanics and Rock Engineering*, 42: 229-258.
- Wang, X., & Cai, M. (2020). A DFN-DEM Multi-scale Modeling Approach for Simulating Tunnel Excavation Response in Jointed Rock Masses. *Rock Mechanics and Rock Engineering*, 53: 1053-1077.
- Wang, X., Jiang, Y., & Li, B. (2017). Experimental and numerical study on crack propagation and deformation around underground opening in jointed rock masses. *Geosciences Journal*, Vol.21: 291-304.
- Wong, L. N., & Einsein, H. H. (2009a). Crack Coalescence in Molded Gypsum and Carrara Marble: Part 1. Macroscopic Observations and Interpretation. *Rock Mechanics and Rock Engineering*, 42: 475-511.
- Wong, L. N., & Einstein, H. H. (2009b). Crack Coalescence in Molded Gypsum and Carrara Marble: Part 2--Microscopic Observations and Interpretation. *Rock Mechanics and Rock Engineering*, 513-545.
- Wong, R. H., & Chau, K. T. (1998). Crack coalescence in a rock-like material containing two cracks. *International Journal of Rock Mechanics and Mining Sciences*, 35: 147-164.
- Wong, R. H., Chau, K. T., & Wang, P. (1996). Microcracking and grain size effect in Yuen Long marbles. *International Journal of Rock Mechanics and Mining Sciences & Geomechanics Abstracts*, 33: 479-485.

- Wong, R. H., Lin, P., & Tang, C. A. (2006). Experimental and numerical study on splitting failure of brittle solids containing single pore under uniaxial compression. *Mechanics of Materials*, 38: 142-159.
- Wu, H., Zhao, G., & Liang, W. (2020). Mechanical properties and fracture characteristics of pre-holed rocks subjected to uniaxial loading: A comparative analysis of five hole shapes. *Theoretical and Applied Fracture Mechanics*, 105: 102433.
- Wu, T., Gao, Y., Zhou, Y., & Li, J. (2020). Experimental and numerical study on the interaction between holes and fissures in rock-like materials under uniaxial compression. *Theoretical and Applied Fracture Mechanics*, 106: 102488.
- Yang, S. Q., Yang, D. S., Jing, H. W., Li, Y. H., & Wang, S. Y. (2012). An experimental Study of the Fracture Coalescence Behaviour of Brittle Sandstone Specimens Containing Three Fissures. *Rock Mechanics and Rock Engineering*, 45: 563-582.
- Yang, S.-Q., & Jing, H.-W. (2011). Strength failure and crack coalescence behavior of brittle sandstone samples containing a single fissure under uniaxial compression. *International Journal of Fracture*, 168: 227-250.
- Yang, S.-Q., Yin, P.-F., Zhang, Y.-C., Chen, M., Zhou, X.-P., Jing, H.-W., & Zhang, Q.-Y. (2019). Failure behavior and crack evolution mechanism of a non-persistent jointed rock mass containing a circular hole. *International Journal of Rock Mechanics and Mining Sciences*, 114: 101-121.
- Yoon, J. S., Zang, A., & Stephansson, O. (2012). Simulating fracture and friction of Aue granite under confined asymmetric compressive test using clumped particle model. *International Journal of Rock Mechanics and Mining Sciences*, 68-83.
- Yu, Q. L., Ranjith, P. G., Liu, H. Y., Yang, T. H., Tang, S. B., Tang, C. A., & Yang, S. Q. (2015). A mesostructure-based damage model for thermal cracking analysis and application in granite at elevated temperatures. *Rock Mechanics and Rock Engineering*, 48: 2263-2282.
- Zeng, W., Yang, S.-Q., & Tian, W.-L. (2018). Experimental and numerical investigation of brittle sandstone specimens containing different shapes of holes under uniaxial compression. *Engineering Fracture Mechanics*, 200: 430-450.
- Zhang, Q., Zhang, X.-P., & Yang, S.-Q. (2021). A numerical study of acoustic emission characteristics of sandstone specimen containing a hole-like flaw under uniaxial compression. *Engineering Fracture Mechanics*, 242: 107430.
- Zhang, Y., & Wong, L. N. (2018). A review of numerical techniques approaching microstructures of crystalline rocks. *Computers and Geosciences*, 167-187.
- Zhou, X. P., Cheng, H., & Feng, Y. F. (2014). An experimental Study of Crack Coalescence Behaviour in Rock-Like Material Containing Multiple Flaws under Uniaxial Compression. *Rock Mechanics and Rock Engineering*, 47: 1961-1986.
- Zhou, Y., Zhao, C., Zhao, C., Yu, Z., & Du, Z. (2018). Mechanical Properties and Damage Evolution of Specimens Containing Single Cracks: An Experimental Study Based on SEM Method. *10th Asian Rock Mechanics Symposium*. Singapore: ARMS10.
- Zhu, W. C., Liu, J., Tang, C. A., Zhao, X. D., & Brady, B. H. (2005). Simulation of progressive fracturing processes around underground excavation under biaxial compression. *Tunnelling and Underground Space Technology*, 20: 231-247.

Zhu, W., Li, Y., Li, S., Wang, S., & Zhang, Q. (2011). Quasi-three-dimensional physical model tests on a cavern complex under high in-situ stress. *International Journal of Rock Mechanics & Mining Sciences*, 48: 199-209.

Zhu, X., Wang, Y., & Ren, Y. (2020). Numerical Simulation to Research on the Fracture Mechanism of the Surrounding Rock in Deep Tunnels. *Geotechnical and Geological Engineering*, 38: 319-327.

Zuo, J. P., Wang, X. S., & Mao, D. Q. (2014). SEM in-situ study on the effect of offset-notch on basalt cracking behavior under three-point bending load. *Engineering Fracture Mechanics*, 131: 504-513.

Every reasonable effort has been made to acknowledge the owners of copyright material. I would be pleased to hear from any copyright owner who has been omitted or incorrectly acknowledged.

**Chapter 3 . Analysis of Mafic Rocks
Microstructure Damage and Failure
Process under Compression Test Using
Quantitative Scanning Electron
Microscopy and Digital Images Processing**

This chapter has been accepted in *Engineering Fracture Mechanics* as:

Tao, R., Sharifzadeh, M., Zhang, Y., Feng, X.-T., 2020. Analysis of mafic rocks microstructure damage and failure process under compression test using quantitative scanning electron microscopy and digital images processing. *Eng. Fract. Mech.* 231, 107019. <https://doi.org/10.1016/j.engfracmech.2020.107019>

Abstract

The micro-structures of rock govern meso- and macro-scale rock behaviours and their failure mechanisms. This paper applied experiment study (uniaxial and triaxial compressive tests) and scanning electron microscope (SEM) method to illustrate the relationship between microscopic damage and mesoscopic fracture. Specifically, this study carried out that there are three main pre-existing micro-structures including heterogeneity (31%), micro-cracks (27%), and crystal lattice boundaries (25%). The pre-existing micro-cracks are investigated and classified as inter-granular cracks (37%), intra-granular cracks (36%), and trans-granular cracks (27%) based on morphological characteristics. According to the deformation types, the micro-cracks after test are divided as tensile crack (53%), shear crack (29%), and mixed shear and tensile crack (18%). Moreover, this paper provides a damage property parameter which is the ratio of tensile damage degree to shear damage degree based on the SEM image processing technique. This parameter could clearly reveal the damage properties (tensile or shear) at different stages including initiating stage, propagation stage and failure stage, which could present microscopic damage development process. Finally, compared with the fractures on two specimens from compressive tests, it could confirm that the meso-scale fracturing process is associated with the micro-scale damage development process.

Keywords: Microstructures, Micro-cracks, Damage degree, Failure process

3.1 Introduction

In nature, rock contains numerous pre-existing micro-structural defects including micro-cracks, pores, cleavage due to complex geological historical factors. Due to loading or stress concentration, these complex pre-existing micro-structures govern the macroscopic rock properties including porosity, modulus, compressive and tensile strength (Zhou & Xiao, 2018). Numerous fundamental theories and studies were carried out to investigate the rock failure mechanism including crack closure, crack initiation, crack propagation

and crack coalescence. Griffith (1920) provided the concept that stress concentration around small discontinuities was the weakness of brittle material. Lajtai (1974) and Wong and Einstein (2009a) systematically indicated the crack types during the rock failure process. Simmons & Richter (1976) and Kranz (1983) classified the micro-crack types based on petrographic characteristics. Martin (1993) revealed the rock failure process according to micro-crack initiation and propagation. Wong and Einstein (2009b) divided the micro-crack coalescence types into nine categories to reveal macroscopic fracture mechanism. In addition, Li et al. (2017) presented the mechanical properties and failure process of rock with a circular or an elliptical hole. These previous studies revealed the failure progress based on a pre-existing microstructure (micro-crack or pore). However, the real natural rock contains numerous and various types of micro-structures. Although both micro-crack and hole could clearly present the process of damage evolution, these micro-structures will interact each other in reality. Thus, it requires a quantitative investigation of the rock micro-structures to present the link between micro-structures, mesoscopic failure (experimental scale) and macroscopic failure. In addition, with the development of numerical simulation technique, numerical modelling could present the rock failure process such as discrete element method (Li et al., 2017; Azevedo et al., 2009; Liu et al., 2018). If there are sufficient geometry data such as micro-structures proportion and size, grain shape and size, the numerical simulation result will be more accurate, which is more similar with the real rock in nature. Therefore, the better understanding and investigation of microstructures distribution (amount and porosity) and geometry properties (shape and size) is very important to determine the rock behaviours under laboratory scale and macroscopic scale.

In this paper, scanning electron microscope (SEM) observation and digital image processing measurement (binarization) are applied on mafic specimens. In order to obtain the characteristics of microstructures before and after test and detect the relationship between microscopic damage and mesoscopic fracture, two kinds of loading tests (uniaxial compression test and triaxial compression test) are applied on specimens. Before tests, the pre-existing microstructures properties including amount and size of cracks are

determined. Finally, for the fractured specimens, the emphasis is to determine the initiating micro-cracks characteristics and confirm that the meso-scale fracturing process is associated with micro-scale damage development process. Figure 3-1 shows the investigation structure which includes six types of micro-structures, three types of pre-existing micro-cracks, and three types of micro-cracks under loading.

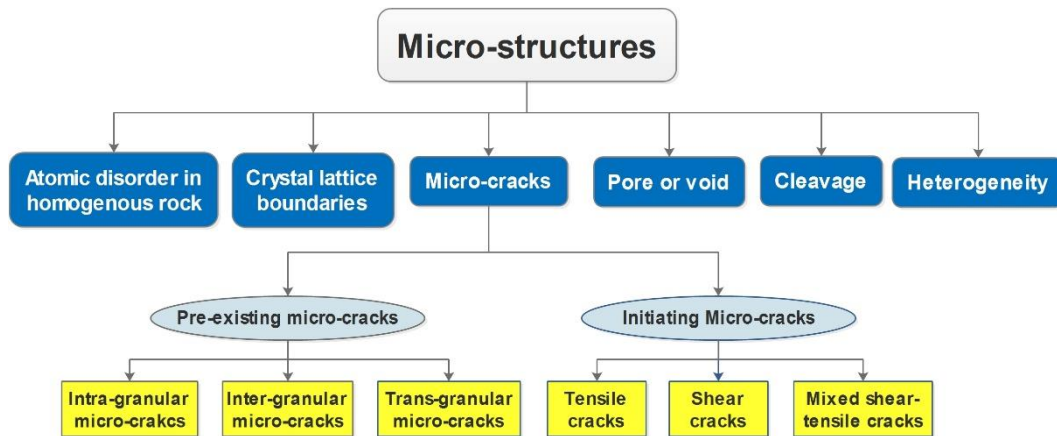


Figure 3-1: Investigation structure

3.2 Background

3.2.1 Classification of Micro-structures before Test

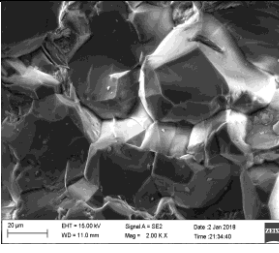
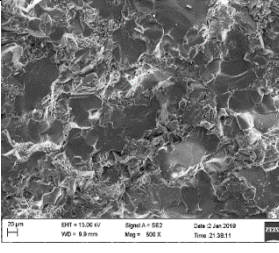
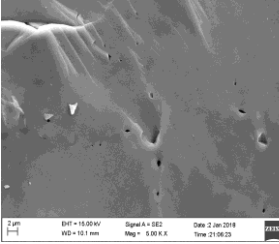
In nature, all rocks suffer from the wide range microstructures or micro-defects, which are regarded as the micro-structural flaws or voids within or between mineral grains. The microstructures have a significant influence on rock mechanical characteristics including strength and anisotropy. They are the main factors of rocks crack initiation, propagation, and failure in macro-scale as well during loading process. Sharifzadeh et al. (2017) classified six micro-structural defects, including atomic disorder in homogenous rocks, crystal lattice boundaries, heterogeneity, pore or void, cleavage, and micro-cracks.

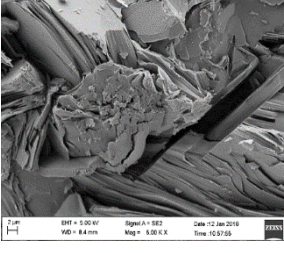
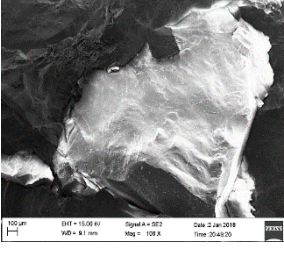
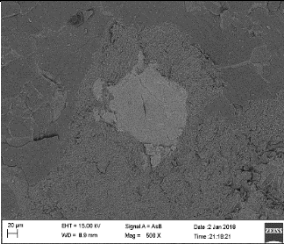
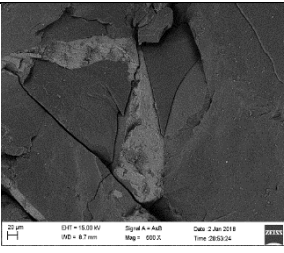
As an important micro-defect, micro-cracks play a significant role during rock failure process. Griffith (1920) considered that there are small discontinuities or flaws in real materials. The weakness of brittle material is the stress concentration around these flaws. These flaws are regarded as Griffith cracks. According to the petrographic characteristics of Griffith cracks, Simmons &

Richter (1976) and Kranz (1983) divided them into four type cracks including grain boundary cracks, intra-granular cracks within mineral grain, inter-granular cracks extending from a grain boundary and crossing into another grain, and multi-granular cracks crossing several grains and grain boundaries. In addition, He et al. (2010) defined three crack types as inter-granular crack that develops almost along the grain boundaries (>86%), intra-granular crack which crosses the mineral grain (>80%), and cracking pairing the two types.

In order to investigate the properties of micro-structural defects of mafic specimens, it requires determine the characteristics and classification of various micro-structures. The specific classification and description of micro-structures and micro-cracks for studied mafic specimens are shown in Table 3-1.

Table 3-1: Classification and characteristics of micro-structures and micro-cracks in mafic rocks.

Micro-defects	SEM Image	Description (Kranz, 1983; He et al., 2010; Sharifzadeh et al., 2017)
Crystal lattice boundaries		The particles of inner grain are kept together by bonds including ionic bonds, molecular bonds, and covalent bonds. However, the surface of grain has a binding force, which is weak than the bonds. Hence, the crystal lattice boundaries are weak.
Heterogeneity		Heterogeneity means that there are uneven distributions on different mineral composition, grain size and shape, and particles arrangement. It is mainly regarded as mixture of weak and strong rock particles. Heterogeneity has major influence on rock anisotropic behaviour.
Pore or void		Pore or void is mainly caused by gas escape in volcanic rocks or the cement incomplete filling during rock generation.

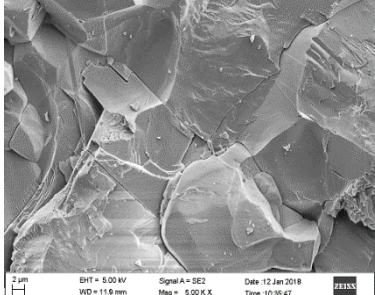
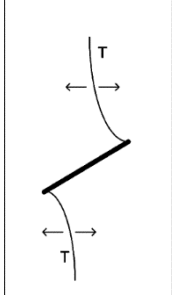
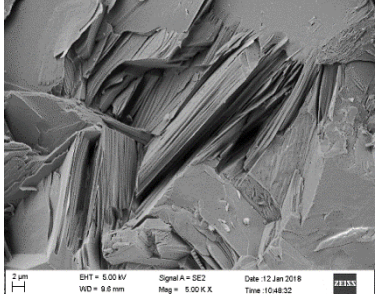
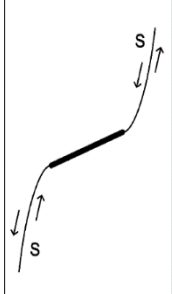
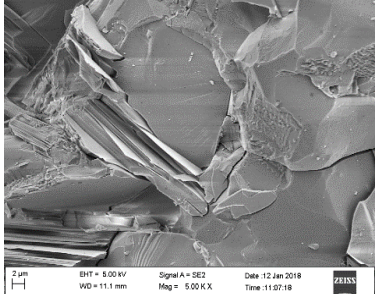
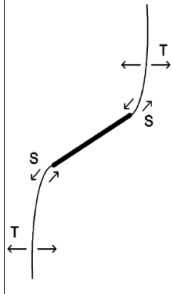
Cleavage			Cleavage is the tendency of a mineral to split along smooth crystallographic planes which are parallel to the weak bonding.
Micro-crack	Inter-granular Crack		Inter-granular crack develops along the grain boundaries.
	Intra-granular Crack		The intra-granular crack lies within the grain.
	Trans-granular Crack		The trans-granular crack crosses several grains, which will contain inter-granular crack and intra-granular crack.

3.2.2 Classification of Crack Types after Tests

Under loading test, the rock will experience a series of cracking process, including cracks initiation, cracks propagation, cracks coalescence, and rupture. In this process, the cracks will present different characteristics due to loading direction and crack inclined angle. Therefore, numerous scholars contribute to the crack types or failure types of rocks during the loading tests. Lajtai (1974) indicated the failure types during the rock failure process including tensile fracture, normal shear fracture, inclined shear fracture, material failure, and rupture. Wong and Einstein (2009a) systematically evaluated the tensile and shear cracks developed from a pre-existing crack. There were seven different crack types including three tensile types, three shear types and one mixed type.

According to the SEM images observation of mafic specimen, there are three main crack types in terms of tensile crack, shear crack, and mixed shear-tensile crack (Table 3-2). The tensile cracks present following characteristics: Firstly, the opening direction is perpendicular with the crack extension direction. Secondly, the boundary of tensile crack is obvious and complete. In addition, the shear cracks present following characteristics: Firstly, there is a sliding along the crack. Secondly, the morphological pattern looks like layered pattern. Moreover, the mixed shear-tensile cracks present both shear crack and tensile crack characteristics. Generally, if the crack has an opening without sliding, it will be regarded as tensile crack. If the crack has a sliding or present layered pattern, it will be regarded as shear crack. These morphological characteristics will be regarded as the basis to distinguish different post-test crack types in later analysis.

Table 3-2: Post-test crack types of mafic specimens.

Crack Types	SEM Image	Mechanism	Description (Wong & Einstein, 2009a; Zhou et al., 2018)
Tensile Crack			There is an opening at the crack. The boundary of tensile cracks is obvious. The grains are not damaged seriously, so there are few grain debris scattering around the cracks.
Shear Crack			There is a sliding at the crack. Some shear cracks look like layered pattern. The boundaries of cracks are not complete or sliding along the cracks.
Mixed Tensile-shear Crack			The crack mixed with shear and tensile cracks. It means that there are sliding and opening at one crack.

3.3 Experiment Procedure and Micro-cracks Measurement

3.3.1 Experiment Procedures

In order to determine hard rock behaviours, two kinds of experiment methods were applied including UCS test and triaxial compressive test. Two mafic specimens were collected from a real nickel mine site in Western Australia. This research is part of a sudden failure mechanism research and ground control management. The collection region consists of mafic to intermediate volcanic rocks with some felsic intrusive rocks. The main mineral composition includes Pyroxene, Plagioclase Feldspar, and Biotite. The dimension of both two specimens is 50mm*50mm*100mm.

According to the tests design from Zhang et al. (2019), in the UCS test, σ_1 was applied on one mafic rock specimen, which gradually increased with a rate of 0.5MPa/s until the specimen fractured (Figure 3-2 Left). In the triaxial compression test, initially, the principal stresses increased at a rate of 0.5MPa/s. When they reached at 20MPa, σ_2 and σ_3 kept constant and σ_1 kept on gradually increasing until the specimen fractured (Figure 3-2 Right). The fractured specimens are shown in Figure 3-3 (left one is specimen under UCS test and right one is specimen under triaxial compressive test).

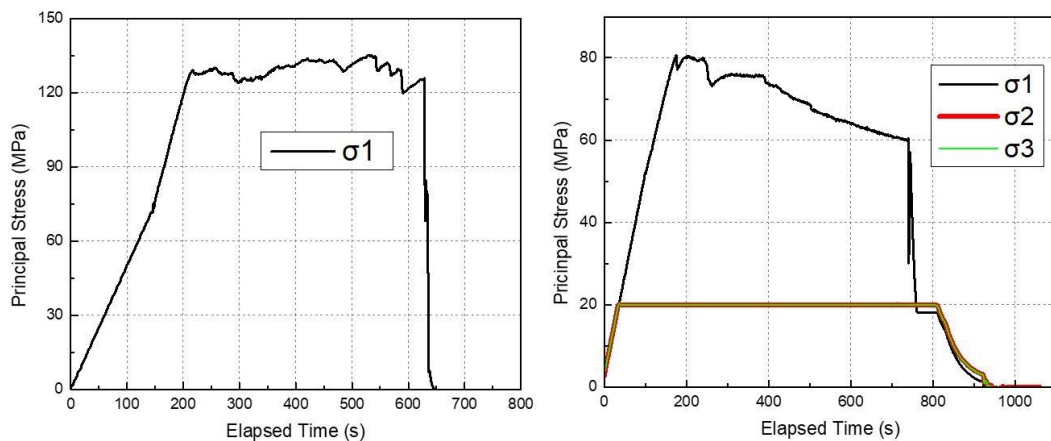


Figure 3-2: Loading path graph (Left: UCS test; Right: Triaxial test)

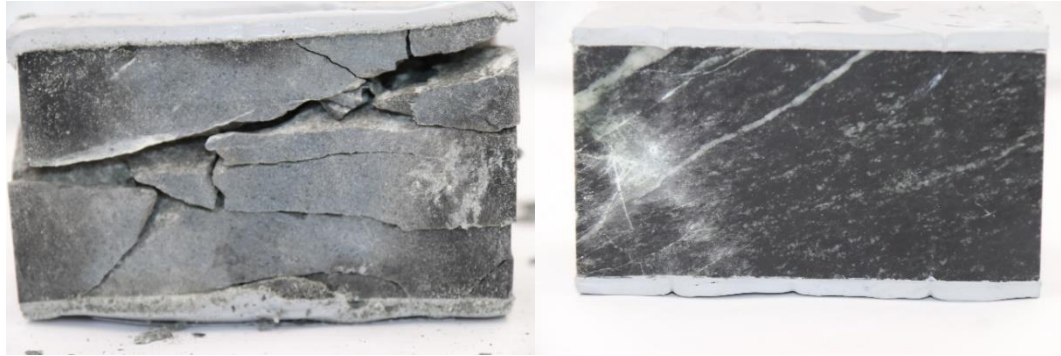


Figure 3-3: Fractured specimens (Left: UCS test; Right: Triaxial test)

After the compressive tests, six fragments with appropriate size were collected from two specimens (No.1~No.3 fragments from UCS test and No.4~No.6 fragments from triaxial compressive test in Figure 3-4). The fragments were collected from three positions of a whole fracture for each specimen. These fragments are regarded as the initiating stage, propagation stage and failure stage of the fracture development process, which were consistent with their number order.

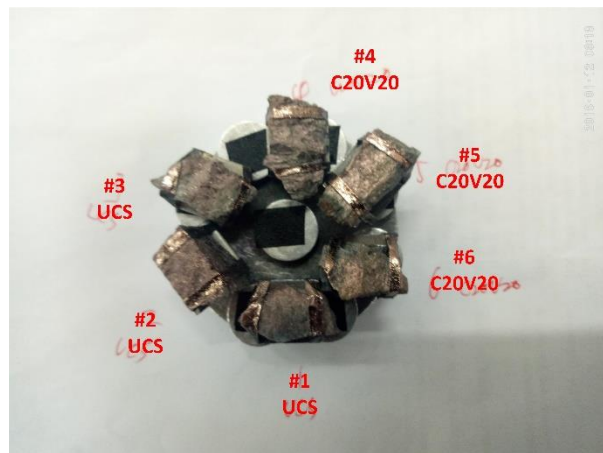


Figure 3-4: Six fragments after tests (1~3 fragments from UCS test; 4~6 fragments from triaxial compressive test)

3.3.2 Micro-cracks Measurement Procedure

In order to determine the micro-cracks geometry characteristics including length and area, software ImageJ was applied to digital image processing and measurement, which could provide a more convenient and accurate result than the manual result. The main procedure of digital image processing consists of SEM images input, binarization, image enhancement,

skeletonization and measurement, which is shown in Figure 3-5 and the detail steps are illustrated in section 3.3.2.2.

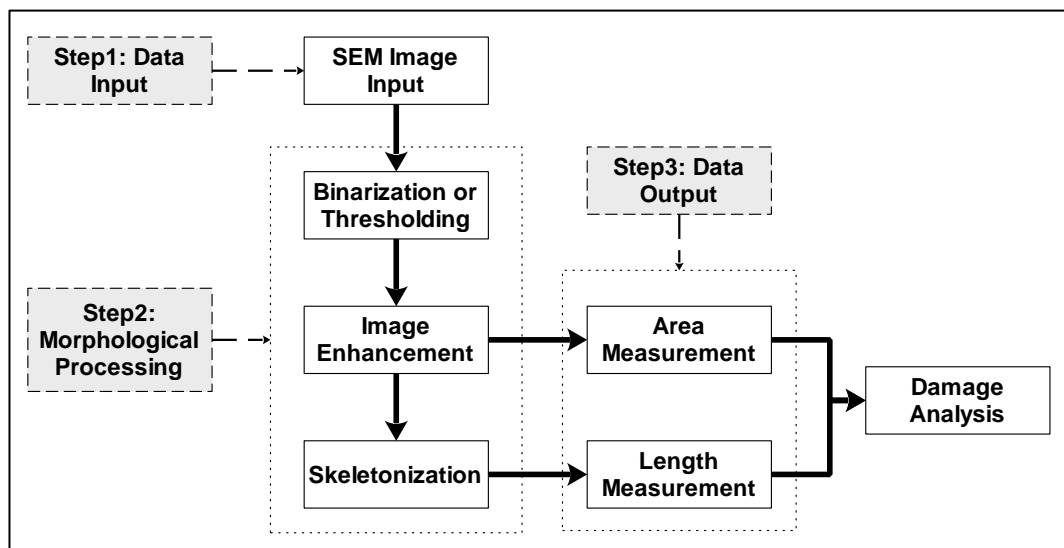


Figure 3-5: Procedure of digital image processing.

3.3.2.1 Digital Image Preparation

In order to quantitatively determine the pre-existing micro-structural defects and crack types after tests, the fragments collected before tests and fragments collected after tests were placed in the SEM system. All fragments were trimmed with appropriate size and polished for a flat surface. Metal coating was applied on the surface of fragments to enhance their conductivity. After the scanning specimen preparation, a total of 144 SEM images (44 images before loading test and 100 images after loading test) were captured by Zeiss Ultra Plus Scanning Electron Microscope, which is supported by Northeastern University, China (Figure 3-6). The magnifications of these micrographs were 100, 200, 500, 1000, 2000 and 5000 times. The initial scanning magnification are different for different specimens and different scanning area, so the micrographs with magnification of 100, 200 or 500 times will be regarded as the images containing the entire fracture according to the specific magnifications of SEM images of each specimen. The micrographs with magnification of 500, 1000, 2000 or 5000 times, which has higher magnification of each specimen, will be used to examine a part of the entire fracture to avoid errors due to extremely small cracks.



Figure 3-6: Zeiss Ultra Plus Scanning Electron Microscope

3.3.2.2 Digital Image Processing and Measurement

In the SEM images, the colour of micro-cracks is darker and the undamaged intact area is shallower (Figure 3-7a). In order to clearly determine the micro-cracks, a method of threshold could transform the SEM images into binarization images. The software of ImageJ was applied in this process, which divided the images into two colours as black and white. It means that the micro-cracks or “empty” area are presented by black pixels and the undamaged area or background is white (Figure 3-7b). In ImageJ software, there are some automatic thresholding methods, such as the Otsu method (Arena et al., 2014). However, under non-uniform lighting conditions, the contrast between the defects and background is not intense. It requires to manually adjust threshold to determine appropriate boundary.

After image binarization, there were a large number of speckles (black speckles and white holes), which is shown in Figure 3-8. According to Lin et al. (2014), these speckles are produced by the interference effect due to rough surface and coherent light. Although these spots have unique properties to evaluate the displacement field, this study focuses on the damage properties, considering the speckles located area. Therefore, the black speckles in the undamaged area should be removed and white holes in the micro-structures should be filled. In this step, the binarized images were enhanced by the methods of “despeckle” and “fillhole”, which are the tools embedded in the

software ImageJ. These methods could reduce the discrete pixel points (black speckles) and fill up the vacancy part (white speckles) of a damage area (Figure 3-7c). After enhancement of binarization images (morphological processing stage), ImageJ, the tool of “region of interest (ROI)” provided by ImageJ could select the damage area. As mentioned before, the damage area was presented by black pixels. The length of one square pixel is $2.78\mu\text{m}$, $1.43\mu\text{m}$, and $0.56\mu\text{m}$ in 100 times, 200 times and 500 times magnitudes respectively. The tool of “measure” embedded in ImageJ could account the number of pixels of each microstructure. Then, the area could be calculated in unit of μm by the pixel length scale.

On the other hand, another stage of morphological processing is skeletonization, which is a thinning stage. Some micro-cracks have larger width, which is overweighting one pixel. Therefore, the tool of “skeleton” could thin micro-cracks into lines with a width of one pixel, by removing the pixels from the edges of micro-cracks (Figure 3-7d). After skeletonization process, total length and average length of micro-cracks could be measured. The selection and measurement is same with the process of area measurement.

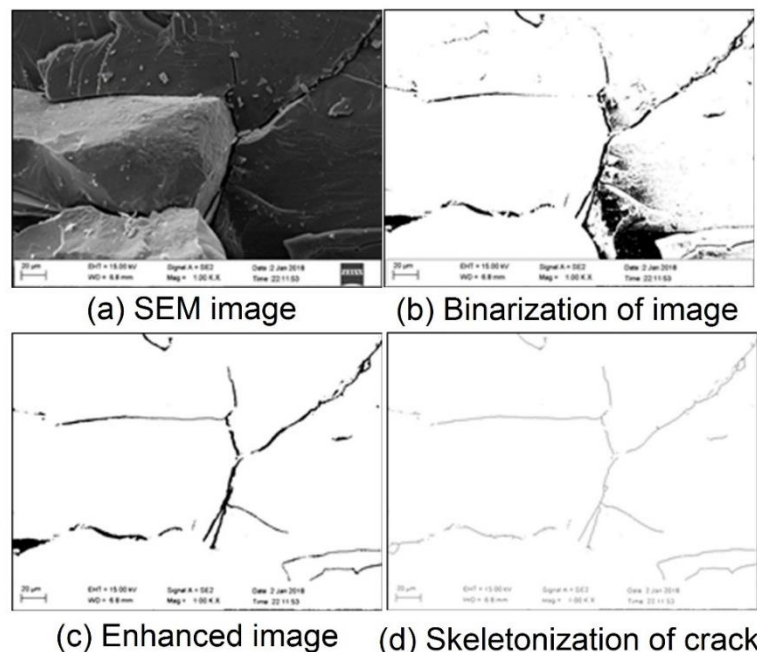


Figure 3-7: The main steps of digital image processing (a: SEM image input; b: Binarization or thresholding; c: Image enhancement including despeckle and fillhole; d: skeletonization or thinning cracks)

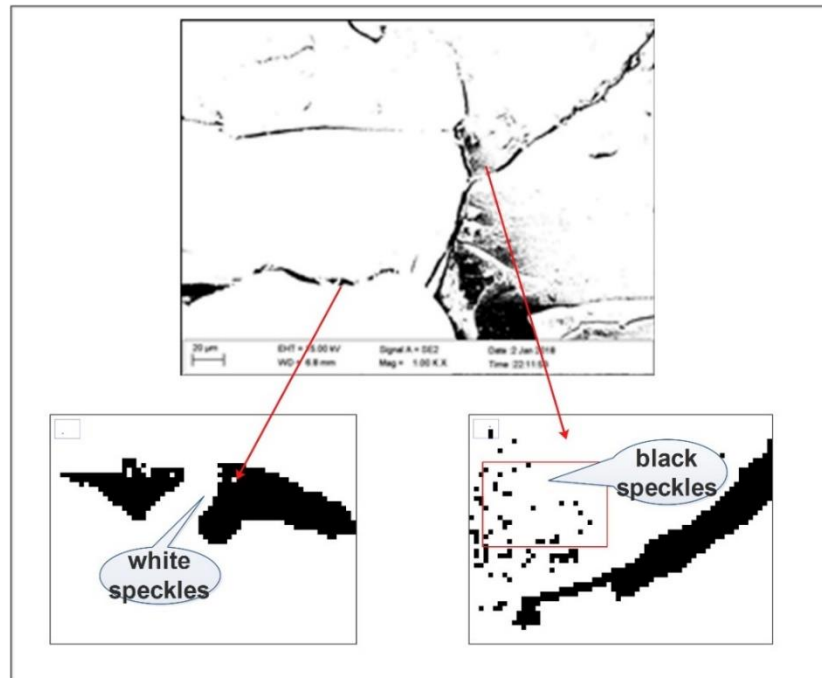


Figure 3-8: Two kinds of speckles

3.4 Statistical Analysis of Results

3.4.1 Pre-existing Micro-structures Analysis

3.4.1.1 Micro-structures Analysis

According to the SEM observation, there are three main pre-existing microstructures including heterogeneity, micro-cracks, and crystal lattice boundaries. They account for 31%, 27% and 25% of total micro-structural defects respectively (Figure 3-9). The microstructures of heterogeneity and crystal lattice boundary perform as a certain area. It is hard to account their number. Therefore, during statistic process, the number of each existing microstructure in each SEM image is defined as 1 and the number of absent microstructure is defined as 0. For example, if the image shows that this part of rock has heterogeneity, the number of heterogeneity is determined as 1. As meanwhile, the number of micro-cracks or pores is still determined as 1 no matter the real number of presence microstructures. According to the statistical result, the composition of microstructural defects is complicated, different microstructures will cause different failure modes under macro-scale at certain area. It requires more attention to analysis their mechanism in the further

study. Here, this paper will illustrate two major microstructural defects: heterogeneity and grain boundary.

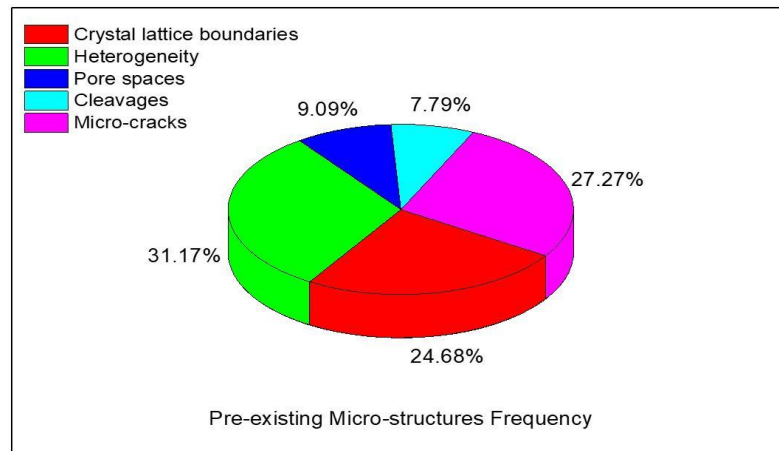
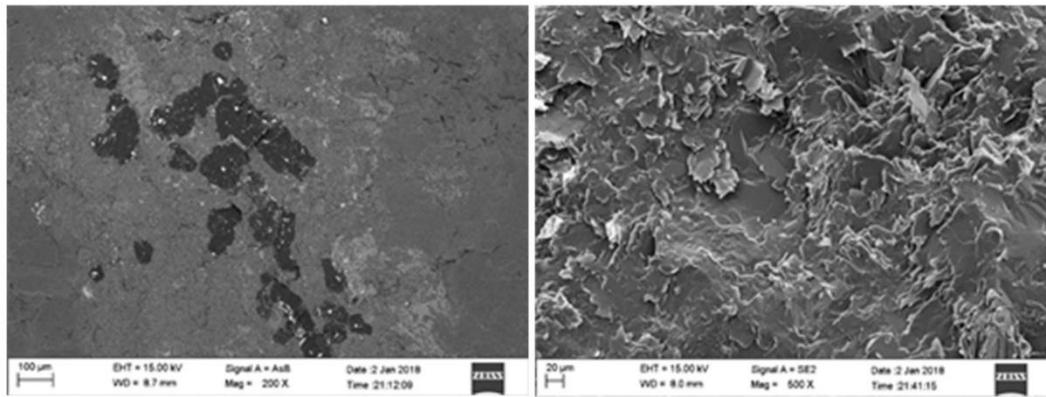


Figure 3-9: Pre-existing microstructural defects classification on mafic specimens

As the most percentage of microstructures, rock heterogeneity plays a marked role on rock mechanical properties. Tang and Kaiser (1998) demonstrated that the heterogeneity has a crucial influence on the fracturing process including cracks nucleation, propagation, interaction and coalescence. The degree of mechanical heterogeneity will influence the failure mode, for example, the distribution of heterogeneity will affect the fracture development path and result in a collapse in fracture zone under macro-scale. Zhou et al. (2018) indicated that heterogeneity is the reason of the flocculent pattern microstructures formation, which is a kind of tensile microstructures. The SEM images shown in Figure 3-10 present two patterns of heterogeneity. Figure 3-10a illustrates that there is heterogeneous distribution of mineral composition. The softer grains (darker area) are embedded into the harder grains (brighter area). When stress concentrates at the boundary of grains, the darker area will be more easily damaged and result in shear failure at macro-scale as the fracture through the dark area. Figure 3-10b presents the flocculent pattern due to grain shape heterogeneity. There is various distribution of curled and rough microstructures. Due to this heterogeneity presence, the stored energy release will be heterogeneous, which may form tensile abruption at macro-scale.



(a) Variable distribution of mineral composition

(b) Flocculent pattern

Figure 3-10: Two patterns of heterogeneity in mafic specimens

Rocks are consisted of minerals or crystals, which are kept together with chemical bonds. Different bonding patterns have different rock mechanical properties and result in different failure modes. Sharifzadeh et al. (2017) indicated that the type of bonds determines the growth type of rock particles, such as massive rocks and foliated rocks due to three dimensional bonds and two-dimensional bonds respectively. According to SEM image observation, there are two main patterns occurring on the specimens (Figure 3-10). Figure 3-10a presents the massive pattern of rock particles growth, which is formed by the three-dimensional bonding particles. Due to the strong chemical bonds, the grain is strong in all direction. However, according to some scholars study (Omella et al., 2004; He et al., 2010), the weakest area of rock with 3D bonds was the bonding area along the grains. Therefore, the boundary of grain is weaker than the chemical bonds, which is easily fractured between grains. The upper part of Figure 3-10b shows the foliated pattern of rock particle growth. As the description of foliated rocks from Sharifzadeh et al. (2017), the bonds in layer are strong, but the bond in third direction is weak. To be specific, the particles formed the layers are bonded by strong chemical bonds, but the layer are kept together by Van Der Waals, which is weak bonding force. When loading is applied to this pattern rock, which is parallel to the layer plane or has small inclined angle with layer plane, shearing or sliding will occur at the layer surface. Therefore, the specimens will suffer from tensile failure and shear failure due to the massive pattern and foliated pattern respectively during the loading tests.

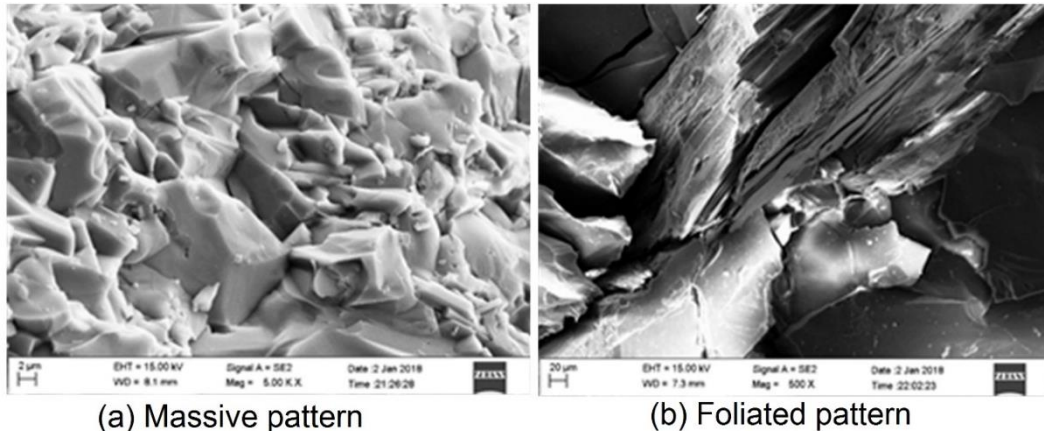


Figure 3-11: Two growth patterns of particle lattice boundaries in mafic specimen

According to above analysis of two major micro-structural defects occurring in mafic specimens, heterogeneity and particle lattice boundary will cause different failure due to their various patterns. In general, mineral composition heterogeneity pattern will lead to shear failure and grain shapes heterogeneity pattern (flocculent pattern) will lead to tensile failure. In addition, the grain boundary with massive pattern will lead to tensile failure and the grain boundary with foliated pattern will lead to shear failure.

3.4.1.2 Micro-cracks Analysis

As a significant microstructure, micro-cracks are widely existing in natural rocks, which play an important role on rock failure process including nucleation, initiation, propagation, coalescence and rupture. Simmons and Richter (1976) defined the micro-crack as an opening in rocks with a length of 100 μ m or less and the ratio of width to length is less than 10^{-2} (i.e. less than 1 μ m), generally in the range of $10^{-3} \sim 10^{-5}$. However, according to the SEM observation, there are many cracks with length exceeding 100 μ m or relatively wide cracks. Kranz (1983) provided the concept that the terms of micro-crack, micro-fracture and crack under SEM could be regarded synonymously. Therefore, in order to collect a more accurate statistical result, both longer cracks and wider cracks will be investigated during the observation process.

On the other hand, the extremely small openings are hardly identified during the digital image processing and will be filtered after image enhancement. To be specific, the length of one pixel under the magnification of 100 times, 200 times and 500 times corresponds to 2.78 μ m, 1.43 μ m and 0.56 μ m respectively.

The micro-cracks with width less than 1 μm could not be presented after image processing under the magnification of 100 times and 200 times. Hence, these micro-cracks could not be counted, if they are not shown in higher magnification SEM images. Moreover, the binary image or skeleton image could not present the micro-cracks types, so it requires combination of two methods of SEM image observation and digital image processing measurement. The method of distinguishing micro-crack types is based on their morphological characteristics, which is mentioned in Section 2 about micro-cracks classification.

According to the SEM images observation and binary images measurement, the amount of each type of micro-crack and their length and area before test are shown in Figure 3-12. According to Figure 3-12A, inter-granular cracks (37%) account for the most proportion of total micro-cracks following by intra-granular cracks (36%) and trans-granular cracks (27%). According to Figure 3-12B, although the trans-granular crack has the least amount, it has the longest length (379 μm) and largest area (6963 μm^2) for average value due to its morphology. Moreover, the intra-granular cracks have shorter average length (119 μm) and smaller average area (720 μm^2) than inter-granular cracks respectively due to the grain limit. In natural rocks, the boundary of grain is relatively weak than the grain. Hence, inter-granular cracks are formed more easily. Moreover, when the crack extends along the boundary, some branches will go into the weak grain, which will lead to the intra-granular cracks. If the intra-granular crack goes through the grain and coalesce with other crack, trans-granular crack will occur. Therefore, these results confirm to micro-cracks formation conditions due to the relationship between bonding force and grains.

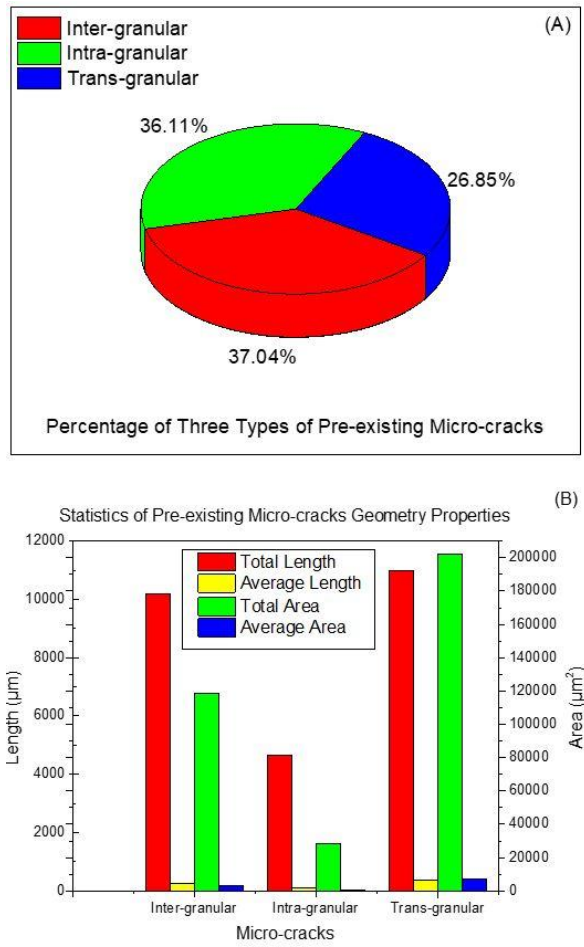


Figure 3-12: Statistics of pre-existing micro-cracks properties of mafic specimens ((A) Percentage of three types of micro-cracks, (B) Geometry properties)

3.4.2 Post-test Crack Types Analysis

According to observation for the SEM images of post-test mafic specimens, there are 53% of cracks showing characteristics of tensile cracks, such as perpendicular opening without sliding. The tensile cracks are formed by inter-granular micro-cracks propagation at the massive grain boundary and intra-granular micro-cracks opening within grains. Approximately 29% of cracks present characteristics of shear cracks, such as sliding or layered. Most of the shear cracks are formed by inter-granular micro-cracks sliding between two kinds of minerals or sliding at foliated grain boundary. As meanwhile, a small part of shear cracks are formed by intra-granular micro-cracks as well, which

extend and go through the entire grain. In addition, about 18% of cracks present both shear and tensile characteristics. To be specific, the mixed crack has a relatively large and rough opening at some of part of crack and has an obvious sliding at other part, which is caused by coalescence of shear and tensile cracks (Figure 3-13A). Based on Figure 3-13B, the mixed type crack has the longest length (244 μm) and largest area (3234 μm^2) for average value. Shear and tensile cracks have similar geometry properties: average length (90 μm and 94 μm) and average area (509 μm^2 and 588 μm^2).

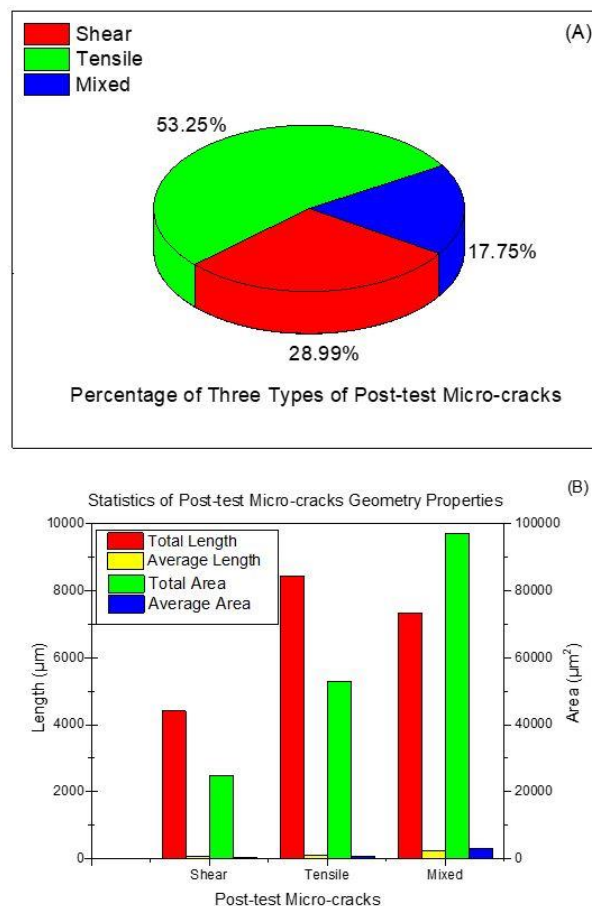


Figure 3-13: Statistics of micro-cracks properties measured after test ((A) Percentage of three types of post-test micro-cracks, (B) Geometry properties of post-test micro-cracks)

As mentioned in experiment procedure, the fragments of No.1~No.3 are from UCS test and the fragments of No.4~No.6 are from triaxial compressive test. The statistics of crack properties based on two types of tests are shown in

Figure 3-14. Comparing two test methods, the shear crack has larger area and longer length under triaxial compressive test. Tensile crack under triaxial test has larger area, but its length is similar with that under UCS test. Due to the few amount of mixed cracks, the geometry properties of mixed cracks have huge difference under two tests. Since the maximum principal stress for UCS test is higher than it for triaxial compressive test (Figure 3-2), the specimen for UCS test is harder than the specimen for triaxial compressive test. Hence, the average tensile cracks area under UCS test is smaller than that under triaxial compressive test. However, comparing the ratio of average tensile crack area to average shear crack area under UCS test with the ratio of average tensile crack area to average shear crack area, there is obvious difference for two tests. To be specific, the ratio under UCS test is much higher than it under triaxial compressive test. It means that the opening width is much larger than the displacement for the UCS test. This result is consistent with the fractured specimens. The fractures on specimen under UCS test have obviously wide opening and limited displacement, but the opening and displacement of fractures on specimen under triaxial compressive test are not obvious.

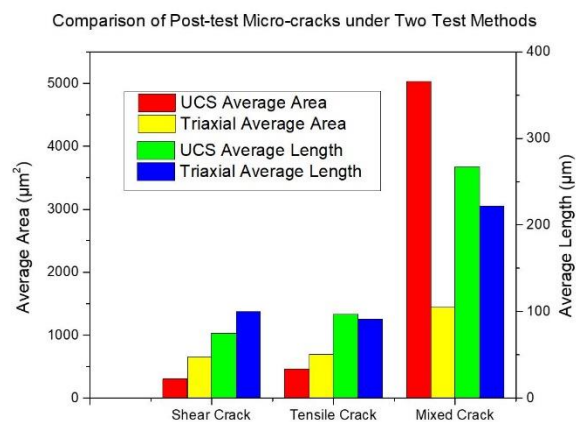


Figure 3-14: Statistics of post-test micro-cracks under two types of tests

3.5 Discussion

In this section, the result from statistic of post-test micro-cracks will be discussed to illustrate the relationship between micro-scale damage and meso-scale failure, based on the damage degree. Moreover, it will discuss the failure mechanism based on the different test methods.

3.5.1 Damage Properties under Micro-scale

According to the statistical results, the tensile cracks account for the major failure. However, the micro-scale damage process is unknown (i.e. initiating stage, propagation stage and failure stage). Kachanov (1958) provided a concept about the material continuity variable Ψ , which is regarded as the ratio of the real carrying area to the initial area. Odqvist and Hult (1961) introduced the damage variable D , which could be regarded as the ratio of the damage area to the total area. In order to determine the crack properties, this study apply variable D to identify the damage degree of tensile crack and shear crack respectively. The ratio of tensile degree to shear degree is taken to present the damage property (tensile or shear) parameter P (Equ.3-1).

$$p = \frac{D_T}{D_S} = \frac{A_T}{A_S} \quad (\text{Equ.3-1})$$

Where P is the parameter to present damage property, if $P > 1$, the rock will present more tensile damage; if $P < 1$, the rock will present more shear damage. D_T is damage degree of tensile crack and D_S is damage degree of shear crack. This equation could be simplified as the ratio of tensile crack area to shear crack area.

As mentioned in Section 3.1, the scanning specimens were collected from three positions of a whole fracture, which could be regarded as the fracture development process in terms of initiating stage (specimens No.1 and No.4), propagation stage (specimens No.2 and No.5), and failure stage (specimens No.3 and No.6). In order to improve the accuracy, each specimen was scanned from three different positions. Unfortunately, the specimens No.3 and No.6 have two overlapping regions, so it only considers two positions for these two

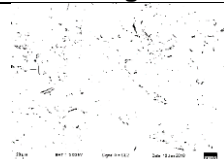
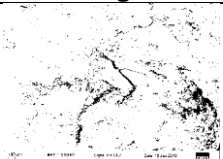
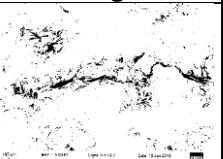
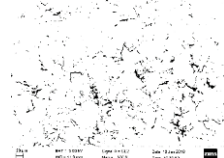
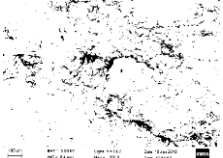
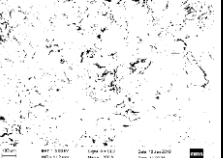
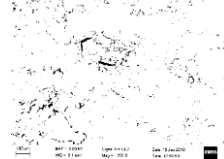
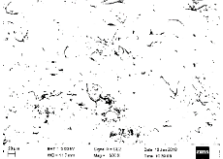

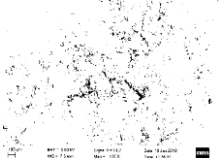
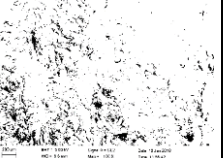
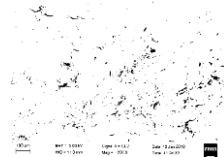
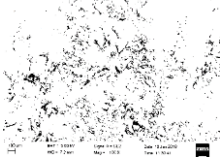
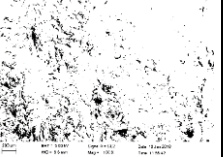
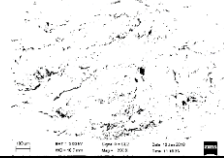
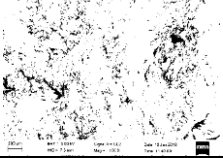
specimens. Table 3-3 shows the damage parameter for 6 specimens under three stages.

According to Table 3-3, the P value of each specimen is various due to different positions. In order to analyse the damage process and fracture development process, the average P value of each specimen was considered. Hence, the P value is 3.31, 3.26, and 2.51 under UCS test at three stages respectively. It means that the tensile cracks account for the majority damage during damage evolution process, because both ratios of tensile cracks area to shear cracks area are large than 1. However, the P value decreases from initiating stage to failure stage. It means that the shear cracks developed rapidly under failure stage. To be specific, the specimen suffered more tensile cracks firstly, but the area of shear cracks developed more rapidly than tensile cracks. Therefore, under UCS test, when the initiating direction and propagation direction of pre-existing micro-cracks are parallel or have a small inclined angle with the loading direction, the tensile cracks are easily occurred firstly due to the cracks opening and limited sliding. With the increase of loading stress, the pre-existing micro-cracks with large inclined angle and the presence tensile cracks almost parallel with the loading direction will start to occur sliding. The shear cracks developed rapidly at final stage with higher loading stress.

On contrast, the average P value is 0.86, 1.22, and 1.63 under Triaxial compressive test at three stages respectively. Since the P value of third image of specimen No.5 is much larger than other two images, it will not be considered in the analysis. Considering the ratios of the tensile cracks area to the shear cracks area increasing from initiating stage to failure stage, the shear cracks account for the majority damage at initiating stage, but the tensile cracks developed rapidly and account for the majority damage at propagation stage and failure stage. Therefore, under Triaxial test, the pre-existing micro-cracks not only initiate and propagate due to maximum principal stress, but also slide due to confining stress. When the confining stress keeps constant, initiation and propagation of pre-existing micro-cracks are similar with them under UCS test. Since a large number of shear cracks occurred at initiating stage, the value of P increases steadily with the increase of loading stress.

Hence, the tensile cracks account for the majority damage at propagation stage and failure stage.

Table 3-3: Damage parameter for each specimen under different stage.

	Initiating Stage (Specimen #1)		Propagation Stage (Specimen #2)		Failure Stage (Specimen #3)	
	Image	P	Image	P	Image	P
UCS Test		5.71		4.36		3.17
		1.37		1.61		1.85
		2.86		3.83	NA	-
	Initiating Stage (Specimen #4)		Propagation Stage (Specimen #5)		Failure Stage (Specimen #6)	
	Image	P	Image	P	Image	P
Triaxial Test		0.66		0,76		1.09
		1.12		1.67		2.17
		0.81		6.05	NA	-

3.5.2 Comparison of Microscopic Damage and Mesoscopic Failure

In order to detect the influence of microscopic damage on the mesoscopic and macroscopic failure, it requires to determine the relationship between damage evolution under micro-scale and rock failure process under meso-scale.

According to the Figure 3-3, it shows the fractured specimens. Under UCS test, all fractures have an obviously wide opening. Although there are limited sliding or displacement on some fractures due the interaction of each fracture,

the mesoscopic failure is still tensile failure, which is consistent with the result of microscopic damage. In addition, the meso-scale fracture has wider opening at initiating position and the opening becomes narrow with the fracture extension. According to the microscopic damage development process, the ratio of the tensile cracks area to the shear cracks area keeps decreasing with the increase of loading stress. The opening width of meso-scale fracture could confirm that the initiating position has much more tensile cracks than that at the extension part. The microscopic damage development process is consistent with the mesoscopic failure process based on the damage degree analysis.

Under triaxial compressive test, the fractures on the specimen are not obvious. The opening of fracture is very small and the displacement is limited as well. This phenomenon is consistent with the microscopic damage. To be specific, the opening width is much more obvious than the displacement under meso-scale in UCS test, so the ratio of the tensile crack area to the shear cracks area under micro-scale in UCS test is much higher. However, the ratio is around 1 during the microscopic damage development process in triaxial compressive test, which is consistent with the meso-scale opening and displacement.

3.6 Conclusion

In this study, investigations of mafic rock based on two compressive tests and SEM method were conducted on pre-existing microstructures and post-test deformed cracks. Specifically, two specimens are applied on two compressive tests in terms of UCS test and triaxial compressive test. Five fragments before test and six fragments after tests were collected for SEM system to capture images. SEM observation and digital image processing measurement are applied on the analysis process. According to the analysis of results and discussion above, the following conclusions were driven:

(1) The main pre-existing micro-structures are heterogeneity, micro-cracks, and crystal lattice boundaries, which account for 31%, 27% and 25% of total

micro-structural defects respectively. Moreover, three types of pre-existing micro-cracks including inter-granular cracks, intra-granular cracks, and trans-granular cracks account for 37%, 36% and 27% of total micro-cracks respectively.

(2) After experiments, there are three kinds of deformed cracks in terms of tensile cracks, shear cracks, and mixed shear and tensile cracks, which account for 53%, 29%, and 18% on amount respectively.

(3) Compared two compressive tests, the scanning specimens exhibit more tensile damage at failure stage under both two tests. However, at the initiating stage, the specimens under triaxial compressive test present more shear damage due to the increase of confining stress.

(4) According to compare the characteristics of the ratio of tensile cracks area to shear cracks area under micro-scale and the characteristics of fracture under meso-scale, it is confirmed that the mesoscopic fracturing process is associated with the microscopic damage development process.

Acknowledgement

We sincerely acknowledge Northeastern University, China provided the laboratory tests. We also thank Mr. Siyu Li at Western Australian School of Mines (WASM), Curtin University, Australia for his valuable support with the digital image processing. We would also like to thank the journal editor and reviewers for their valuable suggestions. In addition, this research did not receive any specific grant from funding agencies in the public, commercial, or not-for-profit sectors.

References

- Zhou, X.-P., & Xiao, N. (2018). Analyzing fracture properties of the 3D reconstructed model of porous rocks. *Engineering Fracture Mechanics*, pp. 175-193.
- Griffith, A. A. (1920). The phenomena of rupture and flow in solids. *Philosophical Transactions of the Royal Society of London, Series A: Mathematical and Physical Sciences*, 163-198.
- Lajtai, E. Z. (1974). Brittle fracture in compression. *International Journal of Fracture*, 525-536.
- Wong, L. N., & Einstein, H. H. (2009a). Systematic evaluation of cracking behavior in specimens containing single flaws under uniaxial compression. *International Journal of Rock Mechanics & Mining Sciences*, 239-249.
- Simmons, G., & Richter, D. (1976). Microcracks in rocks. In R. G. Strens, *The Physics and Chemistry of Minerals and Rocks* (pp. 105-137). Toronto: John Wiley & Sons.

- Kranz, R. L. (1983). Microcracks in rocks: A review. *Tectonophysics*, 449-480.
- Martin, C. D. (1993). Strength of Massive Lac du Bonnet Granite Around Underground Opening. *Ph.D. Thesis, University of Manitoba, Winnipeg, Canada*, 278p.
- Wong, L. N., & Einsein, H. H. (2009b). Crack Coalescence in Molded Gypsum and Carrara Marble: Part 1. Macroscopic Observations and Interpretation. *Rock Mech Rock Eng*, 475-511.
- Li, D., Zhu, Q., Zhou, Z., Li, X., & Ranjith, G. P. (2017). Fracture analysis of marble specimens with a hole under uniaxial compression by digital image correlation. *Engineering Fracture Mechanics*, pp. 109-124.
- Azevedo, M. N., Lemos, V. J., & Almeida, R. J. (2008). Influence of aggregate deformation and contact behaviour on discrete particle modelling of fracture of concrete. *Engineering Fracture Mechanics*, pp. 1569-1586.
- Liu, H.-Z., Lin, J.-S., He, J.-D., & Xie, H.-Q. (2018). Discrete Elements and Size Effects. *Engineering Fracture Mechanics*, pp. 246-272.
- Sharifzadeh, M., Feng, X.-t., Zhang, X., Qiao, L., & Zhang, Y. (2017). Challenges in multi-scale hard rock behaviour evaluation at deep underground excavations. *12th Iranina and 3rd Regional Tunnelling Conference*. Tunnelling and Climate Change.
- He, M., Nie, W., Han, L., & Ling, L. (2010). Microcrack analysis of Sanya granite fragments from rockburst tests. *Mining Science and Technology*, 238-243.
- Zhou, Y., Zhao, C., Zhao, C., Yu, Z., & Du, Z. (2018). Mechanical Properties and Damage Evolution of Specimens Containing Single Cracks: An Experimental Study Based on SEM Method. *10th Asian Rock Mechanics Symposium*. Singapore: ARMS10.
- Zhang, Y., Feng, X.-T., Zhang, X., Wang, Z., Sharifzadeh, M., Yang, C., . . . Zhao, J. (2019). Strain energy evolution characteristics and mechanisms of hard rocks under true triaxial compression. *Engineering Geology*.
- Arena, A., Piane, C. D., & Sarout, J. (2014). A new computational approach to cracks quantification from 2D image analysis: Application to micro-crack description in rocks. *Computers & Geosciences*, 106-120.
- Lin, Q., Yuan, H., Biolzi, L., & Labuz, J. (2014). Opening and mixed mode fracture process in a quasi-brittle material via digital imaging. *Engineering Fracture Mechanics*, pp. 176-193.
- Tang, C. A., & Kaiser, P. K. (1998). Numerical Simulation of Cumulative Damage and Seismic Energy Release During Brittle Rock Failure—Part I Fundamentals. *International Journal of Rock Mechanics and Mining Science*, 113-121.
- Omella, M. E., Tang, C.-A., & Zhang, Z. (2004). Scanning of Essential Minerals in Granite Electron Microscope Study on the Microfracture Behavior. *Geology and Resources*, pp. 129-136.
- Kachanov, L. M. (1958). Time of rupture in creep conditions. *Izvestiia Akademii Nauk SSSR, Otdelenie Technicheskikh Nauk*, 26-31.
- Odqvist, F., & Hult, J. (1961). Some aspects of creep rupture. *Arkiv for Fysik*, 379-382.

**Chapter 4 . The Role of Mineralogical
Characteristics of Mafic Rock on its
Behaviours Based on Grain-Based Model
and Modified Heterogeneity Index und
Uniaxial Compression Tests**

Abstract

This paper applied the concept of grain size classification on the grain-based model (GBM) to investigate the influence of heterogeneity induced by mineralogical characteristics on mafic rock behaviours. The model could mimic the highly heterogeneous specimen with large range of grain distribution according to the observation by scanning electron microscopy (SEM) and measurement by digital image processing. According to the model setup, a modified heterogeneity index (MHI) was proposed to describe the heterogeneity considering the influence of different grain size including fine grain, medium grain, and coarse grain. The basic model was calibrated by the results of experimental tests. The strength and modulus of numerical specimens increased with the decrease of MHI by varying the range of grain size distribution and increased with the increase of grain size for both highly and lowly heterogeneous models. Moreover, the related position of small grain and large grain of different minerals determined the fracture development based on the models with different mineral distribution.

Keywords: Grain-based model, Heterogeneity, Grain size, Uniaxial compression tests

4.1 Introduction

In nature, rock heterogeneity is associated with mineral composition (e.g. grain size and mineral distribution) and microdefects (e.g. micro-cracks, cleavage planes, and voids). Numerous laboratory tests showed that the same rock type specimen could presented different behaviours and mechanical properties due to material heterogeneity (Martin, 1993). Blair and Cook (1998) illustrated that the material heterogeneity could cause stress concentration and accelerate the rock failure in the loading process. Tang et al. (2005) found that the homogeneous specimen has a higher strength than the heterogeneous specimen. Nicksiar and Martin (2014) pointed out that the material heterogeneity due to grain size variation could impact the peak strength and crack initiation stress of specimen.

Numerical models are significantly developed to simulate heterogeneity induced by grain size and grain shape. With the development of numerical simulation, discrete element method (DEM) could represent the actual material and capture complicated mechanical behaviours at micro-scale (Cundall,

2001). There are several DEM methods simulating different rock types with different grain size and grain shape (Figure 4-1). Potyongdy and Cundall (2004) proposed bonded-particle model (BPM) to mimic rock with different grains by using circular particles. However, the ratio between the tensile strength and compressive strength is overweighting than the experimental results (Yoon et al., 2012). Cho et al. (2007) applied a clumped particle model to reduce this problem, which used several clumped particles to mimic rock grains. However, the clumped particles are hard to break due to rigid bodies, which is different with experimental results (e.g. intra-granular crack) (Erarslan & Williamms, 2012). Ivars et al. (2008) introduced smooth-joint model (SJM) to simulate the sliding behaviour at the interface between particle pairs. The smooth-joint contact would loss its effect as the deformation occurrence (Mehranpour & Kulatilake, 2017), which is suitable to be installed as the grain boundaries. Hence, based on two contact models (BPM and SJM), Potyondy (2010) proposed a grain-based model (GBM), which developed the circular grains to polygonal grains to mimic the real crystalline rocks.

Under meso-scale (laboratory scale), many researchers mimic the rock specimens by GBM and reveal the influence of petrographic factors. Hofmann et al. (2015) indicated the influence of mineralogical factors on rock behaviour and fracture development by four groups of specimens with different mean grain size. Peng et al. (2017a) proposed a heterogeneity index based on the mean grain size of each mineral and average grain size of specimen. Saadat and Taheri (2019) compared several lowly heterogeneous grain-based models with different grains size to interpret the influence of grain size on rock behaviours.

With the technical development, more and more approaches were utilized to effectively investigate the influence of microstructures on micro-scale rock behaviours, including Scanning Electron Microscope (SEM) observation (Zhang & Wong, 2018), digital image processing (Tao et al., 2020), and microscopic modelling (Zhang et al., 2020). Numerous researchers were conscious of the significance of microscopic heterogeneity induced by petrographic and mineralogical factors (e.g. grain size, grain shape, mineral

distribution, particle packing, porosity, and voids distribution). In addition, Hofmann et al. (2015) also indicated that the larger standard deviations could not be implemented in the model due to the limitation of Voronoi tessellation. It means that the GBM could effectively mimic the rock specimen with small range of grain size distribution under mesoscale. However, according to the SEM observation and investigation, the grain size distributes at a large range in some real natural rocks. Therefore, it is important to investigate the rock behaviours of highly heterogeneous rock.

Considering above limits, this paper classifies the grain size of the constituent minerals to build a heterogeneous model which could effectively mimic the mineral grain size distribution collected from the SEM images measured by digital image processing. To be specific, this research classified the same mineral into three groups in terms of fine grain, medium grain, and coarse grain. Based on this method, the grain-based model could mimic the specimen with high heterogeneity induced by large range of grain size. Moreover, according to the modelling mechanism, a modified heterogeneity index (MHI) was proposed based on the concept of grain classification, which could effectively describe the heterogeneity induced by grain size distribution. Based on the modified heterogeneity index, the four GBM with different heterogeneity indices were generated to investigate the influence of heterogeneity on rock behaviours. By varying seed numbers, the influence of mineral distribution on rock behaviours of highly heterogeneous specimens and lowly heterogeneous specimens was carried out as well. Finally, this paper not only analysed the grain size influence on lowly heterogeneous specimens, but also analysed that of highly heterogeneous models.

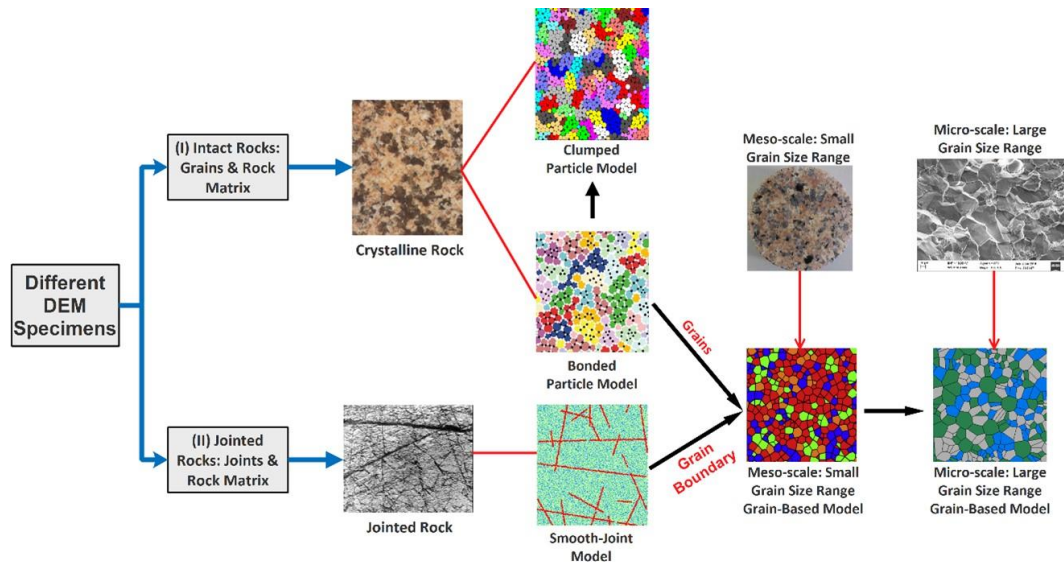


Figure 4-1: Different DEM numerical methods to mimic rock specimens (Modified after Potyondy & Cundall, 2004; Cho et al., 2007; Ivars et al., 2008; Hofmann et al., 2015)

4.2 Grain-Based Model Background

Potyondy (2010) proposed the grain-based model (GBM) in PFC to research the failure process of rock, which could mimic breakable polygon grains. The procedure to create GBM is shown in Figure 4-2, which consist of (a) initial balls packing (i.e. building circular grains), (b) filling circles at internal-void centroids, (c) connecting circles to form polygonal grains, (d) assigning mineral groups from circular grains to polygonal grains, (e) overlapping particles (more than five particles in one grain) and assigning groups based on the mineral groups, and (f) installing contacts, where parallel bond (PB) connects intra-grain particles and smooth-joint contact (SJ) is assigned to the grain boundary.

Figure 4-3 illustrated the movement of particles bonded by two types of contact model, when the loading stress overweights the corresponding strength. The ball connected by parallel bond will move around the fixed ball after bond breakage, which can lead to a “dilation”. As meanwhile, the balls connected by smooth-joint contact will move and overlap along the joint plane after contact breakage, which can lead to a “sliding”.

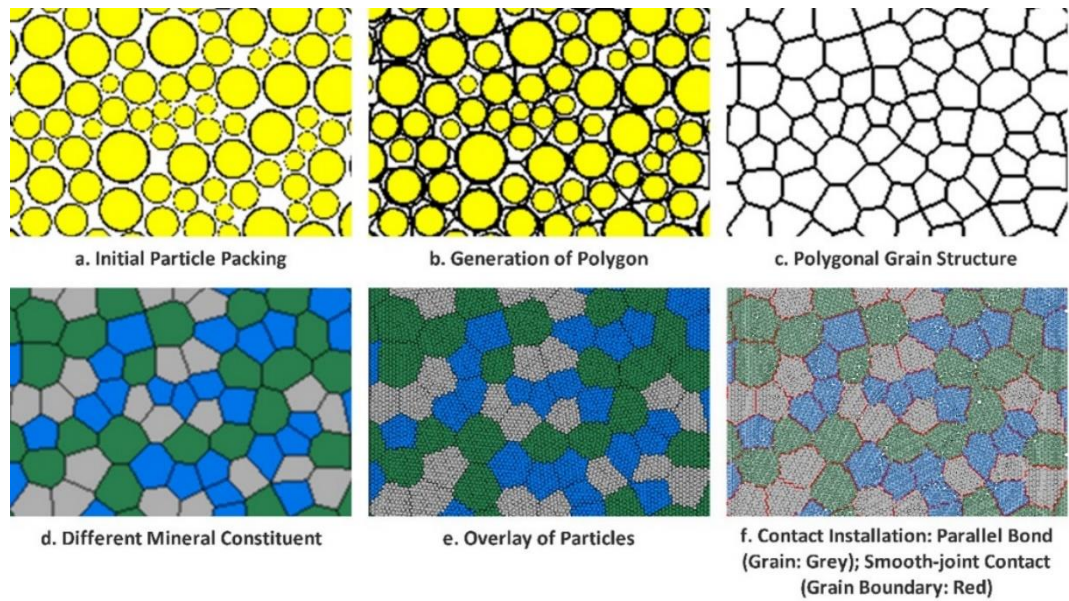


Figure 4-2: Steps of generation of a grain-based model (modified after Hofmann et al., 2015)

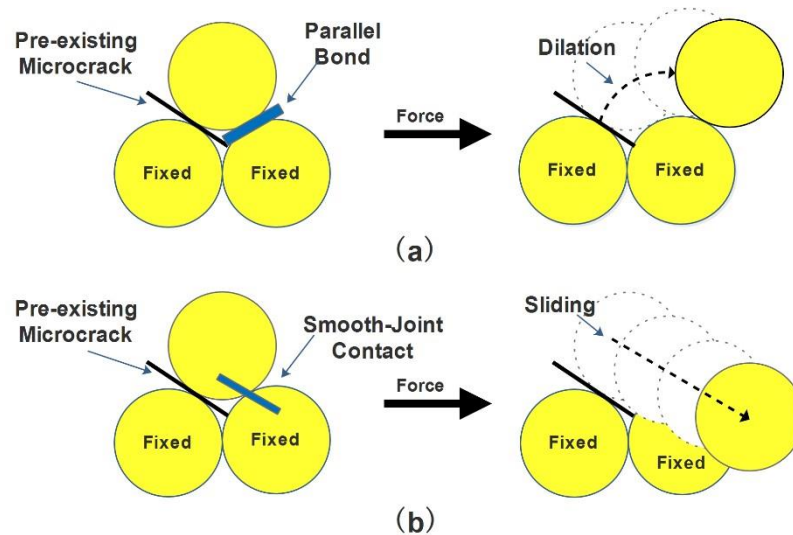


Figure 4-3: Particle movement after contact breakage for (a) parallel bond contact and (b) smooth-joint contact (modified after Bahrani et al., 2014)

4.3 GBM Specimen Preparation Process

4.3.1 Grain Size Distribution and Specimen Dimension

As the comparison sample, the experimental mafic specimens were collected from a mine site in Western Australia. This research is part of a sudden failure mechanism study and ground control management, based on a series of laboratory tests, including scanning electron microscope (SEM) method, UCS test, triaxial compression test, and direct tension test. The dimensions of these

cubic specimens are 50mm*50mm*100mm (height*width*length). According to the observation of cross-section of mafic rock sample (Figure 4-4a), the main mineral composition contains Pyroxene, Plagioclase, and Biotite with the volume fraction of 50%, 30%, and 20% respectively. Moreover, according to previous research from the observation of SEM images and the measurement by digital image processing (Tao et al., 2020), the grain size varies from 8 μ m to 240 μ m. The detail grain size distribution histograms are shown in Figure 4-4b-d.

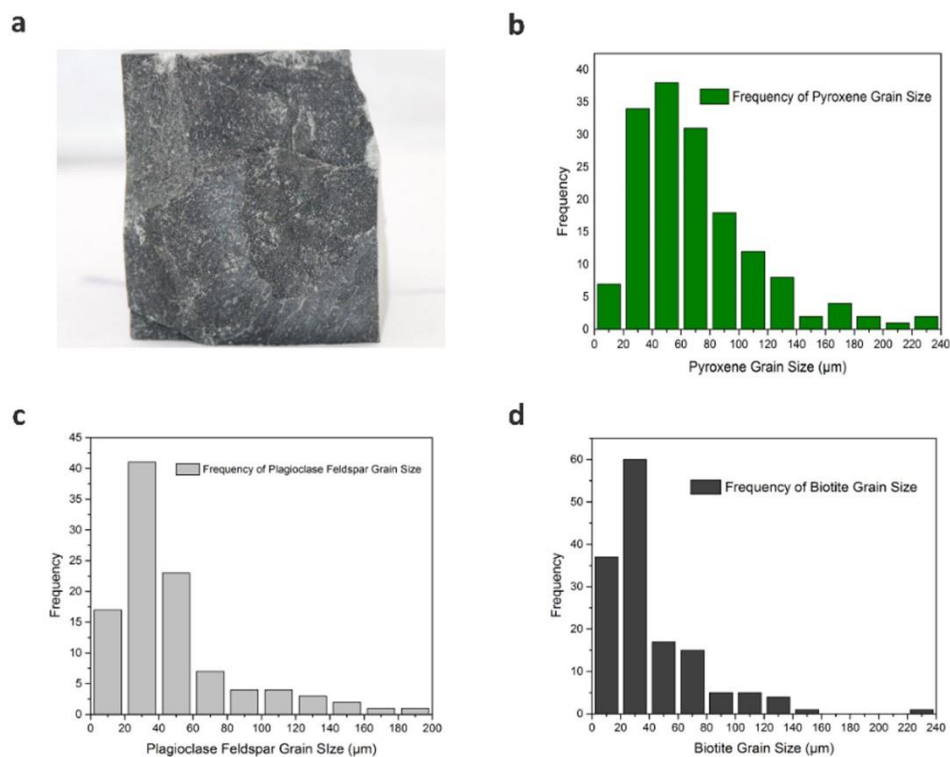


Figure 4-4: Histograms of grain size distribution of each constituent mineral (a: cross-section of mafic sample; b: Pyroxene; c: Plagioclase Feldspar; d: Biotite)

As mentioned in the introduction, the previous researchers build the model based on the average grain size. To be specific, Hofmann et al. (2015) built the specimens with a specific range (i.e. average grain size with small deviation). They also indicated that the larger standard deviations could not be implemented in the model due to limitation of Voronoi tessellation. To be specific, the large range of grain size distribution would lead to obtuse triangle generation based on the nearest neighbour principle. However, the nodes of obtuse triangle would be invalid to voronoi tessellation. Therefore, building the

modelling for heavily heterogeneous rocks (e.g. large range of grain size) may meet errors compared with the natural rocks. However, Bahrani et al. (2014) built the heterogeneous rocks by using different mean grain size for different minerals (i.e. one mineral with coarse grains and other minerals with fine or medium grains). This method indicated that the coarse grains could coexist with medium grains or fine grains as different minerals in one model. In order to build a model that is much more similar with the actual rocks, a method of grains classification was applied based on the concept of particles aggregation. According to particles aggregation (Chen et al., 2020), the primary particles (with size 5 μm) formed the secondary particles. Moreover, the secondary particles could be classified into fine secondary particles and coarse secondary particles, which is determined by the aggregation degree. Therefore, all grain sizes in this research are classified into three groups in terms of fine grain, medium grain, and coarse grain. In general, by dividing one mineral into several groups, it can ensure the different grain size of this mineral could be simulated in the model. The size range and frequency percentage of constituent minerals observed and measured from SEM images are listed in Table 4-1. Based on this method, the numerical specimen could contain a large range of grain size distribution, which could satisfy the actual rock grain structure.

Table 4-1: Mineral content and size of mafic specimen.

Minerals	Volume Fraction (%)	Fine Grain		Medium Grain		Coarse Grain	
		Grain Size (μm)	Frequency (%)	Grain Size (μm)	Frequency (%)	Grain Size (μm)	Frequency (%)
Pyroxene	50	9-20	5	20-140	89	140-240	7
Plagioclase	30	8-20	17	20-80	68	80-200	15
Biotite	20	8-20	26	20-80	63	80-180	11

The scale of grain-scale is micron-sized based on the SEM observation, which cost a huge time to simulate the grain-scale specimen due to the computer performance. In order to time-efficiently compute and mimic the grain structure, the current researchers built the models by increasing the grain size scale to reach at millimetre-sized (Bewick et al., 2013; Saadat & Taheri, 2019). According to Potyondy and Cundall (2004), the effect of scale is not significantly, when the particle size is relatively small compared to the grain size and specimen dimension. Therefore, the minimum grain size and the

particle size are determined as 0.1mm and 0.05mm respectively in this research model, namely, the ratio of grain size to particle size is similar with the real specimens. The dimension of numerical specimen is 25mm (width) *50mm (height) in PFC2D.

4.3.2 Scenarios of Model Setup

4.3.2.1 Heterogeneity Index

In order to investigate the influence of rock heterogeneity induced by mineralogical factors on macroscopic rock behaviours and related mechanical parameters, grain size and mineral composition should be considered in rock heterogeneity degree. Peng et al. (2017a) proposed a heterogeneity index (Equ.4-1), which presented the material heterogeneity induced by the variation of grain size distribution.

$$H = \sqrt{\sum_{i=1}^m \left(\frac{r_i}{R_a} - 1\right)^2} \quad (\text{Equ.4-1})$$

Where, H is heterogeneity index; r_i is the mean grain size of different constituent minerals; m is the number of mineral types; R_a is the average grain size of specimen, which is defined as (Equ.4-2):

$$R_a = \sum_{i=1}^m \omega_i r_i \quad (\text{Equ.4-2})$$

Where, ω_i is the volume fraction of different constituent minerals.

According to this heterogeneity index equation, H is determined by each mineral mean grain size and average grain size of specimen. However, this index is less effective to illustrate the influence of grain size range on material heterogeneity. Specifically, if one material with a large range of grain size has the same average grain size and volume fraction with another material with a small range of grain size, they will exhibit same heterogeneity index following this equation. However, this equation provides an effective approach to present the relationship between heterogeneity and grain size ratio. If each ratio of grain size to average grain size could be determined, the real heterogeneity induced by grain size of constituent minerals could be

determined. However, there are a large amount of grains in the specimen, which will lead to a huge calculation time. Therefore, considering the grain size classification could effectively reduce the calculation time and increase the reliability of the heterogeneity of specimens. Based on the grain size distribution and frequency percentage, the grain size is classified into three groups for each mineral, in terms of fine grain, medium grain, and coarse grain. Therefore, in this research, a modified heterogeneity index (MHI) was defined as:

$$MHI = \sqrt{\sum_{i=1}^n \left[\left(\frac{r_{fi}}{R_a} - 1 \right)^2 + \left(\frac{r_{mi}}{R_a} - 1 \right)^2 + \left(\frac{r_{ci}}{R_a} - 1 \right)^2 \right]} \quad (\text{Equ.4-3})$$

Where, r_{fi} , r_{mi} , and r_{ci} are the mean grain size of each constituent mineral in three types of grain size including fine grain, medium grain, and coarse grain, respectively; n is the number of minerals.

4.3.2.2 Model Setup

In order to determine the influence of microscopic heterogeneity induced by mineral size distribution on rock behaviours, other two modelling setup methods were applied for comparison. One method is building modelling based on mean grain size with small deviation (Hofmann et al., 2015). Another method is building modelling based on grain size of 10% passing and 90% passing (Bewick et al., 2013). Therefore, Scenario 1 utilized the real grain distribution, which ranges from the minimum grain size to maximum grain size observed and by SEM images. Scenario 2 utilized the grain size of 10% passing and 90% passing to determine the size range, namely the range between r_{i10} and r_{i90} . Scenario 3 utilized half of mean grain size as the deviation, namely range between $\frac{1}{2}r_i$ and $\frac{3}{2}r_i$. Scenario 4 utilized quarter of mean grain size as the deviation, namely range between $\frac{3}{4}r_i$ and $\frac{5}{4}r_i$. Four grain-based models with different heterogeneity are shown in Figure 4-5.

The detail heterogeneity index and grain size range are shown in Table 4-2. The modified heterogeneity index could effectively depict the degree of heterogeneity and be much reliable than Equ.4-1 result, which decreased with

the increase of heterogeneity degree induced by the increase of grain size distribution range, namely the ratio of maximum grain size to minimum grain size.

Table 4-2: Data of constituent mineral grain size and heterogeneity index for four scenarios.

Scenario ID		Scenario 1	Scenario 2	Scenario 3	Scenario 4
Grain Size Range (mm)	Pyroxene	0.1~2.4	0.22~1.24	0.35~1.06	0.53~0.88
	Plagioclase	0.1~1.9	0.16~0.99	0.24~0.71	0.35~0.59
	Biotite	0.1~2.2	0.15~0.80	0.21~0.62	0.31~0.52
r_{max}/r_{min}	Pyroxene	24	5.64	3.02	1.66
	Plagioclase	19	6.19	2.96	1.69
	Biotite	22	5.33	2.95	1.68
Heterogeneity Index (H)		0.40	0.46	0.47	0.39
Modified Heterogeneity Index, (MHI)		3.01	1.78	1.37	0.85

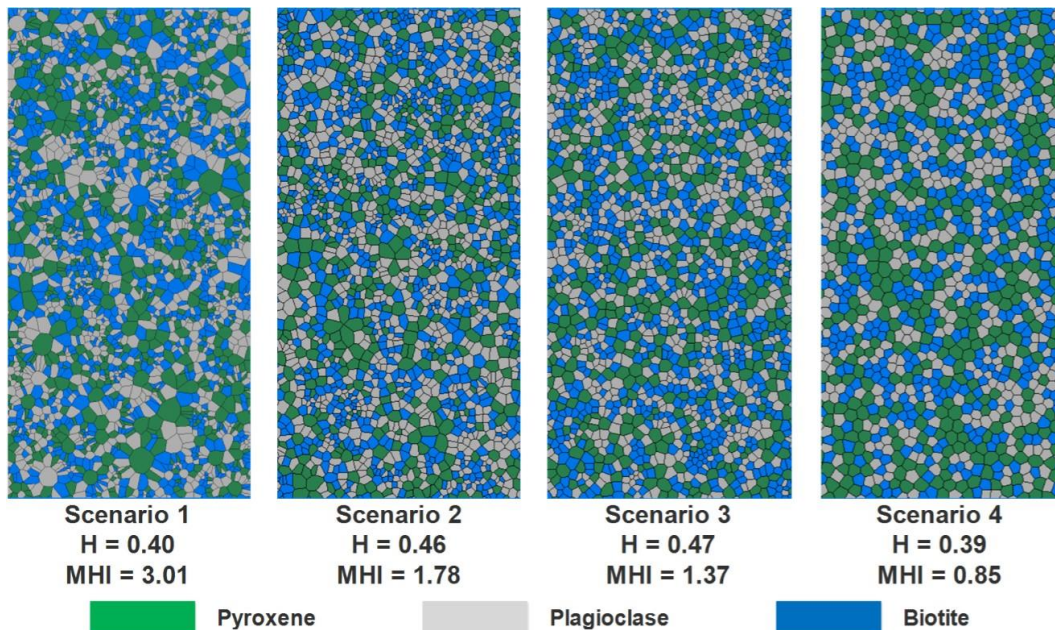


Figure 4-5: Grain-Based Model by different scenarios with different MHI

4.4 GBM Calibration

4.4.1 Calibration Procedure

According to the GBM mechanism, it could not input the macroscopic mechanical parameters to obtain the rock behaviours under loading. It requires inputting microscopic mechanical parameters and assign them as grain properties and boundary properties. According to previous studies (Bahrani et al., 2014; Saadat & Taheri, 2020), the procedure of examining the relationship

between micro-parameters and macro-parameters could be regarded as a guidance for parameters selection. The main calibration procedure includes: (1) input the grain parameters (parallel bond and particle properties), including PB tensile strength and cohesion, PB and particle modulus, ratio of normal to shear stiffness of PB and particle, particle friction coefficient and so on; (2) input grain boundary parameters (smooth-joint contact), including SJ normal stiffness and shear stiffness, SJ tensile strength, SJ cohesion, SJ friction coefficient and so on; (3) perform UCS and direct tension tests to check the Macro-scale properties (UCS, tensile strength, and Young's modulus); (4) compare the macroscopic properties of experimental and numerical result; and (5) if the results are inconsistent, modify the microscopic parameters until the numerical results meeting the experimental results.

Moreover, in the PFC, different seed number of grains and ball could determine different mineral distributions (i.e. grain size and mineral location) and different particle distributions (i.e. particles packing or voids location). In order to collect a group of accurate microscopic mechanical parameters, 10 models with different mineral distribution and particle distribution were built and the model with average mechanical properties were selected as the basic model. The calibration process were only applied on the Scenario 1, which is regarded as the basic model for comparison. The calibrated micro-parameters were applied on other scenarios to determine the influence of micro-scale petrographic and mineralogical factors on rock macro-scale behaviours.

4.4.2 GBM Micro-parameters

The calibration process is a trial-and-error process to verify the reliability of model. According to the calibration method, the micro-parameters for grains are listed in Table 4-3 and the micro-parameters for grain boundaries are listed in Table 4-4. The grains are formed by parallel bond and particles, which have different properties based on different minerals. The boundary is formed by smooth-joint contact, which is assumed as same properties.

Table 4-3: Microscopic mechanical parameters for parallel bond and particles.

Micro-scale Parameters of Grain (Parallel Bond & Particles)			
Element	Pyroxene	Plagioclase	Biotite
Particle size (mm)	0.05	0.05	0.05
Particle density (kg/m ³)	2500	2600	2800
Friction coefficient of particles	1.0	1.0	1.0
Ratio of normal to shear stiffness of particles	1.5	1.5	1.5
Ratio of normal to shear stiffness of bond	2.0	2.0	1.5
Modulus of parallel bond (GPa)	58	65	61
Tensile strength of parallel bond (MPa)	300	330	320
Cohesion of parallel bond (MPa)	250	300	270
Friction angle of parallel bond (°)	35	35	35

Table 4-4: Microscopic mechanical parameters for smooth-joint contact.

Micro-scale Parameters of Grain Boundary (Smooth-joint Contact)	
Smooth-joint contact normal stiffness (N/m)	4*10 ⁹
Smooth-joint contact shear stiffness (N/m)	2*10 ⁹
Mean smooth-joint bond tensile strength (MPa)	10
Mean smooth-joint bond cohesion (MPa)	60
Smooth-joint bond friction coefficient	1.0
Mean smooth-joint bond friction angle (°)	32

4.4.3 Calibrated Model Compared with Experimental Result

The stress-strain plots for experimental result and numerical result under UCS test are shown in Figure 4-6 and the macroscopic properties of specimen from laboratory tests and numerical simulations are compared in Table 4-5. The macro-properties are collected by a series of laboratory tests applied on the specimens from the mine site in Western Australia. The numerical data are collected from the plots of stress-strain obtained from the simulation after UCS test and direct tension test. The error between laboratory tests and numerical simulations are less than 5%, so the microscopic parameters shown in Table 4-3 and Table 4-4 are valid and could be applied in numerical specimens.

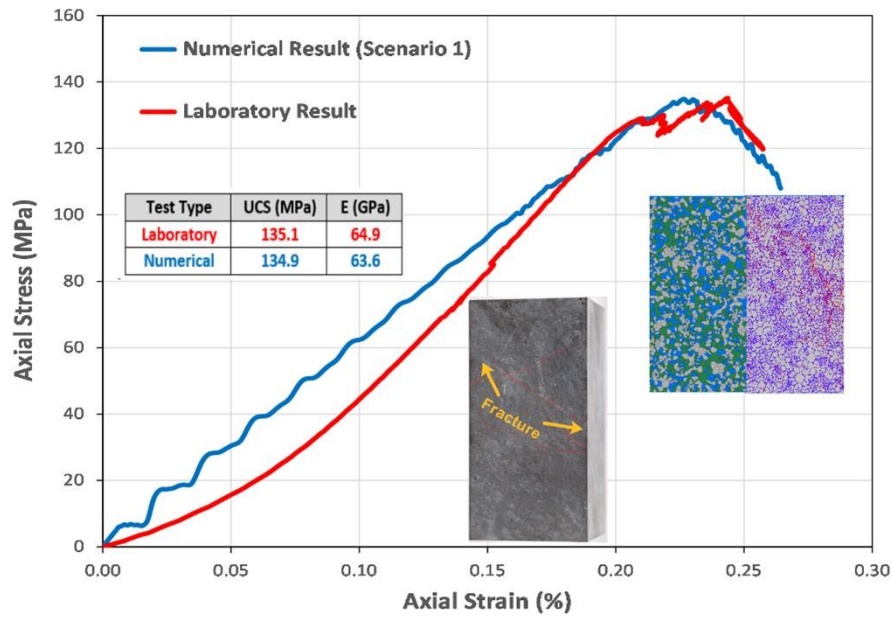


Figure 4-6: The stress-strain plots of numerical result and experimental result under uniaxial compression test

Table 4-5: Comparison of experimental and numerical macroscopic mechanical parameter.

Parameters	Experimental Results	Numerical Results	Error
Young's Modulus (GPa)	65 ± 6	63.6	2.15%
UCS (MPa)	135 ± 10	134.9	0.07%
Tensile Strength (MPa)	18 ± 3	18.7	3.9%

The Experimental and numerical specimens under UCS test were shown in Figure 4-7. The inter-granular cracks dominate the fractures. The fractures of experimental failed specimen are formed of few thin cracks with disordered extension direction. Moreover, the main cracks occurred along the grain boundaries which were located at the interface of different minerals. The inter-grain cracks developed and coalesced the major fracture. The major fracture path of numerical specimen is consistent with the fracture development of laboratory specimen. The extension direction is associated with the grain boundaries direction and mineral distribution.

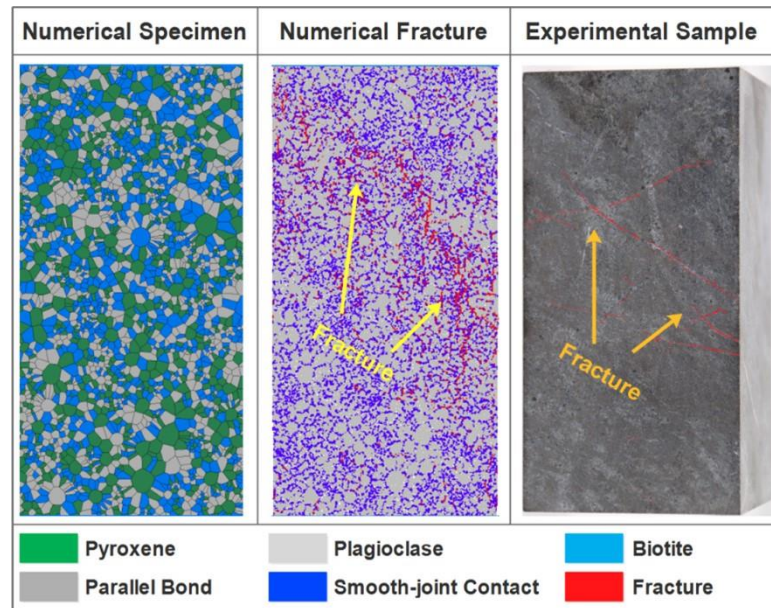


Figure 4-7: Experimental and numerical test comparison

4.5 Results and Discussion

The heterogeneities under micro-scale are associated with petrographic and mineralogical factors, including grain size, grain shape, mineral composition, mineral distribution, and void distribution. Based on the modified heterogeneity index equation, this section will discuss the influence of heterogeneity induced by geometry factor (i.e. grain size distribution). Moreover, the influence of mineral distribution (composition and distribution) and particle distribution (void distribution) for heterogeneous specimens would be discussed as well.

4.5.1 Influence of Heterogeneity Index

As aforementioned, there are four types of models and all scenarios utilized same calibrated microscopic mechanical parameters. The stress-strain curves shown in Figure 4-8 response to the GBM with different heterogeneity index under uniaxial compressive tests. The results reveal that the heterogeneity has a significant influence on the macroscopic mechanical properties of numerical models under uniaxial compressive tests. Specifically, the uniaxial compressive strength of four scenarios increase from 134.9MPa to 304.6MPa, as the heterogeneity index decreases from 3.01 to 0.85. Namely, the more heterogeneous model would have lower UCS. Additionally, the Young's modulus increase with the decrease of heterogeneity index as well, which

varies from 63.6GPa to 92.7GPa. The average grain size of models generated by different scenarios are similar, in terms of 0.56mm, 0.52mm, 0.51mm, and 0.55mm, respectively. Therefore, the macroscopic mechanic properties are mainly influenced by the heterogeneity of specimens. This result is consistent with previous studies (Tang et al., 2000; Ma et al., 2011; Nicksiar & Martin, 2014; Peng et al., 2017a), the homogeneous specimen had a much higher strength than the heterogeneous specimen and the strength gradually increased with the decrease of heterogeneity.

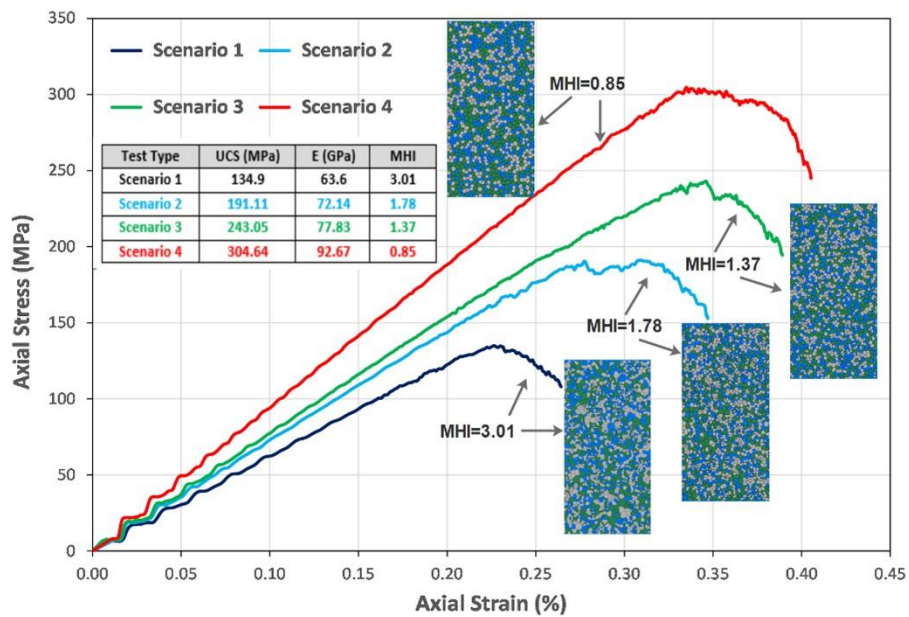


Figure 4-8: Stress-Strain plots of models with different heterogeneity index after UCS tests

The GBM specimens with different MHI induced by grain size range are shown in Figure 4-9a. The value of MHI decrease from Scenario 1 to Scenario 4 with the decrease of grain size range in terms of 3.01, 1.78, 1.37 and 0.85, respectively. The macroscopic fractures of each model after UCS tests are shown in Figure 4-9b. The experimental results are shown in Figure 4-9c, which show that the fractures are associated with the mineral aggregation. The left one has several disordered fractures due to the uniformly distributed minerals, and the right one has an obvious fracture along the interface of different minerals.

According to the micro-cracks classifications (He et al., 2010), there are inter-granular crack, intra-granular crack, and trans-granular crack. In Figure 4-9b, although inter-grain cracks dominate the deformed micro-cracks types for all

models, the intra-grain cracks become more with the MHI increasing. Therefore, the distribution of micro-cracks is different for different MHI. Specifically, when the models have relatively high heterogeneity, the deformed micro-cracks are generally disorderly distributed in the model. When the heterogeneity of models decrease, more intra-grain micro-cracks generated and the interaction of deformed micro-cracks tends to coalesce more macroscopic fractures. The lateral dilation of lowly heterogeneous specimens is much larger than that of highly heterogeneous specimens.

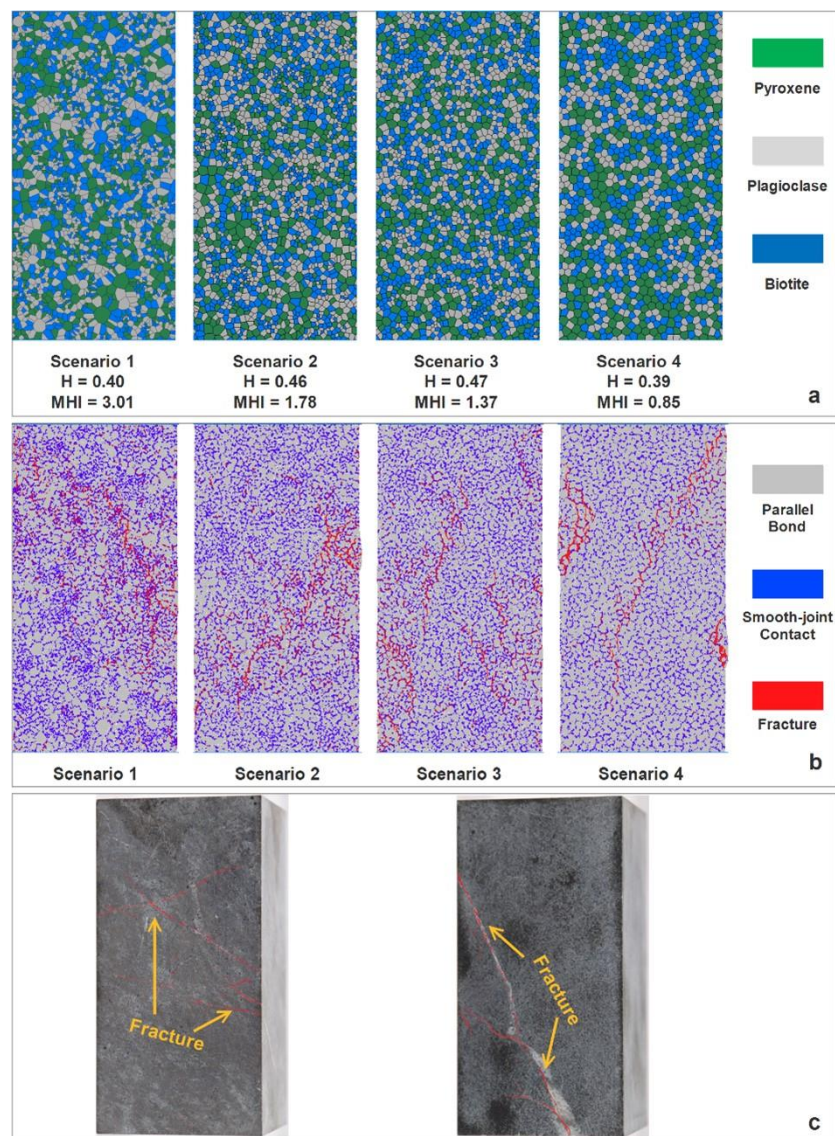


Figure 4-9: The grain-based models with different heterogeneity index: (a) specimen grain structure (b) macroscopic fracture after UCS tests (c) experimental specimen after UCS tests

The results also response to the previous experimental observation and research (Manouchehrian and Cai, 2016; Gao et al., 2016). The

heterogeneous rock has tensile failure mode, which is less violent than the shear failure mode generated in homogeneous rock. In this research, the highly heterogeneous model has more discontinuous micro-cracks, which disorderly distributed in the model. The lowly heterogeneous model has more dilation and the micro-cracks tend to coalesce to macroscopic fracture, especially more intra-grain cracks generated, which leads to a macroscopic shear fracture due to the development path and direction.

In general, the heterogeneity induced by grain size distribution has significant on the macroscopic mechanical properties and fracture development. The strength and modulus increase with MHI increasing. The highly heterogeneous models have more discontinuous inter-grain cracks, and the lowly heterogeneous models have more interaction and coalescence of micro-cracks. Therefore, the lowly heterogeneous models have more violent failure and more dilation of fractures than highly heterogeneous models.

4.5.2 Influence of Mineral Distribution

According to above analysis and observation, although heterogeneity has a significant influence on the rock behaviours, the fracture development is associated with the mineral aggregation. The grain-based model consists of random mineral distribution. By changing the seed number, the minerals would be randomly generated in different position, but the models would keep the same heterogeneity (i.e. same grain size distribution and volumetric fraction of constituent minerals). In this research, all models generated based on different scenarios were operated seven times to build various mineral distribution by setting different seed numbers. The UCS and Young's modulus of models generated by different scenarios and different seed numbers are shown in Figure 4-10.

According to Figure 4-10, the models with different mineral distribution induced by varying seed number have different macroscopic mechanical properties. To be specific, the UCS vary from 133.93MPa to 136.93MPa for Scenario 1, from 189.08MPa to 193.7MPa for Scenario 2, from 236.95MPa to 250.29MPa for Scenario 3, and from 295.58MPa to 314.25MPa for Scenario 4. Additionally,

the Young's modulus vary from 61.79GPa to 65.53GPa for Scenario 1, from 71.04GPa to 73.36GPa Scenario 2, from 76.05GPa to 78.48GPa for Scenario 3, and from 89.26GPa to 93.43GPa for Scenario 4. According to the standard deviations of these macroscopic mechanical properties, the relatively highly heterogeneous models (Scenario 1 & 2) have smaller deviation around their average UCS, and the relatively lowly heterogeneous models (Scenario 3 & 4) have larger deviation around their average UCS. It means that the mineral distribution has insignificant influence on the strength of highly heterogeneous specimens, but it has significant influence on the strength of lowly heterogeneous specimens. Moreover, the mineral distribution has no obvious influence on the Young's modulus of all models generated based on different heterogeneity.

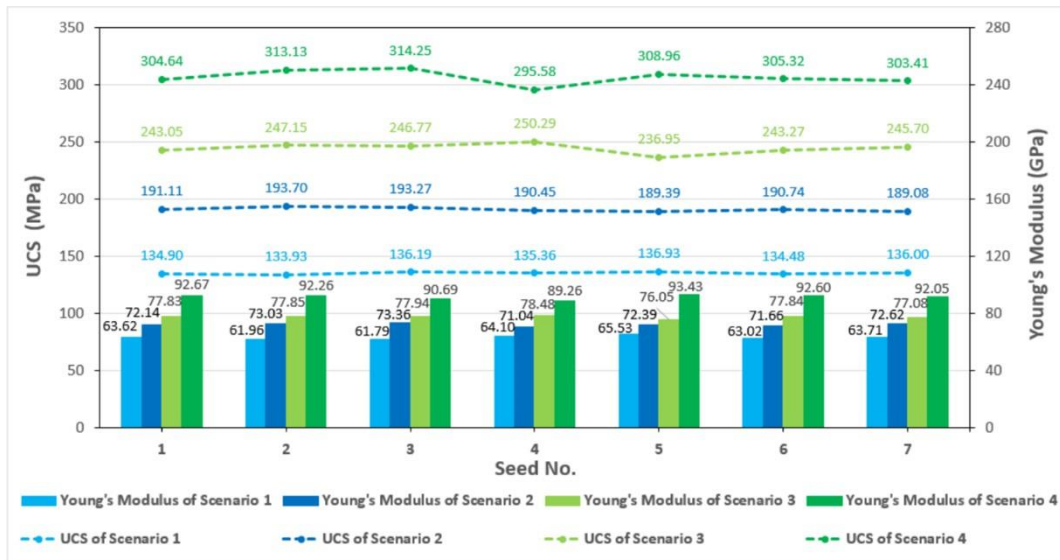


Figure 4-10: Stress-strain plots of models with different mineral distribution types for Scenario 1

The grain structures and fractures of highly heterogeneous model (Scenario 1) and lowly heterogeneous model (Scenario 4) are shown in Figure 4-11 and Figure 4-12. Mineral distribution has significant influence on fractures development both highly heterogeneous model and lowly heterogeneous model. In the different mineral distribution models based on Scenario 1, all models present similar cracks distribution with Scenario 1 in last section. Specifically, the discontinuous micro-cracks dominantly generated at the grain boundaries of relatively smaller grains. The boundaries of clusters of small

grains with high concentration near larger grains are more easily to be broken and coalesce to macroscopic fractures. However, in highly heterogeneous models, the large grains and small grains distribute randomly and uniformly. Therefore, the macroscopic fractures are distributed disorderly based on the randomly aggregation of small grains. Additionally, the lowly heterogeneous models with different mineral distribution have more dilation and the micro-cracks dominantly occur at the interface of different minerals. Since there are no relatively large grains and the minerals are distributed uniformly, the micro-cracks are easily to tend to coalesce fractures. Additionally, the fractures development path are along the interface of different minerals.

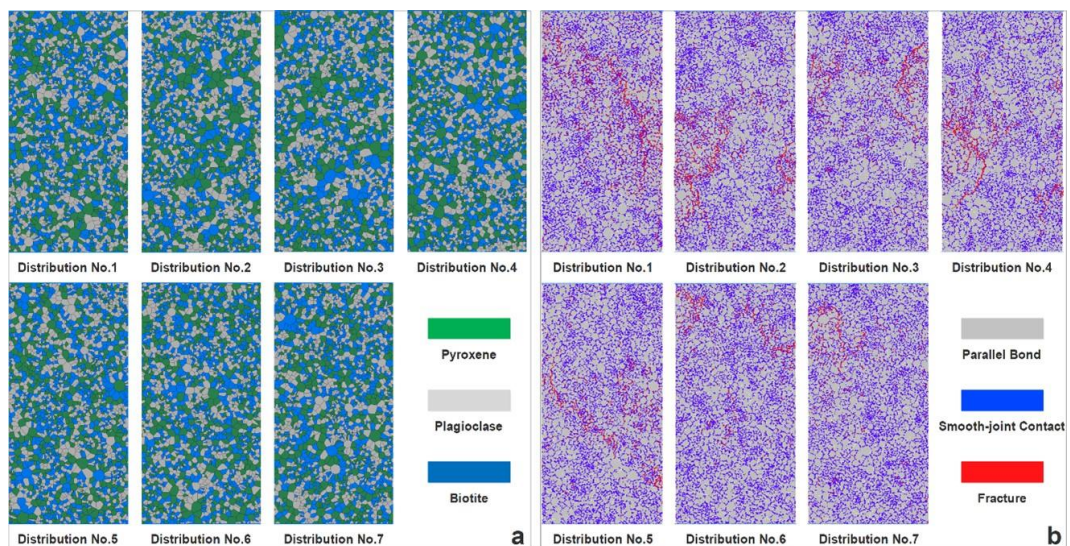


Figure 4-11: The grain-based models with different mineral distribution for Scenario 1: (a) specimen grain structure (b) macroscopic fracture after UCS tests

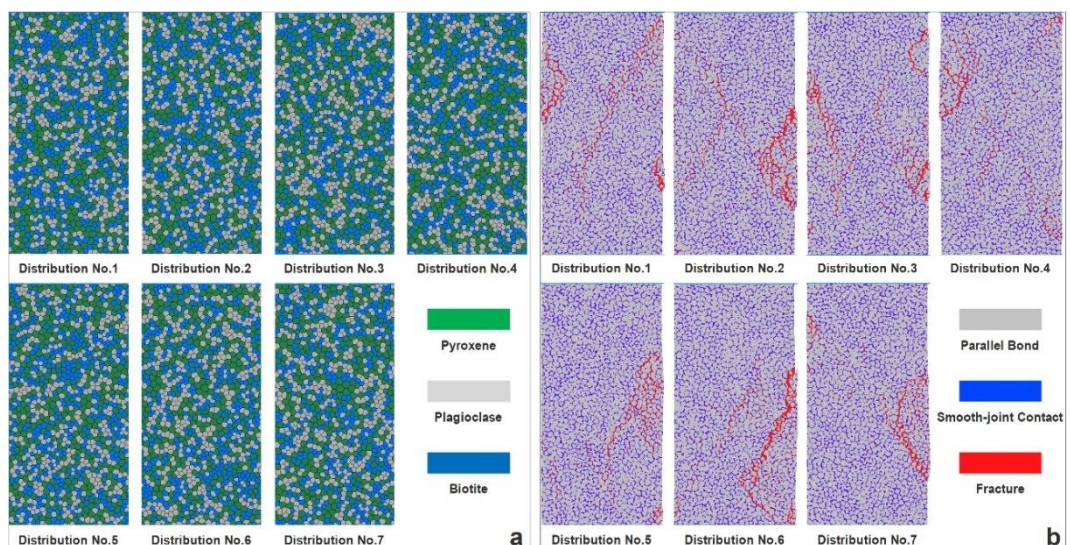


Figure 4-12: The grain-based models with different mineral distribution for Scenario 4: (a) specimen grain structure (b) macroscopic fractures after UCS test

In general, the mineral distribution has an insignificant influence on macroscopic mechanical properties of both highly heterogeneous models and lowly heterogeneous models. However, the mineral distribution has a significant influence on the fracture development. The fracture generation is determined by the related position of small grains and large grains of different minerals.

4.5.3 Influence of Grain Size

As aforementioned, the heterogeneity induced by grain size distribution has a significant influence on macroscopic mechanical properties of specimens and fractures development. However, when the specimens have different average grain size but same MHI, they should have different macroscopic mechanical properties due to different average grain size of specimens, which lead to different fracture development as well. Therefore, five models are generated with different grain size based on Scenario 4 model to investigate the influence of grain size on behaviours of relatively lowly heterogeneous rock, including fine grain, fine-medium grain, medium grain, medium-coarse grain, and coarse grain. The grain sizes are 0.75, 0.875, 1.0, 1.125, and 1.25times of the grain size of Scenario 4, respectively. The grain size of constituent minerals generated by GBM are listed in Table 4-6.

Table 4-6: The grain sizes of five types of models with high heterogeneity index.

Model Types		Fine	Fine-Medium	Medium (S4)	Medium-Coarse	Coarse
Grain Size Range (mm)	Pyroxene	0.40~0.66	0.46~0.77	0.53~0.88	0.60~0.99	0.66~1.10
	Plagioclase	0.26~0.44	0.31~0.52	0.35~0.59	0.39~0.66	0.44~0.74
	Biotite	0.23~0.39	0.27~0.46	0.31~0.52	0.35~0.59	0.39~0.65
Average Grain Size (mm)		0.41	0.48	0.55	0.62	0.69
Ratio to S4		0.75	0.875	1.0	1.125	1.25

MHI	0.85	0.85	0.85	0.85	0.85
-----	------	------	------	------	------

The UCS and Young's modulus of lowly heterogeneous models with different grain size and different seed number based on Scenario 4 is shown in Figure 4-13. The results show that the grain size of models has a significant influence on the macroscopic mechanical properties. Specifically, the strength and modulus increase with the grain size increasing, which is consistent with the previous observation and research (Hofmann et al., 2015; Gui et al., 2016; Peng et al., 2017b; Saddat & Taheri, 2019).

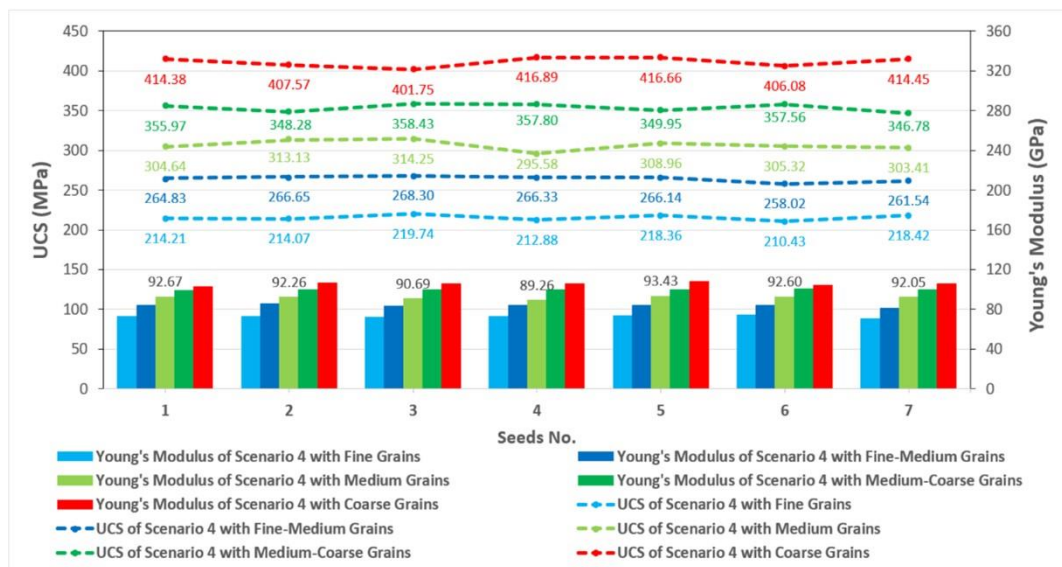


Figure 4-13: Macroscopic mechanical properties of lowly heterogeneous models with different grain size and different seed number.

According to Figure 4-14a, the grain size of specimens increases from left to right. As meanwhile, they have the same MHI, namely the same proportion of related grain size distribution. The macroscopic fractures of relatively lowly heterogeneous specimens with different grain size after UCS tests are shown in Figure 4-14b. According to the analysis in the section of 5.1, Scenario 4 has obvious macroscopic fractures. According to Figure 4-14b, when the grain size increases, the dilation of cracks increase as well, which coalesce to obvious fractures and develop through the specimens. On contrast, when the grain size reduces, the distribution of cracks is similar with the highly heterogeneous specimens, which could not coalesce to a large fracture going through the specimen. However, the macroscopic fractures of lowly heterogeneous

specimens with small grain size are more obvious than that of Scenario 1 model.

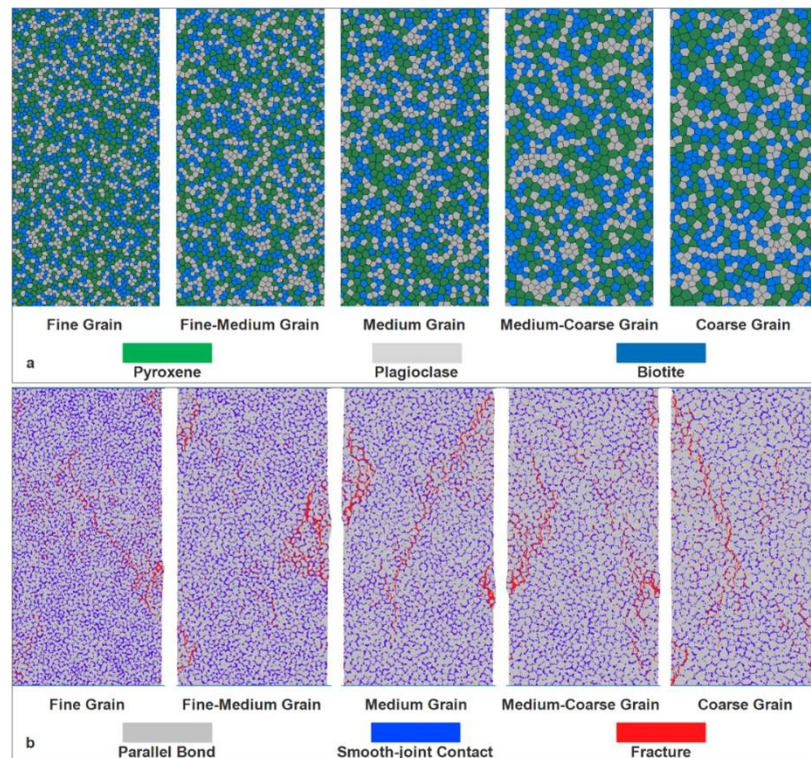


Figure 4-14: Lowly heterogeneous models with different grain size: (a) specimen grain structure (b) macroscopic fracture after UCS test

However, according to the previous research mentioned above, the models applied to investigate the influence of grain size are homogeneous or lowly heterogeneous specimens, which have same grain size or average grain size with small deviation. Therefore, in this research, five highly heterogeneous models are generated with different grain size based on Scenario 1 model as comparison. The models have same MHI (i.e. same proportion of grain size distribution), which could determine the influence of grain size and minimize the impact caused by heterogeneity induced by grain size distribution. Moreover, each grain size model was operated seven times with different seed numbers to minimize the influence of mineral distribution and grain shape. The five highly heterogeneous specimens with different grain size also include fine grain, fine-medium grain, medium grain, medium-coarse grain, and coarse grain. The grain sizes are 1.0, 1.125, 1.25, 1.375, and 1.5 times of the grain size of Scenario 1, respectively. The grain size of constituent minerals generated by GBM are listed in Table 4-7.

Table 4-7: The grain sizes of five types of models with high heterogeneity index.

Model Types		Fine (S1)	Fine-Medium	Medium	Medium-Coarse	Coarse
Grain Size Range (mm)	Pyroxene	0.1~2.4	0.11~2.7	0.13~3.0	0.14~3.3	0.15~3.6
	Plagioclase	0.1~1.9	0.11~2.14	0.13~2.38	0.14~2.61	0.15~2.85
	Biotite	0.1~2.2	0.11~2.48	0.13~2.75	0.14~3.03	0.15~3.30
Average Grain Size (mm)		0.56	0.63	0.70	0.77	0.84
Ratio to S1		1.0	1.125	1.25	1.375	1.5
MHI		3.01	3.01	3.01	3.01	3.01

The UCS and Young's modulus of lowly heterogeneous models with different grain size and different seed number based on Scenario 4 is shown in Figure 4-15. The results show that the grain size of models has a significant influence on the macroscopic mechanical properties. Specifically, the strength and modulus increase with the grain size increasing, which is consistent with the results of lowly heterogeneous models. However, the increment of strength and modulus of two kinds of models with different MHI is different, as the grain size increase. When the grain size increase, the average increment of strength and modulus of highly heterogeneous specimens is 37.5MPa and 8.03GPa. As meanwhile, the average increment of lowly heterogeneous specimens is 48.9MPa and 8.20GPa. Therefore, the grain size of lowly heterogeneous specimens has much more influence on macroscopic mechanical properties than highly heterogeneous specimens.

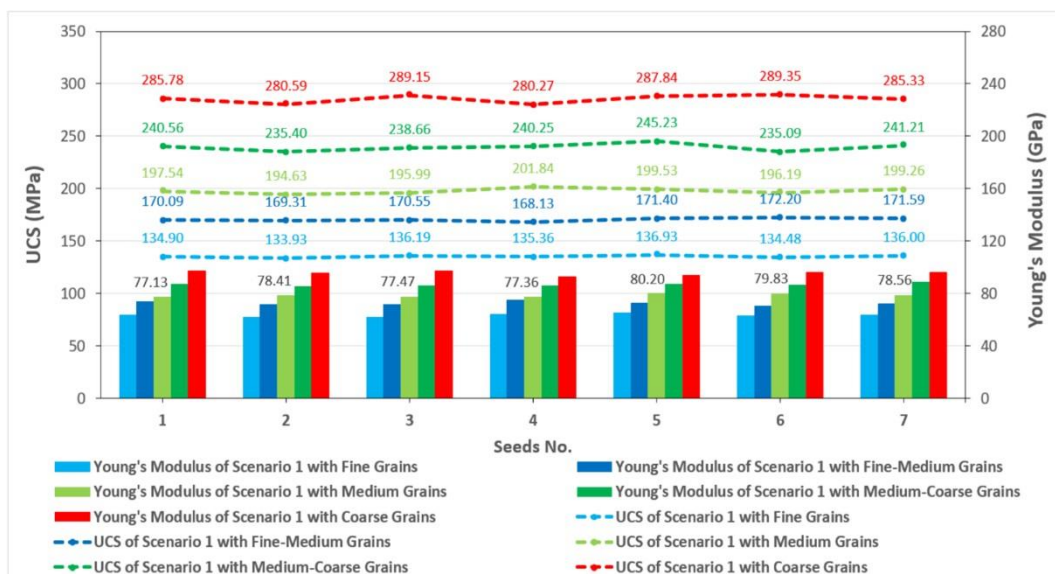


Figure 4-15: Macroscopic mechanical properties of highly heterogeneous models with different grain size and different seed number.

Figure 4-16a shows the grain structures of highly heterogeneous models with different grain size. The macroscopic fractures of highly heterogeneous specimens with different grain size after UCS tests are shown in Figure 4-16b. According to the influence analysis of heterogeneity, Scenario 1 has a large amount of discontinuous inter-grain cracks. With the grain size increasing, more intra-grain cracks occur and the dilation of inter-grain cracks increase as well. Therefore, as the grain size is sufficiently large, the cracks are coalesced to macroscopic fractures, which are developed through the specimens being similar with the lowly heterogeneous specimens.

According to previous studies (Eberhardt et al., 1999; Yilmaz et al., 2009; Sharifzadeh et al., 2017), the grain boundary is weaker than the grain, which is a kind of microstructural defect and could be regarded as the dominant source of stress-concentrating flaws. The stress is distributed over contacts, which leads to bond-break occur earlier at small grain boundary. As meanwhile, the specimens have same dimensions, porosity, particle size, so the number of grain boundaries (smooth-joint contact) decreases with grain size increasing. Therefore, the strength and modulus increase with grain size increasing due to the decrease of grain boundaries. On the other hand, the grain shape (e.g. aspect ratio), and porosity have effect on the experimental observations (Yu et al., 2018; Atapour & Mortazavi, 2018). The large grains have looser structure than small grain due to particle aggregation, which lead to weaker strength for large grains in physical experiments (Tuğrul & Zarif, 1999; Shao et al., 2014; Yu et al., 2018). In this research, all grains are filled by sufficient particles, so the grain size influence is opposite to the observation in physical experiments. In future research, complex grain structures (i.e. loose and tight particle aggregation) or different contact properties assigned to grains based on size could be considered in the GBM.

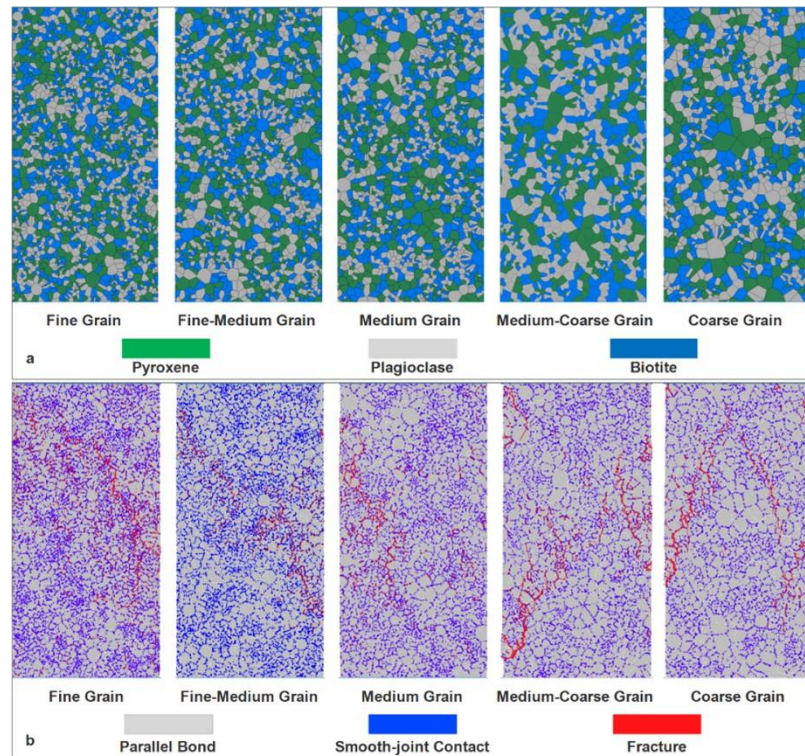


Figure 4-16: Highly heterogeneous models with different grain size: (a) specimen grain structure (b) macroscopic fracture after UCS test

4.6 Conclusion

This paper built a grain-based model according to the concept of grain size classification, which could effectively mimic the highly heterogeneous specimen. The microscopic parameters of grain-based model are calibrated by comparing the macroscopic mechanical properties collected from experimental results. Based on this model, a modified heterogeneity index (MHI) is proposed, which could more effectively describe the heterogeneity of specimens induced by different mineral grain size distribution. Four models with different MHI are generated based on different range of grain size distribution. Moreover, a series of models with different mineral distribution and grain size based on the highly heterogeneous specimen (Scenario 1) and lowly heterogeneous specimen (Scenario 4) are generated and analysed. The observation and analysis are concluded below.

(1) The numerical results indicate that the heterogeneity induced by grain size distribution range has a significant influence on the macroscopic mechanical properties and fractures development under uniaxial compression tests. The

strength and modulus increase with the decrease of MHI. With the heterogeneity decreasing, more and more dilation and macroscopic fractures are generated. The highly heterogeneous models show more tensile failure due to numerous disordered inter-grain micro-cracks, and lowly heterogeneous models show more violent failure due to coalesced fractures.

(2) The mineral distribution has an insignificant influence on the mechanical properties of all models, and the mineral distribution has less influence on strength and modulus of highly heterogeneous models than that of lowly heterogeneous models. However, the mineral distribution has significant influence on the fracture development. The related position of small grains and large grains of different minerals could determine the fractures development.

(3) The grain size has significant influence on the mechanical properties of all models. Especially, the lowly heterogeneous models have more increment of strength and modulus with grain size increasing. Additionally, the macroscopic fractures are more obvious and dilation of cracks increase with the grain size increasing. The intra-grain cracks become more and more as well.

Acknowledgements

We sincerely acknowledge Northeastern University, China provided the laboratory tests. This study is partly supported by National Natural Science Foundation of China the 111 Project under grant no: 51839003 and B17009. We also thank Dr. Mahdi Saadat at School of Civil, Environmental and Mining Engineering, The University of Adelaide, Australia, for his invaluable support with the grain-based model in PFC software. We would also like to thank the journal editor and reviewers for their valuable suggestions. In addition, this research did not receive any specific grant from funding agencies in the public, commercial, or not-for-profit sectors.

Reference

- Atapour, H., & Mortazavi, A. (2018). The influence of mean grain size on unconfined compressive strength of weakly consolidated reservoir sandstones. *Journal of Petroleum Science and Engineering*, 63-70.
- Bahrani, N., Kaiser, P. K., & Valley, B. (2014). Distinct element method simulation of an analogue for a highly interlocked, non-persistently jointed rockmass. *International Journal of Rock Mechanics & Mining Sciences*, 117-130.

- Bewick, R. P., Kaiser, P. K., Bawden, W. F., & Bahrani, N. (2013). DEM simulation of direct shear: 1. rupture under constant normal stress boundary conditions. *Rock Mechanics and Rock Engineering*, 1647-1671.
- Blair, S. C., & Cook, N. G. (1998). Analysis of compressive fracture in rock using statistical techniques: Part II. Effecte of microscale heterogeneity on macroscopic deformation. *International Journal of Rock Mechanics and Mining Sciences*, 849-861.
- Chen, D., Li, K., Yu, H., Zuo, J., Chen, X., Guo, B., . . . Liu, Z. (2020). Effect of secondary particle size distribution on the magnetic properties of carbonyl iron powder cores. *Journal of Magnetism and Magnetic Materials*, 166062.
- Cho, N., Martin, C. D., & Segoo, D. C. (2007). A clumped particle model for rock. *International Journal of Rock Mechanics and Mining Sciences*, 997-1010.
- Cundall, P. A. (2001). A discontinuous future for numerical modelling in geomechanics. *Geotechnical Engineering*, 41-47.
- Eberhardt, E., Stimpson, B., & Stead, D. (1999). Effects of Grain Size on the Initiation and Propagation Thresholds of Stress-induced Brittle Fractures. *Rock Mechanics and Rock Engineering*, 81-99.
- Erarslan, N., & Williams, D. J. (2012). Investigating the effect of cyclic loading on the indirect tensile strength of rocks. *Rock Mechanics and Rock Engineering*, 327-340.
- Gao, F., Stead, D., & Elmo, D. (2016). Numerical simulation of microstructure of brittle rock using a grain-breakable distinct element grain-based model. *Computers and Geotechnics*, 203-217.
- He, M., Nie, W., Han, L., & Ling, L. (2010). Microcrack analysis of Sanya granite fragments from rockburst tests. *Mining Science and Technology*, 238-243.
- Hofmann, H., Babadagli, T., Yoon, J. S., & Zang, A. (2015). A grain based modelling study of mineralogical factors affecting strength, elastic behaviour and micro fracture development during compression tests in granites. *Engineering Fracture Mechanics*, 261-275.
- Ivars, D. M., Potyondy, D. O., Pierce, M., & Cundall, P. A. (2008). The smooth-joint contact model. *8th. World Congress on Computational Mechanics/5th. European Congress on Computational Methods in Applied Sciences and Engineering*. Venics, Italy.
- Manouchehrian, A., & Cai, M. (2016). Influence of material heterogeneity on failure intensity in unstable rock frailure. *Computers and Geotechnics*, 237-246.
- Martin, C. D. (1993). Strength of Massive Lac du Bonnet Granite Around Underground Opening. *Ph.D. Thesis, University of Manitoba, Winnipeg, Canada*, 278p.
- Mehranpour, M. H., & Kulatilake, P. H. (2017). Improvements for the smooth joint contac model of the particle flow code and its applications. *Computers and Geotechnics*, 163-177.
- Nicksiar, M., & Martin, C. D. (2014). Factors affecting crack initiation in low porosity crystalline rocks. *Rock Mechanics and Rock Engineering*, 1165-1181.

- Peng, J., Wong, L. N., & Teh, C. I. (2017a). Influence of grain size heterogeneity on strength and micro-cracking behaviour of crystalline rocks. *Journal of Geophysical Research: Solid Earth*, 1054-1073.
- Peng, J., Wong, L. N., & Teh, C. I. (2017b). Effect of grain size-to-particle size ratio on micro-cracking behavior using a bonded-particle grain-based model. *International Journal of Rock Mechanics and Mining Sciences*, 207-217.
- Potyondy, D. O. (2010). A Grain-Based Model for Rock: Approaching the True Microstructure. *Proceedings of Rock Mechanics in the Nordic Countries 2010*, (p. 10). Kongsberg, Norway.
- Potyondy, D. O., & Cundall, P. A. (2004). A bonded-particle model for rock. *International Journal of Rock Mechanics and Mining Sciences*, 1329-1364.
- Saadat, M., & Taheri, A. (2019). A numerical approach to investigate the effects of rock texture on the damage and crack propagation of a pre-cracked granite. *Computers and Geotechnics*, 89-111.
- Saadat, M., & Taheri, A. (2020). A cohesive grain based model to simulate shear behaviour of rock joints with asperity damage in polycrystalline rock. *Computers and Geotechnics*, 103254.
- Shao, S., Wasantha, P. L., Ranjith, P. G., & Chen, B. K. (2014). Effect of cooling rate on the mechanical behavior of heated Strathbogie granite with different grain size. *International Journal of Rock Mechanics and Mining Sciences*, 70: 381-387.
- Sharifzadeh, M., Feng, X.-t., Zhang, X., Qiao, L., & Zhang, Y. (2017). Challenges in multi-scale hard rock behaviour evaluation at deep underground excavations. *12th Iranina and 3rd Regional Tunnelling Conference*. Tunnelling and Climate Change.
- Tang, C. A., Liu, H., Lee, P. K., Tsui, Y., & Tham, L. G. (2000). Numerical studies of the influence of microstructure on rock failure in uniaxial compression — Part I: effect of heterogeneity. *International Journal of Rock Mechanics and Mining Sciences*, 555-569.
- Tang, C. A., Wong, R. H., Chau, K. T., & Lin, P. (2005). Modeling of compression-induced splitting failure in heterogeneous brittle porous solids. *Engineering Fracture Mechanics*, Vol.72: 597-615.
- Tao, R., Sharifzadeh, M., Zhang, Y., & Feng, X.-T. (2020). Analysis of mafic rocks microstructure damage and failure process under compression test using quantitative scanning electron microscopy and digital images processing. *Engineering Fracture Mechanics*, 107019.
- Tuğrul, A., & Zarif, I. H. (1999). Correlation of mineralogical and texture characteristics with engineering properties of selected granitic rocks from Turkey. *Engineering Geology*, 303-317.
- Yilmaz, N. G., Karaca, Z., Goktan, R. M., & Akal, C. (2009). Relative brittleness characterization of some selected granitic building stones: Influence of mineral grain size. *Construction and Building Materials*, 370-375.
- Yoon, J. S., Zang, A., & Stephansson, O. (2012). Simulating fracture and friction of Aue granite under confined asymmetric compressive test using clumped particle model. *International Journal of Rock Mechanics & Mining Sciences*, 68-83.

Yu, Q., Zhu, W., Ranjith, P. G., & Shao, S. (2018). Numerical simulation and interpretation of the grain size effect on rock strength. *Geomechanics and Geophysics for Geo-Energy and Geo-Resources*, 157-173.

Zhang, X.-P., Ji, P.-Q., Peng, J., Wu, S.-C., & Zhang, Q. (2020). A grain-based model considering pre-existing cracks for modelling mechanical properties of crystalline rock. *Computers and Geotechnics*, 103776.

Zhang, Y., & Wong, L. N. (2018). A review of numerical techniques approaching microstructures of crystalline rocks. *Computers and Geosciences*, 167-187

Every reasonable effort has been made to acknowledge the owners of copyright material. I would be pleased to hear from any copyright owner who has been omitted or incorrectly acknowledged.

**Chapter 5 . Grain Shape Effect on Rock
Behaviours under Uniaxial Compression
Test Using Grain Based Model by Inputting
Controlled Voronoi Tessellation Data**

Abstract

The grain shape has a significant influence on rock behaviours. Current studies on the grain shape effect are based on loose granular particles or rigid clumped grains. This research utilized 2D particle flow code (PFC) to establish a grain-based model (GBM). By controlling nodes distribution of Voronoi tessellation, three different grain shape groups were generated in terms of hexagon grains, rectangular grains, and shield-shaped grains. The slenderness ratio was defined as the ratio of maximum vertical length to maximum horizontal length, which was adopted to describe the difference in grain shape. The range of slenderness ratios were determined as 0.47~2.13, 0.5~3, and 0.67~1.43 in terms of hexagon grains, rectangular grains and shield-shaped grains, respectively. The rectangular grain models have the highest strength and modulus at the slenderness ratio of 1, and the shield-shaped grain models have the lowest strength and modulus at the slenderness ratio of 1.14. The grain shape has a significant influence on fracture characteristics. The mode of splitting failure dominated the fractures of rectangular grain models, and the shield-shaped models presented more faulting failures. The hexagon grain models have complicated failure modes, including splitting failures in the squat hexagon grain models and faulting failures in the slender hexagon grain models.

Keywords: Grain-based model, Grain shape, Slenderness ratio, Uniaxial compression tests

5.1 Introduction

In nature, rock is a heterogeneous material which is consisted of various minerals. The heterogeneity has a significant effect on rock mechanical properties and fracture development characteristics (Martin, 1993). Numerous laboratory tests showed the influence of rock heterogeneity including stress concentration (Blair & Cook, 1998), crack initiation (Nicksiar & Martin, 2014), peak strength (Tang et al., 2005), and cracks evolution (Basu et al., 2013). Lan et al. (2010) indicated that the heterogeneity is mainly caused by mineral composition, mineral distribution, mineral grain geometry and heterogeneous contact.

As one key element of factors inducing the rock characteristics of heterogeneity, grain geometry is often used to analyse the heterogeneity influence on macroscopic properties and cracks evolution, including grain size

and grain shape. Peng et al. (2017a) defined heterogeneity index by constituent mineral grain size and average grain size. Numerous experimental tests and numerical simulations reveal that the grain size has a significant influence on rock strength (Tuğrul & Zarif, 1999; Yilmaz et al., 2009; Hofmann et al., 2015; Peng et al., 2017b; Atapour & Mortazavi; 2018; Saddat & Taheri, 2019). However, the natural rock has complicated grain shapes, so the artificial specimens are used to analyse the influence of grain shapes on mechanical properties, including stainless-steel powder (Shinohara et al., 2000), plastic pellets (Johanson, 2009), glass bead (Härtl & Ooi, 2011), and sand particles (Liu et al., 2011).

Due to the limits of experiments, numerical simulation becomes the widely used method to analyse the influence of grain shape. The discrete element method (DEM) could effectively mimic actual rock materials to determine the rock mechanical properties and rock damage. Generally, there are two main approaches used in DEM to mimic the grain shape in terms of convex particle and clumped multi-spheres (Liu et al., 2021). The convex particle method includes ellipsoid-shaped particles with different aspect ratios (Ting et al., 1995; Ng, 2009) and various polygonal particles (Mirghasemi et al., 2002; Hosseininia, 2012). Cho et al. (2007) proposed the clump method, which could create a cluster of particles to simulate grain shape. Based on the clump method, a series of models with different grain shapes were established to analyse the grain shape effect, including ellipsoid assemblies (Gong & Liu, 2017), circular-clumped clusters (Zhao et al., 2021), circular-attached particles (Rong et al., 2013; Han et al., 2019).

The above DEM models revealed the influence of grain shape on mechanical properties. However, the above models consisted of loose particles or rigid grains. The loose particles models could not present the influence of bonds between mineral grains. Additionally, the clumped particles are hard to break due to rigid bodies, which is different from the experimental results (e.g. intra-grain cracks) (Erarslan & Williams, 2012). Therefore, Potyondy (2010) proposed the grain-based model (GBM), which is consisted of grains (particles connected by parallel bonds) and grain boundaries (smooth-joint contact).

According to the scanning electron microscopes (SEM) images observation (Figure 5-1), there are different grain shapes including circular, quasi-circular, rectangular, hexagon, and other polygons. According to the previous statistical analysis of the aspect ratio (maximum axis length/minimum axis length), the aspect ratio ranges from 1 to 2.5 (Karsli & Dihkan, 2013; He et al., 2019). Therefore, the slender grains could not be ignored while building numerical models, which is a significant element of grain shape. However, in traditional GBM, the grain shapes were randomly generated by voronoi tessellation. The slender grains are neighbouring with a large quasi-circular grain (Figure 5-1). In order to determine the influence of grain shape on rock properties, namely slenderness ratio, this research would build a series of grain-based models with different slenderness ratios by inputting data of controlled nodes distribution to generate the uniform Voronoi tessellation. In this research, by changing the nodes distribution, three main types of grain shapes of models were established in terms of hexagon grain, rectangular grain and shield-shaped grain with different slenderness ratios of grains. Additionally, the grain area was kept constant, which could eliminate the grain size influence. The influence of grain shapes with different slenderness ratios on rock mechanical properties and fracture characteristics would be carried out.

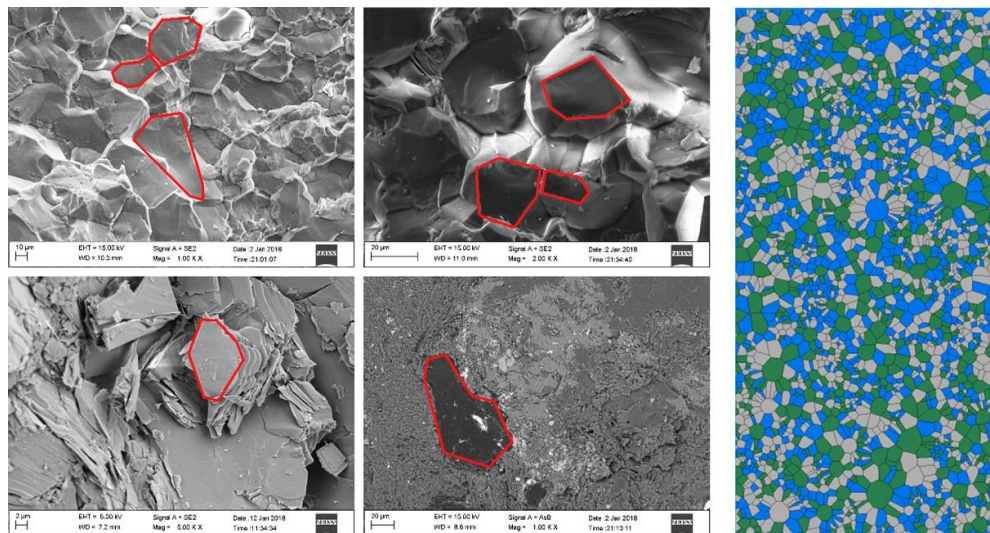


Figure 5-1: Grain shapes shown by SEM images (left) and GBM (right).

5.2 Grain Base Model by Controlled Voronoi Tessellation

According to the fundamental of Voronoi tessellation and GBM generation (Potyondy, 2010; Bewick et al., 2013), the following steps could generate the grains (Figure 5-2): (a) nodes distribution, (b) based on the nearest neighbour principle, the optimised Delaunay triangulation network is established, (c) connecting the perpendicular bisector of boundaries of Delaunay triangulation, the polygon generated by the perpendicular bisectors is Voronoi tessellation, which could be regarded as the grains. When the grains are generated, install particles within the grains and parallel bond connecting these particles to build the grain body and install smooth-joint contact to connect the particles along the grain boundaries, which are regarded as the grain boundaries.

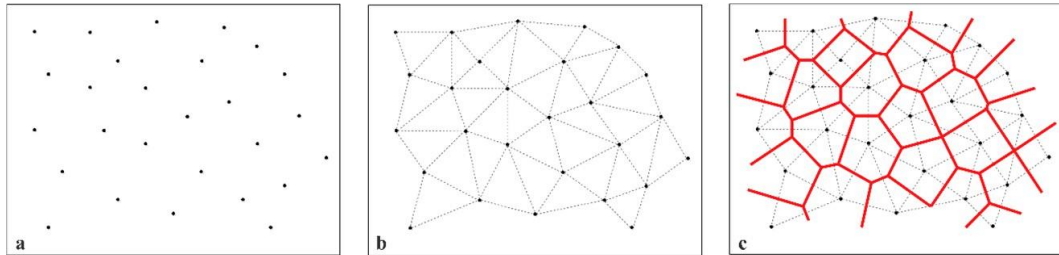


Figure 5-2: Voronoi tessellation generation procedure: (a) nodes distribution (b) Delaunay triangulation network (c) Voronoi tessellation generation.

However, the nodes in normal GBM are distributed randomly, so the polygons were generated randomly in size and aspect ratio. According to Hofmann (2015), the larger standard deviations of mean grain size could not be implemented in the model due to the Voronoi tessellation limitation. To be specific, the large range of grain size distribution would lead to obtuse triangle generation based on the nearest neighbour principle. However, the obtuse triangle could not generate the Voronoi tessellation, and the nodes would be invalid. Therefore, by inputting the controlled nodes distribution, the polygon could be generated under control to get targeted polygons. According to the nodes distribution classification, the grain shapes could be classified into tetragon and hexagon. In PFC-2D, the nodes distribute like a matrix. $N_{i,j}$ is defined as the node numbering, where i and j mean the numbering of a node in the horizontal and vertical direction, namely the numbering of rows and columns. Point $P(x, y)$ is defined as the node location. D_x is defined as the

distance between two nodes in the same row and neighbouring column, as meanwhile D_y is defined as the distance between two nodes in the same column and the neighbouring row. Moreover, the distance of D_x is the same as the distance between any two neighbouring nodes in the same row, which could be presented by Equ.5-1. The distance of D_y is the same as the distance between any two neighbouring nodes in the same column as well.

$$\begin{cases} D_x = |x_{N_{i,2}} - x_{N_{i,1}}| = |x_{N_{i,3}} - x_{N_{i,2}}| = \dots = |x_{N_{i,j+1}} - x_{N_{i,j}}| \\ D_y = |y_{N_{2,j}} - y_{N_{1,j}}| = |y_{N_{3,j}} - y_{N_{2,j}}| = \dots = |y_{N_{i+1,j}} - y_{N_{i,j}}| \end{cases} \quad (\text{Equ.5-1})$$

Based on this restriction, when the position of a node in x-axis direction is the same as that of the neighbouring node in the same column, the generated polygon is rectangular. In contrast, when the position of a node in x-axis is different from that of the neighbouring node in the same column but the node position in x-axis is the same as that of the alternation node, the generated polygon is the hexagon. In addition, when the upper distance and below distance in y-axis around one node are different from each other, the hexagon would be like a shield. It is defined as the equations listed in Table 5-1

Table 5-1: The node position and their distance of each grain shape.

Shape	Nodes Distribution
Rectangular	$if\ x_{N_{i,j}} = x_{N_{i+1,j}}$
Hexagon	$if\ x_{N_{i,j}} \neq x_{N_{i+1,j}}\ and\ x_{N_{i,j}} = x_{N_{i+2,j}}$
Shield-Shaped	$if\ x_{N_{i,j}} \neq x_{N_{i+1,j}}, x_{N_{i,j}} = x_{N_{i+2,j}},$ $and\ y_{N_{i+1,j}} - y_{N_{i,j}} = y_{N_{i+3,j}} - y_{N_{i+2,j}} \neq y_{N_{i+2,j}} - y_{N_{i+1,j}} $

5.3 Experiment Preparation

5.3.1 Experiment Procedure

As the comparison samples, the experimental mafic specimens were collected from a nickel mine site in Western Australia. This study is part of sudden failure mechanism research and ground control management, based on a series of investigation and experiments, including the scanning electron microscope (SEM) method, UCS test, triaxial compression test, and direct tension test (Tao et al., 2020). The macro-mechanical parameters collected from experimental tests include Young's modulus (65 ± 6 Gpa), UCS (135 ± 10 MPa) and tensile

strength (18 ± 3 MPa). Based on the Scanning Electron Microscopy (SEM) image, the mineral grain size distribution and mineral composition were investigated. The dimension of the experimental specimen is 50mm (height) \times 50mm (width) \times 100mm (length).

Based on the mineral investigation of specimens, a heterogeneous grain-based model with a 2D dimension of 50mm (height) \times 25mm (width) was established, which has the same range of grain size distribution and the same mineral composition proportion. By adjusting micro-mechanical parameters, the macro-mechanical parameters of the numerical specimen could be determined until the numerical results satisfy the experimental results. In order to alleviate the influence of grain size and grain shape, the calibrated micro-parameters were applied to the new homogeneous model. The new homogeneous model has only one mineral of pyroxene and the same grain size. After a series of UCS tests on homogeneous models, three suitable models were selected as the basic specimens. The loading rate of all UCS tests is designed as 0.5MPa/s.

In order to determine the influence of grain shape on rock behaviours, there are three main types of models with different grain shapes in terms of rectangular, hexagon, and shield. The shield-shaped grain is axisymmetric in the vertical direction and nonaxisymmetric in the horizontal direction. Moreover, by varying the slenderness ratio of each type of grain, the influence of grain shape parameters on rock behaviours would be carried out. The research procedure was presented in Figure 5-3.

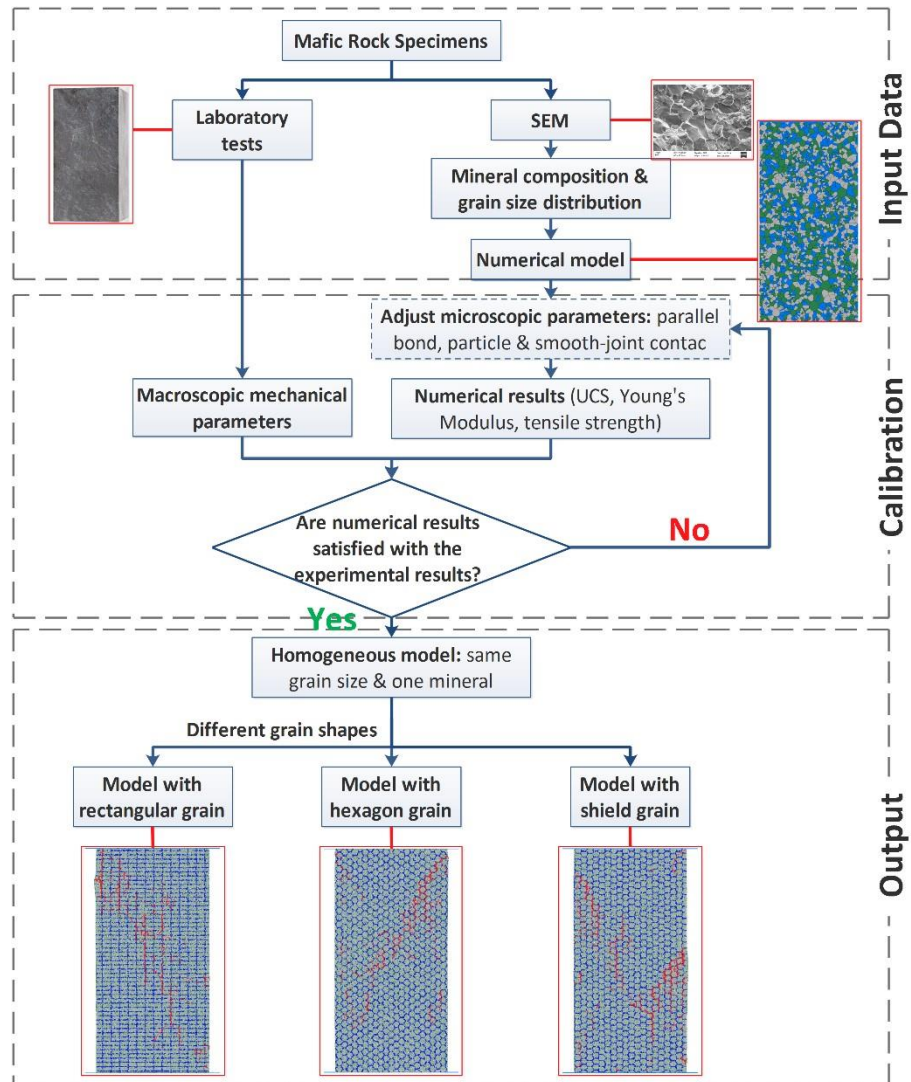


Figure 5-3: Research procedure.

5.3.2 Micro-parameters Calibration

The experimental mechanical parameters could not be directly inputted into the GBM, so the numerical macro-mechanical parameters could be determined by adjusting micro-parameters. According to previous studies (Bahrani et al., 2014; Saadat & Taheri, 2020), the calibration procedure could be regarded as guidance for micro-parameters selection by comparing the numerical macro-parameters with experimental macro-parameters. According to the GBM structure, the grain is formed by parallel bonds and particles and the grains are connected by smooth-joint contact which is regarded as the grain boundary. Therefore, the micro-mechanical parameters include (1) modulus of particles and parallel bond; (2) ratio of normal to shear stiffness of particles, parallel bond and smooth-joint contact; (3) friction coefficient of

particles, parallel bond and smooth-joint contact; (4) tensile strength of the parallel bond and smooth-joint contact; (5) cohesion of parallel bond and smooth-joint contact (6) friction angle of parallel bond and smooth-joint contact.

The calibration procedure is based on the “trial and error” method. To be specific, there are a series of calibrating tests, in terms of uniaxial compression tests and directly tensile tests. After these numerical tests, the stress-strain plots could determine the numerical macro-parameters. The micro-parameters could be determined till the stress-strain plots and macro-parameters of numerical results are consistent with the experimental results. The obtained micro-mechanical parameters calibrated by macroscopic mechanic properties of mafic specimens are shown in Table 5-2 and Table 5-3.

Table 5-2: Microscopic mechanical parameters for parallel bond and particles.

Micro-parameters of grain (Parallel Bond & Particles)			
Element	Pyroxene	Plagioclase	Biotite
Particle radius (mm)	0.1	0.1	0.1
Particle density (kg/m ³)	2500	2600	3000
Friction coefficient of particles	1.2	1.2	1.2
Ratio of normal to shear stiffness of particles	1.5	1.5	1.5
Ratio of normal to shear stiffness of bond	1.5	1.5	1.5
Modulus of parallel bond (GPa)	65	68	62
Tensile strength of parallel bond (MPa)	310	360	320
Cohesion of parallel bond (MPa)	260	280	300
Friction angle of parallel bond (°)	32	35	35

Table 5-3: Microscopic mechanical parameters for smooth-joint contact.

Micro-parameters of grain boundary (Smooth-joint Contact)	
Smooth-joint contact normal stiffness (N/m)	4*10 ⁹
Smooth-joint contact shear stiffness (N/m)	2*10 ⁹
Mean smooth-joint contact tensile strength (MPa)	10
Mean smooth-joint contact cohesion (MPa)	60
Smooth-joint contact friction coefficient	1.0
Mean smooth-joint bond friction angle (°)	30

After adjustment of micro-mechanical parameters, the collected numerical macro-mechanical parameters include Young’s modulus (65.7 GPa), UCS (135.5 MPa), and tensile strength (18.7 MPa), which are consistent with the

experimental results as aforementioned. All errors are less than 5%, so the miro-parameters of the mafic specimen are shown in Table 5-2 and Table 5-3 could be regarded as reliable input parameters.

5.3.3 Construction of Different Grain Shapes

In previous research, the aspect ratio is major length to minor length, so the minimum aspect ratio is 1. If the grains have the same aspect ratio, whose direction of the major length is in the horizontal direction and vertical direction, the UCS is different. Therefore, in this research, use slenderness ratio to determine the grain shape. The slenderness ratio is defined below:

$$\text{Slenderness Ratio} = \frac{\text{Vertical Length}}{\text{Horizontal Length}} = \frac{H}{W} \quad (\text{Equ.5-2})$$

In Equ.5-2, the length in the vertical direction parallel with the loading direction is defined as the height. The length in the horizontal direction is defined as width. All of them go through the centroid of grains. The shield-shaped grains are nonaxisymmetric in the horizontal direction, so the width is the maximum length in horizontal direction. Therefore, when the ratio is over 1, with the increase in ratio, the grain is slender in the vertical direction. When the ratio is less than 1, with the decrease in ratio, the grain is squatter or slender in the horizontal direction. Examples of grain shapes generated by Voronoi tessellation are shown in Figure 5-4.

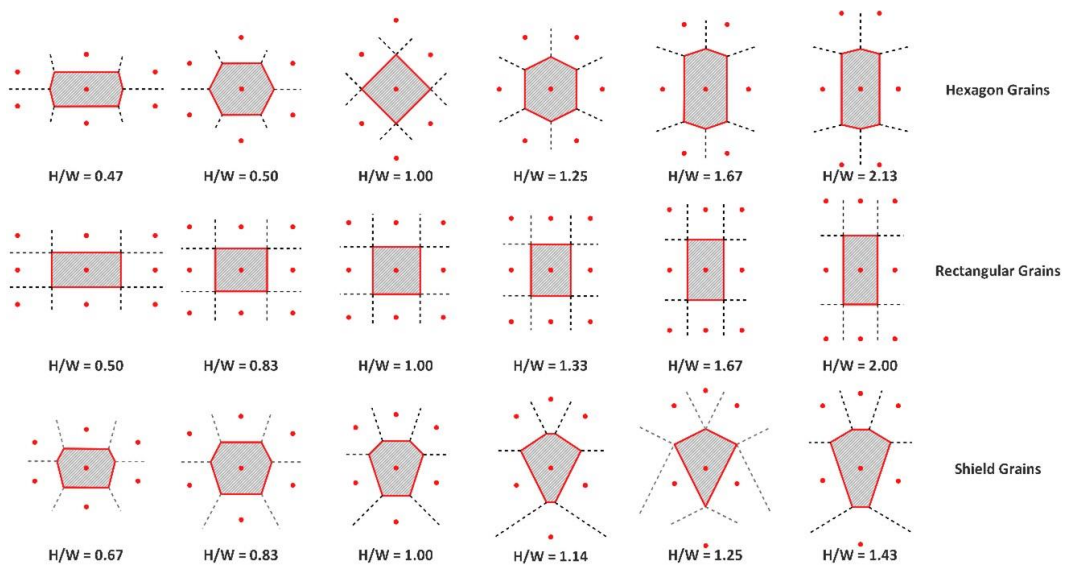


Figure 5-4: The construction of three types of grain shapes by Voronoi tessellation.

According to previous studies on grain size influence by GBM (Hofmann et al., 2015; Saadat & Taheri, 2020), the large grain has more particles and more parallel bond, which would lead to the high strength of the grain. In order to eliminate this influence, the area of each grain in different grain shapes would keep a constant and the ratio of grain size to particle size is enough large. Therefore, the number of particles and parallel bonds would be similar to each other. Meanwhile, the axial height and axial width of each model would be adjusted considering the different slenderness ratios and grain area. The grain area is determined as 1.78mm^2 . Additionally, when the seeds number changes, the particle and mineral distribution are different, which would cause a slight variety of macroscopic mechanical properties of all models with the same microscopic parameters. In this research, each grain shape model was operated 12 times by different seeds number to eliminate the error induced by particle distribution.

5.4 Analysis of Grain Shape Effect

A series of grain-based models were established in terms of hexagon grain models, rectangular grain models and shield-shaped grain models. By controlling the nodes distribution, several different slenderness ratios of grains were constructed for each grain shape. The range of the slenderness ratio was determined based on the two factors. Firstly, the ratio of major axial length to the minor axial length of grains ranges from 1 to 2.5 according to the statistics of rock grains (Karsli & Dihkan, 2013; He et al., 2019). Secondly, the grain has consisted of particles, which means that the shortest width should larger than at least 3 times of particle size. Therefore, the range of slenderness ratios was determined as 0.47~2.13, 0.5~3, and 0.67~1.43 in terms of hexagon grains, rectangular grains and shield-shaped grains, respectively.

In this study, all grains in each model are assumed uniform, including microscopic parameters, grain size and shape. All the models were conducted under uniaxial compressive loading to determine the influence of the slenderness ratio of grain shapes effect on macroscopic mechanical parameters and fracture characteristics.

5.4.1 Influence on Rock Macroscopic Mechanical Properties

Figure 5-5 shows the macroscopic mechanical properties of three kinds of grain shape models with different slenderness ratio. The curves are based on 12 times different particle distributions for each kind of slenderness ratio. The slenderness ratio has a significant influence on the strength and modulus of three types of grain shape models.

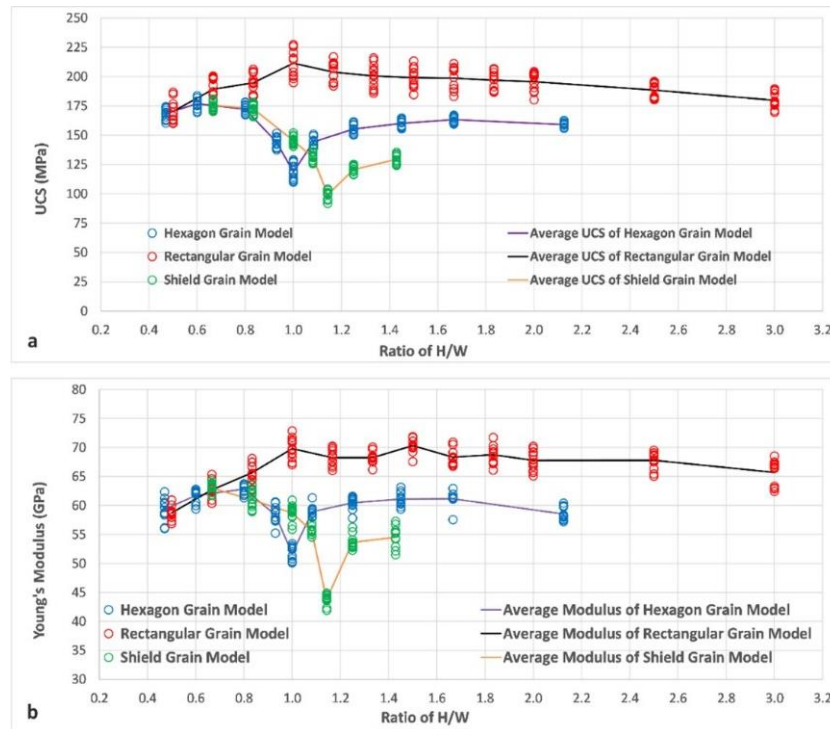


Figure 5-5: UCS and modulus of three types of grain models with different slenderness ratio

The models containing hexagon grain have the lowest strength and modulus when their slenderness ratio is equal to 1. For squat hexagon grain models (slenderness ratio < 1), with the decrease of slenderness ratio, the strength and modulus increase rapidly firstly and then tend to be flat even with a little decrease. For slender hexagon grain models (slenderness ratio > 1), the curves of strength and modulus increase rapidly firstly and then tend to be flat, when the slenderness ratio keeps on increasing. The strength and modulus of shield-shaped grain models with different slenderness ratios have similar curves with the hexagon grain models, but the lowest strength and modulus occurred as the slenderness ratio of 1.14 due to the nonaxisymmetric in the horizontal direction. Furthermore, the strength variation of shield-shaped grain models is larger than hexagon grain models. The curves of strength and

modulus of rectangular grain models with different slenderness ratio are different from the hexagon grain models. The models have the larger strength and modulus, when the slenderness ratio equals to 1. With the increase of the ratio of major axial length to minor axial length, the curves of strength and modulus of rectangular grain models decrease slightly and tend to be flat.

Additionally, the heterogeneous specimens are weaker than homogeneous specimens based on previous experimental and numerical results (Tang et al., 2000; Nicksiar & Martin, 2014; Peng et al., 2017a). Comparing the three types of grain shapes, the shield-shaped grains present more relatively heterogeneous than other two shapes due to the nonaxisymmetric in the horizontal direction. The hexagon grains also present more relatively heterogeneous than rectangular grains due to the inclined grain boundaries. Therefore, the rectangular grain models have higher strength than the other two shapes.

Figure 5-6 shows the comparison of stress-strain curves of hexagon grain models and rectangular grain models with the same ratio of major axial length to minor axial length. According to DEM models as aforementioned, the slender grain is randomly installed into the models, which would influence the results due to the inclination angle between the major axis of grain and horizontal direction. Therefore, comparing the strength of slender grain and squat grain with the same ratio of major axial length to minor axial length is important to understand the grain shape effect.

According to Figure 5-6b, the slender rectangular grain models have higher strengths than squat rectangular grain models. To be specific, the rectangular grain models with the slenderness ratio of 1.5 (3:2) and 2 (2:1) present higher strength than the rectangular grain models with the slenderness ratio of 0.67 (2:3) and 0.5 (1:2), respectively. This result is consistent with the previous research about the influence of the dip angle of grain. Zhao et al. (2021) established the clumped grains with aspect ratio of 2. The grain with the dip angle of 0° is weaker than the grain with the dip angle of 90° , where the dip angle is defined as the angle between the major axis of the grain and the horizontal direction. It means that the squat grain has lower strength than the

slender grain. However, according to Figure 5-6a, the slender hexagon grain models have lower strengths than squat hexagon grain models. To be specific, the hexagon grain models with the slenderness ratio of 1.25 (5:4), 1.67 (5:3) and 2.13 (17:8) have lower strength than the hexagon grain models with the slenderness ratio of 0.8 (4:5), 0.6 (3:5) and 0.47 (8:17), respectively. In the grain-based model, not only grain particle-particle contact, but also grain boundary contact contribute to the mechanical properties. The hexagon grain has four inclined boundaries, which would influence the strength. According to previous experimental and numerical results (Saadat & Taheri, 2019; Yang et al., 2019), the strength of specimens containing the joint or flaw would increase, when the inclined angle of the joint or flaw increases. Under the microscopic view, the grain boundary is regarded as the microstructures, which are easily broken than grain. The inclined boundaries of squat hexagon grains have a larger inclined angle to the horizontal direction than those of slender hexagon grains, which leads to the higher strength of squat hexagon grain models.

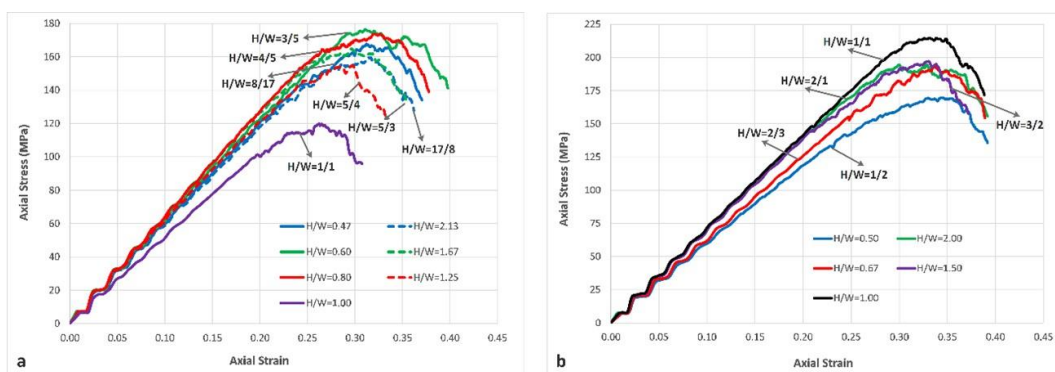


Figure 5-6: Comparison of grain models with the same ratio of maximum axial length to minimum axial length (a) hexagon grain models (b) rectangular grain models.

5.4.2 Influence on Fracture Characteristics

This sub-section will illustrate the influence of grain shapes on the fracture characteristics of specimens. The fractures of different grain shapes models with different slenderness ratios are presented, and all models reach the post-peak stage with 80% of peak strength.

5.4.2.1 Hexagon Grain

Figure 5-7 shows the fractures of hexagon grain models with different slenderness ratios. When the slenderness ratio is close to 1, there are fewer cracks under uniaxial compressive conditions. It means that the slenderer or squatter grain models have more cracks. The micro-cracks in the models are distributed uniformly and randomly when the slenderness ratio is close to 1, which is hard to interact and coalesce macroscopic fractures. In contrast, the slender and squat grain models have more interaction between micro-cracks which leads to coalesce macroscopic fractures. It is consistent with the SEM observation for crack evolution (Ghasem et al., 2020). The study indicated that the new cracks initiated close to the grain boundaries where the grain width is relatively short. To be specific, the grains with large ratio of length to width are subjected to crack propagation during loading. Hence, the slender and squat hexagon grains have higher microcrack density.

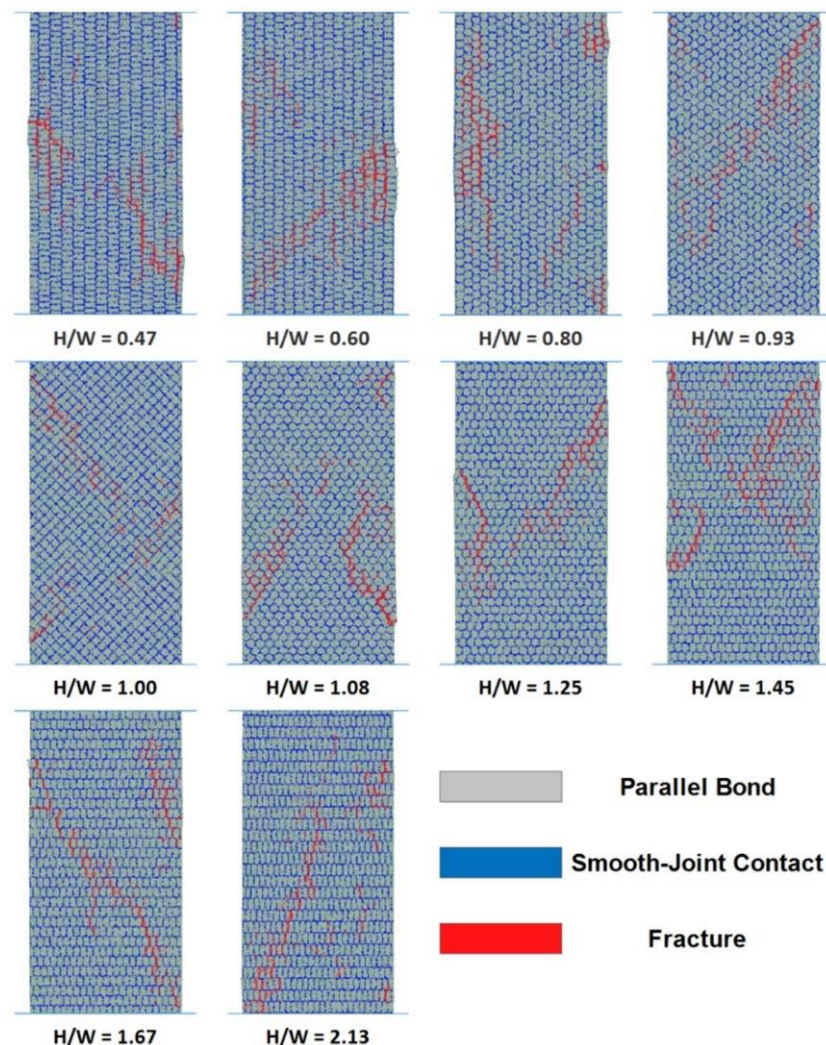


Figure 5-7: Fractures of hexagon grain models with different slenderness ratio

According to Figure 5-7 the squat and slender grain models have more fractures. However, the failure mode of slender grain models is different from the failure mode of squat grain models. The narrow parts of squat grains are combined in vertical direction. Hence, the fractures of squat grain models are induced by the coalescence of subvertical cracks in form of splitting failures. On the other hand, the narrow parts of slender grains are combined in the horizontal direction. Additionally, the experimental results indicated that the cracks propagation direction trend to be parallel to the loading direction under compressive loading (Wawersik & Fairhurst, 1970; Huang et al., 1993; Wong & Einstein, 2009). Hence, the slender grain models presented more shear failure, which resulted in the mode of faulting failure.

Additionally, according to Zhao et al. (2021), the grain with the dip angle of 0° has fewer cracks compared with the dip angle of 90° , when the aspect ratio kept constant. When the crack density is relatively high, the specimens present shear band formation caused by the interaction and coalescence of inter-grain cracks and intra-grain cracks (Moore & Lockner, 1995; Peng et al., 2017a). According to Figure 5-7, the hexagon grain models with slenderness ratio of 1.25 (5:4), 1.67 (5:3) and 2.13 (17:8) have more cracks comparing the fractures of hexagon grain models with the slenderness ratio of 0.8 (4:5), 0.6 (3:5) and 0.47 (8:17), respectively, which results in the mode of faulting failure.

5.4.2.2 Rectangular Grain

Figure 5-8 shows the fractures of rectangular grain models with different slenderness ratios. The influence of the slenderness ratio of rectangular grains on crack evolution is not obvious compared with that of hexagon grain models. The squat and slender rectangular grain models have a relatively large fracture (long and wide opening). In contrast, the localized and relatively small fractures occurred in the quasi-square and square grain models.

Unlike the hexagon grain models, the rectangular grain models have no inclined boundaries, so the vertical cracks contributed to the major fractures, which present splitting failure mode. This result is consistent with the previous

research. Peng et al. (2017a) indicated that the homogeneous specimens have the trend to form more fractures oriented approximately in the vertical direction due to the interaction and coalescence of microcracks. Compared with other grain shapes, the rectangular grain models have relatively high homogeneity, which is hard to form a shear band. However, with the increase in slenderness ratio, the crack density increased. Therefore, the models with relatively large slenderness ratio have complicated failure modes including splitting and faulting failure.

In addition, comparing the fractures of rectangular grains with the same aspect ratio, it has similar results with the hexagon grain models. Specifically, according to Figure 5-8, the rectangular grain models with the slenderness of 1.5 (3:2) and 2 (2:1) present more faulting failures than the rectangular grain models with slenderness ratio of 0.67 (2:3) and 0.5 (1:2), respectively.

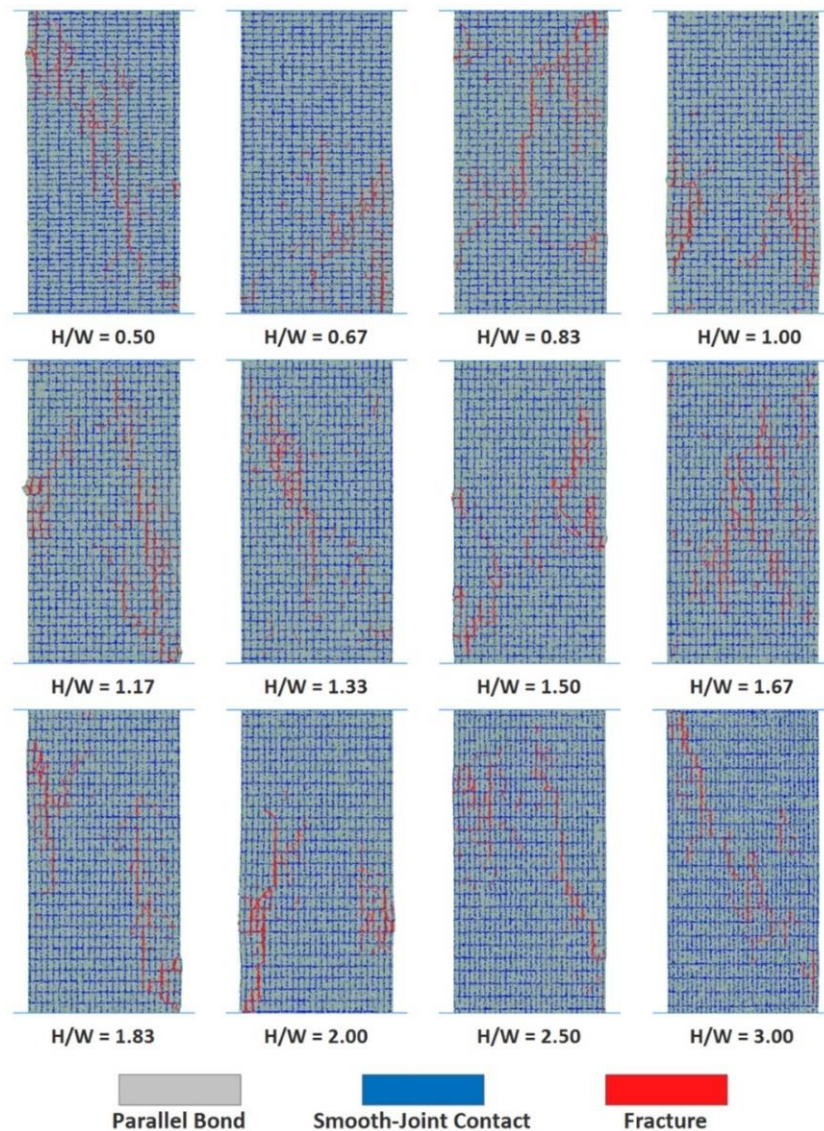


Figure 5-8: Fractures of rectangular grain models with different slenderness ratio

5.4.2.3 Shield-Shaped Grain

Figure 5-9 shows the fractures of shield-shaped grain models with different slenderness ratios. The slenderness ratio of shield-shaped grain has a significant influence on fracture development. The shield-shaped grain models show different fracture modes with other grain shapes. According to the construction of shield-shaped grains, the shield-shaped grains have no vertical boundaries. Therefore, the shield-shaped models present more faulting failures than other grain shapes.

For squat shield-shaped grain models, the fractures are similar to squat hexagon grain models. The narrow parts of squat grains are combined in the vertical direction. Hence, the fractures of squat grain models are induced by

the coalescence of sub-vertical cracks in form of splitting failures. For the model with the slenderness ratio of 1, it presents localized and relatively small fractures. With the increase in slenderness ratio, the slender squat grain models have lower crack density. It is hard to interact and coalesce macroscopic fractures due to the interlocking of grain boundaries, where the models combined the grain boundaries with a large inclined angle and a small inclined angle to the loading direction.

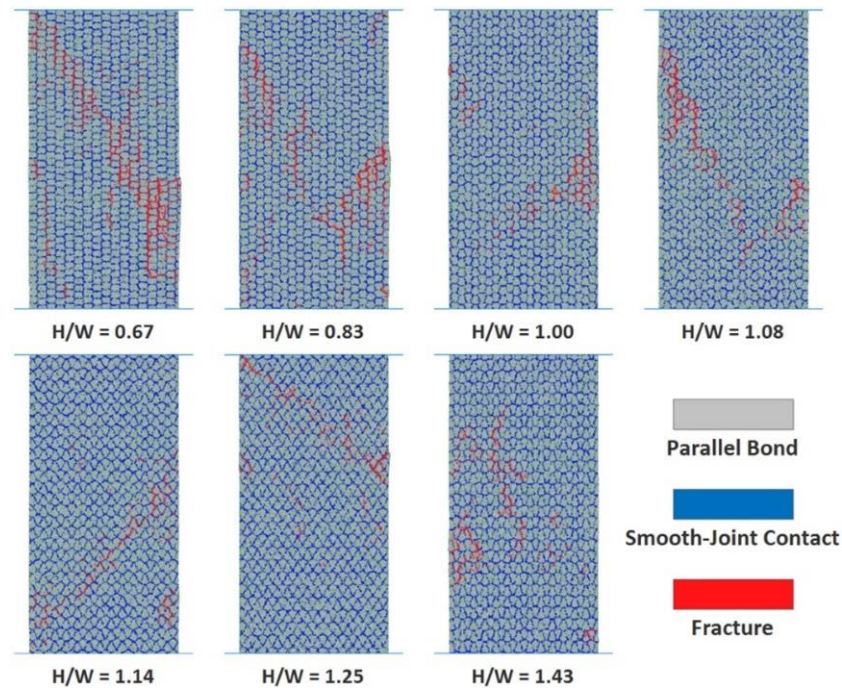


Figure 5-9: Fractures of shield-shaped grain models with different slenderness ratio

5.5 Conclusion

In this study, three different grain shapes with different slenderness ratios were established in terms of hexagon grains, rectangular grains, and shield-shaped grains, based on GBM by controlling node distribution of Voronoi tessellation. The slenderness ratio was defined as the ratio of axial length in the vertical direction and axial length in the horizontal direction. The range of slenderness ratios was determined as 0.47~2.13, 0.5~3, and 0.67~1.43 in terms of hexagon grains, rectangular grains and shield-shaped grains, respectively. Under uniaxial compressive tests, the influence of grain shape on rock macroscopic mechanical properties and fracture development characteristics were analysed.

The grain shape has a significant effect on rock mechanical properties. The rectangular grain models have the highest strength and modulus, and the shield-shaped grain models have the lowest strength and modulus, which is caused by the heterogeneity induced by the grain shape. The slenderness ratio has a significant effect on rock mechanical properties as well. The rectangular grain models have the highest strength and modulus at the slenderness ratio of 1, and they decrease firstly and tend to flat with the increase of the aspect ratio. In contrast, the hexagon grain models and shield-shaped grain models have the lowest strength and modulus at the slenderness ratio of 1 and 1.14 (8:7), respectively.

The slenderness ratio and grain shape have a significant influence on fracture development. The mode of splitting failure is the major fracture in rectangular grain models. The shield-shaped grain models present more faulting failures. The hexagon grain models have a complicated failure mode, which combine splitting and faulting failures. The splitting failures induced by sub-vertical cracks account for the major fractures in squat hexagon grain models, and the slender hexagon grain models present a shear band due to the faulting failures.

Acknowledgements

We sincerely acknowledge Northeastern University, China provided the laboratory tests. This study is partly supported by National Natural Science Foundation of China the 111 Project under grant no: 51839003 and B17009. We also thank Dr. Mahdi Saadat at School of Civil, Environmental and Mining Engineering, the University of Adelaide, Australia, for his invaluable support with the grain-based model in PFC software. We would also like to thank the journal editor and reviewers for their valuable suggestions. In addition, this research did not receive any specific grant from funding agencies in the public, commercial, or not-for-profit sectors.

References

- Atapour, H., & Mortazavi, A. (2018). The influence of mean grain size on unconfined compressive strength of weakly consolidated reservoir sandstones. *Journal of Petroleum Science and Engineering*, 171: 63-70.
- Bahrani, N., Kaiser, P. K., & Valley, B. (2014). Distinct element method simulation of an analogue for a highly interlocked, non-persistently jointed rockmass. *International Journal of Rock Mechanics & Mining Sciences*, 71: 117-130.

- Basu, A., Mishra, D. A., & Roychowdhury, K. (2013). Rock failure modes under uniaxial compression, Brazilian, and point load tests. *Bulletin of Engineering Geology and the Environment*, 72, 457-475.
- Bewick, R. P., Kaiser, P. K., Bawden, W. F., & Bahrani, N. (2013). DEM simulation of direct shear: 1. rupture under constant normal stress boundary conditions. *Rock Mechanics and Rock Engineering*, 1647-1671.
- Blair, S. C., & Cook, N. G. (1998). Analysis of compressive fracture in rock using statistical techniques: Part II. Effecte of microscale heterogeneity on macroscopic deformation. *International Journal of Rock Mechanics and Mining Sciences*, 849-861.
- Cho, N., Martin, C. D., & Segoo, D. C. (2007). A clumped particle model for rock. *International Journal of Rock Mechanics and Mining Sciences*, 997-1010.
- Erarslan, N., & Williams, D. J. (2012). Investigating the effect of cyclic loading on the indirect tensile strength of rocks. *Rock Mechanics and Rock Engineering*, 327-340.
- Ghasemi, S., Khamehchiyan, M., Taheri, A., Nikudel, M. R., & Zalooli, A. (2020). Crack Evolution in Damage Stress Thresholds in Different Minerals of Granite Rock. *Rock Mechanics and Rock Engineering*, 53, 1163-1178.
- Gong, J., & Liu, J. (2017). Effect of aspect ratio on triaxial compression of multi-sphere ellipsoid assemblies simulated using a discrete element method. *Particuology*, 32, 49-62.
- Han, Z., Zhang, L., & Zhou, J. (2019). Numerical Investigation of Mineral Grain Shape Effects on Strength and Fracture Behaviors of Rock Material. *Applied Sciences*, 9, 2855.
- Härtl, J., & Ooi, J. Y. (2011). Numerical investigation of particle shape and particle friction on limiting bulk friction in direct shear tests and comparison with experiments. *Powder Technology*, 212, 231-239.
- He, W., Hayatdavoudi, A., Shi, H., Sawant, K., & Huang, P. (2019). A Preliminary Fractal Interpretation of Effects of Grain Size and Grain Shape on Rock Strength. *Rock Mechanics and Rock Engineering*, 52, 1745-1765.
- Hofmann, H., Babadagli, T., Yoon, J. S., & Zang, A. (2015). A grain based modelling study of mineralogical factors affecting strength, elastic behaviour and micro fracture development during compression tests in granites. *Engineering Fracture Mechanics*, 147: 261-275.
- Hosseininia, E. S. (2012). Discrete element modeling of inherently anisotropic granular assemblies with polygonal particles. *Particuology*, 10, 542-552.
- Huang, J., Wang, Z., & Zhao, Y. (1993). The development of rock fracture: from microfracture to main fracture formation. *International Journal of Rock Mechanics and Mining Science & Geomechanics Abstract*, 30, 925-928.
- Johanson, K. (2009). Effect of particle shape on unconfined yield strength. *Powder Technology*, 194, 246-251.
- Karsli, F., & Dihkan, M. (2013). An image analysis method to detect CSD on rocks with adjusted color images. *Sensor Review*, 33, 323-340.
- Lan, H., Martin, C. D., & Hu, B. (2010). Effect of heterogeneity of brittle rock on micromechanical extensile behavior during compression loading. *Journal of Geophysical Research Solid Earth*, 115, 414-431.
- Liu, Q.-b., Xiang, W., Budhu, M., & Cui, D.-s. (2011). Study of particle shape quantification and effect on mechanical property of sand. *Rock and Soil Mechanics*, 32, 190-197.

- Liu, S., Nie, Z., Hu, W., Gong, J., & Lei, P. (2021). Effect of particle type on the shear behaviour of granular materials. *Particuology*, 56, 124-131.
- Martin, C. D. (1993). Strength of Massive Lac du Bonnet Granite Around Underground Opening. *Ph.D. Thesis, University of Manitoba, Winnipeg, Canada*, 278p.
- Mirghasemi, A. A., Rothenburg, L., & Matyas, E. L. (2002). Influence of particle shape on engineering properties of assemblies of two-dimensional-shaped particles. *Géotechnique*, 52, 209-217.
- Moore, D. E., & Lockner, D. A. (1995). The role of microcracking in shear-fracture propagation in granite. *Journal of Structural Geology*, 17, 95-111.
- Ng, T. T. (2009). Particle shape effect on macro- and micro-behaviors of monodisperse ellipsoids. *International Journal for Numerical and Analytical Methods in Geomechanics*, 33, 511-527.
- Nicksiar, M., & Martin, C. D. (2014). Factors affecting crack initiation in low porosity crystalline rocks. *Rock Mechanics and Rock Engineering*, 1165-1181.
- Peng, J., Wong, L. N., & Teh, C. I. (2017a). Influence of grain size heterogeneity on strength and micro-cracking behaviour of crystalline rocks. *Journal of Geophysical Research: Solid Earth*, 1054-1073.
- Peng, J., Wong, L. N., & Teh, C. I. (2017b). Effect of grain size-to-particle size ratio on micro-cracking behavior using a bonded-particle grain-based model. *International Journal of Rock Mechanics and Mining Sciences*, 207-217.
- Potyondy, D. O. (2010). A Grain-Based Model for Rock: Approaching the True Microstructure. *Proceedings of Rock Mechanics in the Nordic Countries 2010*, (p. 10). Kongsberg, Norway.
- Rong, G., Liu, G., Hou, D., & Zhou, C.-b. (2013). Effect of Particle Shape on Mechanical Behaviors of Rocks: A Numerical Study Using Clumped Particle Model. *The Scientific World Journal*, 2013, 589125.
- Saadat, M., & Taheri, A. (2019). Modelling Micro-cracking Behaviour of Pre-cracked Granite Using Grain-Based Distinct Element Model. *Rock Mechanics and Rock Engineering*.
- Saadat, M., & Taheri, A. (2020). A cohesive grain based model to simulate shear behaviour of rock joints with asperity damage in polycrystalline rock. *Computers and Geotechnics*, 103254.
- Shinohara, K., Oida, M., & Golman, B. (2000). Effect of particle shape on angle of internal friction by triaxial compression test. *Powder Technology*, 107, 131-136.
- Tang, C. A., Liu, H., Lee, P. K., Tsui, Y., & Tham, L. G. (2000). Numerical studies of the influence of microstructure on rock failure in uniaxial compression — Part I: effect of heterogeneity. *International Journal of Rock Mechanics and Mining Sciences*, 555-569.
- Tang, C. A., Wong, R. H., Chau, K. T., & Lin, P. (2005). Modeling of compression-induced splitting failure in heterogeneous brittle porous solids. *Engineering Fracture Mechanics*, Vol.72: 597-615.
- Tao, R., Sharifzadeh, M., Zhang, Y., & Feng, X.-T. (2020). Analysis of mafic rocks microstructure damage and failure process under compression test using quantitative scanning electron microscopy and digital images processing. *Engineering Fracture Mechanics*, Vol.231: 107019.

Ting, J. M., Meachum, L., & Rowell, J. D. (1995). Effect of particle shape on the strength and deformation mechanisms of ellipse-shaped granular assemblages. *Engineering Computations*, 12, 99-108.

Tuğrul, A., & Zarif, I. H. (1999). Correlation of mineralogical and texture characteristics with engineering properties of selected granitic rocks from Turkey. *Engineering Geology*, 303-317.

Wawersik, W. R., & Fairhurst, C. (1970). A study of brittle rock fracture in laboratory compression experiments. *International Journal of Rock Mechanics and Mining Sciences & Geomechanics Abstracts*, 7, 561-564.

Wong, L. N., & Einstein, H. H. (2009). Crack Coalescence in Molded Gypsum and Carrara Marble: Part 2--Microscopic Observations and Interpretation. *Rock Mechanics and Rock Engineering*, 513-545.

Yang, S.-Q., Yin, P.-F., Zhang, Y.-C., Chen, M., Zhou, X.-P., Jing, H.-W., & Zhang, Q.-Y. (2019). Failure behavior and crack evolution mechanism of a non-persistent jointed rock mass containing a circular hole. *International Journal of Rock Mechanics and Mining Sciences*, 114: 101-121.

Yilmaz, N. G., Karaca, Z., Goktan, R. M., & Akal, C. (2009). Relative brittleness characterization of some selected granitic building stones: Influence of mineral grain size. *Construction and Building Materials*, 370-375.

Zhao, X., Elsworth, D., He, Y., Hu, W., & Wang, T. (2021). A grain texture model to investigate effects of grain shape and orientation on macro-mechanical behavior of crystalline rock. *International Journal of Rock Mechanics and Mining Sciences*, 148, 104971.

Every reasonable effort has been made to acknowledge the owners of copyright material. I would be pleased to hear from any copyright owner who has been omitted or incorrectly acknowledged.

**Chapter 6 . Influence of Micro-circular
Defects on Fracture Development of Mafic
Specimen under Uniaxial Compression
Test Using Grain-Based Model**

Abstract

Natural rocks contain crack-like flaws and circular-like flaws. Additionally, non-persistent grain boundaries are easier to create new flaws compared with intact grains. Therefore, it is important to study the interaction between grain boundaries and circular holes. This study applied the grain-based model (GBM) by PFC2D to build the basic intact specimen, which is calibrated by a series of experiments on mafic specimens. At first, a model containing single-hole with different relative location to the grain was established and tested under uniaxial compression, including intra-grain hole, inter-grain hole and trans-grain hole. The results show that the model containing an intra-grain hole has more damaged area around the hole. Compared with the experimental results, three patterns of relationship between hole and inclined grain boundaries were identified to determine the influence of hole on crack evolution and fracture development mechanisms. Moreover, another model containing double-holes were established and testes. The influence of bridge length and bridge angle between two holes were investigated. The results show that the damaged area due to interaction between two holes increases while the bridge length less than the radius of the hole. When the bridge length is larger than the radius of the hole, the interaction between two holes decreases but the damaged area around the holes increases. The double-holes arranged at the bridge angle of 90° have the smallest damaged area and displacement.

Keywords: Grain-based model, Circular defects, Fracture mechanism, Uniaxial compression tests

6.1 Introduction

Natural rocks contain different pre-existing microstructures including micro-cracks, pores, grain boundaries, and cleavage (Tao et al., 2020). These microstructures have a significant influence on the rock mechanical properties due to the size and shape of the micro-defects, which would lead to civil and mining engineering issues. Many scholars contributed to the rock failure process due to cracks propagation and coalescence. Griffith (1920) proposed that stress concentration around small discontinuities caused weakness of brittle material. Simmons and Richter (1976) and Kranz (1983) classified the crack types based on petrographic characteristics (i.e. relative location of cracks to grains). Wong and Einstein (2009a) systematically indicated the

deformed crack types during the rock failure process. Wong and Einstein (2009b) defined the nine crack coalescence modes including tensile, shear, and mixed shear-tensile types. In natural rocks, the discontinuities are not only single pre-existing crack and they are always existing in form of multiple joints. Experimental and numerical results indicated that the geometries of discontinuities could significantly affect the rock mechanical behaviours, such as joint dip angle (Cao et al., 2016) and joint spacing (Liu et al., 2018). As the effective method to investigate the crack development process, Finite Element Model (FEM) (Li & Wong, 2012) and Discrete Element Model (DEM) (Fan et al., 2015) are widely utilized to establish the numerical model to determine the influence of joint on rock behaviours.

However, on the microscopic scale, the natural rocks contain crack-like flaws and pore-like flaws. Additionally, the circular or quasi-circular shapes are often utilized in tunnel and mining engineering, such as the cross-section of tunnel, decline and stope which could be regarded as field-scale circular defects. Therefore, the understanding of the influence of circular defects on fracture development and damage evolution could provide the basis for geotechnical design to reduce failure problems in rock masses with single or multiple circular opening. Lajtai and Lajtai (1975) demonstrated the cracks coalescence mechanism between holes by conducting tests on gypsum samples with holes, which led to the collapse of cavities. Martin et al. (1997) utilised field scale circular test tunnel to examine the failure process around the hole, which indicated that the grain-scale geology had a significant influence on the notch formation and development. Moreover, according to experimental and numerical results, the geometry characteristics of holes have a significant influence on fracture development, including hole size (Wong et al., 2006), hole shape (Zeng et al., 2018; Wu et al., 2020; Zhang et al., 2021), inclination angle of an ellipse hole (Li et al., 2017), holes distribution or arrangement (Lin et al., 2015; Huang et al., 2017), bridge length and bridge angle between two holes (Liu et al., 2019).

With the improvement of understanding and fundamental of failure mechanism of the specimens containing crack-like flaws or circular-like flaws, there is

increasing interest in the rock behaviours and the interaction between pre-existing cracks and circular defects. Wang et al. (2017) applied experiments and DEM to investigate the influence of joint spacing and hole shape. Yang et al. (2019) analysed the influence of dip angle of multiple joints on the specimen containing a circular hole by experiments and DEM. Lin et al. (2020) determined the failure modes of specimens with double holes and multiple joints with different inclination angles. Wu et al. (2020) studied the interaction between holes and cracks by two samples, including a model containing one crack and two holes and another model containing two cracks and one hole.

In previous studies, the influence of pre-existing holes and regularly distributed pre-existing cracks on rock behaviours and the interaction between different defects have been discussed to understand the fracture development and crack evolution mechanisms. However, the natural rocks are complicated, which usually contain irregularly arranged holes, cracks, and non-persistent grain boundaries. To be specific, some micro-circular defects are located within or inter grains without adjacent micro-cracks on micro-scale, and the surrounding rock masses of tunnels may be relatively intact on macro-scale. Although the grain boundary is weaker than grain, it is stronger than pre-existing cracks. Therefore, it is essential to determine the interaction between circular defects and non-persistent grain boundaries (Figure 6-1). With the development of numerical methods, grain-based model (GBM) could mimic the real rock structure based on the grain size distribution and mineral composition (Potyondy, 2010; Bahrani et al., 2014; Hofmann et al., 2015). This research utilized the GBM to mimic a homogeneous model with one mineral and the same grain size, which could reduce the influence of mineral composition and grain size distribution. Based on this model, a single hole would be excavated at different relative location to the grain boundaries, including intra-grain, inter-grain, and trans-grain. The influence of the relative location of single-hole and the inclined angle of grain boundaries on failure modes were investigated. Another model was established with double holes, which has different bridge length and bridge angle between two holes. It could reveal the interaction of two holes based on different distribution or arrangement of two holes.

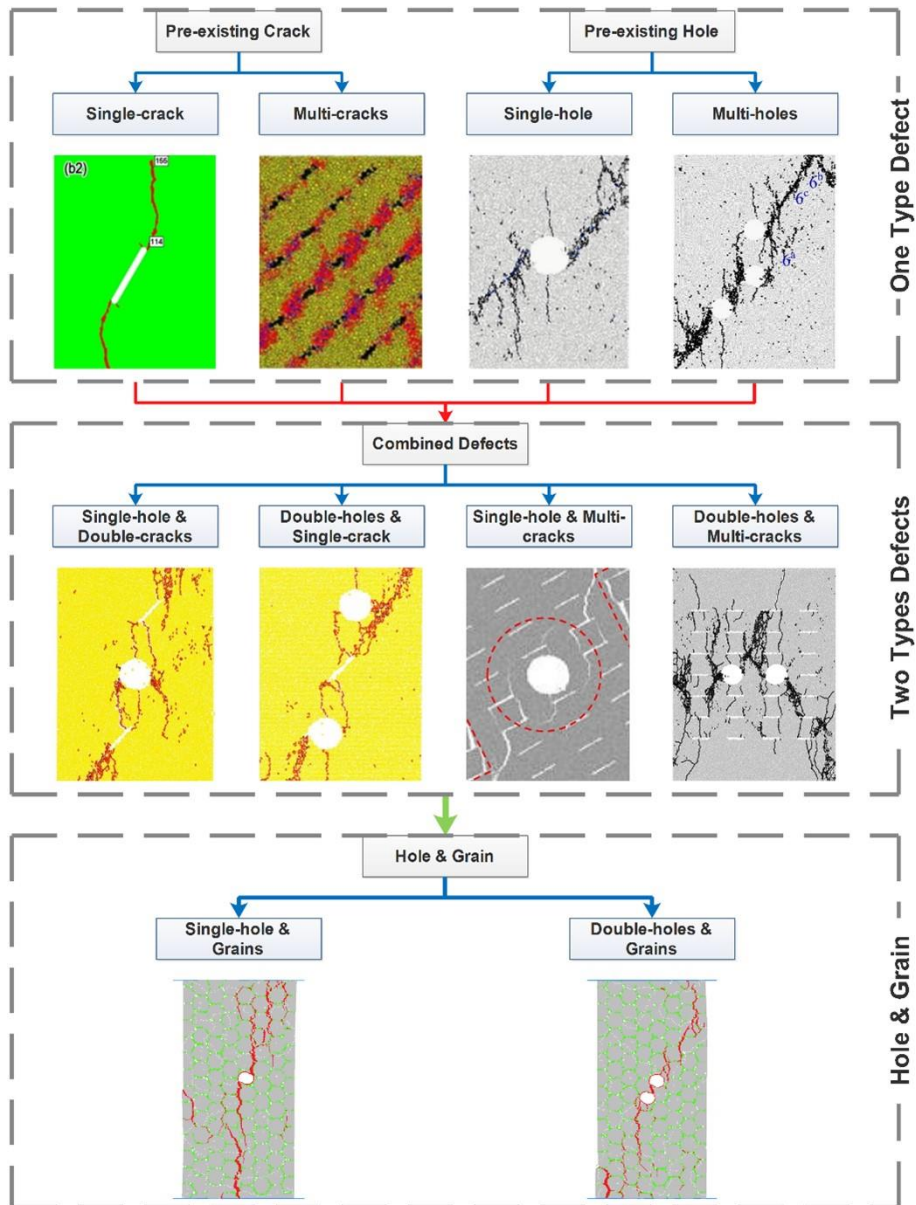


Figure 6-1: Classification of pre-existing defects types (modified after Li et al., 2012; Fan et al., 2015; Lin et al., 2015; Zeng et al., 2018; Yang et al., 2019; Lin et al., 2020; Wu et al., 2020).

6.2 Specimen Preparation

6.2.1 Experiment Procedure

The procedure of this research was illustrated in Figure 6-2. It includes experimental test, numerical specimen calibration, and numerical model analysis to determine hard rock failure mechanism containing circular defects.

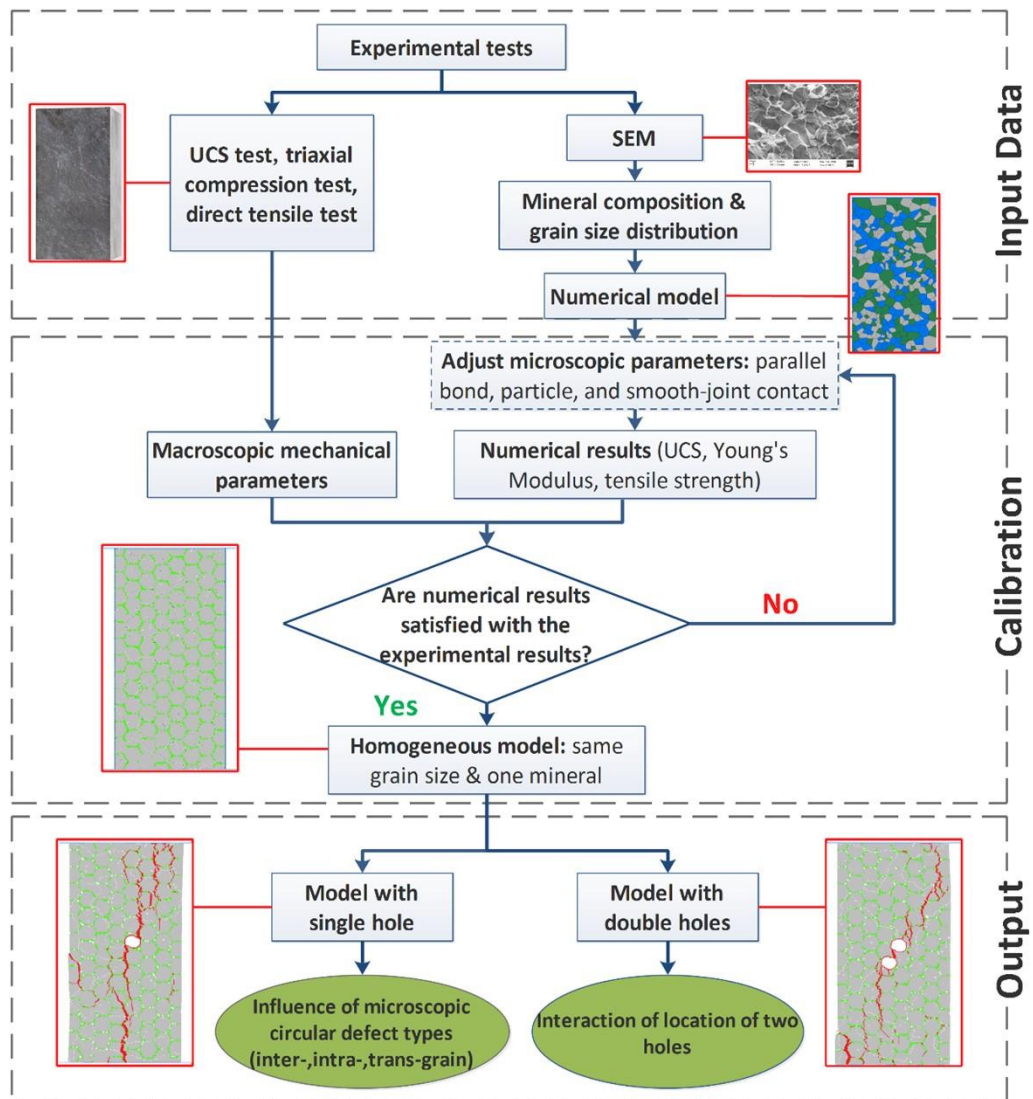


Figure 6-2: Research procedure to investigate hard rock failure mechanisms with single-hole and double-holes by GBM.

The experimental mafic specimens were collected from an underground nickel mine site in Western Australia. This study is part of a sudden failure mechanism research and ground control management, based on a series of investigation and experiments, including scanning electron microscope (SEM) method, uniaxial compression (UCS) test, triaxial compression test, and direct tension test (Tao et al., 2020). The dimension of cubic experimental specimens is 50mm (width)×50mm (height)×100mm (length). The macro-mechanical parameters collected from experimental tests include Young’s modulus (65 ± 6 GPa), UCS (135 ± 10 MPa) and tensile strength (18 ± 3 MPa). According to the SEM image observation and measurement by digital image processing,

the mineral grain size distribution and mineral composition percentage were investigated.

Based on the mineral investigation of specimens, a heterogeneous grain-based model with the 2D dimension of 50mm (width)×100mm (height) was established, which has the same range of grain size distribution and same mineral composition proportion of the experimental specimen. By adjusting micro-mechanical parameters, the macro-mechanical parameters of the numerical specimen could be achieved until the numerical results satisfying the experimental results. Therefore, the numerical model calibrated with real test results was reliable to be used for further research. In addition, to alleviate the influence of grain size and grain shape, the calibrated micro-parameters were applied to the new homogeneous model. The new homogeneous model has only one mineral of pyroxene and the same grain size. After a series of UCS tests on the homogeneous models, three suitable models were selected as the basic models according to their fractures development.

In order to determine the relationship between hole and grain boundary, a hole with different relative location was excavated from the basic models. Moreover, to determine the interaction of holes, two holes with different bridge length and bridge angle were excavated from the basic models.

6.2.2 Calibration and Microscopic Mechanical Parameters

The experimental mechanical parameters could not be directly inputted into the GBM, so the numerical macro-mechanical parameters could be determined by adjusting micro-parameters. According to previous studies (Bahrani et al., 2014; Saadat & Taheri, 2020), the calibration procedure could be regarded as guidance for micro-parameters selection by comparing the numerical macro-parameters with experimental macro-parameters. According to the GBM structure, the grain is formed by parallel bond and particles and the grains are connected by smooth-joint contact which is regarded as the grain boundary. Therefore, the micro-mechanical parameters include (1) modulus of particles and parallel bond; (2) ratio of normal to shear stiffness of particles, parallel bond and smooth-joint contact; (3) friction coefficient of

particles, parallel bond and smooth-joint contact; (4) tensile strength of parallel bond and smooth-joint contact; (5) cohesion of parallel bond and smooth-joint contact (6) friction angle of parallel bond and smooth-joint contact.

The calibration procedure is based on the “trial and error” method. To be specific, there are a series of calibrating tests, in terms of uniaxial compression tests and directly tensile test. After these numerical tests, the stress-strain plots could determine the numerical macro-parameters. The micro-parameters could be determined till the stress-strain plots and macro-parameters of numerical results are consistent with the experimental results. The obtained micro-mechanical parameters calibrated by macroscopic mechanic properties of mafic specimens are shown in Table 6-1 and Table 6-2.

Table 6-1: Microscopic mechanical parameters for parallel bond and particles.

Micro-parameters of grain (Parallel Bond & Particles)			
Element	Pyroxene	Plagioclase	Biotite
Particle radius (mm)	0.15	0.15	0.15
Particle density (kg/m ³)	2500	2600	3000
Friction coefficient of particles	1.2	1.2	1.2
Ratio of normal to shear stiffness of particles	1.5	1.5	1.5
Ratio of normal to shear stiffness of bond	1.5	1.5	1.5
Modulus of parallel bond (GPa)	65	68	62
Tensile strength of parallel bond (MPa)	310	360	320
Cohesion of parallel bond (MPa)	260	280	300
Friction angle of parallel bond (°)	32	35	35

Table 6-2: Microscopic mechanical parameters for smooth-joint contact of mafic specimen

Micro-parameters of grain boundary (Smooth-joint Contact)	
Smooth-joint contact normal stiffness (N/m)	4*10 ⁹
Smooth-joint contact shear stiffness (N/m)	2*10 ⁹
Mean smooth-joint contact tensile strength (MPa)	10
Mean smooth-joint contact cohesion (MPa)	60
Smooth-joint contact friction coefficient	1.0
Mean smooth-joint bond friction angle (°)	30

After adjustment of micro-mechanical parameters, the collected numerical macro-mechanical parameters include Young’s modulus (65.7 GPa), UCS

(135.5 MPa), and tensile strength (18.7 MPa), which are consistent with the experimental results as aforementioned. All errors are less than 5%, so the micro-parameters of mafic specimen are shown in Table 6-1 and Table 6-2 could be regarded as the reliable input parameters.

6.2.3 Model Setup

According to mineralogy and petrographical researches, the different minerals have different strengths and the geometry of grain (i.e. size and shape) will lead to different rock behaviours (Eberhardt et al., 1999; Yilmaz et al., 2009; Atapour & Mortazavi, 2018). In order to determine the influence between micro-circular defects with different location, a homogeneous specimen would be built, which will alleviate the effect of mineral constituent and grain size distribution. According to the previous mineral content investigation, pyroxene accounts for the majority of the mineral constituent, including pyroxene (50%), plagioclase (30%), and biotite (20%). Therefore, in this study, the relatively ideal numerical specimen only has the mineral of pyroxene with the grain size of 4 mm and the particle size of 0.3mm. The micro-parameters are same as the calibrated model. According to Potyondy and Cundall (2004) and Hofmann et al. (2015), there is no scale effect on the rock behaviours when the grain size is large enough comparing with the particles size. In order to improve computing efficiency, the dimension of 2D numerical models is determined as 25mm (width)×50mm (height).

Although the homogeneous model has the same grain size and only has the mineral of pyroxene, changing the seeds number in PFC-GBM could cause the change on grain location and particle location. Therefore, in this research, three intact models with different grain shape and grain distribution were selected as basic models (Figure 6-3). To be specific, although the grain shape looks like hexagon, the grain shape of model #3 looks like the grain shape of model #1 after 90° rotation and the grains of model #2 were distributed as grains of model #1 after half grain movement in vertical direction. According to Hofmann et al. (2015), the different seeds number has a slight influence on the macro-mechanical properties, but it has a significant impact on fracture development. Since this research aims to determine the relationship between

grain boundary and circular defect, it is crucial to select suitable models as the basic specimens according to their fracture development. The models will be tested several times with different mineral distribution and particle distribution by varying seeds number. Firstly, the suitable model should have the average UCS and Young's modulus. Additionally, considering the hole excavated from the centre of the specimen, the suitable models should have a relatively intact centre. It means that there is no fracture through the centre part. There are three suitable models after the UCS test as shown in Figure 6-3. The selected three models have fewer fractures and the fracture or cracks are located at the bottom or top of specimens, which are suitable to be the basic specimen to do further study, such as the influence of micro-circular defect types, and interaction of two holes.

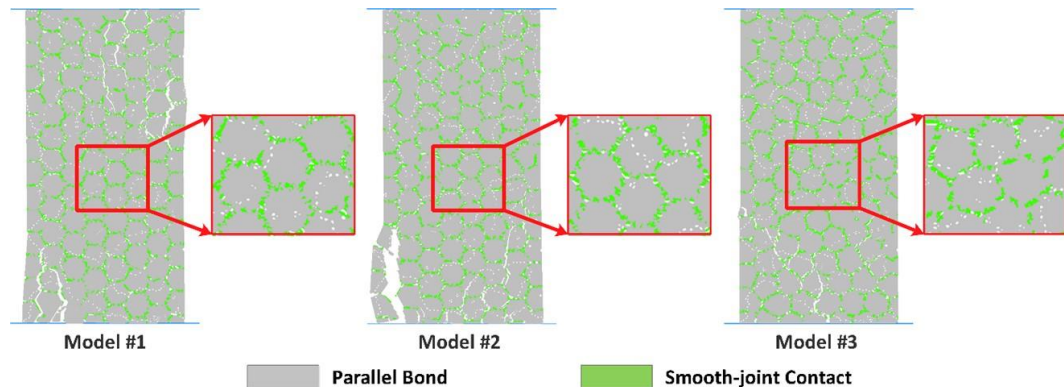


Figure 6-3: Three selected numerical specimens after UCS tests with enlarged view.

6.3 Model Response with Single Hole

According to the relationship between microscopic voids and grain boundary (Chen et al., 2020), the voids types include intra-granular and inter-granular. According to the classification of the micro-cracks types (Simmons & Richter, 1976; Kranz, 1983; He et al., 2010), there are three types of micro-cracks including inter-granular crack along the grain boundary, intra-granular crack within the mineral grain, and trans-granular crack across several grains. Based on the classification approach, the micro-circular defects could be classified into three types according to the hole location, including intra-grain hole, inter-grain hole, and trans-grain hole as shown in Figure 6-4. To be specific, the intra-grain hole is the micro-circular defect within the grain. The inter-grain hole is located at the boundary between two grains. The trans-grain hole is the

micro-circular defect located at the intersection of three or more grains. In this study, there are four types of models. The trans-grain model considers two types which have a hole located at the intersection of three grains and four grains.

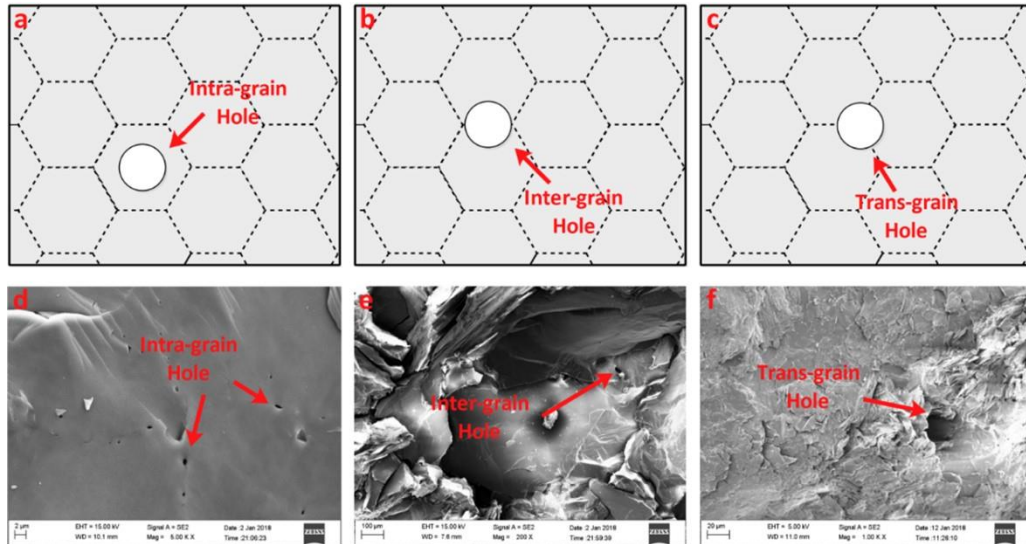


Figure 6-4: Schematic views and SEM images of micro-circular defect types: (a) & (d) intra-grain hole (b) & (e) inter-grain hole (c) & (f) trans-grain hole.

6.3.1 Effect of Circular Defect Location

Considering the grain size of 4mm, the hole sizes are determined as 3mm for intra-grain and trans-grain, and 2mm for inter-grain, respectively. The failures of models with different circular defect types excavated from basic specimens under UCS tests are shown in Figure 6-5.

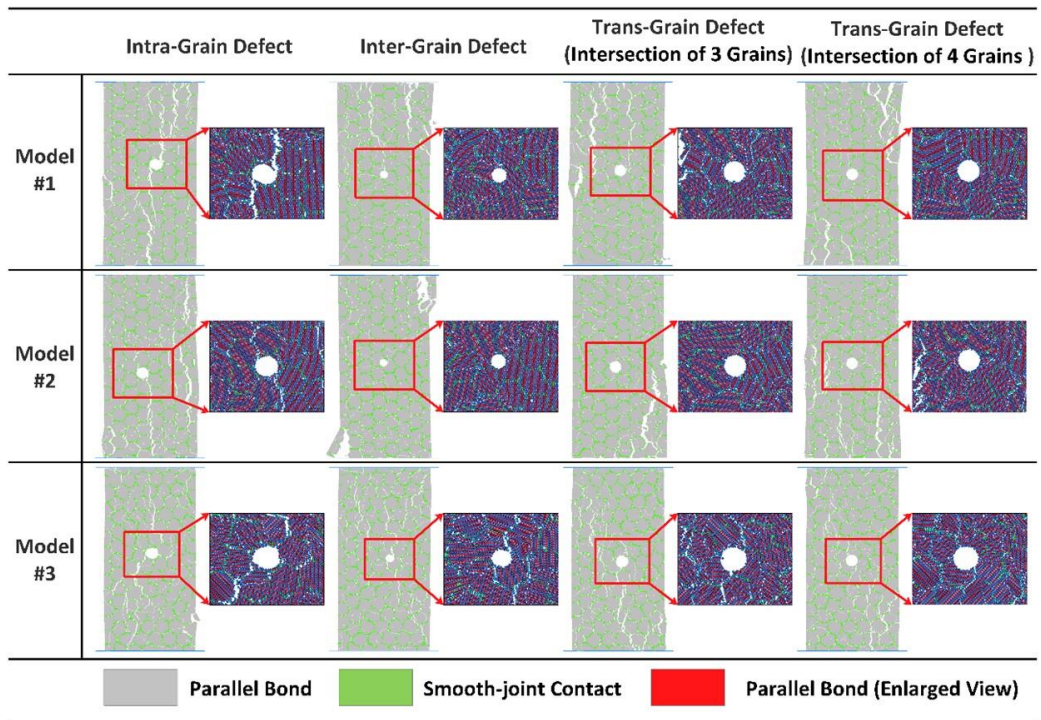


Figure 6-5: Failures of models with different circular defect types under UCS tests.

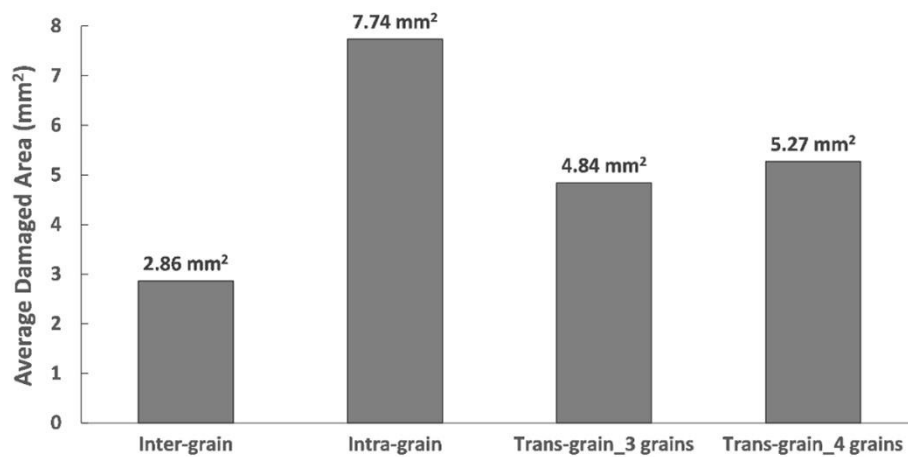


Figure 6-6: Average damaged area of each circular defect type.

According to Figure 6-5, there are the more obvious damaged areas around the intra-grain hole and the fracture of the specimen will go through the hole. To be specific, the opening or dilation around the intra-grain hole has a larger width. Based on the statistical average damage area of each circular defect type shown in Figure 6-6, the model with an intra-grain hole has the most damaged area and the model with an inter-grain hole has the least damaged area. In addition, the model with a trans-grain hole across 4 grains has more damaged area than the model with a trans-grain hole across 3 grains.

In most rock materials, the strength of the grain boundary is weaker than that of the mineral grain (Sharifzadet et al., 2017). Therefore, under UCS tests, it is easier to occur opening along grain boundaries. For the models with inter-grain hole and trans-grain hole, the hole is located at the boundaries or the intersection of several boundaries. When the inter-granular cracks occur along these boundaries, the inter-grain hole and trans-grain hole could be regarded as a pre-existing inter-granular crack. Therefore, these types of circular defects have a slight influence on the rock behaviours, which is similar to the pre-existing cracks and grain boundaries. For the model with the intra-grain hole, the hole is located within the grain. It means that the grain would be weaker than other grains. To be specific, the grains consist of particles and their contacts. If there is a hole within the grain, the number of particles and parallel bond in this grain would be less than in other grains. Therefore, the grain with an intra-grain hole would be easier to be damaged due to the weak strength. When the inter-granular crack extends and transfers into this grain, there would be a large opening and sliding around the intra-grain hole.

According to Zhou et al. (2018)0, there are two patterns of circular microstructures. The first pattern is a complete hole due to pure tensile stress applied, which has a few grain debris. The second pattern is a distorted hole due to the concentration of shear stress among the grains, which has a large amount of grain debris in or around the hole. In this research, the numerical results are consistent with the findings of the experiment. Specifically, the numerical inter-grain models and trans-grain models have more complete hole, the tensile cracks appear along the grain boundaries around the hole. The intra-grain models have distorted holes and large displacement at horizontal direction, which is caused by the shear cracks or mixed tensile-shear cracks around the hole.

6.3.1 Effect of Inclination Angle of Grain Boundary

As aforementioned, the grains of model #3 looks perpendicular to the grains of model #1 and model #2, which caused different fracture propagation pattern. In order to investigate the influence of grain boundaries on failure around the micro-circular defect, the types of arrangement of hole and its adjacent grain

boundaries would be carried out. According to experimental studies (Yang et al., 2019; Lin et al., 2020), the failure modes of the specimen with holes were significantly influenced by the inclined angle of joints and their arrangement. Although the grain boundary is stronger than the pre-existing micro-cracks, it is much easier to be broken than the intact grain. The grain boundary is more complicated than the well-aligned joints. In this research, in order to investigate the grain boundary effect, the grain boundaries were simply depicted as several joints around the hole. According to the inclined angle of grain boundary to the horizontal direction, there are four types of inclined angle (Figure 6-7), including 0° (horizontal), 30° (small angle), 60° (large angle), and 90° (vertical).

Additionally, Yang et al. (2019) classified the relative location of non-persistently joints, in terms of overlapping joint, non-overlapping joint, and coplanar joint. To investigate the effect of the grain boundary, three types of arrangement of hole and grain boundaries were defined following the joint location classification method. Specifically, when the hole is located within two overlapping grain boundaries and has no connection with any grain boundary, it is named overlapping pattern. When the hole connects the tips of two non-overlapping grain boundaries, it is named non-overlapping pattern. When the hole connects the tip of a coplanar grain boundary, it is named coplanar pattern. The schematic views of these three patterns were shown in Figure 6-7 as well.

According to Figure 6-7, the numerical results is consistent with the experimental results about the interaction between the hole and adjacent boundaries. When the inclined angle is 0° , the fracture mode is shear failure around two sides of the hole and the hole has large deformation in overlapping pattern. In coplanar pattern and non-overlapping pattern, there are tensile crack occur at the connection of hole and grain boundaries, and the remote crack is tensile crack as well. When the inclined angle is 30° , there was a shear failure along the boundaries direction at two sides of holes, and the overlapping boundaries have tensile cracks toward the hole in overlapping pattern. In coplanar pattern, the connection and remote grain boundary occur tensile

crack toward the hole. In contrast, shear cracks occur at the connection and remote grain boundary in non-overlapping pattern. When the inclined angle is 60° , the overlapping pattern has similar failure modes with the model at the inclined angle of 30° . In coplanar pattern and non-overlapping pattern, the tensile cracks occur at the connection of hole and grain boundaries, and they break the grain boundaries as well. When the inclined angle is 90° , the shear cracks coalesce the hole and grain boundary tips in overlapping pattern. In coplanar pattern, the shear failure occurs at the connection of hole and grain boundary, and the remote grain boundaries have tensile cracks toward to hole. In non-overlapping pattern, there are shear failures at the adjacent grain boundaries and tensile failure at remote grain boundaries. In summary, the overlapping pattern will cause large shear cracks and a few small tensile cracks. The coplanar pattern has one tip to connect the hole and there are only tensile cracks except for 90° . The non-overlapping pattern has mixed shear-tensile failure around the hole.

In general, when the relative location between hole and grain boundaries is overlapping pattern, there are obvious shear cracks around two sides of the hole. When the location pattern is coplanar, the grain boundaries have limited impact and there are few remote tensile cracks. For non-overlapping pattern, there are shear failures at the sides of the hole, when the connection between grain boundaries and hole is located at the sides of the hole. When the connection between grain boundaries and hole is located at the roof and foot of the hole, there are tensile cracks or unobvious cracks. These phenomena are consistent with the experimental results by Acoustic Emission events (Liu et al., 2015). There were dominant shear cracks at the sides of the hole, and remote cracks were caused by tensile damage. The cracks at the roof and foot were not observed.

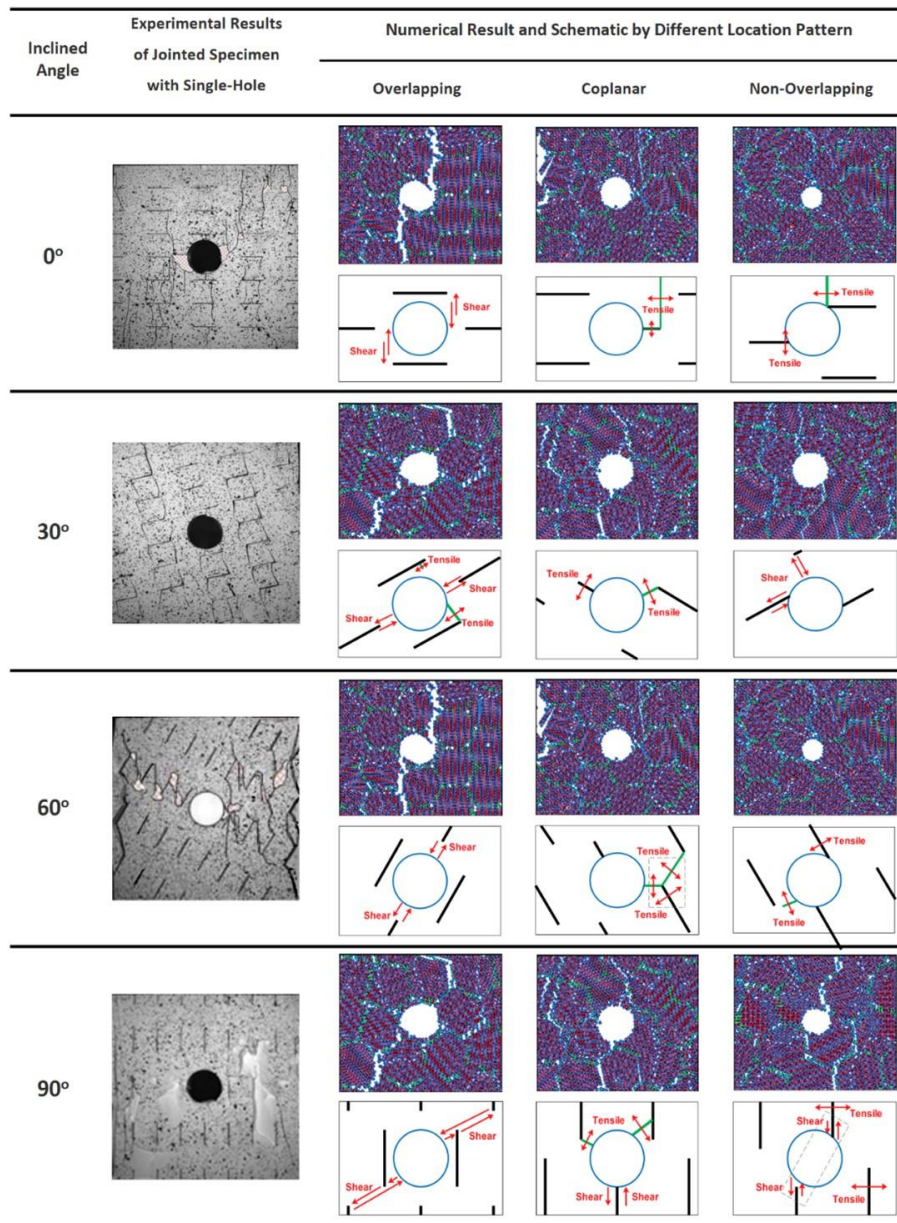


Figure 6-7: Crack propagation and failure types with different pre-existing hole location and grain boundary inclined angle (modified after Yang et al., 2019).

6.4 Model Response with Double Holes

Under micro-scale, the natural rocks have numerous pores, which are aligned disordered. Under field-scale, the tunnel may meet neighbouring tunnel with different alignment ways. For example, the headrace tunnels are parallel with each other and the mine site stopes or declines are located under other openings. Therefore, the influence of the interaction of two tunnels location is significant for civil activities and mining operations. In order to illustrate the influence of the interaction of two holes with different locations, a series of

models were established and tested with different distances between two holes and different inclined angles. Figure 8 shows the schematic views of models with double holes. The angle α is the bridge angle, which is defined as the angle between horizontal direction and the centreline of two holes in an anticlockwise direction. D is the bridge length, which is defined as the distance between the wall to wall of two holes.

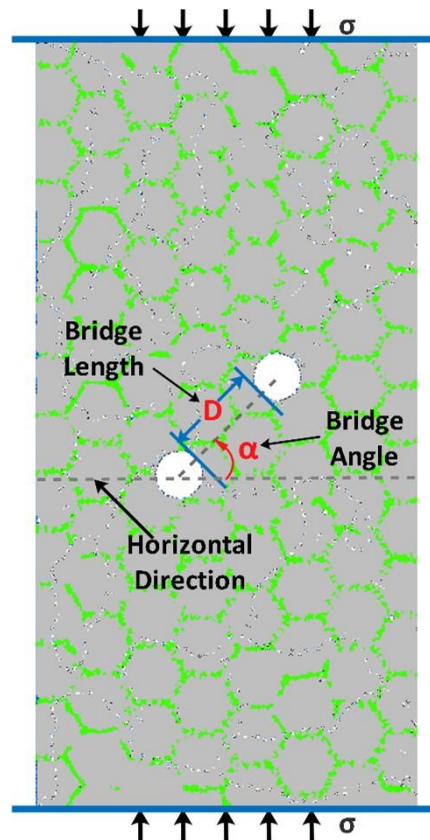


Figure 6-8: The schematic view of the model with double holes.

Figure 6-9 ~ Figure 6-11 show the failure behaviours and enlarged views of damage around holes with different bridge length different bridge angle. The bridge angle α varied at 0° , 30° , 45° , 60° , 90° , 120° , 135° , and 150° . The bridge length was set to $0.5R$, R , $2R$, and $4R$, where R is the radius of the hole which equals 1.5mm . The detail of failure behaviours influenced by the distance and angle is illustrated in the following sections.

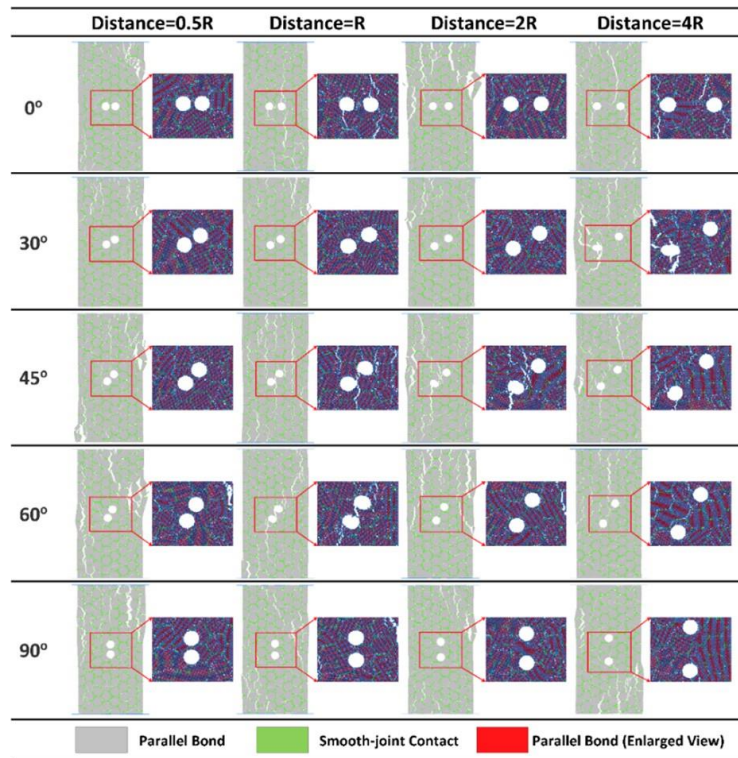


Figure 6-9: Failures of Model #1 specimen with double holes and different bridge length and angle.

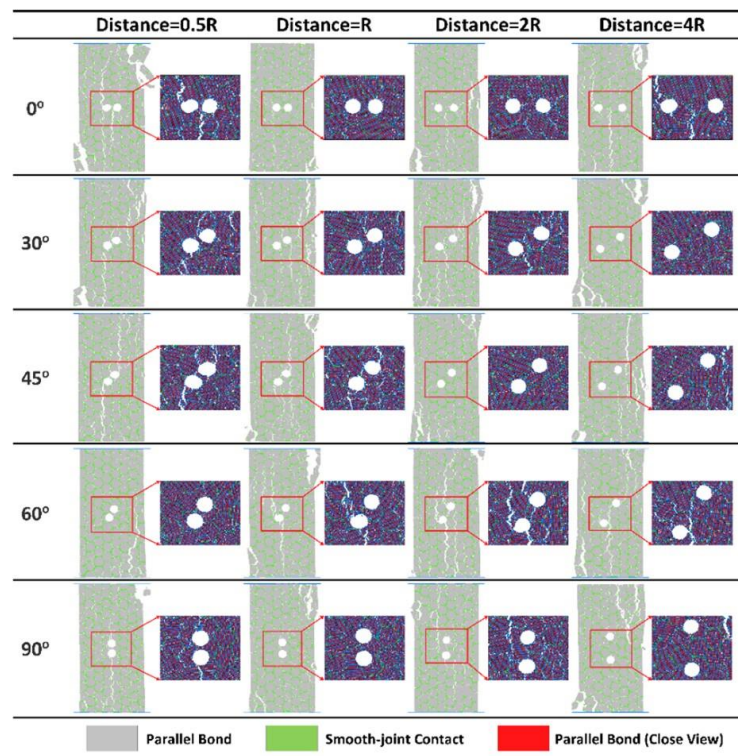


Figure 6-10: Failures of Model #2 specimen with double holes and different bridge length and angle.

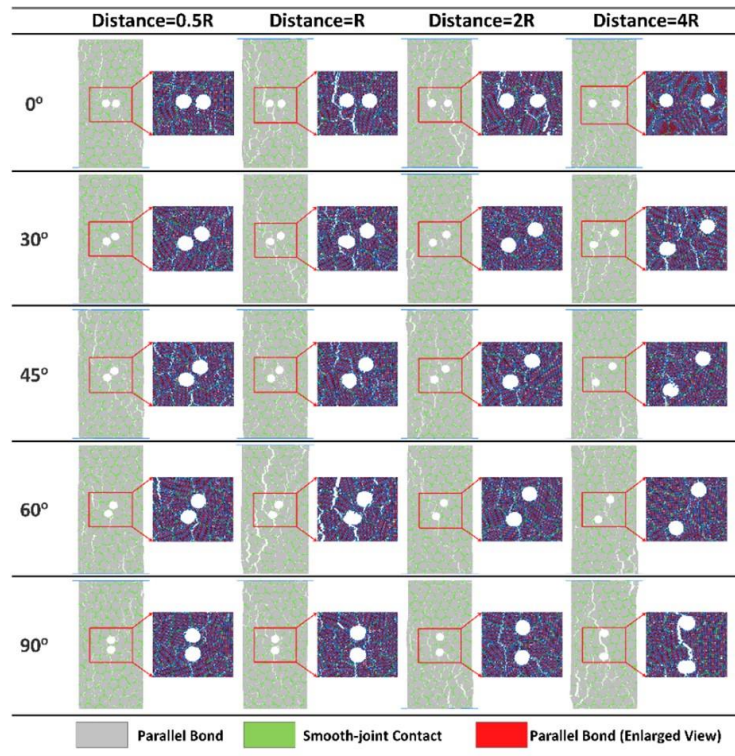


Figure 6-11: Failures of Model #3 specimen with double holes and different bridge length and angle.

6.4.1 Effect of Bridge Length between Two Holes

According to the statistical measurement of the damaged area of all models with bridge length D ranging from $0.5R$ to $4R$ and bridge angle α varying from 0° to 150° , the average damaged area for different bridge length ignored bridge angle was 3.39mm^2 , 3.87mm^2 , 3.37mm^2 , and 4.21mm^2 for the distance of $0.5R$, R , $2R$, and $4R$, respectively. Figure 6-12 shows the average damaged area of models with different bridge length. It also shows the enlarged views and whole fractures of models with different distance at bridge angle α of 120° of Model #3, which has a similar damaged area with the average value in terms of 3.34mm^2 , 4.14mm^2 , 3.30mm^2 , and 5.26mm^2 . According to the statistic of the damaged area of all models, the bridge length has significant on the damaged area. To be specific, the models with the bridge length of $4R$ have the most damaged area, and the models with the bridge length of $2R$ have the least damaged area. The model with the distance of R have more damaged area than the model with the distance of $0.5R$. According to the failure modes and failure location, the damaged area induced by the interaction of two holes at the bridging region increased with the increase of distance from $0.5R$ to R .

When the bridge length kept increasing, the interaction between two holes would weaken and the damaged area at the bridging region would decrease. However, when the bridging length kept increasing, two holes would be regarded as the isolated hole and the interaction between the hole and adjacent grain boundaries have more influence on the specimen fractures.

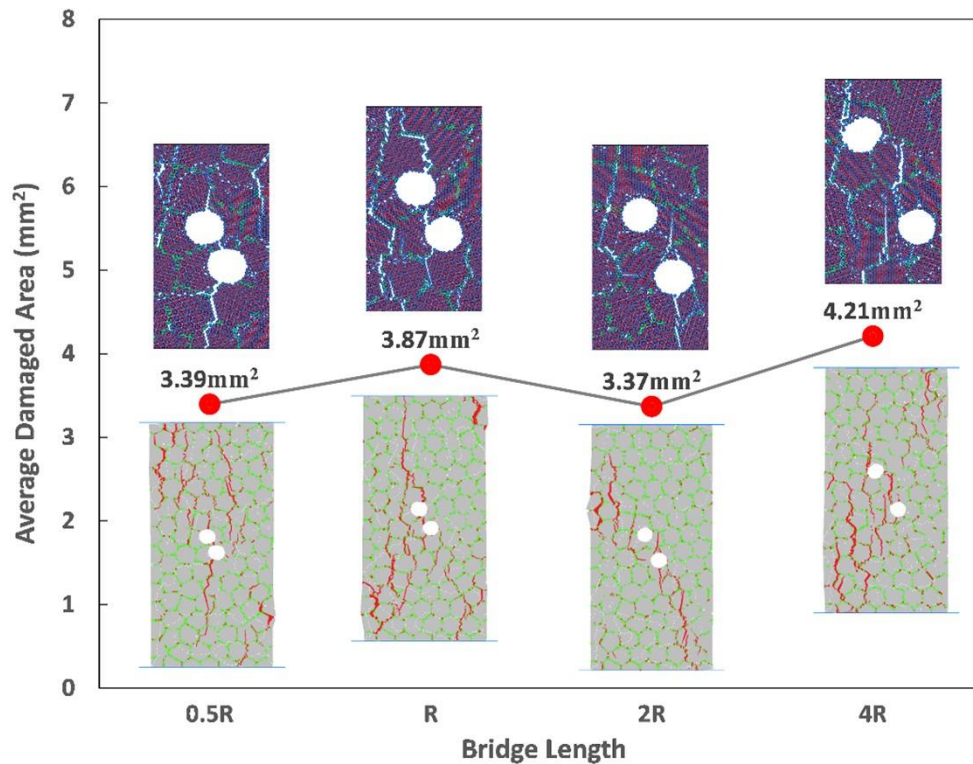


Figure 6-12: Average damage area of models with different bridge length between two holes.

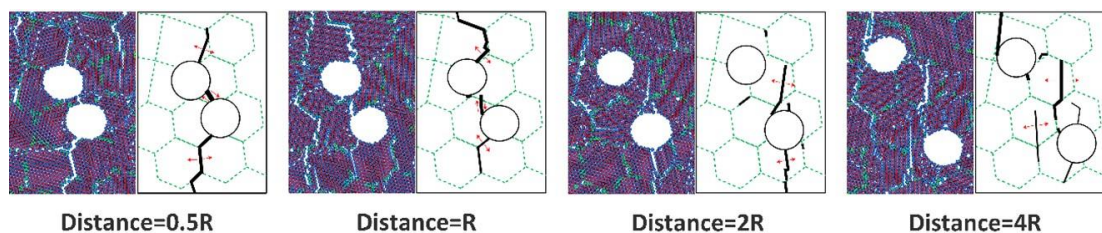


Figure 6-13: Failure mechanisms of interaction of two holes with varying distances for Model #3.

Moreover, according to the enlarged views, there is a significant influence of the bridge length on the failure modes between two holes region. The enlarged views and the failure schematic were shown in Figure 6-13, where utilize Model #3 with 120° of bridge angle as the example. According to the enlarged view of the model with distance of 0.5R, there is a mixed shear-tensile failure between two holes, which transfers from one hole to another hole and has no

direct relationship with the grain boundaries. When the distance between two holes increases to R , there is no failure through two holes. There are a large amount of tensile or shear cracks between two holes based on the inclined angle of grain boundaries between two holes. When the distance increases to $2R$, the direction of failure extension between two holes is not towards two holes and the failure mode is tensile failure. When the distance increases to $4R$, two holes could be regarded as two isolated holes. The failure mainly depends on the direction of stress and the relationship between grain boundaries and holes. Hence, with the increment of the distance between two holes, the influence of mutual interaction of two holes would decrease and the influence of grain boundaries would increase.

6.4.2 Effect of Bridge Angle between Two Holes

The inclination angle of crack have a significant effect on stress concentration and crack development. Lajtai (1971) calculated the stresses around an inclined crack and showed that there was the highest stress concentration when the crack orientation at 30° to the maximum principal stress. Noda et al. (2000) indicated that the stress intensity factors decreased with the decrease of the inclination angle of the crack from 45° to 30° . Tang et al. (2005) indicated that the nearby holes arranged with an inclined angle led to cracks grow easily, compared with the vertical and horizontal model. Li et al. (2019) indicated that there were the largest amount of intra-grain cracks and grain boundary cracks at the angle between 60° and 120° to the horizontal axis by statistical analysis based on GBM under uniaxial compression tests. According to the analysis of the effect of distance between two holes, the failure modes and damage area at the region between two holes were significant influenced by the distance between two holes. However, the failure outside the region between two holes had no discernible relationship with the distance between two holes. Therefore, to determine the failure mechanism, where the failure is outside the region between two holes, two holes would be regarded as an entire defect. According to the influence of the inclination angle of crack, it is important to determine the influence of the inclination angle of this entire defect on the damaged area and maximum displacement.

In this research, α is defined as the angle between horizontal direction and the centreline of two holes in an anticlockwise direction. Figure 6-14 illustrates the damaged area and maximum displacement of numerical models with double holes at different angle α to the horizontal direction. According to the results, there was a maximum damaged area, which is 4.7 mm^2 at the angle α of 60° , namely 30° to the maximum principal stress. Additionally, there was a minimum damaged area, which is 2.9 mm^2 at the angle of 150° . As meanwhile, when two holes have the angle α of 90° and 45° to the horizontal direction, the maximum displacement is the smallest and largest, respectively. In hence, when two holes are aligned with a small angle to the direction of the maximum principal stress, it has more damage area around the pair of holes and the failure modes mainly consist of tensile failure. Moreover, when two holes are aligned with 45° to the maximum principal stress, the failure modes consist of mixed shear-tensile failure. Therefore, it has more displacement than other aligned angles.

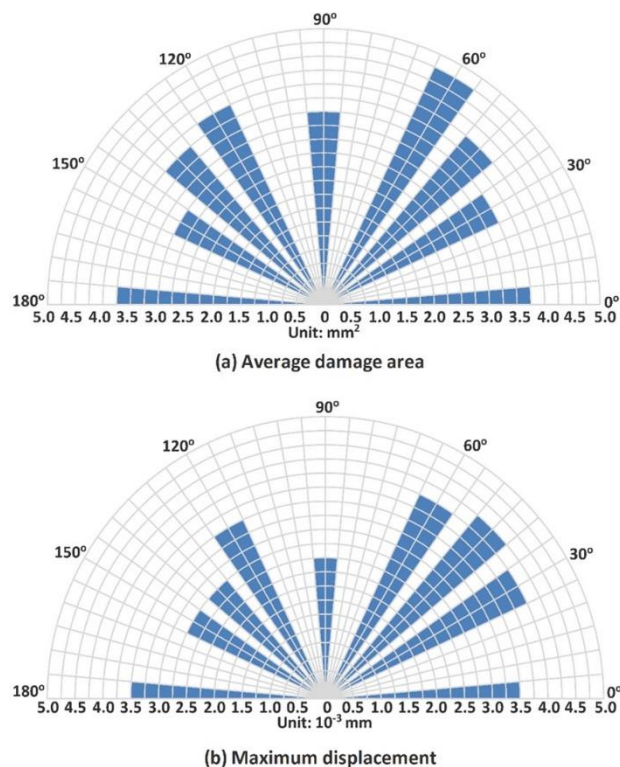


Figure 6-14: (a) Average damage area and (b) maximum axial displacement of numerical specimens with different bridge angles (α) between two holes.

There are lots of experiments about specimen with double or more holes under UCS tests to investigate the interaction of holes and the coalescence types.

Huang et al. (2017) and Liu et al. (2019) excavated two circular holes and elliptical holes respectively and varied the bridge angle to determine the fracture mechanism and crack evolution. The numerical results compared with experimental results with different bridge angle were listed in Figure 6-15.

According to Figure 6-15, the failure modes of numerical results are consistent with the experimental results. To be specific, when the bridge angle is 0° , there is no coalescence between two holes, but there are several tensile cracks around holes, which are along the grain boundaries in the vertical direction. When the bridge angle is 30° , there is a slight shear failure at the bridge to coalesce two holes. The sliding direction is equal to the bridge angle. When the bridge angle is 45° , there is intensive shear failure to coalesce two holes and large deformation around holes, which slide along the bridge angle. Out of the bridging region, there are several intensive tensile failures. When the bridge angle is 60° , the failure modes are similar to the model with the bridge angle of 45° . However, the sliding direction is different, which is an almost vertical shear failure to coalesce two sides of two holes. There is large deformation around holes and tensile failures occur far away from the holes. When the bridge angle is 90° , there is no coalescence at the bridging region, but there are some slight vertical tensile cracks. There are several vertical tensile failures at two sides of holes. These tensile cracks are coalesced to connect two sides of holes in the vertical direction.

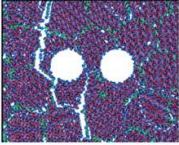
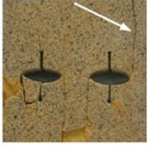

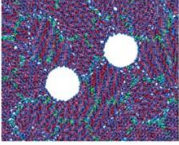
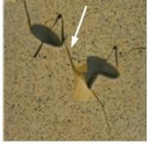
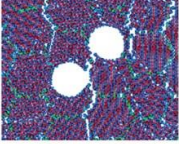

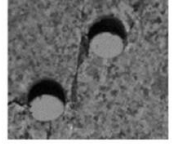
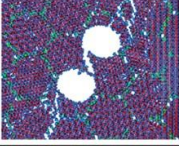

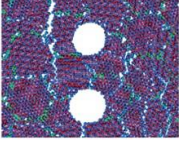
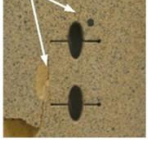
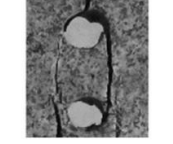
Bridge Angle α	Numerical Model	Experimental Specimen		Description
		Elliptical Holes	Circular Holes	
0°				It has no coalescence. There are tensile cracks around holes in the vertical direction.
30°				It has a thin shear crack to coalesce two holes.
45°				It has a shear crack to coalesce two holes and tensile cracks out of the bridge region. The holes have large deformation.
60°				It has a shear crack to coalesce two holes. The holes have large deformation.
90°				The holes were connected by several tensile cracks at the two sides of holes.

Figure 6-15: Crack propagation and failure types of numerical models and experimental specimens with different bridge angle (modified after Huang et al., 2017; Liu et al., 2019).

6.5 Conclusion

A grain-based model was established and calibrated using two-dimension of Particle Flow Code (PFC2D), according to the mineral investigation by quantitative statistical analysis of SEM images and macro-mechanical parameters collection by a series of experiments. A homogeneous grain-based model with one mineral of pyroxene and the same grain size was established according to the calibrated micro-mechanical parameters. Three suitable models with different grain shapes were selected from quantitative homogeneous models as the basic models. Furthermore, the models containing single-hole and double-holes were established to determine the influence of circular defects on rock behaviours. The detail influence of relative location of hole, grain shape, bridge length and bridge angle of two holes were obtained, which were summarized as follows:

(1) According to the relative location of the hole to grain, the circular defects could be classified into three types, including intra-grain hole, inter-grain hole, and trans-grain hole (across three grains and four grains). The inter-grain hole and trans-grain hole are located on the boundary or interaction of grains. The non-persistent grain boundaries could be regarded as cracks. The intra-grain hole is located within grain, which would reduce the number of contact and particles of grain causing the outstanding decrease of grain strength. Therefore, the intra-grain hole have more damaged area around the hole than other types of circular defects.

(2) According to the grain shape, the influence of different inclination angle between grain boundary and horizontal direction were investigated. Three patterns of relative location between hole and grain boundaries were defined, including overlapping, coplanar, and non-overlapping. When the relative location between hole and grain boundaries is overlapping pattern, there are obvious shear cracks around two sides of the hole. When the location pattern is coplanar, the grain boundaries have limited impact and there are few remote tensile cracks. For non-overlapping pattern, there are shear failures at the sides of the hole, when the connection between grain boundaries and hole is located at the sides of the hole. When the connection between grain boundaries and the hole is located at the roof and foot of the hole, there are tensile cracks or unobvious cracks.

(3) Four model types with different bridge length were established to determine the distance effect, including $0.5R$, R , $2R$, and $4R$. The bridge length has no discernible effect on the whole specimen, but it has a significant influence on the interaction of two holes. With the distance increase from $0.5R$ to $2R$, the damaged area due to the interaction of two holes increased firstly and decreased later. When the bridge length increased to $4R$, the damage around the hole were induced by the interaction between holes and non-persistent grain boundaries, and the interaction between two holes was limited.

(4) The bridge angle between two holes has a significant influence on fracture development and crack coalescence. When two holes were arranged with an inclined angle, there are the most damaged area and the maximum

displacement due to dominant shear cracks. When two holes were arranged horizontally, there is no coalescence and tensile cracks are dominant. When two holes were distributed vertically, there is the least damaged area and displacement.

Acknowledgements

We sincerely acknowledge Northeastern University, China provided the laboratory tests. This study is partly supported by National Natural Science Foundation of China the 111 Project under grant no: 51839003 and B17009. We also thank Dr. Mahdi Saadat at School of Civil, Environmental and Mining Engineering, The University of Adelaide, Australia, for his invaluable support with the grain-based model in PFC software. We would also like to thank the journal editor and reviewers for their valuable suggestions. In addition, this research did not receive any specific grant from funding agencies in the public, commercial, or not-for-profit sectors.

Reference

- Tao, R., Sharifzadeh, M., Zhang, Y., & Feng, X.-T. (2020). Analysis of mafic rocks microstructure damage and failure process under compression test using quantitative scanning electron microscopy and digital images processing. *Engineering Fracture Mechanics*, Vol.231: 107019.
- Griffith, A. A. (1920). The phenomena of rupture and flow in solids. *Philosophical Transactions of the Royal Society of London, Series A: Mathematical and Physical Sciences*, 163-198.
- Simmons, G., & Richter, D. (1976). Microcracks in rocks. In R. G. Strens, *The Physics and Chemistry of Minerals and Rocks* (pp. 105-137). Toronto: John Wiley & Sons.
- Kranz, R. L. (1983). Microcracks in rocks: A review. *Tectonophysics*, Vol.100: 449-480.
- Wong, L. N., & Einsein, H. H. (2009a). Crack Coalescence in Molded Gypsum and Carrara Marble: Part 1. Macroscopic Observations and Interpretation. *Rock Mechanics and Rock Engineering*, 42: 475-511.
- Wong, L. N., & Einstein, H. H. (2009b). Systematic evaluation of cracking behavior in specimens containing single flaws under uniaxial compression. *International Journal of Rock Mechanics & Mining Sciences*, Vol.2: 239-249.
- Cao, R.-h., Cao, P., Fan, X., Xiong, X., & Lin, H. (2016). An experimental and numerical study on mechanical behavior of ubiquitous-joint brittle rock-like specimens under uniaxial compression. *Rock Mechanics and Rock Engineering*, 49: 4319-4338.
- Liu, Y., Dai, F., Lu, D., Xu, N., & Feng, P. (2018). Experimental investigation on the fatigue mechanical properties of intermittently jointed rock models under cyclic uniaxial compression with different loading parameters. *Rock Mechanics and Rock Engineering*, 51: 47-68.
- Li, H., & Wong, L. N. (2012). Influence of flaw inclination angle and loading condition on crack initiation and propagation. *International Journal of solids and structures*, 49: 2482-2499.

- Fan, X., Kulatilake, P., & Chen, X. (2015). Mechanical behavior of rock-like jointed blocks with multi-non-persistent joints under uniaxial loading: A particle mechanics approach. *Engineering Geology*, 190: 17-32.
- Lajtai, E. Z., & Lajtai, V. N. (1975). The collapse of cavities. *International Journal of Rock Mechanics and Mining Sciences & Geomechanics Abstracts*, Vol.12: 81-86.
- Martin, C. D., Read, R. S., & Martino, J. B. (1997). Observations of brittle failure around a circular test tunnel. *International Journal of Rock Mechanics and Mining Sciences*, Vol.34: 1065-1073.
- Wong, R. H., Lin, P., & Tang, C. A. (2006). Experimental and numerical study on splitting failure of brittle solids containing single pore under uniaxial compression. *Mechanics of Materials*, 38: 142-159.
- Zeng, W., Yang, S.-Q., & Tian, W.-L. (2018). Experimental and numerical investigation of brittle sandstone specimens containing different shapes of holes under uniaxial compression. *Engineering Fracture Mechanics*, 200: 430-450.
- Wu, H., Zhao, G., & Liang, W. (2020). Mechanical properties and fracture characteristics of pre-holed rocks subjected to uniaxial loading: A comparative analysis of five hole shapes. *Theoretical and Applied Fracture Mechanics*, 105: 102433.
- Zhang, Q., Zhang, X.-P., & Yang, S.-Q. (2021). A numerical study of acoustic emission characteristics of sandstone specimen containing a hole-like flaw under uniaxial compression. *Engineering Fracture Mechanics*, 242: 107430.
- Li, D., Zhu, Q., Zhou, Z., Li, X., & Ranjith, P. G. (2017). Fracture analysis of marble specimens with a hole under uniaxial compression by digital image correlation. *Engineering Fracture Mechanics*, 183: 109-124.
- Lin, P., Wong, R. H., & Tang, C. A. (2015). Experimental study of coalescence mechanisms and failure under uniaxial compression of granite containing multiple holes. *International Journal of Rock Mechanics & Mining Sciences*, 77: 313-327.
- Huang, Y.-H., Yang, S.-Q., Ranjith, P. G., & Zhao, J. (2017). Strength failure behavior and crack evolution mechanism of granite containing pre-existing non-coplanar holes: Experimental study and particle flow modeling. *Computers and Geotechnics*, 88: 182-198.
- Liu, X.-R., Yang, S.-Q., Huang, Y.-H., & Cheng, J.-L. (2019). Experimental study on the strength and fracture mechanism of sandstone containing elliptical holes and fissures under uniaxial compression. *Engineering Fracture Mechanics*, 205: 205-217.
- Wang, X., Jiang, Y., & Li, B. (2017). Experimental and numerical study on crack propagation and deformation around underground opening in jointed rock masses. *Geosciences Journal*, Vol.21: 291-304.
- Yang, S.-Q., Yin, P.-F., Zhang, Y.-C., Chen, M., Zhou, X.-P., Jing, H.-W., & Zhang, Q.-Y. (2019). Failure behavior and crack evolution mechanism of a non-persistent jointed rock mass containing a circular hole. *International Journal of Rock Mechanics and Mining Sciences*, 114: 101-121.
- Lin, Q., Cao, P., Meng, J., Cao, R., & Zhao, Z. (2020). Strength and failure characteristics of jointed rock mass with double circular holes under uniaxial compression: Insights from discrete element method modelling. *Theoretical and Applied Fracture Mechanics*, 109: 102692.

- Wu, T., Gao, Y., Zhou, Y., & Li, J. (2020). Experimental and numerical study on the interaction between holes and fissures in rock-like materials under uniaxial compression. *Theoretical and Applied Fracture Mechanics*, 106: 102488.
- Potyondy, D. O. (2010). A Grain-Based Model for Rock: Approaching the True Microstructure. *Proceedings of Rock Mechanics in the Nordic Countries 2010*, (p. 10). Kongsberg, Norway.
- Bahrani, N., Kaiser, P. K., & Valley, B. (2014). Distinct element method simulation of an analogue for a highly interlocked, non-persistently jointed rockmass. *International Journal of Rock Mechanics & Mining Sciences*, 71: 117-130.
- Hofmann, H., Babadagli, T., Yoon, J. S., & Zang, A. (2015). A grain based modelling study of mineralogical factors affecting strength, elastic behaviour and micro fracture development during compression tests in granites. *Engineering Fracture Mechanics*, 147: 261-275.
- Saadat, M., & Taheri, A. (2020). A cohesive grain based model to simulate shear behaviour of rock joints with asperity damage in polycrystalline rock. *Computers and Geotechnics*, 103254.
- Eberhardt, E., Stimpson, B., & Stead, D. (1999). Effects of Grain Size on the Initiation and Propagation Thresholds of Stress-induced Brittle Fractures. *Rock Mechanics and Rock Engineering*, 32: 81-99.
- Yilmaz, N. G., Karaca, Z., Goktan, R. M., & Akal, C. (2009). Relative brittleness characterization of some selected granitic building stones: Influence of mineral grain size. *Construction and Building Materials*, 23: 370-375.
- Atapour, H., & Mortazavi, A. (2018). The influence of mean grain size on unconfined compressive strength of weakly consolidated reservoir sandstones. *Journal of Petroleum Science and Engineering*, 171: 63-70.
- Potyondy, D. O., & Cundall, P. A. (2004). A bonded-particle model for rock. *International Journal of Rock Mechanics and Mining Sciences*, 41: 1329-1364.
- Chen, X., Qu, X., Xu, S., Wang, W., Li, S., He, H., & Liu, Y. (2020). Dissolution pores in shale and their influence on reservoir quality in Damintun Depression, Bohai Bay Basin, East China: Insights from SEM images, N₂ adsorption and fluid-rock interaction experiments. *Marine and Petroleum Geology*, 117: 104394.
- He, M., Nie, W., Han, L., & Ling, L. (2010). Microcrack analysis of Sanya granite fragments from rockburst tests. *Mining Science and Technology*, 20: 238-243.
- Sharifzadeh, M., Feng, X.-t., Zhang, X., Qiao, L., & Zhang, Y. (2017). Challenges in multi-scale hard rock behaviour evaluation at deep underground excavations. *12th Iranina and 3rd Regional Tunnelling Conference*. Tunnelling and Climate Change.
- Zhou, Y., Zhao, C., Zhao, C., Yu, Z., & Du, Z. (2018). Mechanical Properties and Damage Evolution of Specimens Containing Single Cracks: An Experimental Study Based on SEM Method. *10th Asian Rock Mechanics Symposium*. Singapore: ARMS10.
- Liu, J.-p., Li, Y.-h., Xu, S.-d., Xu, S., Jin, C.-y., & Liu, Z.-s. (2015). Moment tensor analysis of acoustic emission for cracking mechanisms in rock with a pre-cut circular hole under uniaxial compression. *Engineering Fracture Mechanics*, 135: 206-218.
- Lajtai, E. Z. (1971). A theoretical and experimental evaluation of Griffith theory of brittle fracture. *Tectonophysics*, 11: 129-156.

Noda, N.-A., Yagishita, M., & Kihara, T. (2000). Effect of crack shape, inclination angle, and friction coefficient in cracks surface contact problems. *International Journal of Fracture*, 105: 367-389.

Tang, C. A., Wong, R. H., Chau, K. T., & Lin, P. (2005). Modeling of compression-induced splitting failure in heterogeneous brittle porous solids. *Engineering Fracture Mechanics*, Vol.72: 597-615.

Li, H., Yang, J., Han, Y., Yang, C., Daemen, J. J., & Li, P. (2019). Weibull grain-based model (W-GBM) for simulating heterogeneous mechanical characteristics of salt rock. *Engineering Analysis with Boundary Elements*, 108: 227-243.

Every reasonable effort has been made to acknowledge the owners of copyright material. I would be pleased to hear from any copyright owner who has been omitted or incorrectly acknowledged.

**Chapter 7 . Application of Grain-Based
Model on Rock Behaviours of Field-scale
Tunnel Based on Multiscale Analysis**

Abstract

Under high stress, natural rock shows different mechanisms on different scales. Grain-based model is effectively mimic rock fracturing behaviour on grain-scale and laboratory-scale. It still lacks application on field-scale simulation. This research employs PFC^{2D} to construct efficient grain-based model to simulate field-scale rock mass. The analysis of surrounding rocks behaviours under in-situ stress are carried out by three main excavated models, in terms of the single ore drive at different buried depth, double drives with different dipping angles, and double drives connecting with stope with different width. The results indicate that the failures are highly associated with the damage evolution process. Cracks initiation and coalescence would result in sub-vertical and inclined fractures, which causing buckling and block ejection, respectively. Additionally, the double drives have the most severe damage at the dipping angle of 65° and have the least damage at the dipping angle of 75°. Finally, the numerical results of failure modes and damage severity are compared with the in-situ failure cases, which are in good agreement with the engineering results. The grain-based model is verified to simulate the field-scale rock behaviours based on the concept of microscopic damage evolution and macroscopic fracture development.

Keywords: Grain-based model, Ore drives, Stope dipping angle, In-situ stress, damage mechanisms

7.1 Introduction

In deep underground mining activities, underground opening suffers rock engineering problems due to complicated conditions including high in-situ stress, complex geological structures, and seismic events. In order to accurately investigate the rock response to the underground excavation, numerous physical model tests were carried out. Seki et al. (2008) revealed the relationship between in-situ stress and the curve gradient of the heaving phenomenon in tunnels. He et al. (2010) provided a physical model to enhance the understanding of excavation response in geologically horizontal strata. Zhu et al. (2011) investigated the spalling mechanism based on the physical cavern model under high in-situ stress. Huang et al. (2013) discussed the influence of the weak interlayer on failure patterns around the tunnel based on tunnel-scaled model tests.

Numerical simulation has been widely used in the study of field-scale rock behaviours. Most of the numerical researches utilized continuum methods that were applied to the failure mechanism of surrounding rocks due to efficient computation. The finite element method (FEM) was applied to investigate the mechanical mechanism of failure zone of surrounding rock by displacement (Li et al., 2014) and strain (Zhu et al., 2020). The method of real fracture process analysis (RFPA) was employed to investigate the fracture mechanism of surrounding rock (Zhu et al., 2005; Liang et al., 2019). However, the natural rocks contain heterogeneity and discontinuities, which lead to complicated behaviours. It has a significant influence on responding to underground excavation for the rock mass containing complex geological structures. (Ivars et al., 2011; Turichshev & Hadjigeorgiou, 2017; Farahmand et al., 2018). The continuum methods are effectively present failure regions, but they have limitations in the study of the mechanical behaviours of the jointed rock mass. The discrete element method (DEM) has been proven suitable to capture the deformation behaviour of jointed rock mass due to the ability to consider fracture system and behaviours of discontinuities. Boon et al (2015) employed DEM to simulate the blocky rock mass for support design. Karampinos et al. (2015) constructed DEM to study the mechanism of deformation and buckling in the foliated rock mass. Wang and Cai (2020) proposed the discrete fracture network combined discrete element method (DFN-DEM) to simulate the mechanical response of jointed rock mass based on the field mapping data (i.e. length and orientation) of the fracture system including joints, bedding planes, veins and faults.

Moreover, the rock contains microstructures on the microscopic view, including heterogeneity, grain boundaries, micro-cracks, cleavages, and pores (Sharifzadeh et al., 2017). Recently, numerous researchers investigated the crack development process (Diederichs, 2007; Wong & Einstein, 2009) and macroscopic mechanical properties governed by microstructures (Nicksiar & Martin, 2014; Manouchehrian & Cai, 2016; Ghasemi et al., 2020). Grain-based model (GBM) was widely employed to study mechanical properties under micro-scale and laboratory-scale tests based on microscopic heterogeneities, including mineral size, mineral composition, and grain boundaries. However,

considering the computation time, few researchers employed GBM in the field-scale simulation. Lan et al (2013) used universal distinct element code (UDEC) to build the GBM to mimic the damage evolution of rock mass around the borehole. Farahmand and Diederichs (2021) indicated that Voronoi-shaped grain constructed by UDEC could provide closer resemblance in the shape of blocks with better interlocking. However, Li et al. (2019) indicated that the grain generated by UDEC and three-dimensional distinct element code (3DEC) could not be broken and there is no trans-granular fracturing. Therefore, this research employed the software of particle flow code (PFC) to construct the GBM, which is proposed by Potyondy (2010). Each grain is a breakable block, which is consisted of grain boundaries and bonded particles. After calibration of microscopic parameters, three main field-scale models were constructed in terms of the single ore drive at different buried depths, double drives with different dipping angles, and double drives connecting with stope with different widths. Comparing with the in-situ failure in the ore drive, the grain-based model could effectively mimic the failure of structured rock mass, which reveals the failure characteristics and damage zone.

7.2 Engineering Background and Specimen Construction

Figure 7-1 shows the procedure of this research, where a series of experiments and numerical tests were carried out based on the multi-scale methods. The first step is data collection including in-situ data (e.g. in-situ stress & geometry dimension), mechanical data (e.g. compressive strength, tensile strength, & modulus), and mineral data (e.g. mineral composition & grain size distribution). The second step is the calibration of microscopic parameters. The macroscopic mechanical parameters could not be directly applied to DEM. Comparing the experimental results and numerical results could determine the suitable micro-parameters. The last step is field-scale numerical simulation. Under in-situ stress, three types of models were constructed to determine the failure characteristics, including single drive at different depths, double drives with different dip angles, and double drives with stope with different widths.

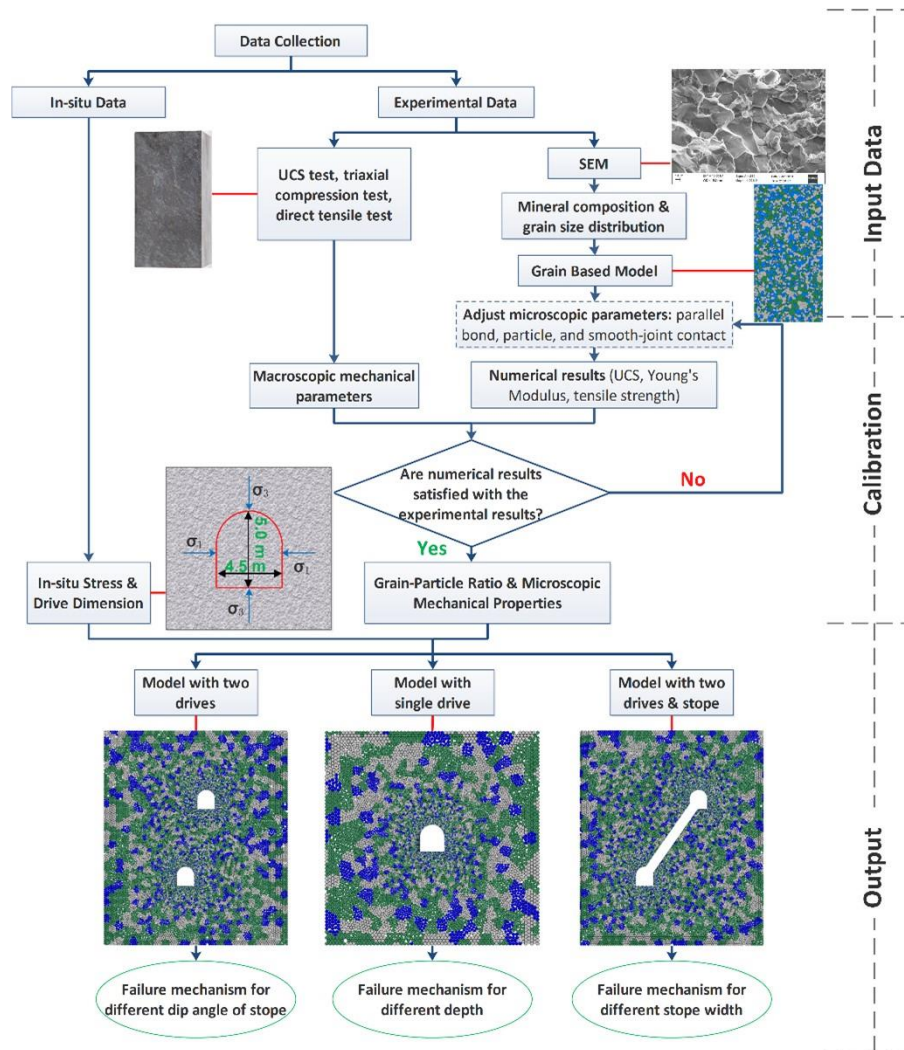


Figure 7-1: Research procedure.

7.2.1 Background of Mine Site

The case of ore drive is located at a real gold mine site in Western Australia, which has a very structured rock mass. The experiment samples were collected from the foot wall. The plots of in-situ stresses VS depth are shown in Figure 7-2, based on the acoustic emission stress measurements. The maximum principal stress is sub-horizontal and the minimum principal stress is sub-vertical. The dimension of the ore drive profile is designed as 4.5m (width)*5.0m (height). The height between two levels is 20m and the dip angle of the stope ranges from 55° to 75°.

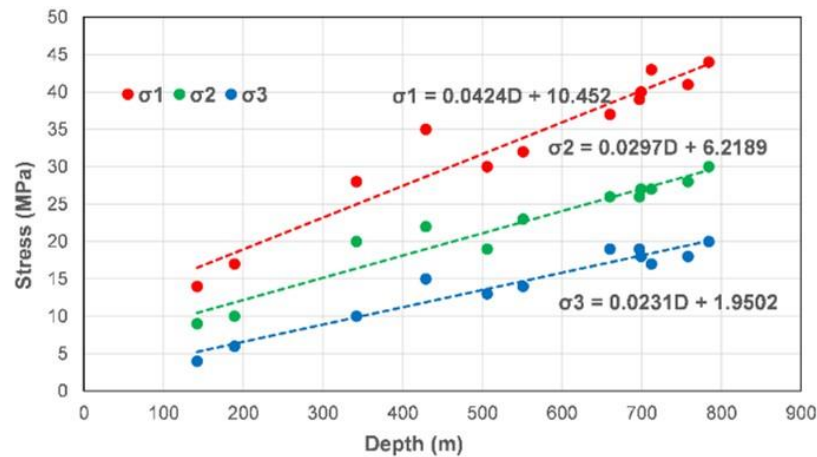


Figure 7-2: In-situ stress vs depth

7.2.2 Experimental Results

According to a series of laboratory tests, including the scanning electron microscope (SEM) method, UCS test, triaxial compression test, and direct tension test (Tao et al., 2020). According to the observation of the rock sample, the main mineral composition contains Pyroxene, Plagioclase, and Biotite with volume fraction of 50%, 30%, and 20% respectively. The macro-mechanical parameters collected from experimental tests include Young's modulus (65 ± 6 GPa), UCS (135 ± 10 MPa) and tensile strength (18 ± 3 MPa). The dimension of the cuboid experimental specimen is 50mm (height) \times 50mm (width) \times 100mm (length).

7.2.3 Microscopic Parameters Calibration

The experimental mechanical parameters could not be directly inputted into the GBM, so the numerical macro-mechanical parameters could be determined by adjusting micro-parameters. According to previous studies (Bahrani et al., 2014; Saadat & Taheri, 2020), the calibration procedure could be regarded as guidance for micro-parameters selection by comparing the numerical macro-parameters with experimental macro-parameters. According to the GBM structure, the grain is formed by parallel bond and particles and the grains are connected by smooth-joint contact which is regarded as the grain boundary. Therefore, the micro-mechanical parameters include (1) modulus of particles and parallel bond; (2) ratio of normal to shear stiffness of particles, parallel bond and smooth-joint contact; (3) friction coefficient of

particles, parallel bond and smooth-joint contact; (4) tensile strength of the parallel bond and smooth-joint contact; (5) cohesion of parallel bond and smooth-joint contact (6) friction angle of parallel bond and smooth-joint contact.

The calibration procedure is based on the “trial and error” method. To be specific, there are a series of calibrating tests, in terms of uniaxial compression tests and directly tensile tests. After these numerical tests, the stress-strain plots could determine the numerical macro-parameters. The micro-parameters could be determined till the stress-strain plots and macro-parameters of numerical results are consistent with the experimental results. The obtained micro-mechanical parameters calibrated by macroscopic mechanic properties of specimens are shown in Table 7-1 and Table 7-2.

Table 7-1: Microscopic mechanical parameters for parallel bond and particles.

Micro-parameters of grain (Parallel Bond & Particles)			
Element	Pyroxene	Plagioclase	Biotite
Particle radius (mm)	0.1	0.1	0.1
Particle density (kg/m ³)	2500	2600	3000
Friction coefficient of particles	1.2	1.2	1.2
Ratio of normal to shear stiffness of particles	1.5	1.5	1.5
Ratio of normal to shear stiffness of bond	1.5	1.5	1.5
Modulus of parallel bond (GPa)	65	68	62
Tensile strength of parallel bond (MPa)	310	360	320
Cohesion of parallel bond (MPa)	260	280	300
Friction angle of parallel bond (°)	32	35	35

Table 7-2: Microscopic mechanical parameters for smooth-joint contact.

Micro-parameters of grain boundary (Smooth-joint Contact)	
Smooth-joint contact normal stiffness (N/m)	4*10 ⁹
Smooth-joint contact shear stiffness (N/m)	2*10 ⁹
Mean smooth-joint contact tensile strength (MPa)	10
Mean smooth-joint contact cohesion (MPa)	60
Smooth-joint contact friction coefficient	1.0
Mean smooth-joint bond friction angle (°)	30

The Experimental and numerical results under the UCS test were shown in Figure 7-3. Figure 7-3(a) indicated that the numerical specimen has the same UCS and similar modulus as the experimental specimen. According to Figure

7-3(b), the fracture of the numerical result is consistent with the experimental result. The inter-granular cracks dominate the fractures. The fractures of the experimental failed specimen are formed of few thin cracks with disordered extension direction. Moreover, the main cracks occurred along the grain boundaries which were located at the interface of different minerals. The inter-grain cracks developed and consisted of the major fracture. The major fracture path of the numerical specimen is consistent with the fracture development of the laboratory specimen. The extension direction is associated with the grain boundaries direction and mineral distribution.

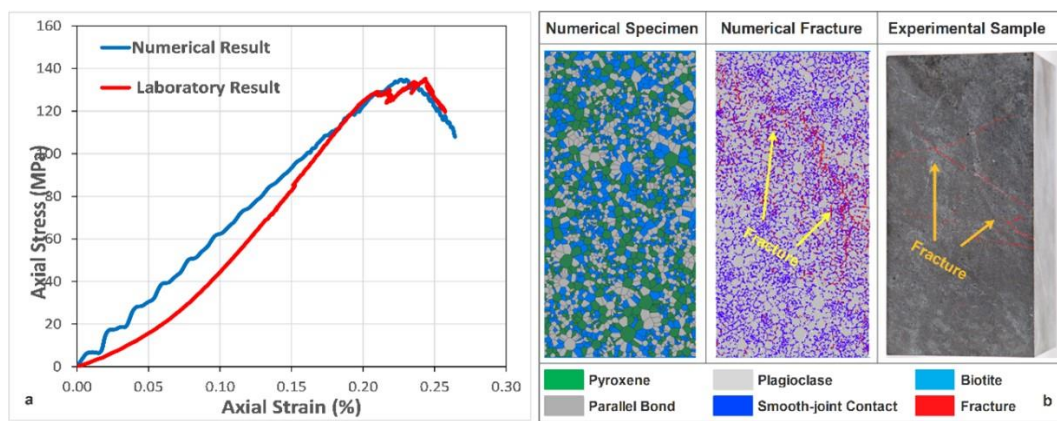


Figure 7-3: Comparison of numerical result and experimental result: (a) stress-strain plot (b) fractures

After adjustment of micro-mechanical parameters, the collected numerical macro-mechanical parameters include Young's modulus (65.7 GPa), UCS (135.5 MPa), and tensile strength (18.7 MPa), which are consistent with the experimental results as aforementioned. All errors are less than 5% (Table 7-3), so the micro-parameters of the mafic specimen shown in Table 7-1 and Table 7-2 are valid and reliable to be applied to numerical specimens.

Table 7-3: Comparison of experimental and numerical macroscopic mechanical parameter

Parameters	Experimental Results	Numerical Results	Error
Young's Modulus (GPa)	65 ± 6	63.6	2.15%
UCS (MPa)	135 ± 10	134.9	0.07%
Tensile Strength (MPa)	18 ± 3	18.7	3.9%

7.2.4 Field-scale Numerical Model Construction

Numerous experimental and numerical results indicated that the grain size has a significant influence on the rock mechanical properties (Tugrul & Zarif, 1999; Hofmann et al., 2015; Gui et al., 2016; Atapour & Mortazavi, 2018). Therefore, the suitable grain size and particle size are the primary parameters for the grain-based model. Previous studies suggested that each grain contains at least 5 particles, which could ignore the scale effect (Potyondy, 2010; Bahrani et al., 2014; Saddat & Taheri, 2020). Peng et al. (2017) suggested that the minimum ratio of grain size to particle size is four. In this study, considering the slenderness and roundness of grain, the ratio of grain-to-particle size was designed as 4 and each grain contained over 10 particles. Moreover, the model with a higher ratio of grain-to-particle size has more contacts, which leads to higher stress concentration requirement for fracturing (Hofmann et al., 2015; Zhang et al., 2022). Therefore, keeping the ratio as constant could carry out fixed rock mechanical properties. Although DEM could effectively simulate rock mass, DEM applied on the field-scale model will cost a huge computation time. In order to minimize the particle number and still have reasonably small particles around the tunnel, nine particle rings were constructed, which have increasing-sized particles and grains with the same ratio of grain-to-particle size. Additionally, when the least ratio of the thickness of the ring to particle radius is around 10, it could minimize the scale effect on the test results (Lan et al., 2013). The grains and particles configuration are shown in Figure 7-4. The detailed particle and grain sizes are presented in Table 7-4.

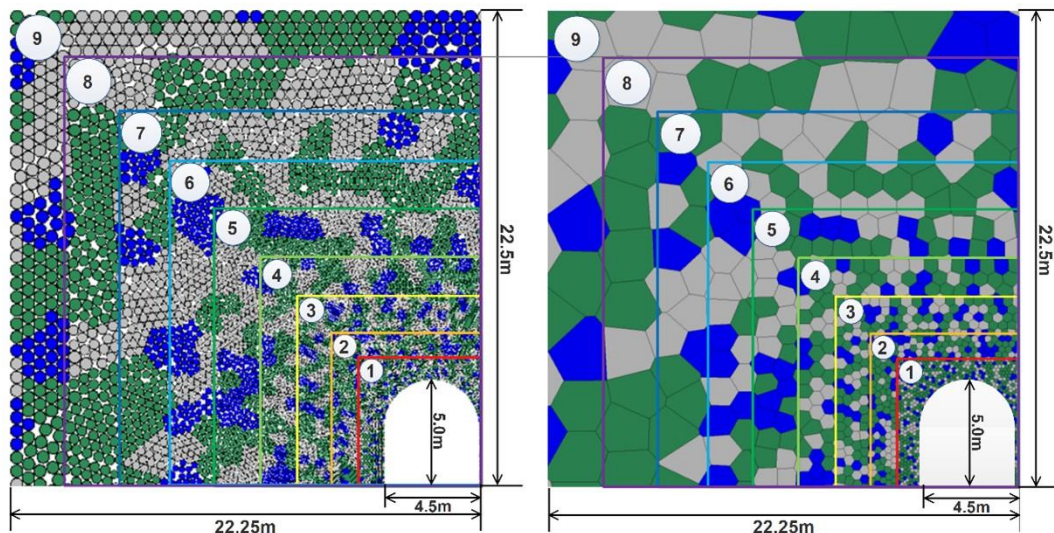


Figure 7-4: Particles (left) and grains (right) distribution for almost ¼ of the model.

Table 7-4: Grain size and particle size distribution in the model

Ring No.	Ring Thickness (m)	Min Grain Size (mm)	Max Grain Size (mm)	Particle Size (mm)	Particle No.
1	1.125	80	100	23	16912
2	1.337	136	186	40	10380
3	1.549	212	272	58	6530
4	1.760	325	407	88	3797
5	1.972	458	563	123	2664
6	2.184	613	740	164	2092
7	2.396	789	939	210	1725
8	2.608	986	1158	261	1426
9	2.819	1204	1399	317	1144

7.3 Numerical Results

In order to reveal the fractures development around the underground opening, there are three main models in terms of the single ore drive at different buried depths, double drives with different dipping angles, and double drives connected by stope with different widths.

7.3.1 One Drive

With the loading increase, the discrete cracks gradually occur, which firstly occur at the bottom of the left wall and the direction is along the boundaries between two minerals. Moreover, with the depth increasing, the initiation stress increases. The maximum damage depth occurred at the bottom of the hanging wall (left wall). The discrete cracks initiated from the surface of the ore drive to the deep rock mass. After crack development and coalescence, two main inclined fractures induced by shear cracks from the surface of the drive to the deep rock mass interacted and formed a V-shaped notch. All models presented large notch due to large block ejection, where the notch angle slightly increased and the maximum damage depth increased with the buried depth increasing.

At the foot wall (right wall) bottom, the mode of slabbing occurred near the surface of the ore drive. A series of cracks initiated and developed to coalesce into a sub-vertical fracture, and then the failed surface rock ejected. The models at different depths show a similar failure mode or damage depth around the ore drive. However, the damage extent is different. With the increase of depth, the failed surface rock varied from large slabs to fragments, and the sub-vertical fracture length is various.

The floor had a serious heaving phenomenon. Several cracks were initiated in the horizontal direction under the floor surface. As stress increased, the cracks developed and coalesced from the centre to the sides. As the buried depth increased, new cracks initiated in the deeper region and they interacted with the cracks in the shallower region, which lead to the shallower blocks splitting and pushing up as a heaving phenomenon. However, the backs had an arch profile, which lead to better performance. The roof had slight crushing at the shallower buried depth, and then the failure mode varied from spalling to slight buckling at two shoulders as the buried depth becomes deeper.

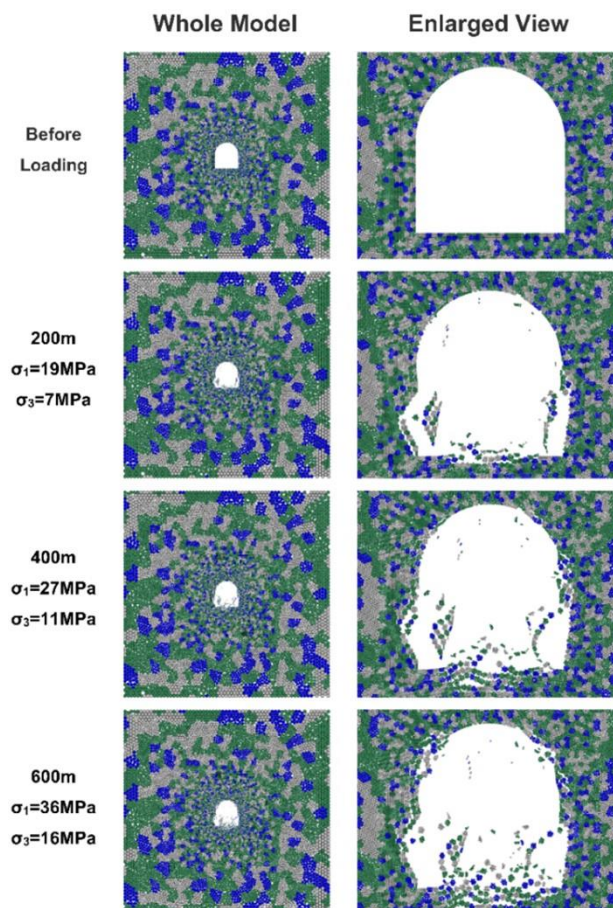


Figure 7-5: Ultimate failure models containing single drive under in-situ stress at different buried depth

7.3.2 Two Drives

In order to investigate the influence of the dip angle between two drives, a series of models with double drives were conducted under in-situ stress at 400m buried depth. According to the design from the site, the height between two levels is 20m and the dip angle of the stope ranges from 55° to 75°. Figure 7-6 presented the ultimate geometry at different dip angles between two drives, which revealed the significant influence of the dip angles on failure modes.

For the upper drives, the most serious damage occurred in the model at 65°. The notch depth and volume of failed blocks increased as the dip angle varied from 55° to 65°. However, as the dip angle increased from 65° to 75°, the damage depth and volume of failed fragments decreased. The numerical results could reflect the experimental results from physical model tests (Liu et al., 2019). At the angle of 55°, fragments ejection occurred at the foot wall due to buckling. As the dip angle increased from 60° to 65°, typical buckling occurred at the foot wall due to a sub-vertical fracture in the rock mass and the height of the notch increased from 55° to 65°. Slabbing occurred at the foot wall due to sub-vertical fracture at the surface of the drives, as the angle varied from 70° to 75°. Moreover, the length of sub-fractures increased from 60° to 75°. Additionally, the damage characteristics of the hanging wall and floor had a similar tendency to that of the foot wall. However, the damage severity of the hanging wall is slighter than that of the foot wall.

For the lower drives, the damage severity around drives is complicated. However, the lower drive at the angle of 65° had better performance compared with other upper drivers. At the angle of 55° and 60°, the serious buckling occurred at the hanging wall due to inclined fractures. When the dip angle reached 60°, there is spalling at the surface of the hanging wall. As the angle increased from 70° to 75°, slight buckling induced by vertical fractures occurred at the hanging wall. Moreover, the large notch induced by buckling occurred at the foot wall at the angle of 55° and 75°. As the angle varied from

60° to 70°, the failure at the foot wall is slabbing or slight buckling near the surface.

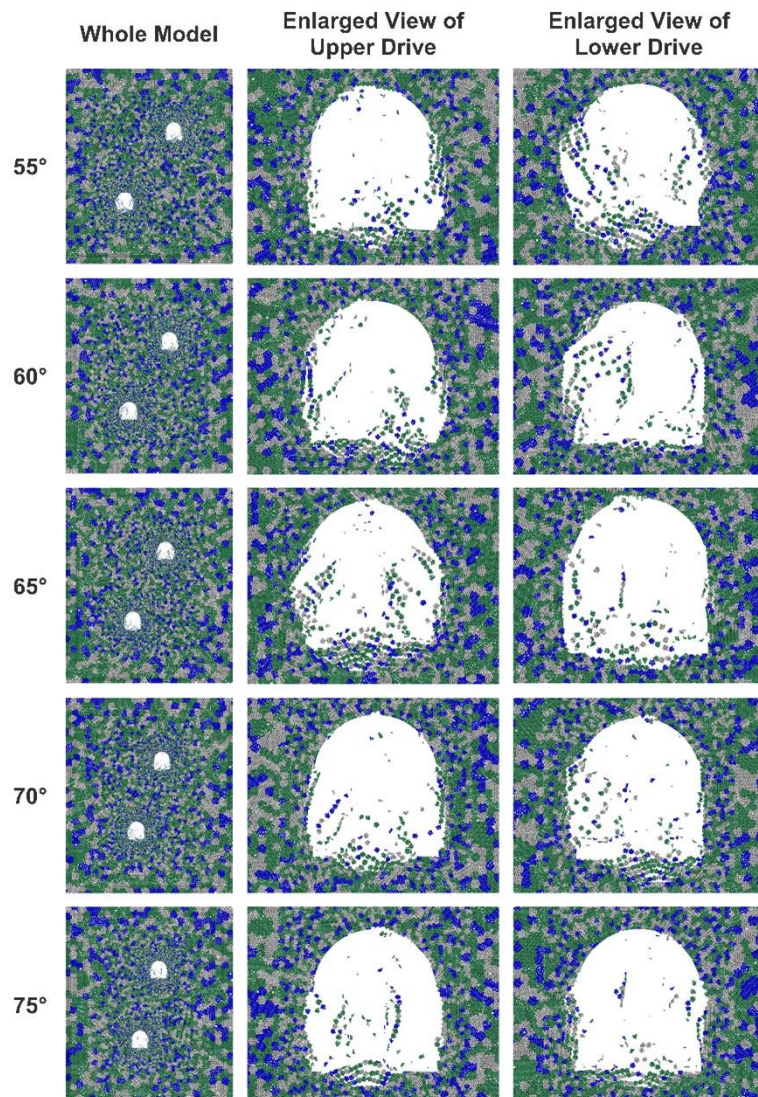


Figure 7-6: Ultimate failure models containing two drives with different dip angles under in-situ stress at 400m depth

7.3.3 Two Drives with Stope

The mined-out area for the stope may act as a large discontinuity, which will interact with other discontinuities. In order to investigate the influence of stope on the stability of stope and drives, a series of models containing two drives connected by stope with different widths at dip angles of 55° and 70°, according to the actual stope designed and mined from the site (Figure 7-7). Figure 7-7a is the model based on scanning using the cavity monitoring system (CMS), and Figure 7-7b is the view from the upper drive. The ultimate failure

modes were shown in Figure 7-8. Generally, when the dip angle of the stope increase, it presented more serious damage around the stope, which is consistent with the experimental results. According to Wu et al. (2020), the number of cracks decreased with the increase in horizontal distance between the fissure and circular hole based on the physical models containing a fissure and two circular holes.



Figure 7-7: Actual stope between two drives: (a) stope scanned by CMS (b) view from upper drive.

For the lower drives with stope at dipping angle of 55° , cracks initiated at the hanging wall bottom and foot wall shoulder. In the ultimate damaged lower drives, the hanging wall had a large notch induced by block ejection due to inclined fractures, and the foot wall shoulder had sliding induced by sub-vertical fractures. Some cracks occurred at the foot wall bottom and extended into the deep rock mass in the sub-horizontal direction. These cracks have not coalesced, but they would cause the loose rock mass. For the upper drives with stope at the dipping angle of 55° , large shear fractures occurred in the deep rock mass behind the hanging wall. As the stope width increased, this deep shear fracture had more influence on the hanging wall damage varying from spalling to buckling. The footwall had buckling at the bottom of the foot wall.

For the lower drives with stope dipping at the angle of 70° , cracks initiated at the surface of two side walls. However, the failure at the hanging wall is slight buckling, and the failure at the foot wall is sliding from the stope similar to the mode at the angle of 55° . Additionally, the backs had more damage due to

blocks sliding compared with the mode at the angle of 55°. For the upper drives with stope dipping at the angle of 70°, cracks initiated at the surface of the foot wall, which is in the mode of spalling. The blocky sliding occurred at the bottom of the hanging wall due to the sub-vertical fractures extending from the hanging wall surface to the stope. Moreover, the damage around upper drives became more severe, as the stope width decreased.

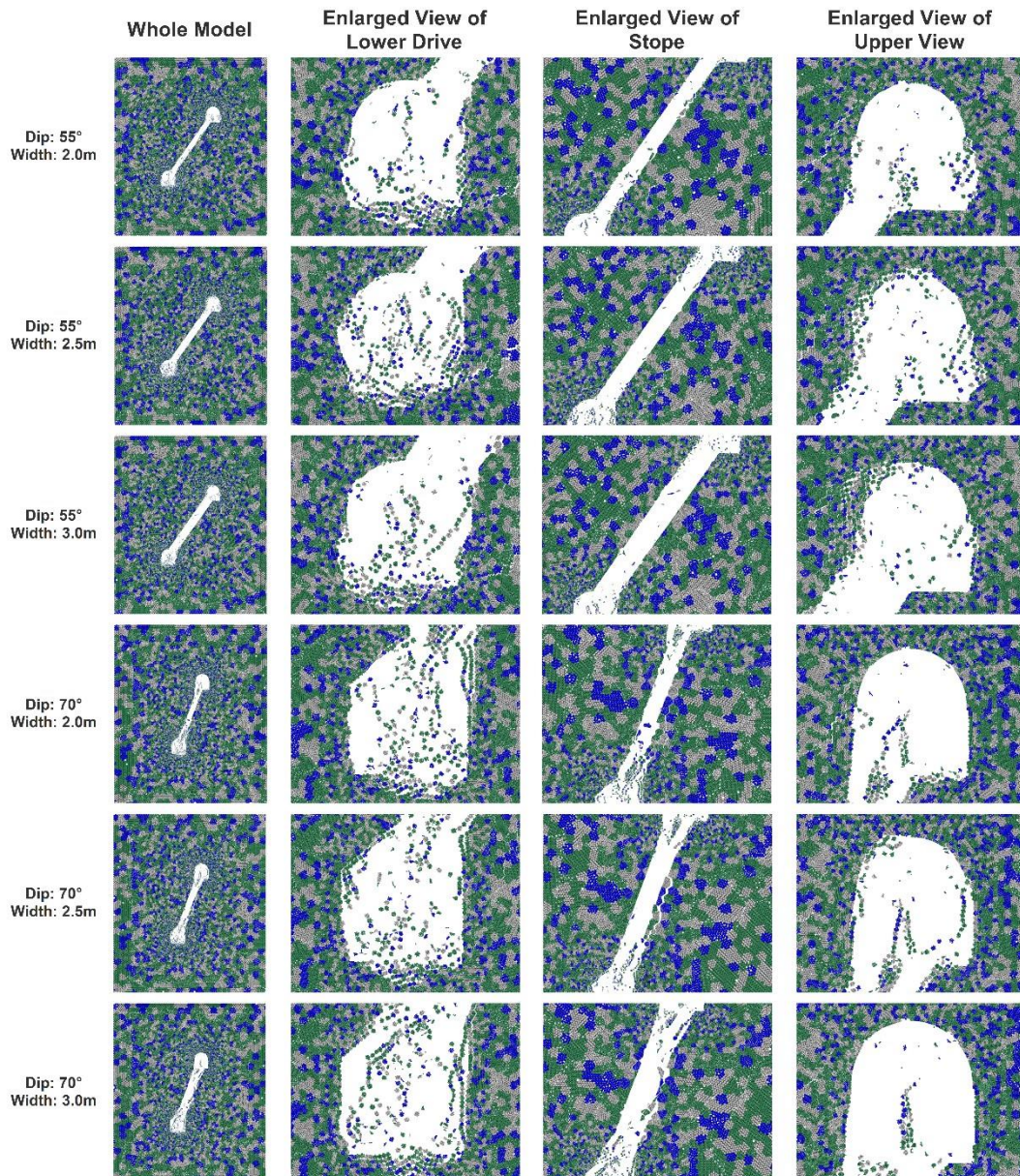


Figure 7-8: Ultimate failure models containing two drives connected by stope with different width at the dip angle of 55° and 70°

7.4 Discussion

7.4.1 Damage Depth

Due to rock ejection, the notch depth or volume of failed rock is often used to determine the rockburst damage severity (Ortlepp & Stacey, 1994; Cai, 2013; Mazaira & Konicek, 2015). Additionally, in the concept of crack coalescence, the pre-existing fissures will cause further fractures. In mining engineering, the ongoing seismic events induced by drilling and blasting will transfer energy into rock mass around the drives. Therefore, it is significant for support design to determine the direct damage depth. Figure 7-9 shows the schematic of damage depth, where R is defined as the distance from the centroid of the drive to the initial profile. The damage depth D is defined as the distance between the centroid of the drive and the fracture location. Comparing the damage ratio of D/R , it could reveal the damage location and severity under different conditions.

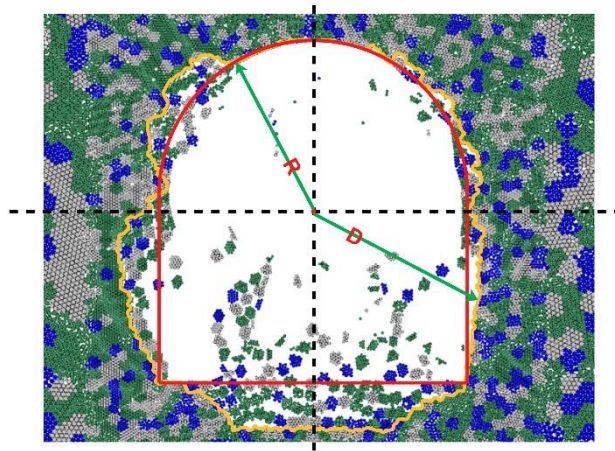


Figure 7-9: Damage depth schematic

7.4.1.1 Damage Depth of Single Drive

Figure 7-10 presented the designed profile and the damaged profile at different buried depths. The foot wall had a similar failure mode and maximum damage depth due to buckling or slabbing induced by sub-vertical fractures, but the length or height of the damaged region increases with an increase in buried depth. The maximum damage depth occurring at the hanging wall increases with the increase of buried depth due to rock ejection caused by inclined fractures. As the buried depth increases, the height of the notch tip is becoming

higher in terms of 1.14m, 1.43m, and 2.05m. Meanwhile, the notch angle varied in terms of 120°, 130°, and 135°.

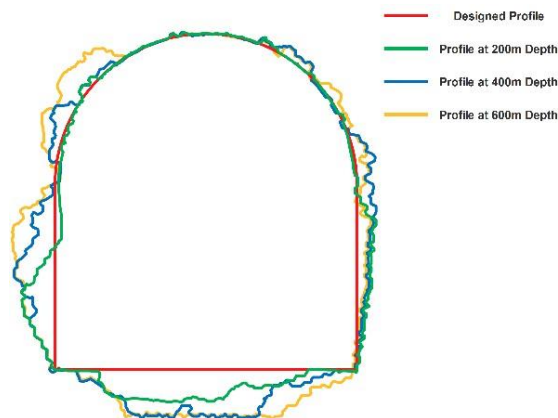


Figure 7-10: One drive at different depth

Figure 7-11 presented the detailed damage ratio around drives at different buried depth. The damage severity increased, as the buried depth increased. The maximum damage depth for the single drive model is about 1.3R, which is located at the lower part of the hanging wall. The floor also had a higher damage ratio, which is caused by the deep horizontal tension fractures.

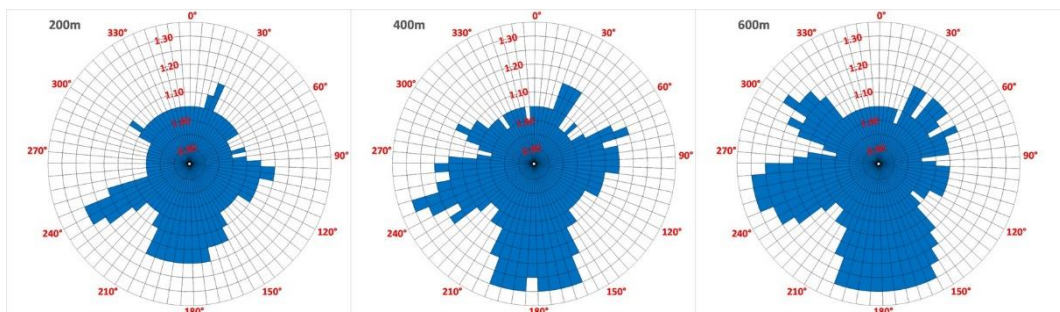


Figure 7-11: The ratio of damage depth to the radius of a drive at different depth

7.4.1.2 Damage Depth of Double Drives

Figure 7-12 presented the damaged region of double drives with different dipping angles. The upper drive had a wider damaged region than the lower drive, which means that there was more severe damage around the upper drive, especially two side walls. Moreover, the major failures were located at the outside of two drives. Specifically, the upper drives had more damage at the foot (right) wall, and the lower drives had more damage at the hanging (left) wall. Within the range of two drives, the upper drives had more damage under the floor and the lower drives had more damage at the left shoulder due to the

mutual influence between two drives. The numerical result was consistent with the physical experimental result based on the specimen containing two holes (Liu et al., 2019).

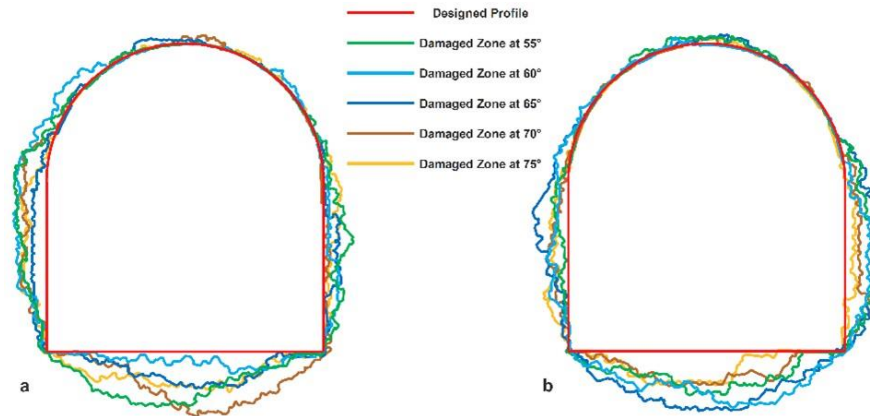


Figure 7-12: Damaged region of ore drives with different dip angles: (a) Lower drive (b) Upper drive

Figure 7-13 presented the detailed damage ratio around drives with different dipping angles. The dipping angle plays a significant role in rock mass behaviours. When the dipping angle is 65° , the upper drive had the largest damage ratio around the drive including the damage that occurred at the foot wall, hanging wall, and floor. However, at the same dipping angle, the lower drive had the smallest damage ratio around the drive. Moreover, the total damage depth around two drives had the lowest value at 75° . According to the physical experimental results (Liu et al., 2019), when the bridge angle between two holes was 75° , the specimen had the strongest strength and modulus than other specimens with the bridge angle varying from 45° to 75° . Similar to the damage ratio of single drive, the floor had a large value as well. However, the severity of damage is more serious than single drive due to the mutual influence.

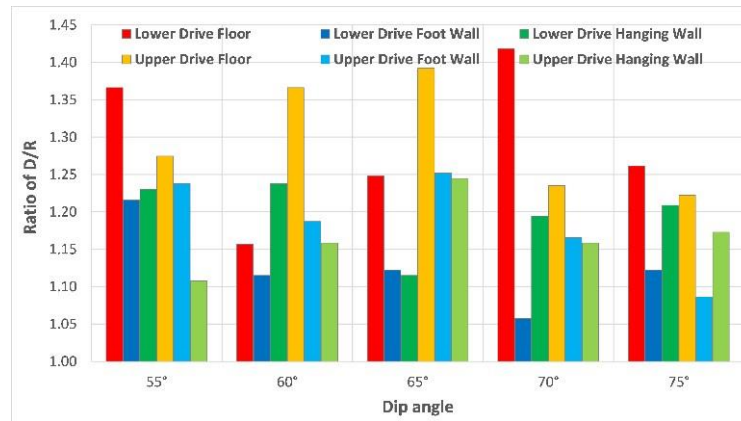


Figure 7-13: Damage ratio at different location and dipping angle

7.4.2 In-situ Failure

7.4.2.1 Damage Mechanism

The most common types of damage around deep excavation in mining and civil engineering activities are categorized as rock ejection, rock deformation induced by laminated rock buckling, large convergence induced by wall buckling and floor heaving, shear displacement due to activation of fault, and collapse due to kinematic movement of geological structures (Ortlepp & Stacey, 1994; Kaiser and Cai, 2012; Mazaira and Konicek, 2015; Li et al., 2019). In jointed rock masses, rock ejection is the most common phenomenon among these damage types. Both rockburst and fault-slip could be the source that produces the ejection in the shape of thin and large slabs or fragments.

Additionally, the natural rock contains numerous pre-existing cracks. On the concept of microscopic damage evolution and macroscopic fracture development, the discontinuities will develop and coalesce, which leads to failure occurring near the surface of the opening. In this study, the main conceptual mechanisms that occurred are shown in Figure 7-14. All failures are initiated by pre-existing cracks or fractures. With the increase of stress concentration, the cracks or fractures develop and coalesce, eventually causing failure around the excavation surface. According to the numerical results and the in-situ failure observation, three main damage mechanisms could be identified. The first failure mode is the buckling of fragments or slabs, which is induced by sub-vertical discontinuities or fractures (Figure 7-14a). The second failure mode is facing rock ejection, which leads to the movement of

fracture-defined blocks or fragments along the large discontinuities (Figure 7-14b). The last failure mode is tensile fractures parallel to the principal stress orientation, which would lead to further buckling at the wall or heaving at the floor (Figure 7-14c).

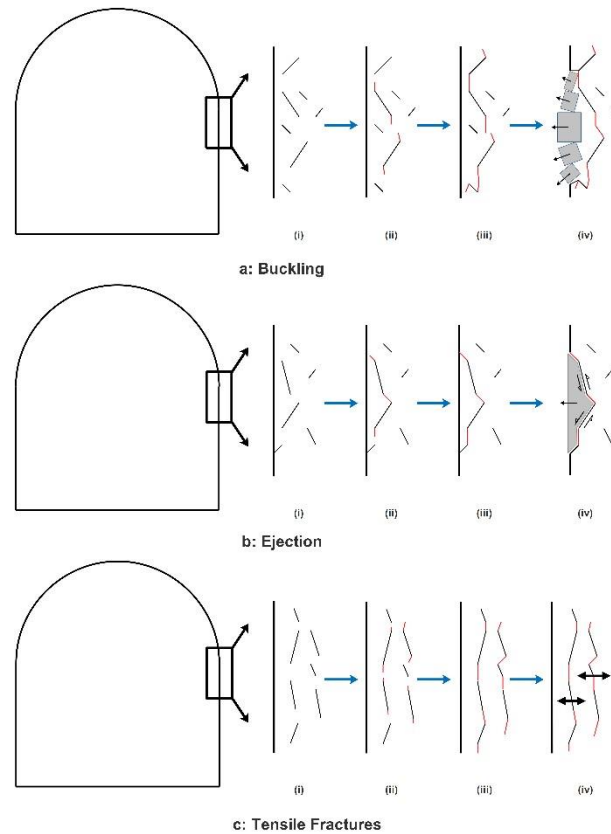


Figure 7-14: The schematics of three main failures around the surface: (a) buckling (b) rock ejection, and (c) tensile fractures formed by the procedure (i) initial geometry (ii) crack initiation (iii) crack propagation (iv) failure (modified after Orlepp & Stacey, 1994; Germanovich & Dyskin 2000; Li et al., 2019).

7.4.2.2 In-situ Failure Cases

In the selected mine site, the rock mass is very structured, where suffered from a large number of seismic events. According to the observation, the damage around ore drives was identified after excavation and seismic events with large magnitude. The following section will present the failure mode and damage depth to verify the numerical results.

Figure 7-15 presented the profile close to the stope after failure. The initial profile was surveyed by total station and the post profile is scanned by ZEB-Horizon 3D mobile scanner. The maximum bagging depth is 0.71m at the

shoulder of the foot wall (Figure 7-15a). The high energy dissipation (HED) system was applied on ground support of the case site, including shotcrete, chain-link mesh, posimix resin bolts and cable bolts (Figure 7-15b). Bagging at the surface instead of rock ejection due to shotcrete and chain-link mesh, but there were fragments behind the bagging according to the in-sight observation.

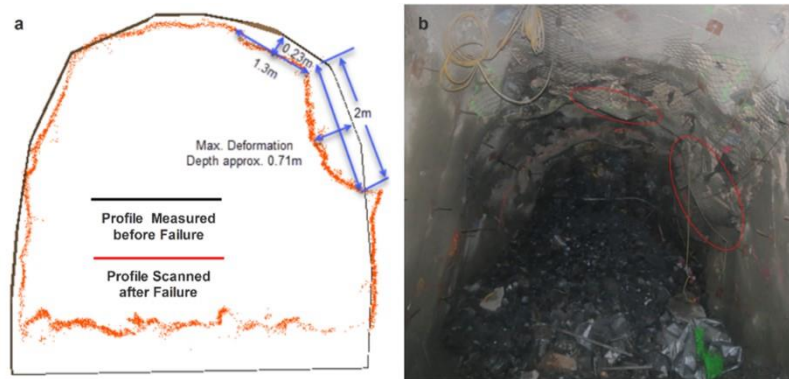


Figure 7-15: Ore drive failure close to stope: (a) cross-section scanning (b) in-situ failure.

Moreover, failure not only occurred close to the stope after firing, but also occurred at other locations after large seismic events. Figure 7-16 shows the failure of the hanging wall. The maximum depth of bagging is 0.73m based on the scanning after failure, and the maximum depth of void is 0.8m based on the scanning after rehab (Figure 7-16a). The hanging wall after failure and rehab are shown in Figure 7-16b and Figure 7-16c, respectively. The maximum ratio of D/R by numerical simulation is 1.3, which means that the maximum damage depth is 0.69m, which is a little smaller than the in-situ failure.

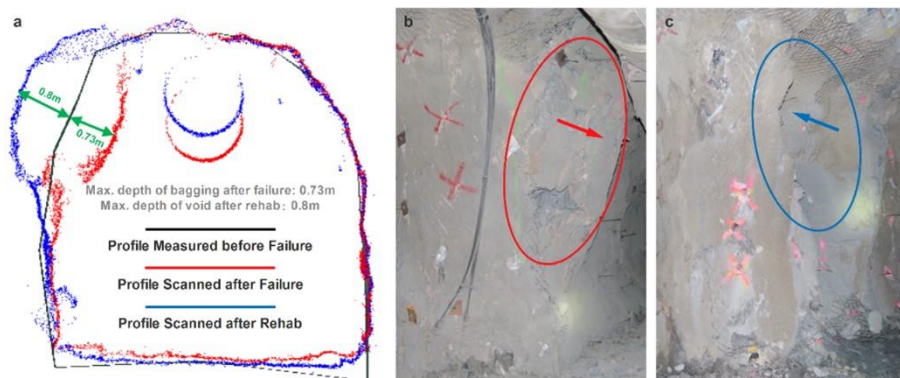


Figure 7-16: Hanging wall failure: (a) cross-section view of scanning, (b) in-situ failure, (c) void after rehab.

Additionally, there were several damages observed at different regions of the profile. According to the in-situ failure (Figure 7-17), the failure modes of the numerical simulation were consistent with the in-situ observation. The backs had better performance due to the arch profile, but it still had slight crushing in the deeper drive. The floor was relatively stable on site. However, when the sill pillar failed, the floor had the heaving or splitting phenomenon. The foot wall and hanging wall had large bagging due to the fragments ejection induced by buckling and rock sliding. Meanwhile, as the drives were close to the stope, the upper part of the profile (i.e. shoulders and backs) had more severe damage.

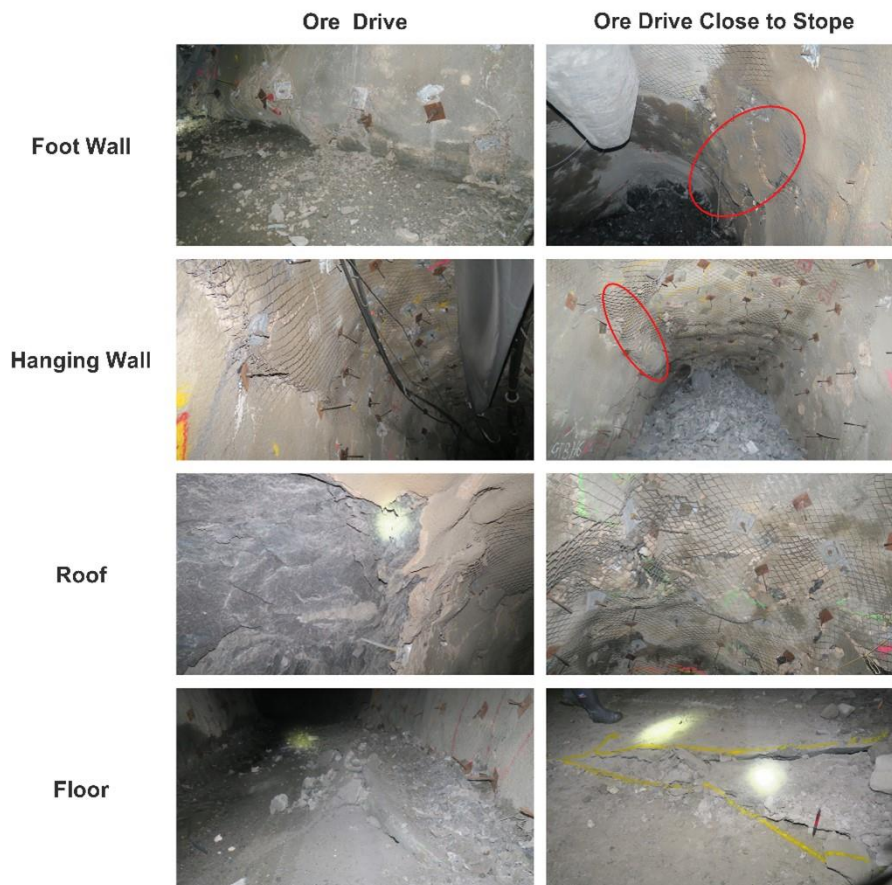


Figure 7-17: In-situ failure

7.5 Conclusion

A field-scale grain-based model for rock mass was constructed and calibrated by the two-dimension of particle flow code (PFC^{2D}), according to the analysis of grain-scale characteristics (e.g. mineral composition and grain size) and laboratory-scale properties (e.g. mechanical properties of intact rock). To

improve computation efficiency, nine rings of grains with the same ratio of grain-to-particle size were constructed with the increase in particle size. In order to analyse the stability and damage mechanism of the field-scale model under different in-situ conditions, three main excavated models were constructed in terms of the single ore drive at different buried depths, double drives with different dipping angles, and double drives connecting with stope with different widths.

According to the relationship between in-situ stress and depth, the rock behaviours responding to mining excavation were analysed for different buried depths at 200m, 400m, and 600m, respectively. Buckling occurred at the foot wall induced by sub-vertical fractures and block ejection occurred at the hanging wall due to inclined fractures. As the buried depth increases, the notch height and notch angle increase.

According to the orebody dipping angle and site design, the double drives models are arranged with the dipping angles varying from 55° to 75° and a fixed height of 20m. The lower drive at 65° has the most severe damage than the drives at other dipping angles. The measurement of damage depth indicates that the drives at the dipping angle of 75° have the lowest value, which means that it has the highest rock mass strength. When the stope is excavated and connects two drives, there is more severe damage around the steeper stope. Moreover, the drives connecting by steeper stope have more damage induced by sliding along discontinuities and fractures. The drives connecting by flatter stope have the main damage induced by buckling.

Finally, the failure modes and damage severity are compared with the in-situ failure cases. The numerical results are in good agreement with the engineering results. The grain-based model is verified to simulate the field-scale rock behaviours based on the concept of microscopic damage evolution and macroscopic fracture development.

Acknowledgements

We sincerely acknowledge Northeastern University, China provided the laboratory tests. This study is partly supported by National Natural Science Foundation of China the 111 Project under grant no: 51839003 and B17009. We also thank Dr. Mahdi Saadat at School of Civil,

Environmental and Mining Engineering, The University of Adelaide, Australia, for his invaluable support with the grain-based model in PFC software. We would also like to thank the journal editor and reviewers for their valuable suggestions. In addition, this research did not receive any specific grant from funding agencies in the public, commercial, or not-for-profit sectors.

Reference

- Atapour, H., & Mortazavi, A. (2018). The influence of mean grain size on unconfined compressive strength of weakly consolidated reservoir sandstones. *Journal of Petroleum Science and Engineering*, 171: 63-70.
- Bahrani, N., Kaiser, P. K., & Valley, B. (2014). Distinct element method simulation of an analogue for a highly interlocked, non-persistently jointed rockmass. *International Journal of Rock Mechanics & Mining Sciences*, 71: 117-130.
- Boon, C. W., Housby, G. T., & Utili, S. (2015). Designing Tunnel Support in Jointed Rock Masses Via the DEM. *Rock Mechanics and Rock Engineering*, 48: 603-632.
- Cai, M. (2013). Principles of rock support in burst-prone ground. *Tunnelling and Underground Space Technology*, 36: 46-56.
- Diederichs, M. S. (2007). The 2003 Canadian Geotechnical Colloquium: Mechanistic interpretation and practical application of damage and spalling prediction criteria for deep tunnelling. *Canadian Geotechnical Journal*, 44: 1082-1116.
- Farahmand, K., & Diederichs, M. S. (2021). Calibration of coupled hydro-mechanical properties of grain-based model for simulating fracture process and associated pore pressure evolution in excavation damage zone around deep tunnels. *Journal of Rock Mechanics and Geotechnical Engineering*, 13: 60-83.
- Farahmand, K., Vazaios, I., Diederichs, M. S., & Vlachopoulos, N. (2018). Investigating the scale-dependency of the geometrical and mechanical properties of a moderately jointed rock using a synthetic rock mass (SRM) approach. *Computers and Geotechnics*, 95: 162-179.
- Germanovich, L. N., & Dyskin, A. V. (2000). Fracture mechanisms and instability of openings in compression. *International Journal of Rock Mechanics and Mining Sciences*, 37: 263-284.
- Ghasemi, S., Khomehchiyan, M., Taheri, A., Nikudel, M. R., & Zalooli, A. (2020). Crack Evolution in Damage Stress Thresholds in Different Minerals of Granite Rock. *Rock Mechanics and Rock Engineering*, 53, 1163-1178.
- Gui, Y., Zhao, Z., Ji, J., Wang, X., Zhou, K., & Ma, S. (2016). The grain effect of intact rock modelling using discrete element method with Voronoi grains. *Géotechnique Letters*, 6: 136-143.
- He, M. C., Gong, W. L., Zhai, H. M., & Zhang, H. P. (2010). Physical modeling of deep ground excavation in geologically horizontal strata based on infrared thermography. *Tunnelling and Underground Space Technology*, 25: 366-376.
- Hofmann, H., Babadagli, T., Yoon, J. S., & Zang, A. (2015). A grain based modelling study of mineralogical factors affecting strength, elastic behaviour and micro fracture development during compression tests in granites. *Engineering Fracture Mechanics*, 147: 261-275.
- Huang, F., Zhu, H., Xu, Q., Cai, Y., & Zhuang, X. (2013). The effect of weak interlayer on the failure pattern of rock mass around tunnel - Scaled model tests and numerical analysis. *Tunnelling and Underground Space Technology*, 35: 207-218.
- Ivars, D. M., Pierce, M. E., Darcel, C., Reyes-Montes, J., Potyondy, D. O., Young, R. P., & Cundall, P. A. (2011). The synthetic rock mass approach for jointed rock mass modelling. *International Journal of Rock Mechanics & Mining Sciences*, 48: 219-244.
- Kaiser, P. K., & Cai, M. (2012). Design of rock support system under rockburst condition. *Journal of Rock Mechanics and Geotechnical Engineering*, 4: 215-227.

- Karampinos, E., Hadjigeorgiou, J., Hazzard, J., & Turcotte, P. (2015). Discrete element modelling of the buckling phenomenon in deep hard rock mines. *International Journal of Rock Mechanics & Mining Sciences*, 80: 346-356.
- Lan, H., Martin, C. D., & Andersson, J. C. (2013). Evolution of In Situ Rock Mass Damage Induced by Mechanical-Thermal Loading. *Rock Mechanics and Rock Engineering*, 46: 153-168.
- Li, C. C., Mikula, P., Simser, B., Hebblewhite, B., Joughin, W., Feng, X., & Xu, N. (2019). Discussions on rockburst and dynamic ground support in deep mines. *Journal of Rock Mechanics and Geotechnical Engineering*, 11: 1110-1118.
- Li, X., Li, H., & Zhao, J. (2019). The role of transgranular capability in grain-based modelling of crystalline rocks. *Computers and Geotechnics*, 110: 161-183.
- Li, Y., Zhang, D., Fang, Q., Yu, Q., & Xia, L. (2014). A physical and numerical investigation of the failure mechanism of weak rocks surrounding tunnels. *Computers and Geotechnics*, 61: 292-307.
- Liang, Z., Gong, B., & Li, W. (2019). Instability analysis of a deep tunnel under triaxial loads using a three-dimensional numerical method with strength reduction method. *Tunnelling and Underground Space Technology*, 86: 51-62.
- Liu, X.-R., Yang, S.-Q., Huang, Y.-H., & Cheng, J.-L. (2019). Experimental study on the strength and fracture mechanism of sandstone containing elliptical holes and fissures under uniaxial compression. *Engineering Fracture Mechanics*, 205: 205-217.
- Manouchehrian, A., & Cai, M. (2018). Numerical modeling of rockburst near fault zones in deep tunnels. *Tunnelling and Underground Space Technology*, 164-180.
- Mazaira, A., & Konicek, P. (2015). Intense rockburst impacts in deep underground construction and their prevention. *Canadian Geotechnical Journal*, 52: 1426-1439.
- Nicksiar, M., & Martin, C. D. (2014). Factors affecting crack initiation in low porosity crystalline rocks. *Rock Mechanics and Rock Engineering*, 1165-1181.
- Ortlepp, W. D., & Stacey, T. R. (1994). Rockburst mechanisms in tunnels and shafts. *Tunnelling and Underground Space Technology*, 9: 59-65.
- Potyondy, D. O. (2010). A Grain-Based Model for Rock: Approaching the True Microstructure. *Proceedings of Rock Mechanics in the Nordic Countries 2010*, (p. 10). Kongsberg, Norway.
- Saadat, M., & Taheri, A. (2020). A cohesive grain based model to simulate shear behaviour of rock joints with asperity damage in polycrystalline rock. *Computers and Geotechnics*, 103254.
- Seki, S., Kaise, S., Morisaki, Y., Azetaka, S., & Jiang, Y. (2008). Model experiments for examining heaving phenomenon in tunnels. *Tunnelling and Underground Space Technology*, 23: 128-138.
- Sharifzadeh, M., Feng, X.-t., Zhang, X., Qiao, L., & Zhang, Y. (2017). Challenges in multi-scale hard rock behaviour evaluation at deep underground excavations. *12th Iranina and 3rd Regional Tunnelling Conference*. Tunnelling and Climate Change.
- Tao, R., Sharifzadeh, M., Zhang, Y., & Feng, X.-T. (2020). Analysis of mafic rocks microstructure damage and failure process under compression test using quantitative scanning electron microscopy and digital images processing. *Engineering Fracture Mechanics*, Vol.231: 107019.

- Tuğrul, A., & Zarif, I. H. (1999). Correlation of mineralogical and texture characteristics with engineering properties of selected granitic rocks from Turkey. *Engineering Geology*, 303-317.
- Turichshev, A., & Hadjigeorgiou, J. (2017). Development of Synthetic Rock Mass Bonded Block Models to Simulate the Behaviour of Intact Veined Rock. *Geotechnical and Geological Engineering*, 35: 313-335.
- Wang, X., & Cai, M. (2020). A DFN-DEM Multi-scale Modeling Approach for Simulating Tunnel Excavation Response in Jointed Rock Masses. *Rock Mechanics and Rock Engineering*, 53: 1053-1077.
- Wong, L. N., & Einstein, H. H. (2009). Crack Coalescence in Molded Gypsum and Carrara Marble: Part 2--Microscopic Observations and Interpretation. *Rock Mechanics and Rock Engineering*, 513-545.
- Wu, T., Gao, Y., Zhou, Y., & Li, J. (2020). Experimental and numerical study on the interaction between holes and fissures in rock-like materials under uniaxial compression. *Theoretical and Applied Fracture Mechanics*, 106: 102488.
- Zhang, T., Yu, L., Wu, B., Tan, Y., & Su, H. (2022). Influence of grain-to-particle size ratio on the tensile mechanical response of granite based on a novel three-dimensional grain-based model. *Engineering Fracture Mechanics*, 259: 108161.
- Zhu, W. C., Liu, J., Tang, C. A., Zhao, X. D., & Brady, B. H. (2005). Simulation of progressive fracturing processes around underground excavation under biaxial compression. *Tunnelling and Underground Space Technology*, 20: 231-247.
- Zhu, W., Li, Y., Li, S., Wang, S., & Zhang, Q. (2011). Quasi-three-dimensional physical model tests on a cavern complex under high in-situ stress. *International Journal of Rock Mechanics & Mining Sciences*, 48: 199-209.
- Zhu, X., Wang, Y., & Ren, Y. (2020). Numerical Simulation to Research on the Fracture Mechanism of the Surrounding Rock in Deep Tunnels. *Geotechnical and Geological Engineering*, 38: 319-327.

Every reasonable effort has been made to acknowledge the owners of copyright material. I would be pleased to hear from any copyright owner who has been omitted or incorrectly acknowledged.

Chapter 8 . Conclusions, Challenges and Recommendations

8.1 Introduction

This chapter presents the contributions, challenges, and recommendations of this research. Firstly, a summary of overall conclusions for multiscale rock behaviours is addressed and the contributions or findings during this research are highlighted as well. Secondly, the current challenges associated with the modelling and data collection are addressed. Finally, the last section provides the recommendations and improvements associated with the modelling approach in the future work

8.2 Overall Conclusions

This thesis presents an advanced approach to investigate rock behaviours from grain scale to field scale. Firstly, the grain scale data is collected by statistical analysis from quantitative SEM observation and digital image processing for the samples under the uniaxial compression test and triaxial compression test. Then, an updated grain-based model is proposed to mimic the highly heterogeneous rock with a large range of grain size distribution based on the grain scale data. A series of UCS tests are carried out to investigate the influence of micro-factors (e.g. heterogeneity, grain size, grain shape, micro-flaws) on macro-mechanical properties. Finally, this grain-based model is firstly applied on field scale simulation to investigate the highly structured rock mass behaviours, and the results are verified by comparison with the in-situ observation. The following main conclusions are carried out based on the SEM observation, experimental results, numerical results, and in-situ observation:

- i. Rock behaviours at the micro-scale (grain scale):
 - The uniaxial and triaxial compression tests are applied to the mafic specimens. Several fragments are conducted by SEM observation, including five fragments before tests and six fragments after tests.
 - Based on the SEM images observation, the grain scale data are collected, such as microstructure types, mineral composition, and grain

size distribution. The microstructures are classified as heterogeneity, grain boundaries, micro-cracks, pore, and cleavage.

- The pre-existing micro-cracks are classified as inter-granular cracks, intra-granular cracks, and trans-granular cracks, which account for 37%, 36%, and 27% of total pre-existing micro-cracks, respectively. The deformed micro-cracks after tests are classified as tensile cracks, shear cracks, and mixed shear-tensile cracks, which account for 53%, 29%, and 18% of total deformed micro-cracks, respectively.
 - The damage area of each type of deformed crack is determined by the technique of digital image processing. All fragments present more tensile damage at the final stages. The fragments show contrasting results at initiating stage under different compression tests. The fragments under the uniaxial compression test show much more tensile damage, and the fragments under the triaxial compression tests show more shear damage due to the increase of confining stress.
 - The microscopic damage evolution from digital image processing results is associated and consistent with the laboratory scale failure from the observation of experimental specimens.
- ii. Rock behaviours at the meso-scale (laboratory scale):
- A series of uniaxial compression tests are applied on groups of numerical specimens by PFC-GBM to investigate the influence of microscopic factors on rock mechanical properties and laboratory-scale fracturing. An updated grain-based model is proposed according to the concept of grain size distribution, which could effectively mimic the highly heterogeneous specimen, namely a large range of grain size distribution. All microscopic parameters are determined and calibrated by comparison of mechanical properties of experimental results and numerical results.
 - A modified heterogeneity index (MHI) is proposed, which could effectively describe the rock heterogeneity induced by constituent

mineral grain size distribution. The numerical results indicate that the heterogeneity induced by grain size distribution has a significant influence on the rock mechanical properties and fractures development. The strength and modulus increase with the increase of MHI. The highly heterogeneous specimens show more tensile failure due to numerous disordered inter-grain cracks, but the lowly heterogeneous specimens show more dilation and fractures due to coalescence induced by intra-grain cracks.

- The grain size has a significant influence on the mechanical properties and fracturing characteristics as well. The strength and modulus increase as the grain size increases. The dilation of cracks increases with the increase of grain size due to the increase of intra-grain cracks, which are subjected to coalesce to larger fractures.
- The mineral distribution with the same volume fraction of constituent minerals has an insignificant influence on rock mechanical properties. However, mineral distribution has a significant influence on fracture development. It is more subjected to fracture development and stress concentration at the interface between a large grain and a small grain with different minerals.
- The controlled Voronoi tessellation is applied to the numerical specimens to investigate the grain shape effect. Three main grain shapes of models with a series of different slenderness ratio are constructed in terms of hexagon grain, rectangular grain, and shield-shaped grain.
- The grain shapes have a significant influence on rock mechanical properties. The rectangular grain models have the higher strength and modulus, and the shield-shaped grain models have the lower strength and modulus, which is caused by the heterogeneity induced by the mineral geometries.
- The slenderness ratio of grain has a significant influence on rock mechanical properties as well. The rectangular grain models have the

highest strength and modulus at the slenderness ratio of 1, but the hexagon and shield-shaped grain models have the lowest strength and modulus at the slenderness ratio of 1 and 1.14, respectively.

- The different grain shape models with different slenderness ratios present different fracturing modes. The rectangular grain models present more splitting failure with larger dilation and the shield-shaped grain models present more faulting failure with a shear band. The squatter hexagon grain models show more splitting failure due to sub-vertical cracks and the slender hexagon grain models show more faulting failures.
- A series of homogeneous GBMs containing circular defects are established to investigate the influence on rock mechanical properties induced by interaction between circular defect and grain boundaries, and the interaction between two circular defects.
- Similar to the classification of pre-existing cracks, the circular defect could be classified as the intra-grain hole (within grain), the inter-grain hole (lying on grain boundaries), and the trans-grain hole (across several grains). The models containing intra-grain hole has more damage area around the hole than other models containing different types of single hole.
- According to the relative location between hole and grain boundaries, there are three patterns including overlapping, coplanar, and non-overlapping, which show different fracturing modes. The overlapping pattern presents shear cracks around two sides of the hole, and the coplanar pattern shows remote tensile cracks. The fracturing mode of the non-overlapping pattern is depended on the connection of the hole and boundary. The shear failures occur at two sides of hole as the connection is located at the side of the hole, and the few tensile failures occur as the connection is located at the roof and foot of the hole.
- The bridge length between two holes has no discernible influence on the damage of specimens containing two holes. The damage induced

by the interaction between two holes increases from the distance of $0.5R$ (radius) to R and decrease from distance of R to $2R$. The interaction between two holes has limited influence on the damage, as the distance increases to $4R$.

- The bridge angle between two holes or holes distribution has a significant influence on fracture development. When the holes are arranged with an inclined angle, the major failure mode is the shear failure, which causes two holes to coalesce. When they are arranged in the vertical or horizontal direction, the major failure mode is the tensile failure and there is no coalescence between two holes.

iii. Rock behaviours at the macro-scale (field scale):

- The GBM is the first time to be applied to field scale simulation to mimic the highly structured rock mass and investigate the influence of different scale fracturing on field scale failure under in-situ stress. Three main excavated models are constructed to investigate the failure modes and predict the damage depth, in terms of single ore drive at different depths, double ore drives with different dipping angles, and double ore drives connected by stopes with different widths.
- The field-scale GBMs with single ore drive under in-situ stress show that buckling occurs at the foot wall induced by sub-vertical fractures and block ejection occurs at the hanging wall due to inclined fractures. The notch height and notch angle increase as the buried depth increases.
- The dipping angle between upper and lower drives has a significant influence on the damage depth around drives. The lower drive at the angle of 65° has the most severe damage than the drives at other dipping angles.
- The dipping angle also impacts the excavated stope connecting two drives, which causes more damage around the steeper stope. The drives connected by steeper stope show more damage induced by sliding along discontinuities and fractures, and the drives connected by flatter stope show more damage induced by buckling.

- The failure modes and damage depth from the numerical results are compared with the in-situ failure cases, which are in good agreement with the engineering results. The approach of GBM is verified to simulate the field-scale rock behaviours and it is useful to investigate the field scale failure induced by microscopic damage evolution and macroscopic fracture development.

8.3 Current Challenges

Firstly, it requires a comprehensive understanding of the methods and data required in a specific project. At different scales, it meets different challenges for data acquisition by different methods. For example, in order to collect accurate grain-scale data, there are a huge amount of SEM images for digital image processing. The software of ImageJ provides several automatic thresholding methods to divide the images into two colours as micro-cracks and background. However, the non-uniform lighting conditions would lead to difficult to distinguish the defects and background, which requires manually adjusting the threshold to determine the appropriate boundary. Moreover, the area and length of defects could be automatically measured by “region of interest (ROI)”. However, the grain size could not be measured automatically, which requires manual measurement to determine the ROI. Additionally, the main geological data collection during the exploration stage could not accurately present the specific rock mass of the ore drive, which requires development cut mapping. Therefore, it requires extra necessary assumptions for numerical modelling.

The challenges of grain-based model construction are mainly associated with the determination and calibration of microscopic parameters. The numerical model should present the heterogeneity induced by mineral geometries (i.e. size and shape). Although this research updates the input approach to mimic the highly heterogeneous rock based on the concept of grain size classification, it still could not represent the actual grain size and the grain shape. Several microscopic parameters require calibration, and all different properties are assigned to different minerals. The only method for calibration

is trail-and-error based on the empirical data against the experimental data under tensile test and uniaxial compression test.

The last challenge is the numerical computational limitation, which is the most common problem in discrete element modelling. The grains in PFC-GBM consist of some particles, which could perform grain fracturing. However, this setup leads to a huge number of particles that should be installed, which is much more than other traditional DEMs. In order to reduce the computation consumption, model simplification is important to be addressed. Therefore, half-scaled specimens are constructed for the laboratory scale tests and nine-scaled rings with the same ratio of grain-to-particle size for the field scale rock mass simulation. Even so, the laboratory scale model still cost approximately 1-2 hours/specimen and the field scale models cost approximately 2-3 days/model.

8.4 Recommendations for Future Work

Despite significant improvements and findings in multiscale rock behaviours using advanced numerical modelling techniques, there still requires further work to improve the accuracy and solve the challenges in multiscale rock behaviours investigation. The main recommendations for future work are listed below:

- The natural mineral grain presents different degree of particle aggregation, which leads to loose or tight structure. Hence, even if the mineral grains have the same shape, they still show different properties. In future work, the particle aggregation should be regarded as a key factor.
- The GBM applied the concept of grain size classification to mimic highly heterogeneous rock, but it is not the same grain size distribution. Hence, in future work, the improvement could consider a similar approach to real fracture process analysis with the aid of digital image processing.

- The equation of heterogeneity index in this research could present the heterogeneity induced by the grain size distribution of constituent minerals, but it is better to consider every grain size in future work.
- The field-scale GBM could simulate the influence of microscopic fracturing evolution on field-scale failure. Hence, in future work, the large-scale pre-existing discontinuities should be applied to the field-scale modelling, which could consider the approach of discrete fracture network. It requires more detailed geological data collection by in-situ mapping.
- In this research, all models are constructed by two dimensions. In future work, 3D models could be constructed under sufficient computation performance.
- In an engineering project, the rockburst is associated with the seismic events. DEM is subjected to load the seismic event. In future work, the seismic data collected by in-situ seismic events monitoring could be applied to the finalised models.

Appendix A: Code of grains construction (Lab-scale)

```
new
set random 10001

; First generate a packing with the desired PSD and volume fractions
; of mineral constituents
domain extent -0.1 0.1 condition destroy
cmat default model linear property kn 1e6
wall gen box -20e-3 20e-3 -30e-3 30e-3
ball distribute resolution 1e-5 ...
    poros 0.08 ...
    numbins 9 ...
    bin 1 ...
        radius 10.00 20.00 ...
        volumefraction 0.03 ...
        group 'pyroxene 01' ...
    bin 2 ...
        radius 20.00 140.00 ...
        volumefraction 0.42 ...
        group 'pyroxene 02' ...
    bin 3 ...
        radius 140.00 240.00 ...
        volumefraction 0.05 ...
        group 'pyroxene 03' ...
    bin 4 ...
        radius 10.00 20.00 ...
        volumefraction 0.05 ...
        group 'plagioclase 01' ...
    bin 5 ...
        radius 20.00 80.00 ...
        volumefraction 0.2 ...
        group 'plagioclase 02' ...
    bin 6 ...
        radius 80.00 190.00 ...
        volumefraction 0.05 ...
        group 'plagioclase 03' ...
    bin 7 ...
        radius 10.00 20.00 ...
        volumefraction 0.05 ...
        group 'biotite 01' ...
    bin 8 ...
        radius 20.00 80.00 ...
        volumefraction 0.12 ...
        group 'biotite 02' ...
    bin 9 ...
        radius 80.00 220.00 ...
        volumefraction 0.03 ...
        group 'biotite 03' ...
    box -20e-3 20e-3 -30e-3 30e-3
ball attribute density 1000 damp 0.7
```

```

cycle 1000 calm 10
solve

geometry set polygons
geometry set seedPoints
define makeSeedPoints
  gs = geom.set.find('seedPoints')
  loop foreach local ball ball.list
    local x = ball.pos.x(ball)
    local y = ball.pos.y(ball)
    local vpos = vector(x,y)
    geom.node.create(gs,vpos)
  endloop
end
@makeSeedPoints

geometry tessellate voronoi toset 'grains'
geometry set 'grains'
geometry delete range x -22e-3 22e-3 not
geometry delete range y -35e-3 35e-3 not

define assign_mtype
  ; loop over all polygons in the 'grains' set and set its material type
  gs = geom.set.find('grains')
  loop foreach p geom.poly.list(gs)
    v = geom.poly.pos(p)
    b = ball.near(v)
    geom.poly.group(p) = ball.group(b)
  endloop
end
@assign_mtype

geometry export 'grains'
save GBM

```

Appendix B: Code of grains construction (Field-scale)

```
new
set random 10001

; First generate a packing with the desired PSD and volume fractions
; of mineral constituents
domain extent -30 30 condition destroy
cmat default model linear property kn 1e6
wall gen box -25 25 -25 25 ; Ring 9 Outside
ball distribute resolution 1e-3 ...
    poros 0.01 ...
    numbins 12 ...
    bin 1 ...
        radius 1139.00 1204.00 ...
        volumefraction 0.125 ...
        group 'pyroxene 01' ...
    bin 2 ...
        radius 1204.00 1269.00 ...
        volumefraction 0.125 ...
        group 'pyroxene 02' ...
    bin 3 ...
        radius 1269.00 1334.00 ...
        volumefraction 0.125 ...
        group 'pyroxene 03' ...
    bin 4 ...
        radius 1334.00 1399.00 ...
        volumefraction 0.125 ...
        group 'pyroxene 04' ...
    bin 5 ...
        radius 1139.00 1204.00 ...
        volumefraction 0.075 ...
        group 'plagioclase 01' ...
    bin 6 ...
        radius 1204.00 1269.00 ...
        volumefraction 0.075 ...
        group 'plagioclase 02' ...
    bin 7 ...
        radius 1269.00 1334.00 ...
        volumefraction 0.075 ...
        group 'plagioclase 03' ...
    bin 8 ...
        radius 1334.00 1399.00 ...
        volumefraction 0.075 ...
        group 'plagioclase 04' ...
    bin 9 ...
        radius 1139.00 1204.00 ...
        volumefraction 0.05 ...
        group 'biotite 01' ...
    bin 10 ...
        radius 1204.00 1269.00 ...
        volumefraction 0.05 ...
```

```

    group 'biotite 02'  ...
bin 11      ...
    radius 1269.00 1334.00 ...
    volumefraction 0.05 ...
    group 'biotite 03'  ...
bin 12      ...
    radius 1334.00 1399.00 ...
    volumefraction 0.05 ...
    group 'biotite 04'  ...
    box -25 25 -25 25
ball attribute density 1000 damp 0.7

;ball delete range box -17.181 17.181 -17.431 17.431
ball delete range x -17.181 17.181 ...
    y -17.431 17.431

wall gen box -17.181 17.181 -17.431 17.431 ; Ring 8 Outside
ball distribute resolution 1e-3  ...
    poros 0.01  ...
    numbins 12  ...
bin 1      ...
    radius 928.00 986.00 ...
    volumefraction 0.125 ...
    group 'pyroxene 01'  ...
bin 2      ...
    radius 986.00 1043.00 ...
    volumefraction 0.125 ...
    group 'pyroxene 02'  ...
bin 3      ...
    radius 1043.00 1101.00 ...
    volumefraction 0.125 ...
    group 'pyroxene 03'  ...
bin 4      ...
    radius 1101.00 1158.00 ...
    volumefraction 0.125 ...
    group 'pyroxene 04'  ...
bin 5      ...
    radius 928.00 986.00 ...
    volumefraction 0.075 ...
    group 'plagioclase 01'  ...
bin 6      ...
    radius 986.00 1043.00 ...
    volumefraction 0.075 ...
    group 'plagioclase 02'  ...
bin 7      ...
    radius 1043.00 1101.00 ...
    volumefraction 0.075 ...
    group 'plagioclase 03'  ...
bin 8      ...
    radius 1101.00 1158.00 ...
    volumefraction 0.075 ...
    group 'plagioclase 04'  ...
bin 9      ...

```



```

radius 928.00 986.00 ...
volumefraction 0.05 ...
group 'biotite 01' ...
bin 10 ...
radius 986.00 1043.00 ...
volumefraction 0.05 ...
group 'biotite 02' ...
bin 11 ...
radius 1043.00 1101.00 ...
volumefraction 0.05 ...
group 'biotite 03' ...
bin 12 ...
radius 1101.00 1158.00 ...
volumefraction 0.05 ...
group 'biotite 04' ...
box -17.181 17.181 -17.431 17.431
ball attribute density 1000 damp 0.7

;ball delete range box -14.573 14.573 -14.823 14.823
ball delete range x -14.573 14.573 ...
y -14.823 14.823

wall gen box -14.573 14.573 -14.823 14.823 ; Ring 7 Outside
ball distribute resolution 1e-3 ...
poros 0.01 ...
numbins 12 ...
bin 1 ...
radius 739.00 789.00 ...
volumefraction 0.125 ...
group 'pyroxene 01' ...
bin 2 ...
radius 789.00 839.00 ...
volumefraction 0.125 ...
group 'pyroxene 02' ...
bin 3 ...
radius 839.00 889.00 ...
volumefraction 0.125 ...
group 'pyroxene 03' ...
bin 4 ...
radius 889.00 939.00 ...
volumefraction 0.125 ...
group 'pyroxene 04' ...
bin 5 ...
radius 739.00 789.00 ...
volumefraction 0.075 ...
group 'plagioclase 01' ...
bin 6 ...
radius 789.00 839.00 ...
volumefraction 0.075 ...
group 'plagioclase 02' ...
bin 7 ...
radius 839.00 889.00 ...
volumefraction 0.075 ...

```

```

    group 'plagioclase 03' ...
bin 8      ...
    radius 889.00 939.00 ...
    volumefraction 0.075 ...
    group 'plagioclase 04' ...
bin 9      ...
    radius 739.00 789.00 ...
    volumefraction 0.05 ...
    group 'biotite 01' ...
bin 10     ...
    radius 789.00 839.00 ...
    volumefraction 0.05 ...
    group 'biotite 02' ...
bin 11     ...
    radius 839.00 889.00 ...
    volumefraction 0.05 ...
    group 'biotite 03' ...
bin 12     ...
    radius 889.00 939.00 ...
    volumefraction 0.05 ...
    group 'biotite 04' ...
    box -14.573 14.573 -14.823 14.823
ball attribute density 1000 damp 0.7

;ball delete range box -12.177 12.177 -12.427 12.427
ball delete range x -12.177 12.177 ...
                y -12.427 12.427

wall gen box -12.177 12.177 -12.427 12.427 ; Ring 6 Outside
ball distribute resolution 1e-3 ...
    poros 0.01 ...
    numbins 12 ...
bin 1      ...
    radius 570.00 613.00 ...
    volumefraction 0.125 ...
    group 'pyroxene 01' ...
bin 2      ...
    radius 613.00 655.00 ...
    volumefraction 0.125 ...
    group 'pyroxene 02' ...
bin 3      ...
    radius 655.00 698.00 ...
    volumefraction 0.125 ...
    group 'pyroxene 03' ...
bin 4      ...
    radius 698.00 740.00 ...
    volumefraction 0.125 ...
    group 'pyroxene 04' ...
bin 5      ...
    radius 570.00 613.00 ...
    volumefraction 0.075 ...
    group 'plagioclase 01' ...
bin 6      ...

```

```

radius 613.00 655.00 ...
volumefraction 0.075 ...
group 'plagioclase 02' ...
bin 7 ...
radius 655.00 698.00 ...
volumefraction 0.075 ...
group 'plagioclase 03' ...
bin 8 ...
radius 698.00 740.00 ...
volumefraction 0.075 ...
group 'plagioclase 04' ...
bin 9 ...
radius 570.00 613.00 ...
volumefraction 0.05 ...
group 'biotite 01' ...
bin 10 ...
radius 613.00 655.00 ...
volumefraction 0.05 ...
group 'biotite 02' ...
bin 11 ...
radius 655.00 698.00 ...
volumefraction 0.05 ...
group 'biotite 03' ...
bin 12 ...
radius 698.00 740.00 ...
volumefraction 0.05 ...
group 'biotite 04' ...
box -12.177 12.177 -12.427 12.427
ball attribute density 1000 damp 0.7

;ball delete range box -9.993 9.993 -10.243 10.243
ball delete range x -9.993 9.993 ...
y -10.243 10.243

wall gen box -9.993 9.993 -10.243 10.243 ; Ring 5 Outside
ball distribute resolution 1e-3 ...
poros 0.01 ...
numbins 12 ...
bin 1 ...
radius 423.00 458.00 ...
volumefraction 0.125 ...
group 'pyroxene 01' ...
bin 2 ...
radius 458.00 493.00 ...
volumefraction 0.125 ...
group 'pyroxene 02' ...
bin 3 ...
radius 493.00 528.00 ...
volumefraction 0.125 ...
group 'pyroxene 03' ...
bin 4 ...
radius 528.00 563.00 ...
volumefraction 0.125 ...

```

```

    group 'pyroxene 04' ...
bin 5      ...
    radius 423.00 458.00 ...
    volumefraction 0.075 ...
    group 'plagioclase 01' ...
bin 6      ...
    radius 458.00 493.00 ...
    volumefraction 0.075 ...
    group 'plagioclase 02' ...
bin 7      ...
    radius 493.00 528.00 ...
    volumefraction 0.075 ...
    group 'plagioclase 03' ...
bin 8      ...
    radius 528.00 563.00 ...
    volumefraction 0.075 ...
    group 'plagioclase 04' ...
bin 9      ...
    radius 423.00 458.00 ...
    volumefraction 0.05 ...
    group 'biotite 01' ...
bin 10     ...
    radius 458.00 493.00 ...
    volumefraction 0.05 ...
    group 'biotite 02' ...
bin 11     ...
    radius 493.00 528.00 ...
    volumefraction 0.05 ...
    group 'biotite 03' ...
bin 12     ...
    radius 528.00 563.00 ...
    volumefraction 0.05 ...
    group 'biotite 04' ...
    box -9.993 9.993 -10.243 10.243
ball attribute density 1000 damp 0.7

;ball delete range box -8.021 8.021 -8.271 8.271
ball delete range x -8.021 8.021 ...
    y -8.271 8.271

wall gen box -8.021 8.021 -8.271 8.271 ; Ring 4 Outside
ball distribute resolution 1e-3 ...
    poros 0.01 ...
    numbins 12 ...
bin 1      ...
    radius 297.00 325.00 ...
    volumefraction 0.125 ...
    group 'pyroxene 01' ...
bin 2      ...
    radius 325.00 352.00 ...
    volumefraction 0.125 ...
    group 'pyroxene 02' ...
bin 3      ...

```

```

radius 352.00 380.00 ...
volumefraction 0.125 ...
group 'pyroxene 03' ...
bin 4 ...
radius 380.00 407.00 ...
volumefraction 0.125 ...
group 'pyroxene 04' ...
bin 5 ...
radius 297.00 325.00 ...
volumefraction 0.075 ...
group 'plagioclase 01' ...
bin 6 ...
radius 325.00 352.00 ...
volumefraction 0.075 ...
group 'plagioclase 02' ...
bin 7 ...
radius 352.00 380.00 ...
volumefraction 0.075 ...
group 'plagioclase 03' ...
bin 8 ...
radius 380.00 407.00 ...
volumefraction 0.075 ...
group 'plagioclase 04' ...
bin 9 ...
radius 297.00 325.00 ...
volumefraction 0.05 ...
group 'biotite 01' ...
bin 10 ...
radius 325.00 352.00 ...
volumefraction 0.05 ...
group 'biotite 02' ...
bin 11 ...
radius 352.00 380.00 ...
volumefraction 0.05 ...
group 'biotite 03' ...
bin 12 ...
radius 380.00 407.00 ...
volumefraction 0.05 ...
group 'biotite 04' ...
box -8.021 8.021 -8.271 8.271
ball attribute density 1000 damp 0.7

;ball delete range box -6.260 6.260 -6.510 6.510
ball delete range x -6.260 6.260 ...
y -6.510 6.510

wall gen box -6.260 6.260 -6.510 6.510 ; Ring 3 Outside
ball distribute resolution 1e-3 ...
poros 0.01 ...
numbins 12 ...
bin 1 ...
radius 192.00 212.00 ...
volumefraction 0.125 ...

```

```

    group 'pyroxene 01' ...
bin 2      ...
    radius 212.00 232.00 ...
    volumefraction 0.125 ...
    group 'pyroxene 02' ...
bin 3      ...
    radius 232.00 252.00 ...
    volumefraction 0.125 ...
    group 'pyroxene 03' ...
bin 4      ...
    radius 252.00 272.00 ...
    volumefraction 0.125 ...
    group 'pyroxene 04' ...
bin 5      ...
    radius 192.00 212.00 ...
    volumefraction 0.075 ...
    group 'plagioclase 01' ...
bin 6      ...
    radius 212.00 232.00 ...
    volumefraction 0.075 ...
    group 'plagioclase 02' ...
bin 7      ...
    radius 232.00 252.00 ...
    volumefraction 0.075 ...
    group 'plagioclase 03' ...
bin 8      ...
    radius 252.00 272.00 ...
    volumefraction 0.075 ...
    group 'plagioclase 04' ...
bin 9      ...
    radius 192.00 212.00 ...
    volumefraction 0.05 ...
    group 'biotite 01' ...
bin 10     ...
    radius 212.00 232.00 ...
    volumefraction 0.05 ...
    group 'biotite 02' ...
bin 11     ...
    radius 232.00 252.00 ...
    volumefraction 0.05 ...
    group 'biotite 03' ...
bin 12     ...
    radius 252.00 272.00 ...
    volumefraction 0.05 ...
    group 'biotite 04' ...
    box -6.260 6.260 -6.510 6.510
ball attribute density 1000 damp 0.7

;ball delete range box -4.712 4.712 -4.962 4.962
ball delete range x -4.712 4.712 ...
    y -4.962 4.962

wall gen box -4.712 4.712 -4.962 4.962 ; Ring 2 Outside

```

```

ball distribute resolution 1e-3 ...
  poros 0.01 ...
  numbins 12 ...
  bin 1 ...
    radius 136.00 149.00 ...
    volumefraction 0.125 ...
    group 'pyroxene 01' ...
  bin 2 ...
    radius 149.00 161.00 ...
    volumefraction 0.125 ...
    group 'pyroxene 02' ...
  bin 3 ...
    radius 161.00 174.00 ...
    volumefraction 0.125 ...
    group 'pyroxene 03' ...
  bin 4 ...
    radius 174.00 186.00 ...
    volumefraction 0.125 ...
    group 'pyroxene 04' ...
  bin 5 ...
    radius 136.00 149.00 ...
    volumefraction 0.075 ...
    group 'plagioclase 01' ...
  bin 6 ...
    radius 149.00 161.00 ...
    volumefraction 0.075 ...
    group 'plagioclase 02' ...
  bin 7 ...
    radius 161.00 174.00 ...
    volumefraction 0.075 ...
    group 'plagioclase 03' ...
  bin 8 ...
    radius 174.00 186.00 ...
    volumefraction 0.075 ...
    group 'plagioclase 04' ...
  bin 9 ...
    radius 136.00 149.00 ...
    volumefraction 0.05 ...
    group 'biotite 01' ...
  bin 10 ...
    radius 149.00 161.00 ...
    volumefraction 0.05 ...
    group 'biotite 02' ...
  bin 11 ...
    radius 161.00 174.00 ...
    volumefraction 0.05 ...
    group 'biotite 03' ...
  bin 12 ...
    radius 174.00 186.00 ...
    volumefraction 0.05 ...
    group 'biotite 04' ...
    box -4.712 4.712 -4.962 4.962
ball attribute density 1000 damp 0.7

```

```
;ball delete range box -3.375 3.375 -3.625 3.625
ball delete range x -3.375 3.375 ...
y -3.625 3.625
```

```
wall gen box -3.375 3.375 -3.625 3.625 ; Ring 1 Outside
```

```
ball distribute resolution 1e-3 ...
poros 0.01 ...
numbins 12 ...
bin 1 ...
radius 80.00 85.00 ...
volumefraction 0.125 ...
group 'pyroxene 01' ...
bin 2 ...
radius 85.00 90.00 ...
volumefraction 0.125 ...
group 'pyroxene 02' ...
bin 3 ...
radius 90.00 95.00 ...
volumefraction 0.125 ...
group 'pyroxene 03' ...
bin 4 ...
radius 95.00 100.00 ...
volumefraction 0.125 ...
group 'pyroxene 04' ...
bin 5 ...
radius 80.00 85.00 ...
volumefraction 0.075 ...
group 'plagioclase 01' ...
bin 6 ...
radius 85.00 90.00 ...
volumefraction 0.075 ...
group 'plagioclase 02' ...
bin 7 ...
radius 90.00 95.00 ...
volumefraction 0.075 ...
group 'plagioclase 03' ...
bin 8 ...
radius 95.00 100.00 ...
volumefraction 0.075 ...
group 'plagioclase 04' ...
bin 9 ...
radius 80.00 85.00 ...
volumefraction 0.05 ...
group 'biotite 01' ...
bin 10 ...
radius 85.00 90.00 ...
volumefraction 0.05 ...
group 'biotite 02' ...
bin 11 ...
radius 90.00 95.00 ...
volumefraction 0.05 ...
group 'biotite 03' ...
```



```

        bin 12          ...
        radius 95.00 100.00 ...
        volumefraction 0.05 ...
        group 'biotite 04' ...
        box -3.375 3.375 -3.625 3.625
ball attribute density 1000 damp 0.7

cycle 1000 calm 10
solve

geometry set polygons
geometry set seedPoints
define makeSeedPoints
  gs = geom.set.find('seedPoints')
  loop foreach local ball ball.list
    local x = ball.pos.x(ball)
    local y = ball.pos.y(ball)
    local vpos = vector(x,y)
    geom.node.create(gs,vpos)
  endloop
end
@makeSeedPoints

geometry tessellate voronoi toset 'grains'
geometry set 'grains'
geometry delete range x -23 23 not
geometry delete range y -23 23 not

define assign_mtype
; loop over all polygons in the 'grains' set and set its material type
gs = geom.set.find('grains')
loop foreach p geom.poly.list(gs)
  v = geom.poly.pos(p)
  b = ball.near(v)
  geom.poly.group(p) = ball.group(b)
endloop
end
@assign_mtype

geometry export 'grains'
save GBM

```

Appendix C: Code of specimen construction (Lab-scale)

```
new
res GBM

wall delete
ball dele

cmat default model linear method deform emod 1.0e9 kratio 0.0
cmat default property dp_nratio 0.5

; create walls that extend past the edges of the sample
wall create vertices -15e-3,25e-3 15e-3,25e-3 id 1 ;top
wall create vertices -15e-3,-25e-3 15e-3,-25e-3 id 2 ;bot
wall create vertices -12.5e-3,-30e-3 -12.5e-3,30e-3 id 3 ;left
wall create vertices 12.5e-3,-30e-3 12.5e-3,30e-3 id 4;right
;wall gen box -50e-3 50e-3 -25e-3 25e-3

set random 10001
ball distribute porosity 0.01 radius 1e-4 box -12.5e-3 12.5e-3 -25e-3 25e-3
ball attribute density 2500 damp 0.7

; Calm the system
cycle 1000 calm 10
; Solve the system to a target limit (here the average force ratio)
; Use density scaling to quickly reach equilibrium
set timestep scale
solve aratio 1e-4
set timestep auto
calm

; now overlay the grains information
geometry import 'grains.geom'

define assignGroups
; loop over all polygons in the 'grains' set
gs = geom.set.find('grains')
loop foreach p geom.poly.list(gs)
  id = geom.poly.id(p)
  mtype = geom.poly.group(p)
  gname = 'grain_' + string(id)
  command
    geometry copy source 'grains' target 'cell' polygons range id @id
    ball group @gname range geometry 'cell' count odd
    ball group @mtype slot 2 range group @gname
    geometry delete set 'cell'
  endcommand
endloop
end
@assignGroups

save specimen
```

Appendix D: Code of rock mass construction (field-scale)

```
new
res GBM

wall delete
ball dele

cmat default model linear method deform emod 1.0e9 kratio 1.0
cmat default property dp_nratio 0.5

; create walls that extend past the edges of the sample
wall create vertices -20,20 20,20 id 1 ;top
wall create vertices -20,-20 20,-20 id 2 ;bot
wall create vertices -20,-20 -20,20 id 3 ;left
wall create vertices 20,-20 20,20 id 4 ;right
;wall gen box -50e-3 50e-3 -25e-3 25e-3

set random 10001
ball distribute porosity 0.1 radius 317e-3 box -20 20 -20 20
ball attribute density 2650 damp 0.7

;wall generate box -17.181 17.181 -17.431 17.431 ; Ring 9 Inside

ball delete range x -17.181 17.181 ...
                y -17.431 17.431

ball distribute porosity 0.1 radius 261e-3 box -17.181 17.181 -17.431 17.431
ball attribute density 2650 damp 0.7

;wall generate box -14.573 14.573 -14.823 14.823 ; Ring 8 Inside

ball delete range x -14.573 14.573 ...
                y -14.823 14.823

ball distribute porosity 0.1 radius 210e-3 box -14.573 14.573 -14.823 14.823
ball attribute density 2650 damp 0.7

;wall generate box -12.177 12.177 -12.427 12.427 ; Ring 7 Inside

ball delete range x -12.177 12.177 ...
                y -12.427 12.427

ball distribute porosity 0.1 radius 164e-3 box -12.177 12.177 -12.427 12.427
ball attribute density 2650 damp 0.7

;wall generate box -9.993 9.993 -10.243 10.243 ; Ring 6 Inside

ball delete range x -9.993 9.993 ...
                y -10.243 10.243

ball distribute porosity 0.1 radius 123e-3 box -9.993 9.993 -10.243 10.243
```

```

ball attribute density 2650 damp 0.7

;wall generate box -8.021 8.021 -8.271 8.271 ; Ring 5 Inside

ball delete range x -8.021 8.021 ...
                y -8.271 8.271

ball distribute porosity 0.1 radius 88e-3 box -8.021 8.021 -8.271 8.271
ball attribute density 2650 damp 0.7

;wall generate box -6.260 6.260 -6.510 6.510 ; Ring 4 Inside

ball delete range x -6.260 6.260 ...
                y -6.510 6.510

ball distribute porosity 0.1 radius 55e-3 box -6.260 6.260 -6.510 6.510
ball attribute density 2650 damp 0.7

;wall generate box -4.712 4.712 -4.962 4.962 ; Ring 3 Inside

ball delete range x -4.712 4.712 ...
                y -4.962 4.962

ball distribute porosity 0.1 radius 35e-3 box -4.712 4.712 -4.962 4.962
ball attribute density 2650 damp 0.7

;wall generate box -3.375 3.375 -3.625 3.625 ; Ring 2 Inside

ball delete range x -3.375 3.375 ...
                y -3.625 3.625

ball distribute porosity 0.1 radius 22e-3 box -3.375 3.375 -3.625 3.625
ball attribute density 2650 damp 0.7

wall generate circle position 0 0.25 radius 2.25 ; Circular

ball delete range circle center 0 0.25 radius 2.25

wall generate box -2.25 2.25 -2.5 0.25 ; Rectangular

ball delete range x -2.25 2.25 ...
                y -2.5 0.25

wall property kn 1e9 ks 1e9

; Calm the system
cycle 1000 calm 10
; Solve the system to a target limit (here the average force ratio)
; Use density scaling to quickly reach equilibrium
set timestep scale
solve aratio 1e-4
set timestep auto
calm

```

```

; now overlay the grains information
geometry import 'grains.geom'

define assignGroups
; loop over all polygons in the 'grains' set
gs = geom.set.find('grains')
loop foreach p geom.poly.list(gs)
  id = geom.poly.id(p)
  mtype = geom.poly.group(p)
  gname = 'grain_' + string(id)
  command
    geometry copy source 'grains' target 'cell' polygons range id @id
    ball group @gname range geometry 'cell' count odd
    ball group @mtype slot 2 range group @gname
    geometry delete set 'cell'
  endcommand
endloop
end
@assignGroups

save specimen

```

Appendix E: Code of contact installation

rest specimen

```
contact model linearpbond range group 'pyroxene 01'
contact method bond gap 0.5e-4 range group 'pyroxene 01'

; set linear stiffness
contact method deform emod 58.0e9 krat 2.0 range group 'pyroxene 01'

; set stiffness of bond material
contact method pb_deform emod 58.0e9 krat 2.0 range group 'pyroxene 01'

; set bond strengths
contact property pb_ten 305.0e6 pb_coh 250.0e6 pb_fa 35.0 range group 'pyroxene 01'

; set some damping at the contacts
contact property dp_nratio 0.5 range group 'pyroxene 01'

; set ball-ball friction to non-zero value
contact property fric 1.0 range group 'pyroxene 01'

; Reset ball displacement
ball attribute displacement multiply 0.0

; Set the linear force to 0.0 and force a reset of the linear contact forces.
contact property lin_force 0.0 0.0 lin_mode 1
ball attribute contactforce multiply 0.0 contactmoment multiply 0.0

contact model linearpbond range group 'pyroxene 02'
contact method bond gap 0.5e-4 range group 'pyroxene 02'
; set linear stiffness
contact method deform emod 58.0e9 krat 2.0 range group 'pyroxene 02'

; set stiffness of bond material
contact method pb_deform emod 58.0e9 krat 2.0 range group 'pyroxene 02'

; set bond strengths
contact property pb_ten 305.0e6 pb_coh 250.0e6 pb_fa 35.0 range group 'pyroxene 02'

; set some damping at the contacts
contact property dp_nratio 0.5 range group 'pyroxene 02'

; set ball-ball friction to non-zero value
contact property fric 1.0 range group 'pyroxene 02'

; Reset ball displacement
ball attribute displacement multiply 0.0

; Set the linear force to 0.0 and force a reset of the linear contact forces.
contact property lin_force 0.0 0.0 lin_mode 1
ball attribute contactforce multiply 0.0 contactmoment multiply 0.0
```

```

contact model linearpbond range group 'pyroxene 03'
contact method bond gap 0.5e-4 range group 'pyroxene 03'

; set linear stiffness
contact method deform emod 58.0e9 krat 2.0 range group 'pyroxene 03'

; set stiffness of bond material
contact method pb_deform emod 58.0e9 krat 2.0 range group 'pyroxene 03'

; set bond strengths
contact property pb_ten 305.0e6 pb_coh 250.0e6 pb_fa 35.0 range group 'pyroxene 03'

; set some damping at the contacts
contact property dp_nratio 0.5 range group 'pyroxene 03'

; set ball-ball friction to non-zero value
contact property fric 1.0 range group 'pyroxene 03'

; Reset ball displacement
ball attribute displacement multiply 0.0

; Set the linear force to 0.0 and force a reset of the linear contact forces.
contact property lin_force 0.0 0.0 lin_mode 1
ball attribute contactforce multiply 0.0 contactmoment multiply 0.0

contact model linearpbond range group 'plagioclase 01'
contact method bond gap 0.5e-4 range group 'plagioclase 01'

; set linear stiffness
contact method deform emod 65.0e9 krat 2.0 range group 'plagioclase 01'

; set stiffness of bond material
contact method pb_deform emod 65.0e9 krat 2.0 range group 'plagioclase 01'

; set bond strengths
contact property pb_ten 333.0e6 pb_coh 300.0e6 pb_fa 35.0 range group 'plagioclase 01'

; set some damping at the contacts
contact property dp_nratio 0.5 range group 'plagioclase 01'

; set ball-ball friction to non-zero value
contact property fric 1.0 range group 'plagioclase 01'

; Reset ball displacement
ball attribute displacement multiply 0.0

; Set the linear force to 0.0 and force a reset of the linear contact forces.
contact property lin_force 0.0 0.0 lin_mode 1
ball attribute contactforce multiply 0.0 contactmoment multiply 0.0

contact model linearpbond range group 'plagioclase 02'
contact method bond gap 0.5e-4 range group 'plagioclase 02'

```

```

; set linear stiffness
contact method deform emod 65.0e9 krat 2.0 range group 'plagioclase 02'

; set stiffness of bond material
contact method pb_deform emod 65.0e9 krat 2.0 range group 'plagioclase 02'

; set bond strengths
contact property pb_ten 333.0e6 pb_coh 300.0e6 pb_fa 35.0 range group 'plagioclase 02'

; set some damping at the contacts
contact property dp_nratio 0.5 range group 'plagioclase 02'

; set ball-ball friction to non-zero value
contact property fric 1.0 range group 'plagioclase 02'

; Reset ball displacement
ball attribute displacement multiply 0.0

; Set the linear force to 0.0 and force a reset of the linear contact forces.
contact property lin_force 0.0 0.0 lin_mode 1
ball attribute contactforce multiply 0.0 contactmoment multiply 0.0

contact model linearpbond range group 'plagioclase 03'
contact method bond gap 0.5e-4 range group 'plagioclase 03'

; set linear stiffness
contact method deform emod 65.0e9 krat 2.0 range group 'plagioclase 03'

; set stiffness of bond material
contact method pb_deform emod 65.0e9 krat 2.0 range group 'plagioclase 03'

; set bond strengths
contact property pb_ten 333.0e6 pb_coh 300.0e6 pb_fa 35.0 range group 'plagioclase 03'

; set some damping at the contacts
contact property dp_nratio 0.5 range group 'plagioclase 03'

; set ball-ball friction to non-zero value
contact property fric 1.0 range group 'plagioclase 03'

; Reset ball displacement
ball attribute displacement multiply 0.0

; Set the linear force to 0.0 and force a reset of the linear contact forces.
contact property lin_force 0.0 0.0 lin_mode 1
ball attribute contactforce multiply 0.0 contactmoment multiply 0.0

contact model linearpbond range group 'biotite 01'
contact method bond gap 0.5e-4 range group 'biotite 01'

; set linear stiffness
contact method deform emod 61.0e9 krat 1.5 range group 'biotite 01'

```



```

; set stiffness of bond material
contact method pb_deform emod 61.0e9 krat 1.5 range group 'biotite 01'

; set bond strengths
contact property pb_ten 317.0e6 pb_coh 270.0e6 pb_fa 35.0 range group 'biotite 01'

; set some damping at the contacts
contact property dp_nratio 0.5 range group 'biotite 01'

; set ball-ball friction to non-zero value
contact property fric 1.0 range group 'biotite 01'

; Reset ball displacement
ball attribute displacement multiply 0.0

; Set the linear force to 0.0 and force a reset of the linear contact forces.
contact property lin_force 0.0 0.0 lin_mode 1
ball attribute contactforce multiply 0.0 contactmoment multiply 0.0

contact model linearpbond range group 'biotite 02'
contact method bond gap 0.5e-4 range group 'biotite 02'

; set linear stiffness
contact method deform emod 61.0e9 krat 1.5 range group 'biotite 02'

; set stiffness of bond material
contact method pb_deform emod 61.0e9 krat 1.5 range group 'biotite 02'

; set bond strengths
contact property pb_ten 317.0e6 pb_coh 270.0e6 pb_fa 35.0 range group 'biotite 02'

; set some damping at the contacts
contact property dp_nratio 0.5 range group 'biotite 02'

; set ball-ball friction to non-zero value
contact property fric 1.0 range group 'biotite 02'

; Reset ball displacement
ball attribute displacement multiply 0.0

; Set the linear force to 0.0 and force a reset of the linear contact forces.
contact property lin_force 0.0 0.0 lin_mode 1
ball attribute contactforce multiply 0.0 contactmoment multiply 0.0

contact model linearpbond range group 'biotite 03'
contact method bond gap 0.5e-4 range group 'biotite 03'

; set linear stiffness
contact method deform emod 1.0e9 krat 1.5 range group 'biotite 03'

; set stiffness of bond material
contact method pb_deform emod 61.0e9 krat 1.5 range group 'biotite 03'

```

```

; set bond strengths
contact property pb_ten 317.0e6 pb_coh 270.0e6 pb_fa 35.0 range group 'biotite 03'

; set some damping at the contacts
contact property dp_nratio 0.5 range group 'biotite 03'

; set ball-ball friction to non-zero value
contact property fric 1.0 range group 'biotite 03'

; Reset ball displacement
ball attribute displacement multiply 0.0

; Set the linear force to 0.0 and force a reset of the linear contact forces.
contact property lin_force 0.0 0.0 lin_mode 1
ball attribute contactforce multiply 0.0 contactmoment multiply 0.0

geometry import 'grains.geom'

dfn gimport dominance ordered geometry grains name grain_1
; Set dfn properties to be assigned to intersecting contacts
; Friction angle is 35 degrees
dfn property sj_kn 4e9 sj_ks 2e9 sj_fric 1.2 sj_coh 60.0e6 sj_ten 10.0e6 sj_fa 32.0 sj_large 1

; Apply smoothjoint contact model to contacts intercepted by fracture
dfn model name smoothjoint install dist 0.5e-4

; Ensure that new contacts intersecting the fracture are set to the sj contact model
dfn model name smoothjoint activate

cycle 1000
solve aratio 1e-5
save parallel_bonded_smooth_joint

```

Appendix F: Code of pre-existing fracture or stope excavation

```
res parallel_bonded_smooth_joint

wall delete range x -10 -4 y -13 -7
wall delete range x 4 10 y 7 13

[ballFriction=0.0]
[wallFriction=0.0]
;[filename='loose']
;-----set pre-existing fracture angle-----
[frac_dip=55]

;;;fracture length and width
[a_val=12.208] ;half length of fracture
[w_val=1.000] ;half width of fracture
[dip_val=55*math.pi/180] ;pre-existing fracture angle
; Load utility |FISH| functions for later use

;;;set pre-existing fracture angle----dip>0 degree, using the follow
def frac_para
  _xleft=(-1)*a_val ;left position of pre-existing fracture
  _xright=a_val ;right position of pre-existing fracture
  _ydown=(-1)*w_val ;bottom position of pre-existing fracture
  _yup=w_val ;top position of pre-existing fracture
  ;-----if dip>0 the following command use ;
  k1_val=-1/math.tan(dip_val) ;slop of left-down and right-up
  b1_val=a_val/math.sin(dip_val) ;y position of line cut y axial
  k2_val=math.tan(dip_val) ;slop of left-up and right-down
  b3_val=w_val/math.cos(dip_val) ;y position of line cut y axial
end
@frac_para

;wall generate group w1 box @_xleft @_xright @_ydown @_yup onewall

;-----if dip>0 the following command use ;
;wall rotate angle @frac_dip point 0 0 range group w1

;;;dip=0 degree
;define mydel(dummy,bp)
;mydel=0
;local _x=ball.pos.x(bp)
;local _z=ball.pos.y(bp)
;if _z <= _yup
  ;if _z >= _ydown
    ;if _x>=_xleft
      ;if _x<=_xright
        ; mydel=1
      ;endif
    ;endif
  ;endif
;endif
;endif
;endif
```

```

;end
;@frac_para
;;;dip>0 degree
;-----if dip>0 the following command use ;
define mydel(dummy,bp)
mydel=0
local _x=ball.pos.x(bp)
local _z=ball.pos.y(bp)
if _z <= k2_val*_x+b3_val
  if _z >= k2_val*_x-b3_val
    if _z>=k1_val*_x-b1_val
      if _z<=k1_val*_x+b1_val
        mydel=1
      endif
    endif
  endif
endif
end
@frac_para

ball del range fish @mydel

save hole

```